
Environmentally driven suppression of star formation in galaxies over the last 10 billion years

Matteo Fossati



München 2016

Environmentally driven suppression of star formation in galaxies over the last 10 billion years

Matteo Fossati

Dissertation
an der Fakultät für Physik
der Ludwig-Maximilians-Universität
München

vorgelegt von
Matteo Fossati
aus Monza, Italien

München, den 22.09.2016

Erstgutachter: Priv.-Doz. Dr. Roberto P. Saglia

Zweitgutachter: Prof. Dr. Andreas Burkert

Tag der mündlichen Prüfung: 07.11.2016

Zusammenfassung

Die große Menge an photometrischen und spektroskopischen Daten, die uns in den letzten Jahrzehnten aus umfangreichen Datensätzen zur Verfügung stehen, hat zu bedeutenden Erkenntnissen über die Galaxienentwicklung in den unterschiedlichen kosmischen Epochen geführt. Beobachtungen und Simulationen zeigen übereinstimmend, dass zwei Klassen von Prozessen für die Entwicklung von Galaxien ausschlaggebend sind: i) Innere Prozesse, die eng mit der Form und der Tiefe des Gravitationspotentials der Galaxie korreliert sind (Kauffmann et al., 2003; Smith et al., 2009; Lang et al., 2014). ii) Äußere Prozesse, die abhängig von der jeweiligen Umgebung der Galaxie durch Wechselwirkungen innerhalb der Galaxiengruppen und Galaxienhaufen hervorgerufen werden (Balogh et al., 2000; Boselli & Gavazzi, 2006, 2014). Die Natur der zugrundeliegenden physikalischen Prozesse und die relative Wichtigkeit von äußeren bzw. inneren Prozessen unterschiedlicher kosmischer Epochen und Galaxienmassen gehört zu den wichtigsten offenen Fragen der modernen Astronomie.

In dieser Arbeit untersuchen wir die Rolle der Galaxienumgebung. Wir entwickeln eine neuartige Methode zur Kalibration physikalisch motivierter Größen (z.B. Masse des Halos) ausgehend vom lokalen Dichtefeld der Galaxien (durch das Zählen benachbarter Objekte). Mit Hilfe dieses Verfahrens können wir auch ermitteln, ob sich die Galaxie im tiefsten Punkt des Gravitationspotentials ihres Halos befindet, d.h. ob es sich um eine zentrale Galaxie oder eine Satellitengalaxie handelt. Jede Galaxie hat dann zum einen genau definierte beobachtbare Eigenschaften (z.B. stellare Masse, lokale Galaxiendichte), zum anderen werden die Eigenschaften ihrer Umgebung probabilistisch aus unserer Kalibrationsmethode gewonnen (z.B. Masse des Halos, Klassifikation als zentrale oder Satellitengalaxie). Letzteres erreichen wir, indem wir die beobachteten Galaxien einem synthetischen Datensatz zuordnen, den wir anhand von semi-analytischen Modellen zur Galaxienentstehung erzeugen. Dabei wählen wir die synthetischen Datensätze so, dass sie auf die Eigenschaften der jeweils beobachteten sample von Galaxien abgestimmt sind.

Wir wenden unsere Methode auf den 3D-HST Survey an, welcher mit dem *Hubble Space Telescope* durchgeführt wurde und genaue Rotverschiebungen durch spaltlose Spektroskopie für die große Mehrzahl der beobachteten Galaxien gemessen hat. Der gewonnene Datensatz besteht aus Galaxien in fünf Gebieten mit langer Belichtungszeit (engl. deep fields) und ist magnitudenlimitiert (engl. magnitude limited). Die Genauigkeit der Rotverschiebungsmessungen ist ausschlaggebend für die Rekonstruktion des Dichtefelds. Bisherige Datensätze mit genauen Rotverschiebungen sind jedoch durch ihre geringe Objektzahl begrenzt und

werden dadurch verfälscht, dass sie überwiegend besonders helle Galaxien untersuchen. Die Verbindung von 3D-HST Spektroskopie mit tiefer Photometrie aus dem CANDELS Survey ermöglicht es, diese bisherigen Beschränkungen aufzuheben, und stellt somit einen idealen Datensatz für eine genaue Quantifizierung der Galaxienumgebung für eine Rotverschiebung von $0.5 < z < 2.0$ zur Verfügung. Wir wenden unsere Methode auch auf einen Datensatz bzgl. des lokalen Universums an, der vom Sloan Digital Sky Survey stammt. Dadurch können wir den Einfluss der Galaxienumgebung an einem homogenen Datensatz in einer kosmischen Zeitspanne von 10 Milliarden Jahren auswerten.

Wir verwenden die dadurch gewonnenen Kataloge der Galaxienumgebungen (die wir veröffentlichen), um das von der Umgebung verursachte “Quenching” (Unterdrückung aus dem engl.) der Sternentstehung in Satellitengalaxien zu untersuchen. Wir berechnen den Anteil von passiven Zentralen- und Satellitengalaxien in Abhängigkeit von stellarer Masse, Halo-Masse und Rotverschiebung. Daraus ermitteln wir die Effizienz von Quenching in Satelliten: Darunter verstehen wir den Anteil der Galaxien, deren Sternentstehung durch Prozesse in ihrer Umgebung stärker unterdrückt worden ist als nur durch innere Prozesse. Anhand unserer synthetischen Kataloge schätzen wir die Zeitskala des Quenching in Satelliten auf $t_{\text{quench}} \sim 2 - 5$ Gyr; wobei wir längere Zeitskalen bei geringerer stellarer Masse und niedrigerer Rotverschiebung finden, diese allerdings unabhängig von der Halo-Masse sind. Das deutet darauf hin, dass “Quenching” eintritt, wenn das Gasreservoir der Satelliten erschöpft ist, ohne dass zusätzliches Gas von Aussen einfällt. Außerdem folgt daraus, dass der dynamische Verlust des Gases (z.B. durch das Entfernen des Kaltgasreservoirs durch hydrodynamische Prozesse) ineffizient im Massenbereich der betrachteten Halos aus dem 3D-HST-Datensatz ist. Die sogar deutlich längere Zeitskala des “Quenching” bei $z=0$ weist darauf hin, dass die Erschöpfung des Gasreservoirs von allen Prozessen in der Umgebung hauptsächlich für das “Quenching” verantwortlich ist. Für die massereichsten Halos beobachten wir dagegen kürzere “Quenching”-Zeiten, welche man durch eine erhöhte Effizienz schneller dynamischer Prozesse in der Halo-Umgebung erklären kann. Aus der Verteilung der Sternentstehungsraten in den 3D-HST Galaxien ermitteln wir, dass man die zeitliche Entwicklung des Quenching einteilen kann in eine Verzögerungsphase, in der sich Satelliten ähnlich wie zentrale Galaxien der gleichen stellaren Masse verhalten, und eine Phase in der die Sternentstehungsrate schnell sinkt, wie bereits für das lokale Universum gezeigt (Wetzell et al., 2013). Daraus schließen wir, dass Satelliten während des Einfalls in den Galaxienhaufen große Reserven von mehrphasigem Gas beibehalten, und dass dieses Gas ein normales Maß an Sternentstehungsraten für die langen beobachteten Zeitskalen des Quenching aufrechterhalten muss.

Statistische Auswertungen großer Galaxien-Datensätze ergänzt man üblicherweise mit detaillierten Untersuchungen von Einzelobjekten, die eindeutig eine Entwicklung durchlaufen, die durch äußere Prozesse aus der Umgebung hervorgerufen wird, um die zugrundeliegende Physik, sowohl bei niedrigen als auch bei hohen Rotverschiebungen, zu verstehen. In dieser Dissertation führen wir anhand von aufgelöster Spektroskopie die erste Analyse eines solchen Objekts durch, nämlich der Galaxie ESO137-001, im den Norma-Galaxienhaufen einfällt. Diese Galaxie weist eindrucksvolle Gasschweife auf, die aus mehrphasigem Gas bestehen, welches von der Scheibe der Galaxie durch Staudruck

(engl. ram pressure) abgestreift wird. Um ein vollständiges Bild der Wirkungsweise des Staudrucks in dieser Galaxie zu erhalten, benötigt man ein umfassendes Verständnis der Gaskinematik und der Diagnostik der Emissionslinienspektren. Diese erhalten wir, indem wir die einzigartigen Möglichkeiten des Multi Unit Spectroscopic Explorer (MUSE), seit kurzem am Very Large Telescope, ausschöpfen. Durch die Untersuchung der Flächenhelligkeit der Rekombinationslinie $H\alpha$ des Wasserstoffs und der Kinematik im gesamten Gasschweif in Verbindung mit dem stellaren Geschwindigkeitsfeld finden wir, dass der Staudruck das Kaltgasreservoir der äußeren Scheibe der Galaxie vollständig entfernt hat, und dass dem Schweif nur noch aus dem inneren Bereich der Galaxie mit Gas versorgt wird. Unsere Analyse zeigt auch, dass das Abstreifen des Gases nicht das Rotationsmuster des ionisierten Gases verändert, welches mit der Rotationskurve der stellaren Komponente übereinstimmt. Die Ionisation des Schweifes wird durch turbulente Schocks angetrieben sowie durch die Photoionisation durch junge, massereiche Sterne: Im abgeschweiften Gas findet man tatsächlich eine signifikante Sternentstehung.

Die Quantifizierung der Galaxienumgebung in größeren und tieferen Galaxiendatensätzen aus erdgestützten und Weltraumbeobachtungen wird in naher Zukunft wichtige Beiträge zum Verständnis des Einflusses der Galaxienumgebung leisten (über einen großen Bereich von stellarer und Halo-Masse und Rotverschiebung). Diese Datensätze werden zusammen mit detaillierten Untersuchungen kleinerer Datensätze ermöglichen, die zugrundeliegende Physik und das Zusammenwirken der Prozesse in der Galaxienumgebung besser zu verstehen.

Abstract

The availability of photometric and spectroscopic data for large samples of galaxies in the last decades has led to significant progress towards understanding the evolution of galaxies across cosmic epochs. Both observations and simulations consistently reveal that the fate of galaxies is determined by two main classes of process: i) the evolution driven by internal processes that are tightly correlated to the gravitational potential of the galaxy (Kauffmann et al., 2003; Smith et al., 2009; Lang et al., 2014); and ii) environment-driven evolution in the form of external interactions within groups of galaxies (Balogh et al., 2000; Boselli & Gavazzi, 2006). The nature and relative importance of internal versus external processes across cosmic time and galaxy mass, however, remains one of the open questions of modern astronomy.

In this thesis we study the role of environment. We derive a novel method to calibrate physically motivated quantities (e.g. halo mass) from the local density of galaxies (by counting neighboring objects). We also classify if a galaxy lives at the bottom of the global potential well of its halo i.e., is a central or a satellite galaxy. Each galaxy has well defined observational properties (e.g. stellar mass, local galaxy density) while the calibrated quantities describing environment (e.g. halo mass, central/satellite status) are probabilistic. We reach this goal by linking observed galaxies to a mock sample drawn from semi-analytic models of galaxy formation, which we select to match the sample properties of each observational survey.

Our method is applied to the 3D-HST survey, which through slit-less spectroscopic observations with the *Hubble Space Telescope* has provided accurate redshifts for the majority of galaxies from a magnitude limited sample in five well studied deep fields. In the past, the samples of galaxies with accurate spectroscopic redshifts, which are critical for the reconstruction of the density field, have been limited in the number of objects and biased to bright galaxies. The synergy between 3D-HST spectroscopy and photometry from the CANDELS survey lifted these limitations, making this sample ideal for an accurate quantification of the environment at redshift $0.5 < z < 2.0$. Our method is also applied to a local Universe sample drawn from the Sloan Digital Sky Survey, thus providing a homogeneous dataset to study the effects of environment across 10 billion years of cosmic time.

We use these environment catalogues (which we publicly release to the astronomical community) to investigate the environmental suppression of star formation (quenching) in satellite galaxies. We compute the fraction of passive central and satellite galaxies as a

function of stellar and halo mass, and redshift. We then derive the efficiency of satellite quenching: the fraction of galaxies that were quenched by environment specific processes above and beyond what would be quenched by internal processes alone. Using the mock sample, we estimate that the timescale for satellite quenching is $t_{\text{quench}} \sim 2 - 5$ Gyr; longer at lower stellar mass or lower redshift, but remarkably independent of halo mass. This indicates that satellites are quenched by exhaustion of their gas reservoir in absence of cosmological accretion, and that dynamical stripping processes (e.g. removal of the cold gas reservoir by hydrodynamical processes) are ineffective in the range of halo mass commonly found within the 3D-HST sample ($M_{\text{h}} \lesssim 10^{14} M_{\odot}$). At $z = 0$, quenching times are even longer, suggesting that gas exhaustion is the main environmental process responsible for quenching. However, we observe shorter quenching times in the most massive haloes which we interpret as an increased efficiency of rapid dynamic quenching processes in these environments. From the distribution of star formation rates for 3D-HST galaxies, we find that the quenching times can be separated into a delay phase during which satellite galaxies behave similarly to centrals at fixed stellar mass, and a phase where the star formation rate drops rapidly, as shown previously in the local Universe (Wetzel et al., 2013). We conclude that this scenario requires satellite galaxies to retain a large reservoir of multi-phase gas upon accretion, and that this gas is required to sustain normal levels of star formation for the long quenching times observed.

Statistical studies of large samples of galaxies are commonly complemented by detailed investigations of objects clearly undergoing environmental processes, to improve our understanding of the detailed physics, important both at low- and high-redshift. In this thesis we present the first analysis, using resolved spectroscopy, of such an object: ESO137-001, a galaxy infalling into the Norma Cluster. This galaxy shows spectacular tails of multi-phase gas being removed from the galaxy disk by ram-pressure stripping. A complete picture of how ram pressure operates in this galaxy requires a detailed knowledge of the gas kinematics and of emission-line diagnostics which we obtain by exploiting the unprecedented capabilities of the Multi Unit Spectroscopic Explorer (MUSE), recently commissioned at the Very Large Telescope.

By studying the surface brightness of the $\text{H}\alpha$ hydrogen recombination line and kinematics throughout the tail, in tandem with the stellar velocity field, we found that ram pressure has completely removed the cold gas reservoir from the outer disk of the galaxy, and that the tail is still fed by gas from the inner regions. Our study reveals that the stripping does not alter the rotation pattern of the ionized gas, which is consistent with the rotation curve of the stellar component of the galaxy. The ionization of the tail is powered by turbulent shocks as well as photo-ionization from young massive stars: indeed, significant star formation is found in the stripped gas.

The quantification of environment for larger and deeper samples of galaxies from ground- and space-based missions will, in the near future, unveil the role of environment over a larger range of stellar and halo mass and redshift. This will be combined with detailed studies of smaller samples to understand the physics and the interplay of environmental processes.

Contents

Zusammenfassung	v
Abstract	viii
1 Introduction	1
1.1 Galaxy formation and Evolution in a Hierarchical Universe	1
1.1.1 Redshift, recessional velocity, and the Hubble law	1
1.1.2 The standard model of cosmology and initial conditions	2
1.1.3 Distance and lookback time	3
1.1.4 Structure formation	3
1.2 The life cycle of galaxies	5
1.2.1 Observational evidence	6
1.2.2 The regulator model	12
1.3 The role of environment	14
1.3.1 Observational evidence	15
1.3.2 Environmental processes	18
1.4 Metrics to quantify the environment across cosmic time	23
1.5 This thesis	27
2 The environment of mock galaxies in a Hierarchical Universe	31
2.1 Models	31
2.1.1 The model galaxy sample	34
2.2 Quantification of environment	35
2.3 The correlation of density with halo mass	37
2.3.1 A multi-scale approach	43
2.4 Mass rank as a method to disentangle centrals and satellites	45
2.4.1 Identification of central galaxies	47
2.4.2 Identification of satellite galaxies	48
2.4.3 Dependence of Purity and Completeness on the stellar mass limit	51
2.4.4 Dependence on Redshift Accuracy	51
2.5 Relation between environment and passive fraction	55
2.5.1 The growth of a passive population in the models	55
2.5.2 Recovering predicted trends with observational proxies	56

2.6	Conclusions	59
3	The environment of observed galaxies from 3D-HST and SDSS	61
3.1	The high redshift sample from 3D-HST	61
3.1.1	Redshift accuracy	63
3.2	Quantification of the environment	66
3.2.1	Density	66
3.2.2	Edge corrections	68
3.3	Overdensities in the 3D-HST deep fields	76
3.4	The model galaxy sample	82
3.4.1	Sample selection	82
3.4.2	Matching the redshift accuracy	83
3.5	Calibration of physical parameters	85
3.5.1	The stellar mass rank in fixed apertures	86
3.5.2	Matching mock to real galaxies	90
3.5.3	Testing calibrations	95
3.5.4	The environment catalog	96
3.6	The Local Universe sample from SDSS	99
3.6.1	Observational data	99
3.6.2	The model sample	99
3.7	Conclusions	102
4	Satellite quenching efficiency and timescales at $0 < z < 2$	105
4.1	Passive fractions as a function of halo mass	105
4.2	Recovering the “pure” passive fractions for satellite galaxies	109
4.3	Passive fraction as a function of density	113
4.4	Satellite quenching efficiency	115
4.5	Quenching timescales	117
4.6	Redshift evolution of the quenching timescales	119
4.7	Discussion	123
4.7.1	Identification of the main mechanism	124
4.7.2	Delayed then Rapid or Continuous Slow quenching?	125
4.7.3	The gas content of satellite galaxies	128
4.8	Conclusions	130
5	Environmental quenching caught in the act. The case of ESO137-001	133
5.1	The galaxy	134
5.2	Observations and data reduction	135
5.3	Emission line measurements	138
5.4	Kinematics	141
5.5	Emission line diagnostics	142
5.5.1	Line ratio maps	143
5.5.2	Composite spectra	146

5.5.3	Properties of the diffuse gaseous tails	148
5.5.4	Properties of the HII regions	154
5.6	Conclusions	157
6	Conclusions	161
6.1	Future prospects	165
	Acknowledgements	184

List of Figures

1.1	A schematic merger tree	4
1.2	The Hubble tuning fork	6
1.3	Color mass diagram at $z = 0$ from SDSS	8
1.4	Rest-frame $U - V$, $V - J$ color-color diagram from Williams et al. (2009)	9
1.5	A compilation of SFR as a function of stellar mass at $0 < z < 3$	11
1.6	The cosmic star formation rate density as a function of redshift	12
1.7	Illustration of the regulator model presented by Lilly et al. (2013)	13
1.8	Morphology-density relation from Dressler (1980)	16
1.9	Color magnitude diagram in bins of density in the Coma supercluster	17
1.10	Example of ram pressure stripped galaxy and best hydro model.	21
2.1	Specific star formation rate as a function of M_* at redshifts of 1.08 and 2.07.	33
2.2	Halo mass vs density for centrals and satellites at $z = 1.08$, and $z = 2.07$	38
2.3	Distributions of halo mass at fixed density on three scales at $z = 1.08$	41
2.4	Density distributions for the hires- z and photo- z samples	42
2.5	Halo mass vs density on multiple scales	44
2.6	Halo mass distributions in the three bins selected from Figure 2.5	44
2.7	Purity and completeness for the identification of centrals and satellites	46
2.8	Purity and completeness as a function of the stellar mass limit	50
2.9	Purity and completeness as a function of spectroscopic sampling rate	53
2.10	Passive fractions as a function of halo mass for centrals and satellites	54
2.11	Passive fractions as a function of density for centrals and satellites	56
2.12	Passive fractions as a function of density for different redshift accuracies	58
3.1	Redshift uncertainty for the 3D-HST sample	64
3.2	Comparison of spec- z and grism- z in the 3D-HST fields	65
3.3	Volume density of 3D-HST galaxies as a function of redshift	67
3.4	Footprints of the 3D-HST fields	68
3.5	Density bias versus the distance from the nearest spec- z galaxy	73
3.6	Density bias versus the fraction of the aperture in the 3D-HST footprint	74
3.7	Overdensities in the GOODS-S field in different redshift slices	76
3.8	Overdensities in the COSMOS field in different redshift slices	77
3.9	Overdensities in the UDS field in different redshift slices	78

3.10	Overdensities in the AEGIS field in different redshift slices	79
3.11	Overdensities in the GOODS-N field in different redshift slices	80
3.12	Mass-to-light ratio as a function of U-V color for 3D-HST galaxies at $0.5 < z < 0.6$	84
3.13	Emission line S/N for observed and mock galaxies	85
3.14	Purity and completeness for the central/satellite identification in 3D-HST .	88
3.15	Density and stellar mass distributions for 3D-HST and mock galaxies . . .	91
3.16	Average probability for a 3D-HST galaxy of being central or satellite . . .	92
3.17	Average probability of being a satellite versus DeltaRA and DeltaDEC . .	93
3.18	Average probability of being a satellite versus radial distance	94
3.19	Example halo mass PDFs for three 3D-HST galaxies	95
3.20	Comparison of the halo mass distributions for mock and 3D-HST galaxies .	96
3.21	Density and stellar mass distributions for SDSS and mock galaxies	100
3.22	Comparison of the halo mass distributions for mock and SDSS galaxies . .	101
4.1	Rest-frame UVJ diagram for 3D-HST galaxies in two redshift bins	106
4.2	Passive fractions in bins of M_* , M_h , and redshift	107
4.3	Marginalized likelihood distributions of model parameters for a stellar mass and redshift bin	111
4.4	Probability that a satellite galaxy is passive as a function of M_h in bins of M_* and redshift	112
4.5	Passive fractions in bins of M_{star} , density, and redshift.	114
4.6	Conversion fractions for satellite galaxies in bins of M_* and M_h	116
4.7	Quenching times for satellite galaxies in bins of M_* and M_h	118
4.8	Top Panels: passive fraction for central and satellite galaxies in bins of M_* and M_{halo} for the SDSS sample. The median (log) halo masses for satellites are 12.39, 13.77 for the lower and higher halo mass bin respectively. Points and lines are color coded as in Figure 4.2. Middle panels: conversion fractions for satellite galaxies in bins of M_* and M_h obtained from equation 4.9 for the SDSS sample. Bottom Panels: quenching times for satellite galaxies in bins of M_* and M_h for the SDSS sample.	120
4.9	Conversion fractions for satellite galaxies as a function of redshift in bins of M_* and M_h	121
4.10	Quenching timescales for satellite galaxies as a function of redshift in bins of M_* and M_h	122
4.11	Schematic diagram of the evolution of the MS offset for two toy models of satellite quenching	125
4.12	Offset from the main sequence in two stellar mass bins for 3D-HST observed satellites and for mock galaxies	127
4.13	Ratio of the delay time (T_d) to the fading time (T_f) as a function of redshift in bins of stellar mass.	129
5.1	Location of ESO137-001 in the Norma cluster	135

5.2	Overview of the MUSE observations of ESO137-001	136
5.3	Sky residuals from different algorithms for sky subtraction.	137
5.4	Emission line maps of ESO137-001	140
5.5	Velocity map of the H α emission of ESO137-001	142
5.6	Velocity dispersion map of the H α emission of ESO137-001	143
5.7	Line ratio maps of ESO137-001	144
5.8	H α map of ESO137-001. Five regions of interest are highlighted	147
5.9	Coadded spectra of the five regions of ESO137-001 shown in Figure 5.8 . .	148
5.10	Map of the mean electron density of the ionized gas	149
5.11	BPT diagrams for the composite spectra of the regions shown in Figure 5.8	152
5.12	Maps of metallicity, ionization parameter and extinction for HII regions . .	156

List of Tables

2.1	Purity and completeness for the identification of central galaxies	49
2.2	Purity and completeness for the identification of satellite galaxies	49
3.1	Example of the environmental catalog table made available with this work.	98
4.1	Table of the model parameters.	109
5.1	Emission lines considered in this study	139
5.2	Fluxes measured in the composite spectra of the five regions shown in Figure 5.9	154

“There are more things in heaven and earth, Horatio,
Than are dreamt of in your philosophy.”

William Shakespeare, Hamlet, Act 1, Scene 5

“Telescopes are in some ways like time machines.
They reveal galaxies so far away that their light
has taken billions of years to reach us.
We in astronomy have an advantage in studying the
Universe, in that we can actually see the past.”

Martin Rees

Chapter 1

Introduction

As soon as galaxies were identified as objects outside our Milky Way, questions raised among the astronomical community included: “Why do they appear in such different shapes and sizes?” and “How is the great variety of spectral shapes and morphologies produced by different physical processes?” Studies of the formation and evolution of galaxies aim at gaining insight on the physical mechanisms that have dominated their formation and assembly, and on the transformations they underwent throughout cosmic ages. However, explaining the great diversity of the galaxy population is one of the main difficulties in generating a comprehensive theory of galaxy evolution. This requires a full understanding of complex physical mechanisms (that in some cases produce nearly identical observational signatures) over a large range of cosmic time, and mass of the galaxy and local gravitational potential.

1.1 Galaxy formation and Evolution in a Hierarchical Universe

Because galaxies do not evolve in isolation in an otherwise empty Universe, the study of galaxy formation and evolution must involve cosmology, i.e. the description of the properties of space and time, and the distribution of matter within it.

1.1.1 Redshift, recessional velocity, and the Hubble law

One of the most important discoveries in modern observational astronomy was made by Edwin Hubble in 1929. He found that almost all galaxies appear to move away from us and that their recession velocities increase proportionally with their distance: $v = H_0 \times d$, where H_0 is the Hubble constant (Hubble, 1929). This relation, called the Hubble law, is explained naturally if we assume that the Universe as a whole is expanding with time.

The value of the Hubble constant was highly uncertain for many years, ranging from ~ 50 to ~ 500 km s⁻¹ Mpc⁻¹. With the observational data available today, H_0 has been measured with higher accuracy and its best value is ~ 70 km s⁻¹ Mpc⁻¹, with

an uncertainty of a few $\text{km s}^{-1} \text{Mpc}^{-1}$. To parametrize this uncertainty it has become customary to write $H_0 = 100h \text{ km s}^{-1} \text{Mpc}^{-1}$, and to express all quantities that depend on H_0 in terms of the reduced Hubble constant h .

In an expanding Universe, the wavelength of the spectral features of extragalactic objects is shifted towards the red, providing a direct measurement of a quantity known as redshift (z):

$$z = \frac{\lambda - \lambda_0}{\lambda_0} \quad (1.1)$$

where λ_0 is the rest-frame wavelength of a spectral feature. When $z \ll 1$, as in the Local Universe, this quantity can be related to the recessional velocity $z = v/c$ where c is the speed of light.

In 1929 Hubble had redshift measurements for 46 galaxies. However, in order to quantify the value of H_0 , a redshift independent distance estimate is needed. Hubble used Cepheid star observations available in 24 of those galaxies. These stars pulsate radially, thus inducing periodic changes in their observed flux. The period of variation is tightly related to the stars luminosity (see e.g. Feast & Catchpole, 1997). Hence, the distance of the star can be measured by measuring the period of pulsation and its observed flux.

1.1.2 The standard model of cosmology and initial conditions

From the early discovery made by Hubble, several observations have unveiled the properties of our Universe. For instance, the discovery of the cosmic microwave background (CMB, which shows the geometry of the Universe at very early times, when matter and radiation decoupled) in 1965 proved that our Universe is (nearly) homogeneous and isotropic (Penzias & Wilson, 1965; Dicke et al., 1965). The presence of the CMB is a relic of the dense and hot initial state from which the Universe evolved, generally known as Big Bang.

From that point on, several other observations led astronomers and physicists to the “concordance” cosmological model in use today.

This model, dubbed Λ cold dark matter (ΛCDM) has three main components: baryonic matter (which forms the visible Universe), and two other components: cold dark matter (matter that interacts only through gravity) and dark energy (Λ). Although their nature is still unknown, those two latter components are required to explain the geometry of the Universe as we observe it, and the history of growth of structures in it. This is achieved using several proxies (e.g. the CMB power spectrum, the distribution of galaxies, the mass of clusters of galaxies, the use of standard candels, e.g. Cepheid stars or Supernovae Ia or standard rulers which are used to infer cosmological parameters from the luminosity-distance and angular size-distance relations respectively). The mass-energy budget of the Universe requires that only $\sim 4\%$ of the total mass is made by ordinary baryonic matter, $\sim 26\%$ is made by dark matter, and $\sim 70\%$ is in form of dark energy.

The first CMB maps initially showed a smooth temperature gradient across the sky. It was quickly realized that this dipole was the result of our Galaxy moving with respect to the CMB reference frame.

Once the CMB dipole is removed, the temperature maps appear uniform, convincingly showing that our Universe is very homogeneous. But structures could not have formed in a uniform density field, so there must have been small fluctuations.

In 1992 the Cosmic Background Explorer (COBE, Smoot et al., 1992) satellite detected for the first time tiny ($\Delta T/T \sim 10^{-5}$) anisotropies in the CMB map. Those primordial initial perturbations, which are almost perfectly Gaussian, are the seeds for the gravitational collapse of matter leading to the structures we see today. The COBE results have since been confirmed and refined by two other key CMB space missions: the Wilkinson Microwave Anisotropy Probe (WMAP, Bennett et al., 2003) and the Planck satellite. Their superior sensitivity and angular resolution provided revolutionary datasets which have been fundamental for the development of more accurate cosmological and structure formation models.

1.1.3 Distance and lookback time

The comoving distance between two nearby objects in the Universe is the distance between them which remains constant with time if the two objects are moving with the expansion (or contraction) of the Universe. In a flat Λ CDM Universe, we define the function:

$$E(z) = \sqrt{\Omega_M \times (1+z)^3 + \Omega_\Lambda} \quad (1.2)$$

where Ω_M and Ω_Λ are the matter and lambda density parameter respectively. With this definition, the comoving distance from us to redshift z can be computed as follows:

$$D_C = \frac{c}{H_0} \int_0^z \frac{dz'}{E(z')} \quad (1.3)$$

where H_0 is the Hubble constant and c is the speed of light. The proper distance between the same two objects, instead, increases in an expanding Universe (decreases in a contracting Universe). It is defined as $D_P = D_C/(1+z)$.

Because the speed of light is finite, it takes longer for the light from a distant object to reach us compared to nearby objects, hence the redshift is also a measure of the look-back time (t_L). The look-back time for an object at redshift z is computed as follows:

$$t_L = \frac{1}{H_0} \int_0^z \frac{dz'}{(1+z') \times E(z')} \quad (1.4)$$

where $1/H_0$ is commonly referred as the Hubble time. Throughout this thesis we use slightly different values of Ω_M and Ω_Λ in each chapter, therefore the assumed values are specified at the beginning of each chapter.

1.1.4 Structure formation

Having specified the initial conditions and assuming an expanding universe it is possible to show that perturbations grow with time. A region initially slightly over-dense will attract

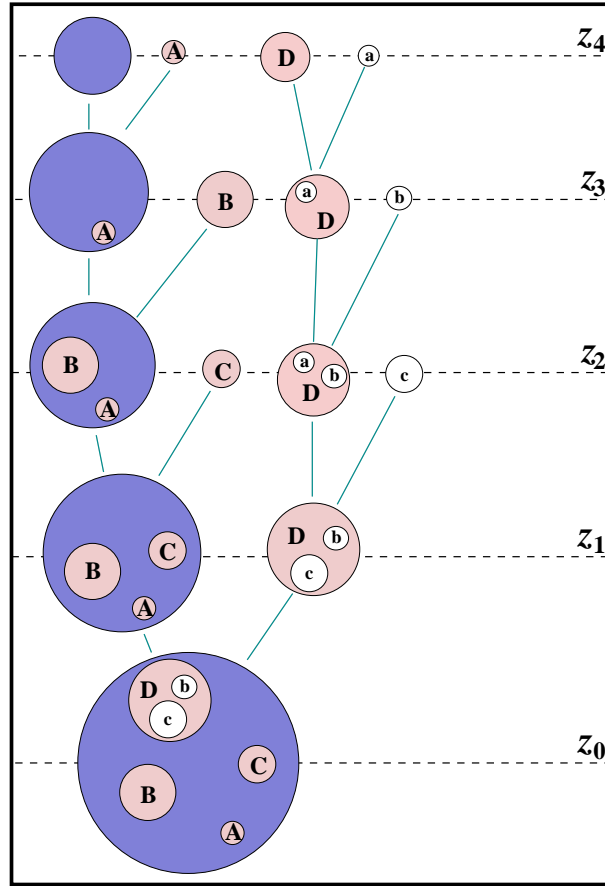


Figure 1.1: A schematic merger tree, illustrating the assembly history of dark matter haloes, in discrete time steps. Time increases from top to bottom, while redshift decreases from z_4 to z_0 . The size of each circle represents the mass of the halo. At z_0 , haloes A , B , C , and D are satellites (sub-haloes) of the main halo in blue. Haloes b , and c are satellites of another satellite. Halo a is completely dissolved and does not survive until the last timestep. Image taken from Giocoli et al. (2010).

other matter a bit more strongly than average. Therefore, over-dense regions become even more over-dense. On the other hand, under-dense regions become even more empty.

In an expanding universe, the cosmic expansion damps the accretion flows which would be present in a static universe, and the growth rate is usually a power law of time, $\delta\rho/\rho \propto t^\alpha$ where $\alpha > 0$. At early times, when the perturbations are still in the so-called linear regime, the size of an over-dense region increases due to the expansion of the universe. Once the perturbation reaches an over-density $\delta\rho/\rho = 1$, it starts to collapse.

This marks the transition to the non-linear regime. If the perturbation is made entirely of baryonic matter, the collapse creates strong shocks that raise the entropy (disorder) of the material. The system relaxes to hydrostatic equilibrium, with its self-gravity balanced by pressure gradients (this is what happens for instance in a star). If the perturbation

consists of collisionless matter (e.g. cold dark matter), no shocks develop, but the system still relaxes to a quasi-equilibrium state which is characterized by a universal radial profile shape known as the Navarro, Frenk and White (NFW) profile (Navarro et al., 1997).

Through this channel a dark matter halo is born. Dark matter haloes, however, do not live in isolation. As a result, nearby haloes get closer and closer until they coalesce (merge). Such a formation process is usually called “hierarchical clustering”.

The formation history of a dark matter halo can be described by a “merger tree” that traces progenitors and descendants over cosmic time. Figure 1.1 shows a schematic picture of a merger tree. We now introduce the concept of central and satellite galaxies and their evolution with time. All galaxies are born as centrals of their own halo at very high redshift. As the universe evolves, dark matter haloes merge. The galaxy hosted by the most massive halo remains the central galaxy of the halo. The smaller halo (sometimes called a sub-halo), instead orbits within the main halo for an extended period of time during which two processes occur. Dynamical friction causes it to spiral inwards, while tidal effects remove mass from its outer regions. Dynamical friction is more effective for more massive satellites, but if the mass ratio of the initial halos is large enough, the smaller object (and any galaxy associated with it) can maintain its identity for a long time. The final fate of the satellite galaxy is to merge with the central galaxy, and from thereon does not appear as a separate entity anymore.

This is the process for the build-up of groups or clusters of galaxies: a cluster may be considered as a massive dark matter halo hosting a relatively massive galaxy near its center and many satellites that have not yet merged with the central galaxy.

1.2 The life cycle of galaxies

Galaxies are the building blocks of the visible Universe. Their formation and evolution is the result of a complex balance and interplay between gas related processes which fuel (or interrupt) the formation of new stars, gravitational interactions with the local environment where they live, merger events with other galaxies, and the presence (or absence) of powerful nuclear activity.

This variety of processes, giving rise to a colorful and diverse population of galaxies, implies that individual galaxies do not follow a predictable “life-cycle”. However, significant developments in the observational facilities during the last couple of decades, have allowed astronomers to observe larger and deeper samples of galaxies not only in the local Universe but for the first time also at high redshift when the Universe was younger. This placed constraints on several properties of the average galaxy population across a large range in age of the Universe.

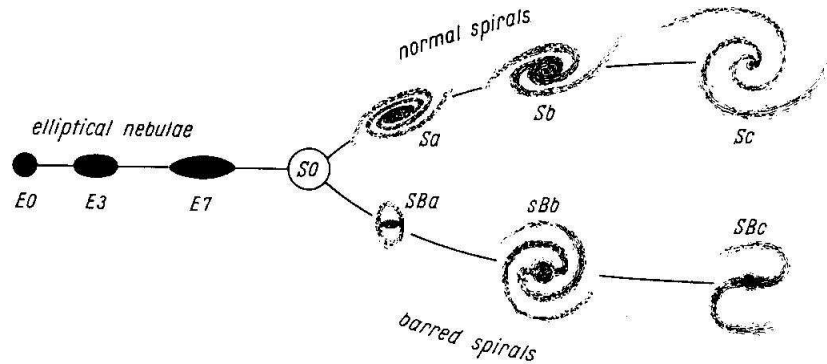


Figure 1.2: The morphological classification scheme proposed by Edwin Hubble. Tuning Fork (Hubble, 1936).

1.2.1 Observational evidence

Morphological classification

As soon as Edwin Hubble identified galaxies as extragalactic objects he started to classify them based on their morphological appearance. His classification scheme (Hubble, 1936), known as the “Hubble sequence” or “Hubble tuning fork” (for the shape of the diagram) is shown in Figure 1.2. Hubble classified the galaxies in three main classes:

- Ellipticals (E): These galaxies have smooth, nearly elliptical morphologies and are divided into subclasses from E0 to E7 where the number is the closest integer to $10 \times (1 - b/a)$, with a and b the lengths of the semi-major and semi-minor axis.
- Spirals (S): These have disks with spiral arm structures. They are divided into two subclasses, barred spirals and normal spirals, according to whether or not a bar-like structure is visible. Each class is further divided into a, b and c, according to the fraction of the light in the central bulge (decreasing from a to c), and the tightness with which the spiral arms are wound.
- Lenticulars or S0 galaxies: This class is intermediate between ellipticals and spirals. Like ellipticals, they have a smooth light distribution with no spiral arms. Like spirals they have a disk and a bulge; they may also have a central bar, in which case they are classified as SB0.

To complement the Hubbles scheme, de Vaucouleurs (1959) proposed a more elaborate classification system that, for instance, introduced Sd for bulge-less spirals, and the class of irregular galaxies. Nonetheless the main criteria of Hubble’s scheme are still largely used nowadays.

Ellipticals, and S0s are commonly referred as early type galaxies, while spirals are also known as late type galaxies. It should be remarked that, contrary to popular belief, Hubble didn’t intend this nomenclature to suggest an evolutionary path.

Bimodality in the star formation activity

Besides the morphological type, another important property of galaxies is their color, which is the ratio of their luminosities in two photometric bands. In observational astronomy it is common to define the magnitude m of an object in a photometric band as: $m = -2.5 \times \log(f/f_0)$, where f is the flux and f_0 is the flux of a reference source (that defines the zero-point of the magnitude scale). With this definition of the magnitude, the color becomes $m_1 - m_2 = -2.5 \times \log(f_1/f_2)$, where the subscripts denote the bands.

Galaxy colors, measured in two bands dominated by the stellar black body emission (from ultraviolet to near-infrared), are to first order a measure of the (light-weighted) age of the stellar populations, or of the recent star formation rate of galaxies. Star forming galaxies have a significant fraction of massive and hot stars (mainly O, B stellar types). The spectrum of those stars peaks in the Ultra Violet (UV) region of the electromagnetic spectrum and remain strong in optical blue bands, therefore it is common to refer to them as blue stars. However, massive stars are short lived and after a star formation event they explode as supernovae in few tens of million years. Instead, galaxies with a small amount of recent star formation are characterized by redder optical colors because they are dominated by low mass main sequence stars and red giant branch stars. It is common to refer to those galaxies as “passive” (or “quiescent”) galaxies; we define the decline of the star formation activity leading a galaxy to transition from the active to the passive population as the “quenching” phenomenon.

Galaxy colors should, however, be interpreted with caution as the presence of a significant mass of dust in the galaxy absorbs UV photons more efficiently than lower energy photons. As a result a galaxy appears redder than the average color of its stellar population. Nonetheless, by combining models of the dust absorption with data from observations, it is possible to estimate dust corrected colors.

Another important property of galaxies is their stellar mass. This can be estimated from the observed luminosity in an optical (near-infrared) band. However, for the reasons described above, blue band luminosities correlate less strongly with the total stellar mass than those observed in redder filters (ideally covering the rest-frame near-infrared emission), the latter tracing the bulk of the population of stars in a galaxy. For a given filter it is common to define the stellar mass-to-light ratio M_*/L as the ratio of the stellar mass to the luminosity. The mass-to-light ratio can be derived from scaling relations using a single color (see Bell et al., 2003; Zibetti et al., 2009), or from template fitting of the spectral energy distribution using multiple photometric datapoints (see Papovich et al., 2001; Wuyts et al., 2009; Conroy et al., 2009; Maraston et al., 2010). The stellar mass can then be derived from the mass-to-light ratio and the luminosity in a filter.

Arguably one of the most significant legacies of large scale surveys, as for instance the Sloan Digital Sky Survey (SDSS), is the discovery of a well defined color bimodality in the galaxy population. Figure 1.3 shows the dust corrected $u - r$ optical color as a function of stellar mass for a large sample of galaxies in the local Universe ($z = 0$) from Schawinski et al. (2014). Larger values of $u - r$ correspond to redder colors and smaller values to bluer colors. The presence of two separate galaxy populations is immediately

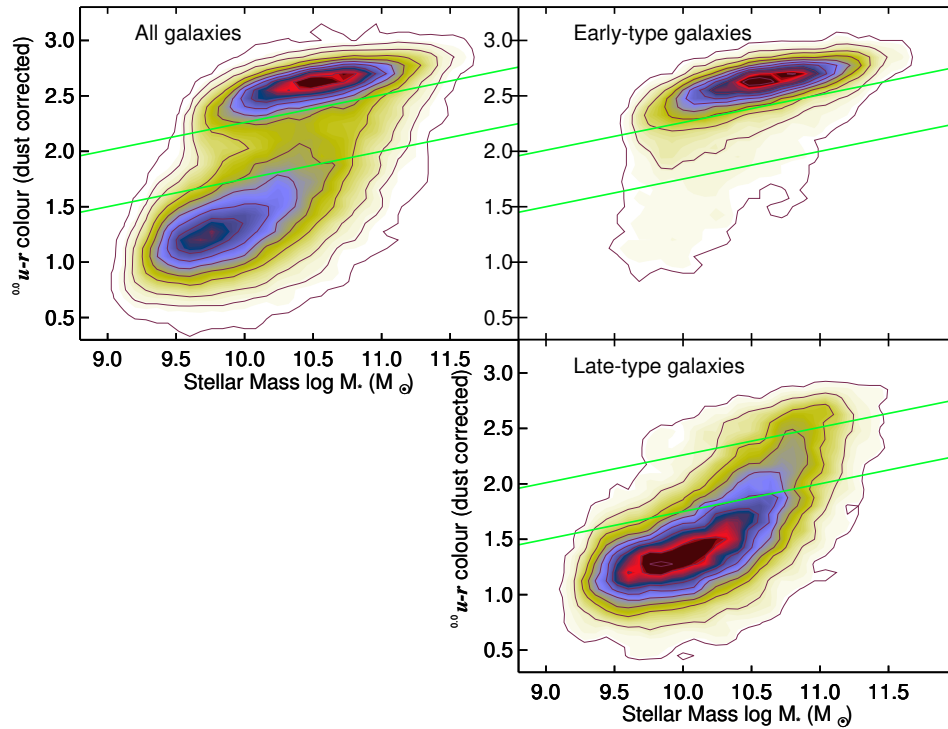


Figure 1.3: The dust corrected $u - r$ color as a function of stellar mass for a sample of local galaxies from SDSS. The left panel shows the color-mass distribution of all galaxies. A clear bimodality in the population of galaxies appears. The right panels show the color-mass distribution for early and late type galaxies respectively. The bimodality seen in the full population is broken-up when the morphological types are separated. Image taken from Schawinski et al. (2014).

clear (see also Strateva et al., 2001; Baldry et al., 2004). The right panels show how these two populations can be linked (at least at $z = 0$) to their morphological type. The “blue cloud” is typically populated by late type galaxies while the “red sequence” is almost entirely made of early types.

The same color bimodality has also been observed at $z \sim 1 - 3$ (Bell et al., 2004; Weiner et al., 2005; Brammer et al., 2009), suggesting that the first quenched galaxies were already present when the Universe was only a few billion years old.

Another effective method to identify star forming and passive galaxies is the use of color-color diagrams. Several combinations of colors have been proposed (see e.g. Labbé et al., 2005; Shapley et al., 2005; Wuyts et al., 2007). One of the most adopted makes use of rest-frame $U - V$ and $V - J$ colors (Williams et al., 2009; Whitaker et al., 2012). Figure 1.4 shows the $U - V$, and $V - J$ colors of a sample of observed galaxies in five redshift bins from Williams et al. (2009). These authors found that star-forming and quiescent galaxies

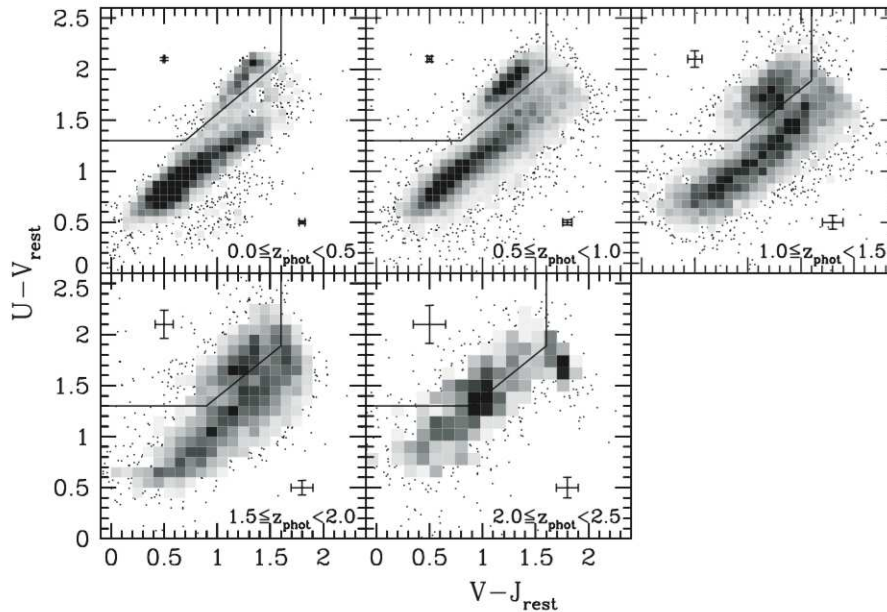


Figure 1.4: Rest-frame $U - V$ vs. $V - J$ colors of a magnitude selected sample of galaxies in five redshift bins. The gray scale represents the density of points in the central region of each plot, while scattered points are plotted individually. The solid lines show the adopted divisions between the star-forming and passive galaxy samples at each redshift. Image taken from Williams et al. (2009).

segregate themselves in this plane, with the star-forming galaxies forming a diagonal track and quiescent galaxies populating mostly the upper left region. The solid lines show the adopted divisions between the star-forming and passive galaxy samples at each redshift. One of the main issues of single optical color selections is the degeneracy between dusty star forming galaxies, and passive galaxies, which can have very similar red colors. The UVJ diagram breaks this degeneracy: at fixed $U - V$ color, dust-free passive galaxies are bluer in $V - J$ than dusty star forming galaxies, allowing the two populations to be empirically separated.

Star formation estimators

Star formation rates, measured in $M_{\odot} \text{ yr}^{-1}$, are estimated by observing the young stellar populations. If L_{λ} is the luminosity of the young stellar populations in a given band of the electromagnetic spectrum, the star formation rate (SFR, which indicates the mass in new stars produced per year) can be determined as follows: $SFR = L_{\lambda} \times K_{\lambda}$, where K_{λ} is a conversion factor that can be inferred from population synthesis models. This factor is universal only if some conditions are met. First, the fraction of mass formed in the stars which dominate the observed signal, to the total mass of stars formed must be universal (i.e. does not depend on the galaxy type or mass, and redshift). Second, the star formation

activity has to be well approximated by a constant value over a timescale defined by the lifetime of the young stellar populations observed. This is required in order to have a roughly constant number of young and massive stars in the galaxy over the lifetime of those stars ($10^7 - 10^9$ yr depending of the SFR tracer).

We now briefly summarize the most common tracers of star formation. For a detailed discussion we refer to the review by Kennicutt (1998a).

In the wavelength range $\sim 1250 - 2500\text{\AA}$ the spectrum of a galaxy is dominated by the emission of young stars (O,B types), therefore the star formation rate scales linearly with the luminosity in this band. The main limitation of this method is dust obscuration which is significant in the UV. Therefore the estimated UV SFR is only a fraction of the total SFR.

Dust grains absorb UV photons which are re-emitted at longer wavelengths in the medium and far infrared. Observations made in those bands can therefore be converted into a SFR, provided that the physics of radiative transfer onto the grains is well understood. The IR SFR is usually combined with the UV SFR to account for the dust obscured and unobscured components of the total star formation activity.

Hydrogen recombination lines can also be used to estimate the SFR. Hydrogen atoms are ionized by photons shortward of the Lyman limit, and their recombination provides a direct, sensitive probe of the young massive stellar population. The brightest of these lines is $H\alpha$ and it is one of the most widely used tracer of star formation. However also this tracer suffers from dust extinction ($H\alpha$ photons can be absorbed by dust grains before they leave the galaxy). Because extinction attenuates bluer lines more than redder lines, the amount of extinction is traditionally estimated by observing another hydrogen recombination line (usually $H\beta$) and comparing the observed ratio of the two lines to the theoretical ratio. Another caveat of using hydrogen recombination lines arises from the absorption of these lines in the stellar atmospheres of young stars, therefore the intensity of the line must be corrected for underlying absorption before the flux can be used to estimate the SFR.

All those SFR estimates suffer from contamination in case the galaxy hosts an active galactic nucleus (AGN). In this case ionizing photons not associated to star formation produce an increased flux in the UV continuum spectrum, in the hydrogen recombination lines and in the infrared luminosity (because the dust is heated by the AGN). In this cases, the estimated SFR becomes an upper limit for the real SFR.

Evolution in the cosmic star formation activity

The presence of a clear bimodality in the colors of the galaxy population is complemented by another clear observational evidence: for star forming galaxies the SFR is tightly correlated to the existing stellar mass of the galaxy with a small scatter of 0.3 dex¹. This relation, typically called “Main Sequence” (MS) of star forming galaxies extends out to $z \sim 3 - 4$ (Noeske et al., 2007; Daddi et al., 2007; Peng et al., 2010; Whitaker et al., 2012, 2014; Schreiber et al., 2015).

¹We use dex to refer to the difference between powers of ten. Therefore 0.3 dex approximately corresponds to a factor of 2 in linear units

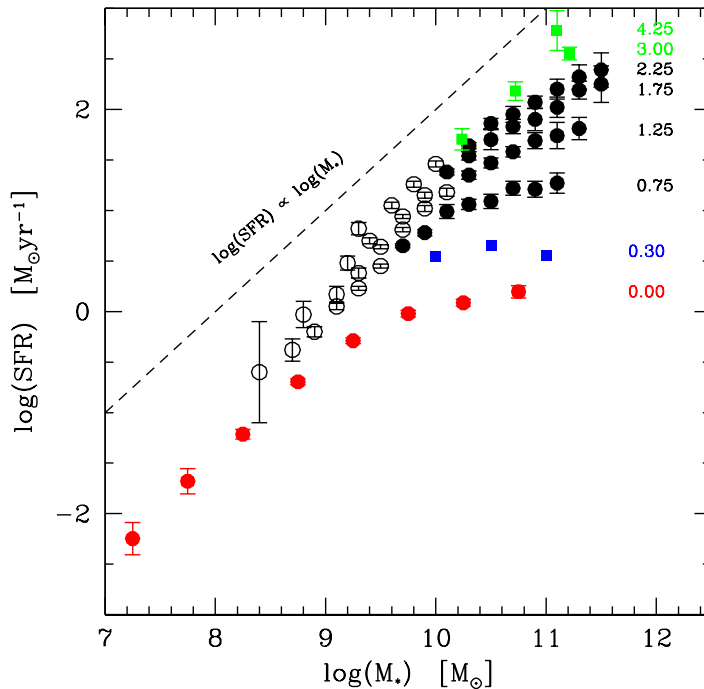


Figure 1.5: Star formation rate as a function of stellar mass at different redshifts. Data at $z = 0$ (red) are from Gavazzi et al. (2015). Data at $z = 0.3$ (blue) are from Bauer et al. (2013). Measurements in the interval $0.75 < z < 2.25$ (black) are from Whitaker et al. (2014); the points at $z = 3$ and $z = 4.25$ (green) are from Schreiber et al. (2015). Image taken from Gavazzi et al. (2015).

A small fraction ($\sim 1 - 2\%$) of galaxies lie above the main sequence and they are called starbursting galaxies; however those galaxies only contribute of the order of $\sim 10\%$ to the total star formation of the full galaxy population (Sanders et al., 1988; Rodighiero et al., 2011; Sargent et al., 2012). There is also a significant population of passive (or “quenched”) galaxies whose SFR is much lower than MS galaxies at fixed stellar mass. It is then clear that most of the stars form in MS galaxies and this places fundamental constraints on models of galaxy formation and evolution.

Recently, Whitaker et al. (2014), Erfanianfar et al. (2016), and Gavazzi et al. (2015) have shown (see Figure 1.5) that the MS is not a single power law, but rather a broken power law where the SFR per unit stellar mass flattens above a certain break mass (which is a function of redshift). Erfanianfar et al. (2016), and Gavazzi et al. (2015) interpreted the downturn at high stellar mass as due to the presence of massive bulges or bars in the center of those galaxies which locally suppress the star formation activity leading to a decrease of the SFR per unit stellar mass.

It is clear from Figure 1.5 that the characteristic SFR of the MS evolves strongly with

redshift, increasing by a factor of ~ 20 from $z = 0$ to $z = 2$.

When the MS is multiplied with the number density of galaxies of a given stellar mass (the stellar mass function) as a function of cosmic time, the average cosmic star formation rate per unit volume (ψ) is obtained. The diagram of ψ as a function of redshift, usually known as the ‘‘Madau plot’’ (see Madau et al. 1996, and Madau & Dickinson 2014 for an up-to-date review) is shown in Figure 1.6. This is obtained from a recent compilation of star formation rate and stellar mass function measurements from several galaxy surveys in the range $0 < z < 8$.

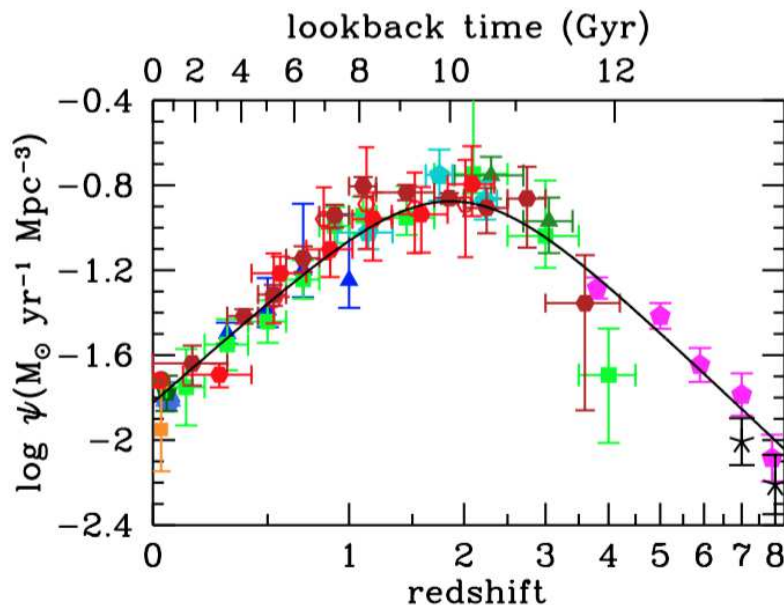


Figure 1.6: The history of cosmic star formation from a compilation of measurements of the star formation rate from $z = 0$ to $z = 8$. Image taken from Madau & Dickinson (2014).

These state-of-the-art surveys provide a remarkably consistent picture of the cosmic star formation history: a rising phase, peaking at $z \sim 2$, when the Universe was ~ 3.5 Gyr old, followed by a gradual decline to the present day, roughly as $\psi(z) \propto (1 + z)^{2.7}$.

The shape of the decline of the cosmic star formation history from $z \sim 2$ to the present-day Universe is well matched to the shape of the fraction of the gas (mainly molecular) mass to the stellar mass as a function of redshift (see e.g. Tacconi et al., 2013; Genzel et al., 2015). This suggests that the star formation rate at a given epoch is somewhat linked to the amount of gas available to form new stars in the galaxy.

1.2.2 The regulator model

An empirical and simple model that proposes to explain the star formation properties of galaxies across cosmic time (e.g. their mass growth and quenching) has been proposed by

Lilly et al. (2013).

These authors have shown that by regulating the instantaneous star formation rate by the amount of gas in the galaxy, they are able to explain the evolution of the cosmic star formation rate density, of the amount of metals in the galaxies and how the stellar mass of the galaxy is correlated to the mass of the hosting dark matter halo.

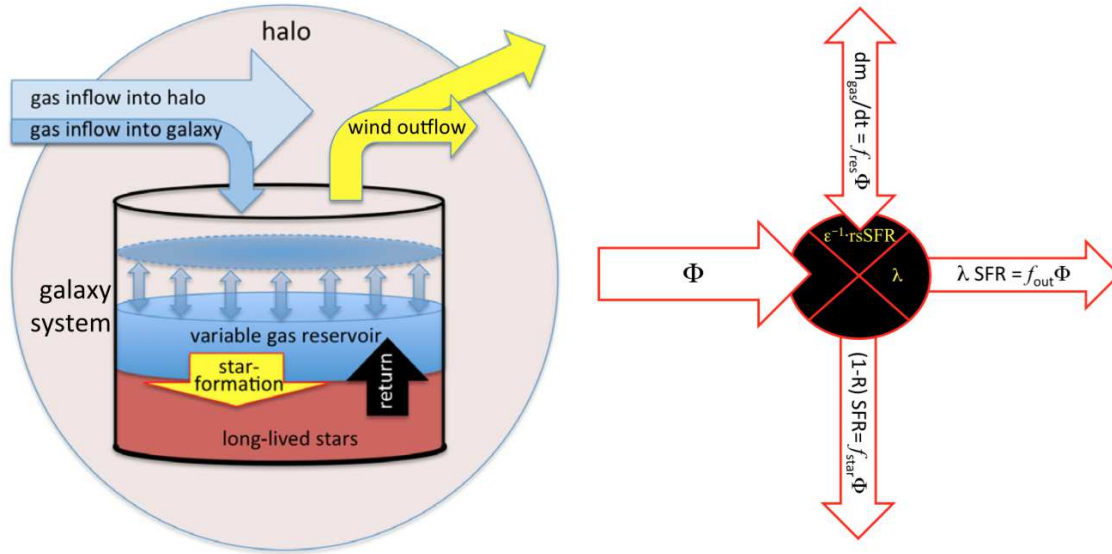


Figure 1.7: Illustration of the gas-regulated model presented by Lilly et al. (2013), in which the SFR is regulated by the mass of gas in a reservoir within the galaxy. The diagram on the right shows, the net flows through the system. The incoming gas flow Φ settles into the gas reservoir which is depleted by star formation and outflows.

The basic idea of the regulator for a galaxy system builds on the similarity of the specific dark matter mass accretion rate (the accretion rate divided by the existing dark matter halo mass) and the specific star formation rate (sSFR, the star formation rate divided by the existing stellar mass) as a function of redshift. By assuming that dark matter and baryons are well mixed when flowing from the cosmic web into the galaxy system, this implies that the accretion of matter has a direct impact on the star formation activity of the galaxy.

The operation of the gas regulator assumes that the galaxy system is made of long lived stars (the existing stellar mass) and a variable gas reservoir which is fed by the cosmological accretion Φ and depleted by two channels. The first is star formation, where gas is turned into stars. This follows a simple law (usually known as the integrated Kennicutt-Schmidt relation; Schmidt, 1959; Kennicutt, 1998a): $SFR = \epsilon \times M_{\text{gas}}$, where ϵ is the efficiency of the conversion of gas into stars. However during the phases of stellar evolution, newly formed stars lose a fraction of their mass ($\sim 40\%$) which is returned into the gas reservoir.

The second channel which depletes the gas reservoir is wind outflows, i.e. the ejection of gas from the galaxy into the halo or even beyond its virial radius. Stellar outflows are

produced by powerful supernovae explosions; their rate depends on the number of massive and young stars in the system and therefore on the SFR. The mass loss through stellar outflows is assumed to increase linearly with SFR: $\Psi = \lambda \times \text{SFR}$, where the scaling factor λ is called the mass-loading factor.

The mass of gas in the reservoir of the system is free to increase or decrease with time and it is this change which gives the regulator its ability to regulate the SFR of the galaxy. Changes in M_{gas} must be associated with a net flow into or out of the reservoir.

When the gas reservoir is depleted or is heated to temperatures preventing efficient radiative cooling and formation of giant molecular clouds, the SFR decreases moving galaxies from the main sequence to the passive cloud.

Observationally, it is nowadays fairly clear that quenching is correlated to “internal” parameters, such as stellar mass (Kauffmann et al., 2003; Baldry et al., 2004), velocity dispersion (Smith et al., 2009; Graves et al., 2009), central stellar surface mass density (Cheung et al., 2012; Fang et al., 2013), or bulge fractions (Omand et al., 2014; Lang et al., 2014), which are in some way related to the potential of the galaxy. This phenomenon, which has been recently dubbed “mass-quenching” (Peng et al., 2010), can be the result of a combination of mechanisms.

The physical processes involved have been claimed to be feedback from AGN (Bower et al., 2006; Croton et al., 2006). In this case radiation, winds and jets from active galactic nuclei can interact with the cold gas reservoir leading to ejection or heating of the gas. Alternatively mergers of spiral galaxies leading to the formation of massive elliptical galaxies can lead to a central starburst and a rapid consumption of the cold gas (Hopkins et al., 2006; Wilman et al., 2013). Similarly disc instabilities can form massive central bulges, which heat the star forming disc, significantly suppressing further star formation (Dekel et al., 2009). The relevance and role of each of these processes and their interplay as a function of galaxy mass, type and redshift remains one of the open problems of modern galaxy formation.

1.3 The role of environment

In the previous Section we described how the star formation of a galaxy is regulated by internal processes. However, the advent of large galaxy surveys unveiled that the environment in which a galaxy lives also plays a role. Once the galaxy falls into a massive halo (or a dense environment, such as a group or a cluster of galaxies) and becomes a satellite galaxy, additional processes increase the probability of being quenched above and beyond the mass related quenching. In Section 1.4 we present the metrics which are most commonly used to describe the environment of galaxies. In this Section we generally refer to local projected density (usually derived from counting neighboring galaxies) or a physically calibrated halo mass.

1.3.1 Observational evidence

It has been known for decades that there is a correlation between galaxy Hubble type and the local density of galaxies. Hubble & Humason (1931); Morgan (1961); Abell (1965), and Oemler (1974) found that the low density field is largely composed of late type galaxies, while the densest regions of clusters of galaxies are predominantly hosting early types.

By studying a sample of 55 local galaxy clusters, Dressler (1980) proposed the morphology-density relationship. His analysis is shown in Figure 1.8, the percentage of spiral (late types) galaxies decreases from 80% in field regions, to 60% in the cluster outskirts and to $\sim 10\%$ in the cores of rich clusters, with the opposite increase of the percentage of early types (E+S0). A significant difference is also seen between the fraction of ellipticals and S0, suggesting a different formation mechanism which depends on the local density within the clusters. Indeed, it must be stressed that the local density increases at decreasing cluster-centric distance, therefore most of the trends relate to the efficiency of environmental processes with distance from the cluster center.

Postman & Geller (1984) extended this work to lower density environments, finding that the fraction of early types smoothly increases over six orders of magnitude in galaxy density. The morphological segregation, revisited also by Dressler et al. (1997), is probably the most evident signature of the environmental dependencies that drive the evolution of galaxies.

Another important observational evidence of environmental processes in action is the deficiency of atomic hydrogen (HI) in dense environments. The atomic gas is the principal component of the interstellar medium (ISM) in late-type galaxies at $z = 0$: this provides the fuel that cools into molecular hydrogen and feeds star formation. In normal, isolated galaxies the HI gas distribution extends to 1 – 2 times the optical diameter. (Cayatte et al., 1994; Broeils & Rhee, 1997). The outskirts of the HI disks are weakly bound to the galaxy’s gravitational potential well, thus they can be easily removed. A quantitative determination of the amount of atomic gas in dense environments compared to the field at fixed size (which correlates with mass) was first achieved by Haynes & Giovanelli (1984) who compared cluster galaxies and a reference sample of isolated galaxies using data from the Arecibo radio telescope. These authors defined the HI-deficiency parameter as the logarithmic difference between the observed HI mass and the expected value in isolated objects of similar morphological type and linear size. By comparing the statistical HI properties of galaxies in 9 nearby clusters with those of isolated objects, Giovanelli & Haynes (1985) showed that relaxed (evolved) clusters contain a large fraction of HI deficient galaxies. This fraction is a strong function of the angular distance from the X-ray center (see e.g. Boselli, 1994; Gavazzi et al., 2013a).

Several other physical properties of galaxies correlate with environment: various works based on the SDSS survey, and complemented by multifrequency observations from the UV to far-infrared (Lewis et al., 2002; Gómez et al., 2003; Balogh et al., 2004; Kauffmann et al., 2004; Hogg et al., 2004; Blanton et al., 2005; Baldry et al., 2006; Weinmann et al., 2006; Gavazzi et al., 2010; Boselli et al., 2014c) confirm that, at $z = 0$, most star forming, late type, blue galaxies reside in low density environments, while the high density environments

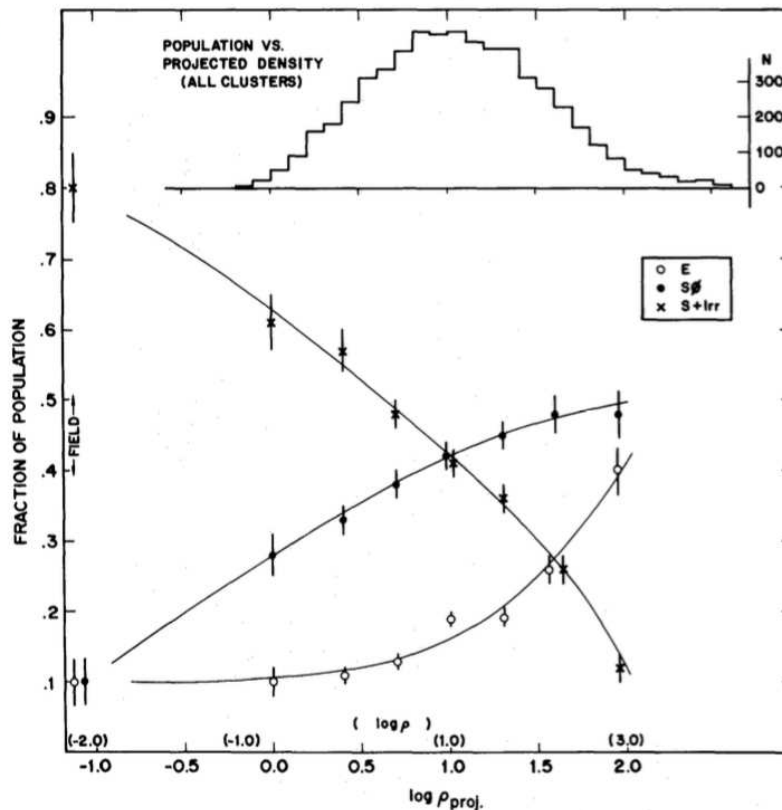


Figure 1.8: The fraction of Elliptical, S0, and Spiral+Irregular galaxies as a function of the local projected density (in galaxies per Mpc^{-2}) within 55 Local clusters. The first point for each type, on the left of the plot, is from a field sample. The upper histogram shows the number distribution of the galaxies in bins of projected density. Image taken from Dressler (1980).

are dominated by quiescent, old, early type, red galaxies. The transition is smooth and continuous across intermediate densities (or halo masses), suggesting a physical mechanism which increases in efficiency at increasing density.

Figure 1.9 shows the $g - i$ color-magnitude diagram for galaxies in the Coma/A1367 supercluster region from Gavazzi et al. (2010). This sample spans a large range in local density from the core of massive clusters (UH panel in Figure 1.9) to isolated objects (UL panel). Blue dots are for late type galaxies and red dots are for early types. The red sequence (the locus of old and quiescent systems) is only formed at the bright end (massive galaxies) in the UL density bin by “mass quenching” processes. Moving through the low (L) and intermediate-high (H) density bins, the faint end of the red sequence is gradually built-up by environment specific processes. At the highest densities, the cloud of star forming objects disappears and the galaxy population is almost entirely made of early type red objects. The transition from star forming to passive must be relatively quick

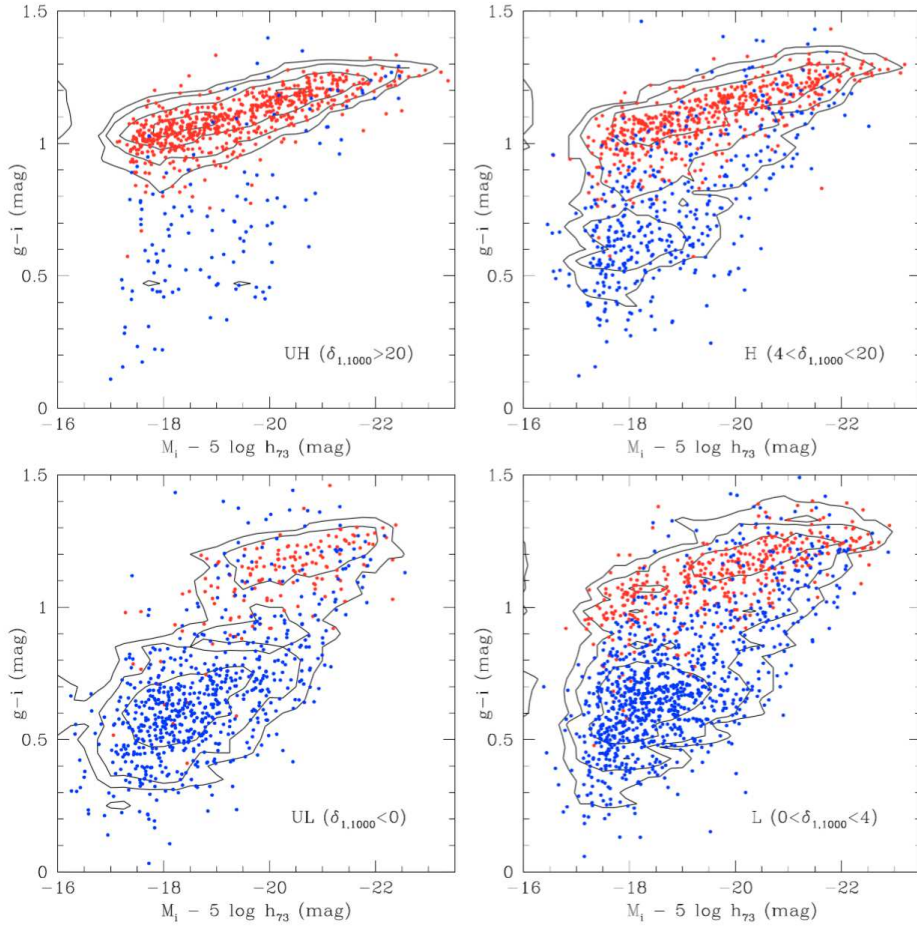


Figure 1.9: The $g - i$ color-magnitude diagram for 4132 galaxies in the Coma/A1367 supercluster region for bins of local galaxy density increasing from ultra-low (UL) to ultra-high (UH). Blue dots are for late type galaxies and red dots are for early types.

to explain the lack of objects with intermediate colors (see also Boselli et al., 2014c; Mok et al., 2014; Schawinski et al., 2014).

Peng et al. (2010, 2012) developed an empirical model in which “mass” and “environment” quenching are separable processes acting independently. While mass quenching operates on all galaxies, environment quenching only affects satellite galaxies (galaxies orbiting in a more massive halo). In their model the fraction of passive satellites increases with increasing local density, while the fraction of passive centrals is only a function of stellar mass.

Several authors investigated the timescales required for a satellite galaxy to be quenched by environmental processes (usually correcting for the contribution of mass quenching). Wetzel et al. (2012, 2013) found the quenching timescale to be $\sim 5 - 7$ Gyr at $z = 0$. This time starts from the first time the galaxy becomes a satellite of any halo. However, in order to reproduce the observed SFR distribution, it is required that satellite galaxies

remain star forming at the same rate of central galaxies of similar stellar mass for the majority of this quenching time. Only in the final ~ 1 Gyr, the star formation rate drops and the galaxy moves from the blue cloud to the red sequence. Similar conclusions have been reached by De Lucia et al. (2012), and Hirschmann et al. (2014) by comparing the fraction of quenched galaxies as a function of density or group-centric radius to the time spent in the satellite phase as derived from semi-analytic models of galaxy formation.

Recently, Oman & Hudson (2016) by using simulated orbits of galaxies in (and around) massive haloes ($M_h > 10^{13} M_\odot$) found that their data are consistent with a hypothesis where the quenching is 100% per cent effective (all satellites are quenched), over a timescale < 1 Gyr, once a galaxy reaches the highest densities, as found in the core of massive structures. This requires a rapid mechanism that removes (or heats) the star forming gas such that no fuel for further star formation is available.

However, even in well studied massive clusters, where a wealth of multiwavelength data is available, a complete consensus on this short timescale is not found in the literature. Haines et al. (2015), by studying the spatial distribution and kinematics of a sample of 30 massive clusters with available UV+IR star formation estimates, derived that the star formation rates decline exponentially on quenching timescales of $\sim 2-3$ Gyr upon accretion into the cluster. Paccagnella et al. (2016) investigated the distribution of galaxies in the SFR- M_* plane for 76 nearby clusters. These authors found a significant population of cluster galaxies with reduced SFRs compared to MS objects (but not as low as for passive objects), which preferentially occurs within the cluster virial radius. The analysis of the star formation histories suggests that transition galaxies have had a reduced SFR for the past 2-5 Gyr. These values are longer than times for the fading of the SFR described above, and the origin of this discrepancy is still not well understood.

At higher redshift the situation is made even more complex due to the more limited availability of samples for which the environment is accurately characterized. Nonetheless, Quadri et al. (2012); Knobel et al. (2013); Kovač et al. (2014), and Balogh et al. (2016) have shown that the environment plays a role in quenching the star formation activity of satellite galaxies up to $z \sim 1$, although the samples are limited to massive galaxies or a relatively small number of objects.

1.3.2 Environmental processes

We now briefly review the mechanisms which can affect satellite galaxies. At low redshift detailed studies of post-merger objects (Yagi et al., 2010; Fossati et al., 2012, 2016a; Merluzzi et al., 2013; Fumagalli et al., 2014; Boselli et al., 2016) coupled with state of the art models and simulations (Mastropietro et al., 2005; Kapferer et al., 2009; Tonnesen & Bryan, 2010) have started to explore the rich physics governing those processes (see e.g. Boselli & Gavazzi, 2006, 2014; Blanton & Moustakas, 2009, for reviews). Broadly speaking they can be grouped into two classes. The first of them includes gravitational interactions between cluster or group members or with the potential well of the halo as a whole. The second class includes hydrodynamical interactions between galaxies and the hot and dense gas that permeates massive haloes (ram pressure, viscous stripping, and thermal evaporation).

Tidal interactions between galaxies

Tidal interactions are the disturbances experienced by a galaxy due to the presence of other nearby massive objects. Since tidal forces are dependent on the gradient of a gravitational field, rather than its strength, the perturbation parameter can be defined as:

$$P_{gg} = (M_{\text{comp}}/M_{\text{gal}})/(d/r_{\text{gal}})^3 \quad (1.5)$$

where M_{comp} is the mass of the companion, d is the distance between the galaxies and M_{gal} , and r_{gal} are the galaxy mass and size respectively. A companion can therefore produce strong tidal effects on the gas, stars and dust of a galaxy only if their relative separation is of the same order of magnitude as the galaxy size.

The simulations of Byrd & Valtonen (1990) (applied to spiral galaxies in clusters) show that tidal interactions can produce a significant gas inflow from the disk to the circumnuclear regions, provided that the perturbation parameter is $P_{gg} > 0.1$. This can cause occasional bursts of star-formation which depletes the star-forming gas faster. Also, it can lead to tidal stripping of dark matter, stars and gas.

While it is intuitive that tidal interactions among galaxies are boosted in dense environments, the high relative velocities make the interaction time scale short ~ 0.1 Gyr (Boselli & Gavazzi, 2006), therefore the perturbations are less severe than in less dense environments.

Typical examples of cluster galaxies which recently underwent a gravitational interaction are NGC 4438 and NGC 4435 in the Virgo cluster. Tidally interacting objects in clusters are difficult to identify since tidal tracers are short-lived: while in the field most of the ejected material in tidal tails remains bound to the main galaxy, in clusters the tidal field strips the unbound material, which may be the origin of intracluster stars, visible as diffuse intracluster light (Mihos, 2004).

Tidal interactions with the cluster potential and galactic harassment

Given the high halo mass of groups and clusters, tidal interactions between galaxies and the whole halo potential well can effectively perturb cluster galaxies, inducing gas inflow, bar formation, and bursts of star formation (Merritt, 1984; Miller, 1986; Byrd & Valtonen, 1990; Villalobos et al., 2012).

In this case the perturbation parameter is defined as:

$$P_{gh} = (M_{\text{halo}}/M_{\text{gal}})/(d/r_{\text{gal}})^3 \quad (1.6)$$

where d is the distance of the galaxy from the center of the halo (observationally traced by the central galaxy or the peak of the X-ray emission of the hot gas in the halo). Because the perturbation parameter scales as $(d/r_{\text{gal}})^3$, the most affected galaxies are extended objects which pass close to the halo core ($d \lesssim 200\text{kpc}$).

Moore et al. (1996, 1998) proposed that the evolution of cluster galaxies is governed by the combined effect of multiple high speed galaxy-galaxy close encounters and the

interaction with the halo potential, in a process named “galaxy harassment”. The strength of the perturbation depends on the encounter frequency, and on the cluster’s tidal field.

Their numerical simulations show that the multiple encounters heat the stellar component increasing the velocity dispersion and decreasing the angular momentum, while gas sinks toward the galaxy center, driving additional central star formation (Moore et al., 1996).

Ram-pressure stripping

Gunn & Gott (1972) first proposed that the ISM could be removed from galaxies moving at $\sim 1000 - 3000 \text{ km s}^{-1}$ through the hot ($\sim 10^7 - 10^8 \text{ K}$) and dense ($\sim 10^{-3} - 10^{-4} \text{ atoms cm}^{-3}$) intracluster medium (ICM) by a process called ram-pressure stripping.

Ram pressure can remove a parcel of gas in the galaxy disk if the force exerted overcomes the gravitational restoring force of the galaxy potential (which we assume to be dominated by the stellar component):

$$\rho_{\text{ICM}} V_{\text{gal}}^2 \geq 2\pi G \Sigma_{\text{star}} \Sigma_{\text{gas}} \quad (1.7)$$

where ρ_{ICM} is the ICM density, V_{gal} is the galaxy velocity in the halo, Σ_{star} is the stellar surface density, and Σ_{gas} is the gas surface density. This is particularly true in low mass systems, where the gravitational potential well is shallower than in massive galaxies.

Ram pressure stripping can remove both the atomic (e.g. Cayatte et al., 1990; Solanes et al., 2001; Gavazzi et al., 2013a; Fossati et al., 2013) and in the strongest cases a fraction of the molecular gas (Fumagalli et al., 2009; Boselli et al., 2014a), as well as the associated dust (Cortese et al., 2010b, 2012a). Hydrodynamical models and observations consistently indicate that ram pressure stripping can be efficient in and around the virial radius of the cluster, especially for galaxies moving towards the cluster core at very high velocities on radial orbits. (Roediger & Hensler, 2005; Boselli & Gavazzi, 2006; Tonnesen & Bryan, 2009).

The stripping process is quite rapid since it is able to remove most of the gas content on time scales of $\sim 1.5 \text{ Gyr}$ (Roediger & Brüggen, 2007; Tonnesen & Bryan, 2009). This time scale even reduces to $\sim 500 \text{ Myr}$ in dwarf systems because of their weak restoring forces (Boselli et al., 2008, Boselli et al. 2016). Some retention of gas, with the associated dust, might be present in the core of the stripped galaxies where the gravitational potential well is at its maximum (Fumagalli et al., 2009; Cortese et al., 2010b). This gas might feed star formation for longer times. Indeed, gas removal is an outside-in process which perturbs only the gaseous component while not affecting the stellar component. Stripped galaxies often show normal optical morphologies in the older stellar components, while they exhibit asymmetries, truncated star forming disks, and extraplanar star forming regions visible in the blue bands tracing the youngest stellar populations (Fossati et al., 2012; Poggianti et al., 2016; Merluzzi et al., 2016).

Figure 1.10, left panel, shows the velocity field of the ionized gas of a galaxy undergoing ram pressure stripping in the Shapley supercluster from Merluzzi et al. (2016). The right panel shows the best model for the velocity field obtained from a hydrodynamical simulation of ram pressure stripping tailored to reproduce the observed galaxy. The synergy

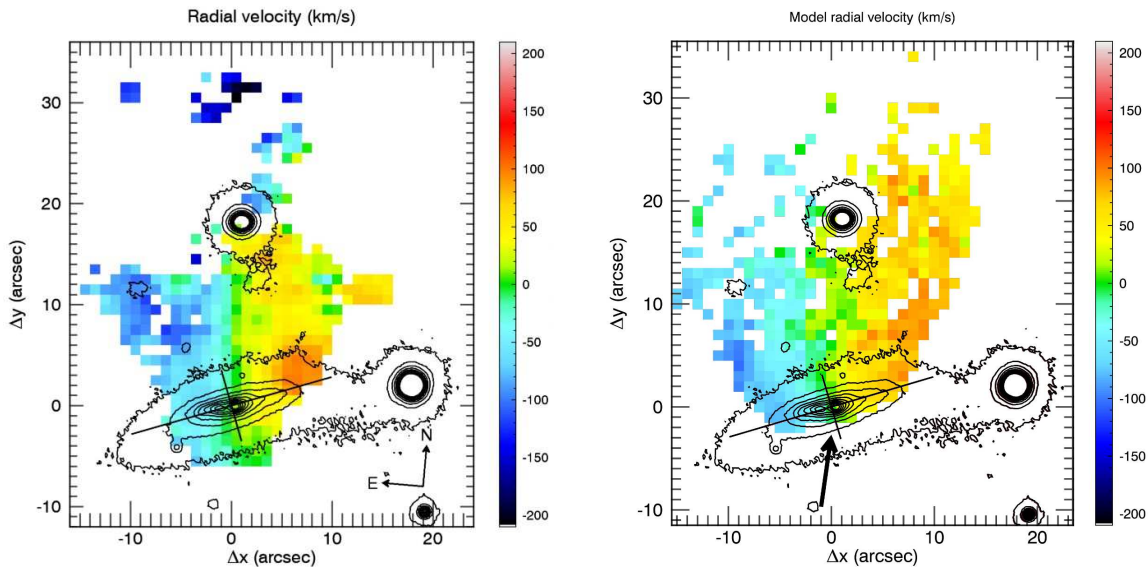


Figure 1.10: Left panel: Velocity field of the ionized gas ($H\alpha$) for the galaxy SOS61086. The black contours mark the surface brightness distribution of the r -band image, while the black lines, show the positions of the minor and major axis. Right panel: Best fit hydrodynamical model of ram pressure stripping acting on SOS61086. The galaxy is moving at ~ 750 km s^{-1} in the hot ICM. The black arrow indicates the wind direction. Images from Merluzzi et al. (2016).

between deep and detailed observations and accurate simulations allowed the authors to estimate the strength of ram pressure and the timescale of gas removal ($t = 250$ Myr).

Viscous Stripping and Thermal Evaporation

Viscous stripping was proposed by Nulsen (1982) as a possible mechanism capable of dragging gas out of galaxies in clusters. If a galaxy, filled by its cold and dense ISM, travels across the hot and tenuous intergalactic medium, the outer layers of its ISM experience a viscosity momentum transfer sufficient for dragging out gas at the edges of the disk at some rate depending on whether the flux is laminar or turbulent. The signature of viscous stripping on the structural, kinematic properties, molecular gas content and star formation activity of galaxies is expected to be similar to that of ram-pressure (Boselli & Gavazzi, 2006). However, because of this similarity it is difficult to clearly identify which objects are shaped primarily by viscous stripping.

Another hydrodynamical process which can remove a fraction of the cold ISM in galaxies in massive haloes is thermal evaporation, first proposed by Cowie & Songaila (1977). This is the mechanism of gaseous mixing at the interface between the hot ICM and the cold ISM. The ISM is heated and evaporates from the cold atomic phase into hotter phases, eventually mixing completely with the ICM (Sun et al., 2007). Ram-pressure stripped tails, like the

one shown in Figure 1.10 have been generally detected in the hydrogen $H\alpha$ recombination line. This line, tracing ionized gas, is bright and easier to observe than tracers of other gas phases. However, X-Ray stripped tails have been observed in a small number of objects (see e.g. Sun et al., 2010), demonstrating that ISM at higher temperatures is present in the stripped gas. The observed X-ray emission is likely from the interface of the hot ICM to the cold stripped ISM, reflecting the evidence of gaseous mixing.

Hot gas stripping and overconsumption

When a galaxy falls into a more massive halo and becomes a satellite, a multi-phase medium (e.g. cold, ionized, hot gas) is associated to the galaxy itself. The hotter phases, which are less bound, should be easier to strip than the cold gas. This mechanism was first proposed by Larson et al. (1980) to explain the increasing fraction of S0 galaxies in dense environments compared to the field. When the hot gas reservoir is removed, star formation proceeds only as long as cold gas is available. When this reservoir is depleted star formation fades and the galaxy becomes passive. Recently Bahé et al. (2013) found that the hot gas can be efficiently stripped out to several virial radii of a massive structure, leading to an increase of the fraction of passive galaxies at large distances from the core of massive haloes.

Even easier, the filamentary accretion onto the galaxy from the surrounding cosmic web will be truncated as the galaxy is enveloped within the hot gas of the more massive halo (White & Frenk, 1991). McGee et al. (2014) proposed that the simple interruption of the fresh gas supply may quench satellite galaxies long before they reach ICM densities where stripping becomes effective, a process which they call “overconsumption”.

Both of these processes will suppress the ongoing accretion onto the cold gas disk of the galaxy and lead to the more gradual suppression of star formation (compared to processes directly acting on the cold gas, like ram pressure), in a process variously labelled “strangulation” or “starvation” (e.g. Larson et al., 1980; Balogh et al., 1997).

In conclusion, the relative importance of the processes described in this section is a function of several parameters (e.g. halo mass, velocity of the galaxy in the halo, orbit, halo assembly history) and therefore it is hard to quantify the impact of each process on the observed properties of individual galaxies. However, environmental studies have gained momentum during the last couple of decades and astronomers have focussed on two complementary observational strategies. On one hand the study of a few clear examples where a single phenomenon can be identified improved our understanding of the key physical parameters governing each mechanism. On the other hand statistical studies, allowed by the growing number of large scale surveys, provided several indicators (e.g. quenching timescales, effects of the environment on the stellar and gaseous components, density or halo mass dependence) which help identifying the impact of different processes on the galaxy population as a whole.

1.4 Metrics to quantify the environment across cosmic time

In the paradigm of hierarchical structure formation, the growth of structures is driven by mergers of dark matter haloes. The properties of galaxies should therefore be correlated with the properties of the parent halo in which they are embedded (i.e. halo mass and whether the galaxy is a central or a satellite).

Probing dark matter haloes directly is not easy. One way to detect the most massive haloes is through gravitational lensing techniques: measurements of the distortion of background objects due to the presence of a massive foreground structure (see e.g. Gavazzi & Soucail, 2007; Limousin et al., 2009). Another method involves the detection of the hot and dense gas that permeates groups and clusters of galaxies, either from their extended X-Ray emission (see e.g. Ebeling et al., 1996; Finoguenov et al., 2007). The main limitation of observing extended X-ray emission is that the X-Ray surface brightness² decreases rapidly with redshift, thus requiring ultra-deep observations to detect less massive systems at high redshift. Another issue comes from the difficulty in separating the diffuse emission from the hot gas in the halo from point sources (e.g. integrated contribution of X-ray binaries in a galaxy or active galactic nuclei) with the point spread function of current X-Ray missions. The *Chandra* satellite, with its superior spatial resolution, alleviated this issue, leading to the detection of more compact structures even at high redshift (Finoguenov et al., 2015).

Finally, the hot gas within massive clusters can be detected through the thermal Sunayev-Zeldovich (tSZ) effect (Sunyaev & Zeldovich, 1972). This effect is caused by the scattering of CMB photons by the hot gas in the halo. This imprints a characteristic spectral distortion to the CMB, which is detected as a local temperature difference compared to the global CMB temperature. One advantage of this technique is that the surface brightness of the tSZ effect is redshift independent. However, even the most massive clusters produce a temperature difference of a few $10^{-6}K$ compared to the average CMB temperature (Bleem et al., 2015), therefore high sensitivity observations are required to detect galaxy clusters with this technique.

These direct methods have primarily been successful in detecting and estimating the mass of the most massive haloes. But clusters (or massive groups) account for a small fraction of galaxies at $z = 0$ ($\lesssim 10\%$). A significant fraction of galaxies in the local universe are instead living in smaller groups with at least two members (Eke et al., 2004). A method that robustly detects intermediate mass haloes is therefore paramount to understanding galaxy evolution in the most common galaxy environment.

In order to explore the large scale structure of the Universe, the availability of accurate spectroscopic redshifts is critical. One of the first surveys that provided a clear picture of the three dimensional distribution of galaxies was the Center for Astrophysics (CfA) redshift survey (Davis et al., 1982) which provided ~ 2400 redshift measurements for a magnitude limited sample of galaxies in the Northern hemisphere. With the work by de Lapparent et al. (1986) it became clear that the galaxies are distributed in clusters

²The surface brightness is the magnitude of an extended astronomical object per unit area.

and groups, connected by a network of filaments and surrounded by voids (underdense regions). In less than a decade, the number of available redshifts increased significantly with the release of data from Las Campanas Redshift survey (LCRS, Shectman et al., 1996). At the beginning of the new century two large area surveys revolutionized this field: the 2 degree Field Galaxy Redshift Survey (2dFGRS; Colless et al., 2001) and the Sloan Digital Sky Survey (SDSS; York et al., 2000) (and their extensions) have provided millions of spectra for objects in the local universe and beyond. This massive amount of observational data opened the way to a large number of works aimed at characterizing the environment of galaxies.

One method to describe the environment is to use group finding algorithms to link galaxies tentatively belonging to the same dark matter halo. During the past two decades, numerous group catalogs have been constructed from various local galaxy redshift surveys (e.g. Eke et al., 2004; Yang et al., 2005; Einasto et al., 2007; Goto, 2005; Berlind et al., 2006; Yang et al., 2007), but also high-redshift surveys (Gerke et al., 2005; Knobel et al., 2012). These works generally used Friends-of-Friends (FOF) algorithms to link galaxies as it is done for dark matter particles in N-body simulations³. The central galaxy of a group is usually defined as the most massive (in stellar mass), or by using a combination of mass and distance from the center of the group (Knobel et al., 2012). As a result, in the most recent group catalogs each galaxy is assigned to a group (even if it is only populated by one galaxy) and centrals and satellites are separated in a binary fashion.

A different approach is to reconstruct the density field by counting the number of neighbors around each galaxy. In this case the choice of environmental metrics is important. Different metrics have been used in the literature, with the choice driven by different survey selections, scientific goals, and availability of accurate redshifts. A disadvantage of this method is that two galaxies can be close on the plane of the sky but their are separated by a large distance in redshift space. To overcome this issue and increase the fidelity of the 3D density field reconstruction, the availability of accurate redshifts for a large majority of the galaxies in the sample is critical. Indeed in order to minimize the number of interlopers, the neighboring galaxies are counted only among those which are close in redshift space to the galaxy of interest. For galaxies with similar redshifts z_1 , and z_2 , their difference in recessional velocity is defined as:

$$\Delta v = c \times \frac{z_1 - z_2}{1 + z_1} \quad (1.8)$$

where c is the speed of light. The volume where neighboring galaxies are counted is typically a cylinder with a circular base (see below the description of the radius) and a depth which is usually defined in units of Δv . The depth of the cylinder depends on the typical redshift uncertainty of each sample.

Redshift estimates obtained from spectroscopic observations of emission lines are typically very accurate since they are obtained from a comparison of the observed wavelength of

³The main difference in the two methods is that FOF algorithms are used in observed space (R.A., Dec., redshift) for a real survey, while in a simulation box they are run in 3D cartesian space.

an emission line with the res-frame wavelength measured on the Earth. Instead, estimates of the distance of astronomical objects obtained using only photometric data, and therefore called photometric redshifts, are more uncertain. The methodology for determining photometric redshifts using template-fitting can be summarized as follows: the photometric data are compared to synthetic photometry for a large range of template spectra and redshifts, and the most likely redshift follows from a statistical analysis of the differences between observed and synthetic data. Photometric redshifts benefit from having high-quality photometry in many bands and from sampling strong continuum features (such as a Lyman or Balmer break), possibly by means of intermediate- or narrow-band filters. The accuracy of photometric redshifts ultimately depends on the brightness of the object and the number of photometric datapoints leading to a fine sampling of the galaxy spectrum.

For samples with complete coverage of spectroscopic redshifts this is set to $\Delta v = \pm(1000 - 1500) \text{ km s}^{-1}$. Instead, if only photometric redshifts are available the depth needs to be increased in order to count all the real neighbors of the galaxy of interest which are scattered in redshift space by inaccurate redshifts. In these cases $\Delta v = \pm(5000 - 10000) \text{ km s}^{-1}$ (see Gallazzi & Bell, 2009; Muldrew et al., 2012; Shattow et al., 2013; Etherington & Thomas, 2015).

The choice of the radius of the base of the cylinder is instead defined by the physical scale that needs to be probed. We recall that a $10^{14} M_{\odot}$ cluster has a virial radius⁴ of $\sim 1 \text{ Mpc}$. Therefore apertures smaller than this radius will probe the density on a scale which is smaller than the size of the cluster (intra-halo scale). However, the same aperture might match the virial radius of less massive structures (e.g. groups) thus probing the halo scale. Larger apertures probe the large scale structure around a galaxy (super-halo scale). With the exception of the lowest density regions, the redshift is not a reliable indicator of distance because of the peculiar velocities that galaxies have inside a gravitationally bound structure. Therefore it is typically preferred to describe the environment using the surface density of galaxies in the cylinder rather than the volume density (see however Croton et al., 2005). The surface density of galaxies in a circular aperture can be defined as:

$$\Sigma_n = \frac{n}{\pi \times r^2} \quad (1.9)$$

where n is the number of neighbors within r . This equation can be equally applied in the case n is a fixed value and r is computed accordingly or viceversa if r is fixed and n is the derived quantity.

In the first case the distance r to the n^{th} nearest neighbor is searched, after the velocity cut is applied. (see Dressler, 1980; Baldry et al., 2006; Cooper et al., 2006; Poggianti et al., 2008). This method builds on the principle that galaxies which are closer together are in denser environments. Variations of this method have been used by Baldry et al. (2006) where the average of two different neighbor densities are taken (the fourth and the fifth), or by Cowan & Ivezić (2008) which combined the distance of every neighbor up to the

⁴This virial radius is that radius for which $\langle \rho \rangle = 200\rho_{crit}$, where $\langle \rho \rangle$ is the mean density in a sphere of radius R_{200} and ρ_{crit} is the critical density of the Universe. Cole & Lacey (1996) showed that this radius approximately separates the virialized and infall regions.

10^{th} to compute the density. The main feature of this method is that it naturally probes different scales in different environments. For example, it probes a very small scale in the densest environments (e.g. groups or clusters) while it extends beyond the virial radius of haloes in under-dense regions of the Universe.

An alternative approach, more sensitive to high-mass over densities, and possibly easier to interpret, is to choose a fixed aperture (r) and count the number of galaxies (n) inside (see Hogg et al., 2003; Kauffmann et al., 2004; Croton et al., 2005; Gavazzi et al., 2010; Wilman et al., 2010). The radius of the aperture typically ranges from 0.2 Mpc (Hirschmann et al., 2014) to a few Mpc, therefore probing different physical scales. A variation of this method has been proposed by Wilman et al. (2010), where counts are taken in several independent annuli of increasing inner and outer radii, instead of a fixed single aperture. By combining the densities on different scales, it is possible to better constrain the effects of environment both inside and outside massive haloes.

At higher redshift two major issues prevented a detailed description of galaxy environment. First, high redshift surveys are typically limited to small areas on the sky, and therefore edge effects have to be carefully taken into account when deriving the density. Second, spectroscopic redshifts are typically only available for a fraction of the objects (the brightest or the most star forming). For the rest of the galaxy population, less accurate photometric redshifts are often used.

Scoville et al. (2007) used an adaptive smoothing technique to identify large scale structures in the COSMOS survey at $0.1 < z < 1.1$. Only photometric redshifts are available for their sample, thus making the density field reconstruction more uncertain in the redshift direction. Moreover the adaptive smoothing method does not constrain the physical size of individual haloes, therefore it is likely that the identified structures (which have sizes up to 10 Mpc in diameter) are a combination of haloes. Similarly, Salimbeni et al. (2009) used a three dimensional algorithm (Trevese et al., 2007) that defines the probability that a galaxy is associated to a given overdensity. This is obtained by computing the galaxy densities in volumes proportional to the positional uncertainties in each dimension (R.A., Dec., and redshift).

Kovač et al. (2010) presented a derivation of the density field in the zCOSMOS survey using a method which combines a spectroscopic redshift sample with a photometric redshift sample. Their method modifies the photometric redshift probability distributions of each galaxy using the spectroscopic redshifts of nearby galaxies. These authors also performed a large number of tests using mock galaxy samples to assess the robustness of the density field reconstruction. Cooper et al. (2005) studied the applicability of several galaxy environment measures to deep high-redshift surveys. Using mock galaxy catalogs to mimic the properties of photometric and spectroscopic surveys at $z \sim 1$, these authors investigated the effects of survey edges, redshift uncertainty, and target selection on each environment measure. A key result is that even accurate photometric redshifts ($\sigma_z/(1+z) = 0.02$) smear out the line-of-sight galaxy distribution, limiting the application of photometric redshift surveys to environment studies. Moreover accurate edge corrections are critical in the relatively small high-redshift fields.

In conclusion very different techniques have been used in the literature to define the

“environment”, with the choice typically driven by the specific goals and features of each dataset. Moreover a calibration of physical quantities (e.g. halo mass, central/satellite status) is rarely performed, thus hampering unbiased comparisons of the results and a comprehensive understanding of the underlying physical processes.

1.5 This thesis

With this thesis we aim to understand the role of environment in shaping satellite galaxies across the last 10 billion years. Our goal is to robustly define the local environment of galaxy and identify centrals and satellites. Then we investigate the star formation properties of satellites and how they are quenched as a function of stellar mass, and halo mass across cosmic time.

To do so, we need two fundamental ingredients: first, we need to study advantages and disadvantages of using different apertures (and different depths) to compute the local density. This goal requires the use of mock galaxy catalogs to construct a projected density field evaluated in redshift space, in order to test how the local density correlates with halo mass, for different choices of the aperture. We also need to define an observationally motivated parameter that can be used to separate central and satellite galaxies. To do so we use the rank in stellar mass in an adaptive aperture. As mentioned above, an accurate description of the density field is not enough to understand the impact of physical processes, which are instead fundamentally linked to theoretically important parameters such as halo mass and whether a galaxy is a central or satellite of its halo. We therefore calibrate our observational parameter set (local density, stellar mass, rank in stellar mass within an aperture), to reach a probabilistic determination of theoretical parameters (halo mass, central or satellite status). This probabilistic approach is best suited to statistical studies where the application of selection functions and observational uncertainties of each dataset, combined with the limitations of the calibration methods, can be taken into full account.

The second necessary ingredient for an accurate and comprehensive study of environment at high redshift is the quality of redshift estimates. In the deepest fields, space and ground based imaging surveys have provided up to ~ 30 photometric data points covering the spectral energy distributions of galaxies from the rest-frame optical to the near-infrared. This turns into an accuracy of photometric redshifts of $\sim 3000 - 5000 \text{ km s}^{-1}$. Cooper et al. (2005); Muldrew et al. (2012) claim that even those state of the art photometric redshifts are not accurate enough to robustly reconstruct the density fields. On the other hand, the availability of more accurate spectroscopic redshift at $z > 1$ has been traditionally limited to bright galaxies or biased to the star forming population (where emission lines can be more easily identified). The advent of highly multiplexed spectroscopic instruments at 8-10 meter class telescopes (e.g. VIMOS, KMOS at the ESO VLT, GMOS at Gemini South, MOSFIRE at the Keck telescopes) opened the way to large redshift surveys, which in some cases probed the rest frame optical emission lines by observing in the near-infrared. None the less these observations remain difficult and costly in terms of observational time.

In the last few years, a new technique employing low-resolution space-based slit-less spectroscopy has revolutionized this field through deep, highly complete samples of intermediate accuracy redshifts. These redshift measurements (called “grism” redshifts, because of the technique employed) have an accuracy of $\sim 1000 \text{ km s}^{-1}$, which is significantly better than photometric redshifts. Taking advantage of the near-infrared observations and the low background of HST, it is possible to detect breaks in the (rest-frame optical) spectrum (in combination with the photometric data) as well as emission lines. As a result the 3D-HST redshift catalog is not biased towards bright blue objects, which are the easiest to observe from optical telescopes on the ground.

The largest of those efforts is the 3D-HST survey (Brammer et al., 2012) which, by combining a large area, deep grism observations and a wealth of ancillary photometric data, provides redshifts for a large sample of objects down to low stellar masses ($\sim 10^9 M_\odot$, and $\sim 10^{10} M_\odot$ at $z \sim 1$ and $z \sim 2$ respectively). The public release of the grism observations (Momcheva et al., 2016), in synergy with deep photometric observations (Skelton et al., 2014) has opened the way to an accurate quantification and calibration of the environment at high-redshift which we present in this thesis.

In chapter 2 we describe tools we have developed to quantify the environment in an “ideal” high-redshift survey using a mock catalog generated from a semi-analytic model. We explore how the local density (in fixed apertures) correlates with the dark matter halo mass; how the stellar mass rank in a circular aperture can be used to identify central and satellite galaxies; and how the size of this aperture needs to be optimized to achieve the best separation of these two galaxy types. We also test the effect of a variable redshift accuracy on our measurements.

Chapter 3 presents the application of our methods to two observational datasets. First we present the 3D-HST survey and its observational strategy. We derive the local density for a magnitude limited sample of galaxies in 3D-HST including accurate edge corrections using photometric catalogs extending beyond the 3D-HST footprint. We build a mock galaxy catalog that matches the 3D-HST selection function, and redshift uncertainty. The synergy between these two catalogs allows us to assign a probability that each 3D-HST galaxy is a central or a satellite and a halo mass probability density function. Lastly we apply an identical method to a $z = 0$ sample selected from the SDSS survey.

In chapter 4 we study the role of environment in quenching the star formation activity of galaxies at $0 < z < 2$ by combining the 3D-HST data at high redshift with the local SDSS sample. We derive the fraction of passive central and satellite galaxies as a function of stellar mass and halo mass, and the characteristic timescale that leads to the quenching of star formation after a galaxy becomes a satellite. We discuss which is the main environmental process that is responsible for the quenching. We conclude by discussing the implications of our results on the gas content of galaxies at the epoch of their first infall as satellites.

In chapter 5 we present a detailed analysis of a galaxy (ESO137-001) which is falling for the first time into a massive cluster. In this case the galaxy is clearly subject to ram pressure stripping of its cold gas. Thanks to deep integral field spectroscopic observations

provided by the revolutionary new instrument MUSE (which recently saw the first light at the ESO VLT), we have been able to study the kinematics and ionization conditions of the stripped gas, to obtain a better understanding of how ram pressure shapes the formation of the red sequence in local massive clusters. This work complements the results of the statistical analysis on the galaxy population described in chapter 4.

Finally we conclude this thesis in chapter 6 by summarizing our key findings, and we describe the future prospects of this thesis. First we present the legacy value of the environment catalog based on the 3D-HST dataset, especially when combined with the properties of a large sample of galaxies for which we have integral field spectroscopic data from the KMOS^{3D} survey. Then we present how the analysis of ESO137-001 can be extended to a mass complete sample of galaxies in a local massive cluster. Lastly, we discuss which future observational facilities will provide new revolutionary datasets to understand the role of environment across cosmic times.

Throughout this thesis, we use the notation $\log(x)$ for the base 10 logarithm of x . All magnitudes are given in the AB system (Oke, 1974) unless otherwise specified.

Chapter 2

The environment of mock galaxies in a Hierarchical Universe

This chapter is adapted from Fossati et al. 2015, MNRAS, 446, 2582.

As described in Section 1.4 a significant effort has been invested in testing measurements of density in the face of difficult selection and redshift errors at $z \sim 1$ – including survey edge effects, magnitude selection, incompleteness and limited redshift accuracy. These efforts, and the interpretation of resulting correlations of environment with galaxy properties, are hampered by the inhomogeneity of methods used for different surveys and by the lack of calibration to theoretically important parameters such as halo mass.

In this chapter we describe the development and calibration of new methods to define galaxy environment in a physically motivated framework. These can be applied to different surveys, overcoming the inhomogeneity of density based methods and facilitating comparisons across redshift and target selection strategies of each observational survey. These methods will be applied to observational data from the SDSS (York et al., 2000) and 3D-HST (Brammer et al., 2012; Momcheva et al., 2016) surveys in chapter 3.

Throughout this chapter we assume a flat Λ CDM cosmology with the following values derived from WMAP7 (Komatsu et al., 2011) observations: $\Omega_m = 0.272$, $\sigma_8 = 0.807$ and $h = 0.704$.

2.1 Models

Our work makes use of a “semi-analytic models of galaxy formation” in order to calibrate the environment of galaxies. A semi-analytic model builds on the results of a dark matter only N-body simulation and then deals with baryonic processes responsible for galaxy formation and evolution using a set of analytic equations. This has the advantage of being computational inexpensive once the dark matter simulation has been run. Different physical recipes can be implemented and compared to a set of observables in a short amount of time compared to hydrodynamical simulations, which instead numerically solve

the equations of gravity and hydrodynamics to evolve dark matter and baryonic particles at the same time.

The first attempts to construct a self-consistent semi-analytic model of galaxy formation began with White & Rees (1978); White & Frenk (1991); Cole (1991), and Lacey & Silk (1991). Since then different groups have developed increasingly sophisticated models, including more physical recipes which have been compared with an increasing amount of observational constraints (e.g. Somerville & Primack, 1999; Bower et al., 2006; Croton et al., 2006; De Lucia & Blaizot, 2007; Monaco et al., 2007; Guo et al., 2011, 2013b; Henriques et al., 2015; Hirschmann et al., 2016).

Each semi-analytic model starts with a dark matter only N-body simulation. One of the largest and most widely used of these simulations is the Millennium simulation (Springel et al., 2005). This includes $N = 2160^3$ particles in a cubic box of size $500h^{-1}$ Mpc. The particle resolution of the original Millennium run is $9.31 \times 10^8 h^{-1} M_\odot$. The simulation starts with a Gaussian random field of density perturbations consistent with the power spectrum of the CMB as obtained by the first year WMAP observations. The evolution with time is obtained by applying non-relativistic Newtonian dynamics, which consists of summing forces (scaling as $1/r^2$) between pairs of particles. The computational cost of this problem scales as N^2 , however several numerical techniques are implemented to reduce the computational time (see e.g. Springel et al., 2005).

The simulation outputs are stored at 64 output times. For each output snapshot, the haloes (groups of bound particles) are identified with a friends-of-friends (FOF) algorithm. Then the individual substructures (sub-haloes) are detected by the algorithm SUBFIND (Springel et al., 2001). Each halo is then classified either as central (the most massive subhalo within the FOF group) or as a satellite. Satellite haloes experience tidal truncation and stripping (De Lucia et al., 2004; Gao et al., 2004). When their mass is reduced below the detection limit of SUBFIND (20 particles, i.e. $1.86 \times 10^{10} h^{-1} M_\odot$ for the Millennium simulation), the subhalo cannot be traced anymore in the simulation and its position is traced only by the most bound particle (this particle is defined at the last snapshot the halo was detected and the galaxy is called an ‘‘orphan’’ galaxy.). After the time defined by the dynamical friction (see De Lucia et al., 2010) has elapsed the galaxy is assumed to merge with the central galaxy of the main halo. Although crude, this assumption reproduces well some observational results like the radial density profile of galaxy clusters (which are dominated by orphan galaxies in the central regions, Gao et al. 2004), and the clustering amplitude on small scales (Wang et al., 2006).

A few years after the Millennium run a second simulation was completed with the same cosmological initial conditions and number of particles but a box size 5 times smaller ($100h^{-1}$ Mpc on a side) and a mass resolution 125 times higher. This run, called Millennium-II, allows the exploration in the realm of dwarf galaxies $M_* \lesssim 10^9 M_\odot$ (Boylan-Kolchin et al., 2009). Together, the two simulations provide excellent statistics over a very large range of scales, from haloes similar to those hosting Local Group dwarf galaxies ($M_h \sim 10^8 M_\odot$) to haloes corresponding to the richest galaxy clusters ($M_h \sim 10^{15} M_\odot$).

In this chapter we make use of the Munich model as introduced by Guo et al. (2011, hereafter G11) and later updated to WMAP7 cosmology by Guo et al. (2013b, hereafter

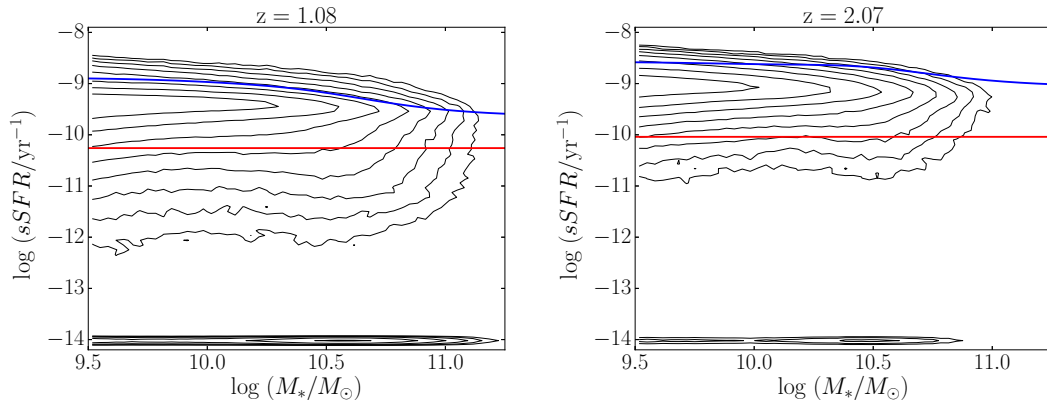


Figure 2.1: Specific star formation rate ($sSFR$) as a function of M_* at redshifts of 1.08 (left panel) and 2.07 (right panel). The blue line is the main sequence parametrisation from Wisnioski et al. (2015) for the 3D-HST sample presented in Whitaker et al. (2014). The red line marks the limit we set to define the passive galaxies in the models. The contour levels are log-spaced with the outermost contour at 25 objects and the innermost at 10^4 per bin. We set all galaxies with $\log(sSFR/\text{yr}^{-1}) < -14$ equal to that value.

G13). This model takes advantage of a new run of the Millennium N-body simulation with cosmological initial conditions consistent with WMAP7 observational constraints. These are in reasonable agreement with the most recent results from both the WMAP9 (Hinshaw et al., 2013) and the Planck (Planck Collaboration et al., 2014) missions. The most significant difference between the assumed cosmological parameters and those used in the original Millennium run (which assumes WMAP1 cosmology) is a lower value of σ_8 . This implies a lower amplitude for primordial fluctuations which is partially compensated by a higher value of Ω_m . G13 performed a detailed comparison of several statistical properties of the galaxy population in WMAP1 and WMAP7 cosmologies. The impact of a lower σ_8 on the galaxy population was also studied in detail in Wang et al. (2008, using WMAP3 cosmology), and we refer the reader to these papers for the details. G13 model is therefore well suited for our purposes due to the combination of a more appropriate cosmology and the large volume.

The G13 model is based on earlier versions of the Munich model, e.g. Croton et al. (2006) and De Lucia & Blaizot (2007). It includes prescriptions for gas cooling, star formation, size evolution, stellar and AGN feedback, and metal enrichment. G13 assumes a new and more realistic implementation (compared to the simple model by Mo et al. 1998) of the sizes of gas disks. Both supernovae (SN) and active galactic nuclei (AGN) feedback are implemented. The first implies that massive stars explode as supernovae and the energy released converts a fraction of the cold gas into the hot phase or even expels it from the halo. AGN feedback is implemented following the model by Croton et al. (2006). For more details on these prescriptions we refer the reader to G11, G13 and De Lucia & Blaizot (2007).

Current SAMs suffer from an overproduction of low-mass galaxies at high-redshift. Recently, Henriques et al. (2015) presented a new model in which the reincorporation timescales of galactic wind ejecta are a function of halo mass. As a result they obtain a better fit of observed stellar mass functions out to $z \sim 3$. However, because these prescriptions are not implemented in G13 we perform a statistical correction to the number densities as presented in Sect. 2.1.1.

In most SAMs the satellite population has been quenched too quickly due to instantaneous stripping of the hot gas (e.g. Weinmann et al., 2006, 2010). G11 proposed a more gentle action of strangulation and ram pressure stripping which are active only when a galaxy falls into the virial radius of a more massive halo. Although this improves the treatment of environmental effects, the fraction of passive galaxies is still significantly overestimated compared to observational results at $z = 0$ as shown by Hirschmann et al. (2014). While this discrepancy is reduced in G13, the passive fraction is still too large. In this chapter we do not require that the fraction of passive galaxies matches the observations: we only use the passive fraction trends as a function of environment in the models to test our ability of recovering them with observational proxies.

2.1.1 The model galaxy sample

From the 62 outputs of the simulation, we make use of those at $z = 1.08$ and $z = 2.07$. We select galaxies above a fixed stellar mass limit of $10^{9.5} M_{\odot}$ in both the redshift snapshots. Setting the same mass limit at different redshifts allows us to witness the increase in number density as the Universe evolves, and we get $\log(n/\text{Mpc}^3) = -2.08, -2.28$ at $z = 1.08, 2.07$ respectively. Those values are higher than the observed number densities recently obtained by Muzzin et al. (2013) integrating the stellar mass functions (SMFs) from the COSMOS/ULTRAVista observational data down to $M_* = 10^{9.5} M_{\odot}$ ($\log(n/\text{Mpc}^3) = -2.19, -2.68$ at $z = 1.08, 2.07$). Indeed, the models fail to match the observed SMFs at $z > 1$ by over-predicting the number of galaxies below the characteristic mass (M_*) of the SMF (Fontanot et al., 2009; Hirschmann et al., 2012; Wang et al., 2012). This discrepancy, which gets worse at higher redshifts, arises in the central galaxy population of intermediate mass haloes, but also affects satellites (as centrals become satellites in a hierarchical Universe). We statistically correct this problem by assigning to each galaxy a weight (w) which is the ratio between the predicted and the observed SMFs (i.e. number densities) at the stellar mass of the galaxy. To derive this correction, the model stellar masses are convolved with a gaussian error distribution with sigma 0.25 dex in order to match the uncertainties on the observed stellar masses. We use the observed SMFs from Muzzin et al. (2013)¹ because the mass limit of their dataset is well below M_* at the redshifts of our interest allowing a robust determination of the faint end slope. Moreover the data are deep enough that the SMFs are not extrapolated to the stellar mass limit we use at $z = 1.08$, and extrapolated by only 0.5 dex at $z = 2.07$. This weight is then used when computing the local density around each galaxy as presented in Section 2.2 and when

¹We make use the single Schechter (Schechter, 1976) fit where the faint end slope (α) is a free parameter.

statistical properties of galaxies or of their parent haloes are computed, unless otherwise stated.

To define passive galaxies we make use of the specific star formation rate ($sSFR$), i.e. the star formation rate per unit mass. We set the $sSFR$ limit, for passive galaxies, as follows:

$$sSFR < b/t_z \quad (2.1)$$

where b is the birthrate parameter $b = SFR / \langle SFR \rangle$ as defined by Sandage (1986) and t_z is the age of the universe at redshift z . Inspection of the $sSFR$ distribution in our models revealed there is little, if any, dependence on stellar mass, thus we use the value proposed by Franx et al. (2008): $b = 0.3$ (see Figure 2.1). The $sSFR$ limits are $\sim 5.5 \times 10^{-11}$, and $9.1 \times 10^{-11} \text{ yr}^{-1}$ at $z = 1.08$ and 2.07 respectively. The quantitative results presented in this chapter would slightly change if a different limit is set. None the less the qualitative trends are unchanged.

2.2 Quantification of environment

As described in Section 1.4, there are many ways to describe the environment in which galaxies live. We focus on a set of simple density measurements using neighboring galaxies. This is straightforward to correct for incompleteness and calibrate for survey selection and for redshift errors. Recently, Shattow et al. (2013) have demonstrated that the fixed apertures method is more robust across cosmic time, is less sensitive to the viewing angle, and closer to the real over density measured in 3D space than the Nth nearest neighbor. For those reasons, we use this method to quantify the environment.

For the following analysis, we use model galaxies to reproduce and test different possible measurements of the density on scales ranging from intra-halo to super-halo. First of all we convert one of the comoving axes of the simulation box into a physically motivated redshift. The centre of the box is taken to be at the exact redshift of the snapshot under investigation. We compute the positional offset of each galaxy from the centre and convert this into a redshift offset using a cosmology calculator (Wright, 2006). Then, the effect of peculiar velocities is included to produce redshift distortions. This produces redshifts with a quality similar to high spectral resolution observations (hires-z hereafter).

We also create two sets of less accurate redshifts. The first one is obtained by convolving the hires-z with a gaussian error distribution with $\sigma = 1000 \text{ km s}^{-1}$. This roughly corresponds to the redshift accuracy of low spectral resolution (lowres-z) surveys such as those obtained using slit-less spectroscopy on HST. Those surveys have the huge advantage of obtaining a redshift for most of the objects in the observed field, thus reducing the selection bias of pointed spectroscopic surveys and increasing the sampling rate to $\sim 90 - 95\%$. In the next chapter we quantify the environment for the largest of those surveys 3D-HST (Brammer et al., 2012) and we characterise in details the redshift accuracy (see Figure 3.1). In general an average redshift uncertainty of $\sigma = 1000 \text{ km s}^{-1}$ is appropriate for those surveys.

The second set is a photometric redshift (photo-z) sample obtained by convolving the hires-z with a gaussian error distribution with $\sigma = 5000 \text{ km s}^{-1}$. This value is consistent with the accuracy of photometric redshifts for galaxies as faint as our mass selection limit in the deep fields where a wealth of multiwavelength data is available (see e.g. Ilbert et al., 2009; Whitaker et al., 2011).

When the redshifts accuracy is decreased, galaxies can be scattered outside the redshift interval (which is set by the size of the simulation box). In those cases we assume a periodic box such that galaxies scattered beyond the maximum redshift are included at the front of the box and viceversa. We make use of those three samples to test the performances of our methods in different scenarios.

In order to obtain measurements of density we apply a method similar to the one described in Wilman et al. (2010). We consider all the galaxies more massive than the limit set in Section 2.1 and we calculate the projected density of weighted neighboring galaxies Σ_{r_i, r_o} in a combination of annuli centered on these galaxies with inner radii r_i and outer radii r_o . Our set of apertures ranges from 0.25 Mpc to 1.5 Mpc. This allows us enough flexibility to use either a single circular annulus ($r_i = 0$) or a combination of a circular annulus ($r_{i_1} = 0$) and an outer annulus that does not overlap with the previous one ($r_{i_2} = r_{o_1}$). As shown by Wilman et al. (2010) this method allows us to test the correlation between galaxy properties and the density on different scales. For an annulus described by r_i and r_o , the projected density is computed as follows:

$$\Sigma_{r_i, r_o} = \frac{w_{r_i, r_o}}{\pi(r_o^2 - r_i^2)} \quad (2.2)$$

where w_{r_i, r_o} is the sum of the weights of neighboring galaxies living at a physical projected distance² $r_i \leq r < r_o$ from the primary galaxy, and within a rest-frame relative velocity range $\pm dv$. Hereafter, the density in a circle will simply be labelled as Σ_{r_o} . The primary galaxy is not included in the sum, thus isolated galaxies have $\Sigma_{r_o} = 0$.

The use of weights effectively changes the number of galaxies per halo or aperture in order to match the stellar mass function, without altering the clustering properties of haloes from the simulation. At intermediate to high densities this approach is sufficient to mimic the real universe, while at lower densities there is little dependence of the quantities we study (median halo mass, passive fraction) with density. In the end, the qualitative trends presented in this work are not different if the weights are not applied.

We use the velocity cut at $dv = 1500 \text{ km s}^{-1}$ for the hires and lowres-z samples. This is indeed adequate for a sample with complete spectroscopic redshift coverage (Muldrrew et al., 2012; Shattow et al., 2013), which will be the case for deep field surveys in the near future. Because the photometric redshifts are less accurate, we increase the velocity cut at $dv = 7000 \text{ km s}^{-1}$, when we use this sample. This keeps the ratio between dv and the redshift accuracy roughly constant across the three samples.

We remove from the analysis the galaxies living near the edges of the box. In spatial coordinates this affects objects closer to the edges than r_o . In redshift space we remove

² The choice of physical apertures in place of comoving is motivated by the fact that they do not depend on redshift and they allow for a straightforward comparison with halo sizes.

all objects in the first and the last $70/h$ Mpc to ensure that the cylindrical apertures are always within the redshift limits of the sample. The final impact on the overall statistics is negligible.

In addition, we record the stellar mass rank of each galaxy with respect to its neighbors in the same set of cylinders. For each primary galaxy we record its rank in stellar mass with respect to the neighboring galaxies in the volume defined by a cylindrical aperture. If the primary galaxy is the most massive it scores rank 1, if it is the second most massive it has rank 2 and so on. Then the cylinder is put on the following primary galaxy and the procedure is repeated. Because the rank in a cylindrical annulus is of little physical interest, we use regular cylinders ($r_i = 0$). We show in Section 2.4 how the mass rank can be used to discriminate between the central and satellite populations.

2.3 The correlation of density with halo mass

In this section we examine correlations of density measured on different scales with halo mass for both central and satellite galaxies at $z = 1.08$ and $z = 2.07$. This complements recent works in the local Universe by Muldrew et al. (2012), Haas et al. (2012), Etherington & Thomas (2015) and Hirschmann et al. (2014).

Figure 2.2 shows the correlation of median (and 25th and 75th percentile) halo mass with density on three scales: $\Sigma_{0.25}$ (left panels), $\Sigma_{0.75}$ (central panels), and $\Sigma_{1.50}$ (right panels) for central galaxies (red solid lines) and satellites (blue solid lines). In each panel, the histograms at bottom show the weighted distribution of density for centrals and satellites on the same scales. The top and bottom rows refer to $z = 1.08$ and $z = 2.07$, respectively. The binning is logarithmic in density and galaxies with no neighbors within the aperture ($\Sigma_{r_o} = 0$) are included in the first bin that is populated with objects at each scale. From a first look at the distributions it is clear that the three different scales probe different ranges of density. The bigger the aperture the lower is the density that can be measured.

For satellite galaxies the correlation is remarkably good at all scales and all redshift: in this redshift range even the smallest aperture we use (0.25 Mpc) is big enough to recover a density dependence for the satellites.

The halo mass dependence on density for centrals is a strong function of the aperture size. The typical virial radius of a $10^{13}M_{\odot}$ (resp. $10^{14}M_{\odot}$) halo is 0.30 (resp. 0.63) Mpc. As a result the 0.25 Mpc aperture probes intra-halo scales for all reasonably massive haloes, and a good correlation with density (which is almost indistinguishable from that of satellites) arises. Despite the low number counts in this small aperture, the correlation we find is not unexpected. It follows from a power law dependence of median halo mass on group size (defined as the number of galaxies above the stellar mass limit which live in the same dark matter halo). This correlation extends to small group sizes (2 – 3 members per group) and holds for centrals as well as for satellites. This happens whenever the aperture size does not extend well beyond the halo virial radius. Taking a look at the distribution of density on 0.25 Mpc scale it is clear that, while a population of isolated centrals exists at $\Sigma_{0.25} < 5\text{Mpc}^{-2}$, the higher densities are also well populated by central galaxies. It is

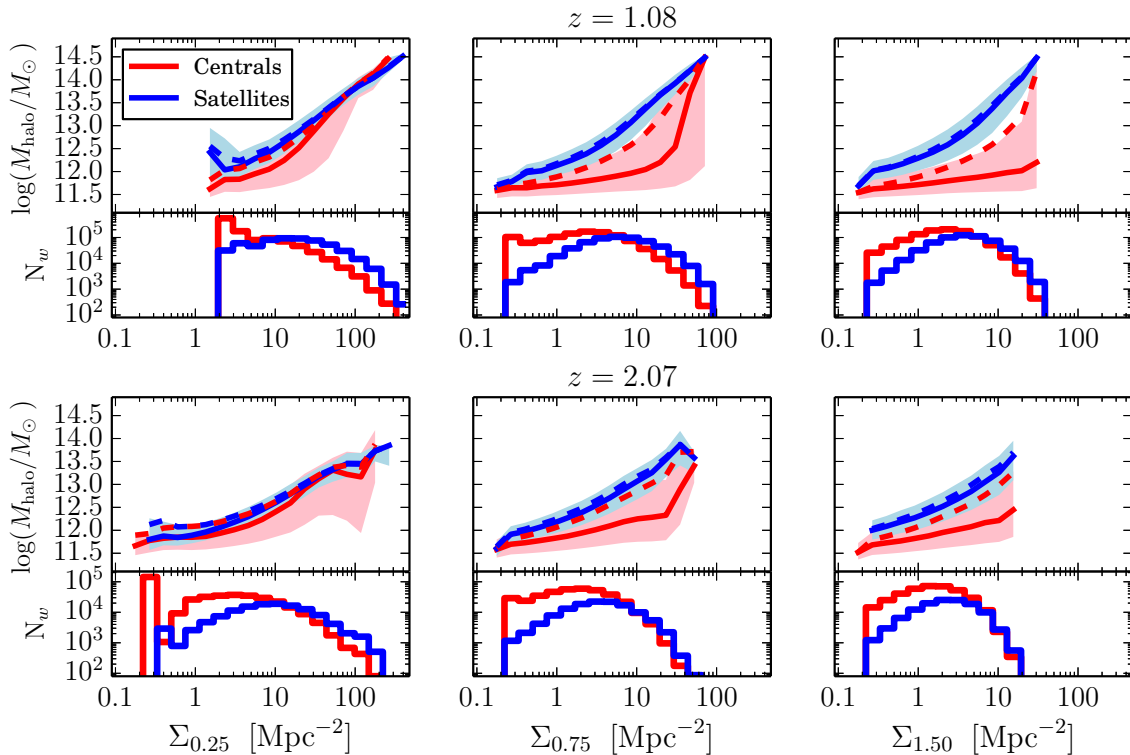


Figure 2.2: Median mass of the parent halo of each galaxy as a function of density measured on three scales $\Sigma_{0.25}$ (left panels), $\Sigma_{0.75}$ (central panels), and $\Sigma_{1.50}$ (right panels) for central galaxies (red solid lines) and satellites (blue solid lines) at $z = 1.08$ (top panels), and $z = 2.07$ (bottom panels). The shaded areas are bounded by the 25th and 75th percentiles of the distributions. Dashed lines correspond to the mass of the most massive halo within 1 Mpc ($M_{h,1\text{Mpc}}$, see text). The distribution of densities for centrals and satellites are shown in the lower part of each panel.

indeed at those high densities that we find a good correlation with the group size.

Looking at the 25th and 75th percentiles of the halo mass distribution at fixed density (shaded region in Figure 2.2) we notice that the trend is much tighter (smaller scatter) for satellite galaxies than for centrals. Indeed the 75th percentile for centrals tracks, albeit with some changes, the halo mass of satellites at fixed density on all scales, while the median and to a greater extent the 25th percentile drops to much lower halo mass as the scale and density increases (almost erasing any correlation with halo mass). In other words: there exists a significant population of central galaxies at high density which inhabit low mass haloes, and the size and relevance of this population increases to larger scales.

We quantify this statement in Figure 2.3 which shows the halo mass distributions in a fixed bin of density (15-20 Mpc^{-2}) on scales 0.25 Mpc (top panel), 0.75 Mpc (middle panel), and 1.50 Mpc (bottom panel) at $z = 1.08$. This bin is chosen to probe a fairly high density with good statistics on the three scales although it is a more unusually large density

when measured on larger scales. Satellites at this density occupy a peak of relatively high halo mass, demonstrating the tight correlation between halo mass and density seen in Figure 2.2. A significant fraction of central galaxies live in the same peak, illustrating the relative insensitivity of a “density within an aperture” statistic to whether a galaxy is the central or a satellite galaxy of a massive halo. However there is also a second significant population of central galaxies at low halo mass: 52% (61%, 65%). Hereafter the first value refers to the 0.25 Mpc aperture while those in parenthesis refer to the 0.75 Mpc and 1.50 Mpc apertures respectively. These galaxies live in small haloes (which is why they are usually centrals) but have a high number of neighboring galaxies which live within the cylindrical aperture used to measure density – a number which can only increase with the aperture size. This phenomenon is important when a significant fraction of the neighboring galaxies used to trace density live outside the galaxy’s own host halo – i.e. when the aperture scale is larger than the virial radius of the halo. This explains why the scatter becomes small when densities are measured on a 0.25 Mpc scale, while on the 0.75 Mpc scale (at $z = 1.08$) the median halo mass shoots up at the very highest densities – such densities are most often obtained at the centers of massive haloes which have virial radii close to 0.75 Mpc. However, in all other regimes, the low halo mass population is the dominant one for central galaxies at intermediate to high density.

Our goal is to calibrate the environment of galaxies using measurements of density: Figure 2.3 shows that this is a degenerate problem where we have only a single measurement of density within an aperture. In Section 2.3.1 we examine how the combination of two scales can break this degeneracy, while in Section 2.5 we ignore the second peak by excluding low (stellar) mass galaxies at high density. Trends driven by the population of low halo (or stellar) mass centrals at high density are difficult to interpret because they can have actual physical association with the nearby massive halo to which they have (at the current snapshot) not been assigned. Using an N-body simulation and accurately tracing the trajectories of ejected satellites, Wetzel et al. (2014) have shown that infalling galaxies can pass through a massive halo on radial orbits and emerge out the other side, where they extend out to 2.5 times the virial radius of the halo they crossed. They compose 40% of all central galaxies out to this radius and their evolution is likely to have been influenced by satellite-specific processes. This “backsplash” population has also been investigated by Balogh et al. (2000), Mamon et al. (2004), Ludlow et al. (2009), and Bahé et al. (2013), as well as Hirschmann et al. (2014) who also find that such additional processing of low mass, high density galaxies is necessary to explain the density dependence of the passive fraction of central galaxies at low redshift. Thus an accurate accounting for this population is essential.

To examine the actual real-space proximity of galaxies to massive haloes, we consider the most massive halo within a sphere of 1 Mpc ($M_{h,1\text{Mpc}}$). In Figure 2.3 we show the distribution of $M_{h,1\text{Mpc}}$ (black, dashed line). This does not completely exclude the low halo mass population, but reduces it substantially. The fraction of centrals with $M_{h,1\text{Mpc}} < 10^{12.5} M_{\odot}$ is 37% (32%, 30%), far fewer than where the host halo mass is used. Most remaining such galaxies are in this high-density bin due to redshift space projection. However this tells us that almost half of low halo mass central galaxies at this density are within 1 Mpc of

a massive halo and many may have already passed through that halo. Thus for a clean selection of central galaxies which have not suffered such effects, it seems sensible to exclude those at high density. In Figure 2.2 we overplot the median relation of density with $M_{h,1\text{Mpc}}$ (dashed line). The reduced peak at low mass means that this more closely follows the 75th percentile of halo mass, and approaches that of satellites (for which the low halo mass peak is negligible).

In order to test the effect of redshift accuracy, we repeat the analysis on the low-redshift sample. None of the trends presented in this section notably change, the main effect being a smoothing of the highest density peaks, slightly reducing the median halo mass. Conversely, when photometric redshifts are used we notice two effects. First, the median halo mass at fixed density is reduced both for centrals and satellites on all scales. The 0.75 and 1.50 Mpc scales are the most affected. The median halo mass for centrals is constant with density at $10^{12}M_{\odot}$. For satellites this is 0.5 dex higher and increases with density only at $\Sigma > 10\text{Mpc}^{-2}$. On the 0.25 Mpc scale a good correlation of median halo mass with density still exists, but with a larger scatter both for centrals and satellites. The second effect we find is in the distributions of density, which are narrower than in the hires-z case, reducing the density dynamic range. In Figure 2.4 we compare the density in the hires-z sample to those in the photo-z sample for the 0.75 Mpc aperture. The black dashed line marks the 1:1 relation. We show two velocity cuts for the photo-z sample: $dv = \pm 1500\text{ km s}^{-1}$ (red) and $dv = 7000\text{ km s}^{-1}$ (blue). In the upper panel the distribution of densities is plotted for the hires-z sample and in the right panel we show the density distributions for the two apertures used for the photo-z sample. Both from the contours and the histograms it is evident that $dv = \pm 1500\text{ km s}^{-1}$ misses many objects in the most dense regions, while with a larger depth $dv = \pm 7000\text{ km s}^{-1}$ we re-incorporate those galaxies obtaining a good correlation with the hires-z measurements. Moreover, using photo-z, the low densities are devoid of galaxies which end up at intermediate densities. Also this effect is less severe for the 0.25 Mpc aperture. Recently, Etherington & Thomas (2015) came to very similar conclusions on how to optimise the cylindrical aperture parameters for surveys with reduced redshift accuracy. They find that the radius of the aperture plays a minor role, while the velocity cut should be increased with poorer redshift accuracy. This is to ensure that galaxies that are scattered along the line of sight by the uncertain redshifts are captured within the cylinder.

It must also be noted that the large statistics of mock catalogs, allows us to probe a wide range of density, however this would be significantly reduced when considering the number of objects in a real survey. In conclusion, although the radius and depth of the cylindrical aperture can be optimized for the redshift accuracy of a specific survey, the completeness of the spectroscopic coverage remains a fundamental parameter for an accurate quantification of the environment.

Finally we test if the distributions shown in figure 2.3 would change at the low halo-mass end due to the resolution of the N-body simulation. The history of galaxies whose parent haloes are below $10^{12}M_{\odot}$ cannot be traced accurately along the halo merger trees, thus their physical properties might be inaccurate. We perform the same exercise using the G13 model applied to the Millennium-II simulation scaled to WMAP7 parameters

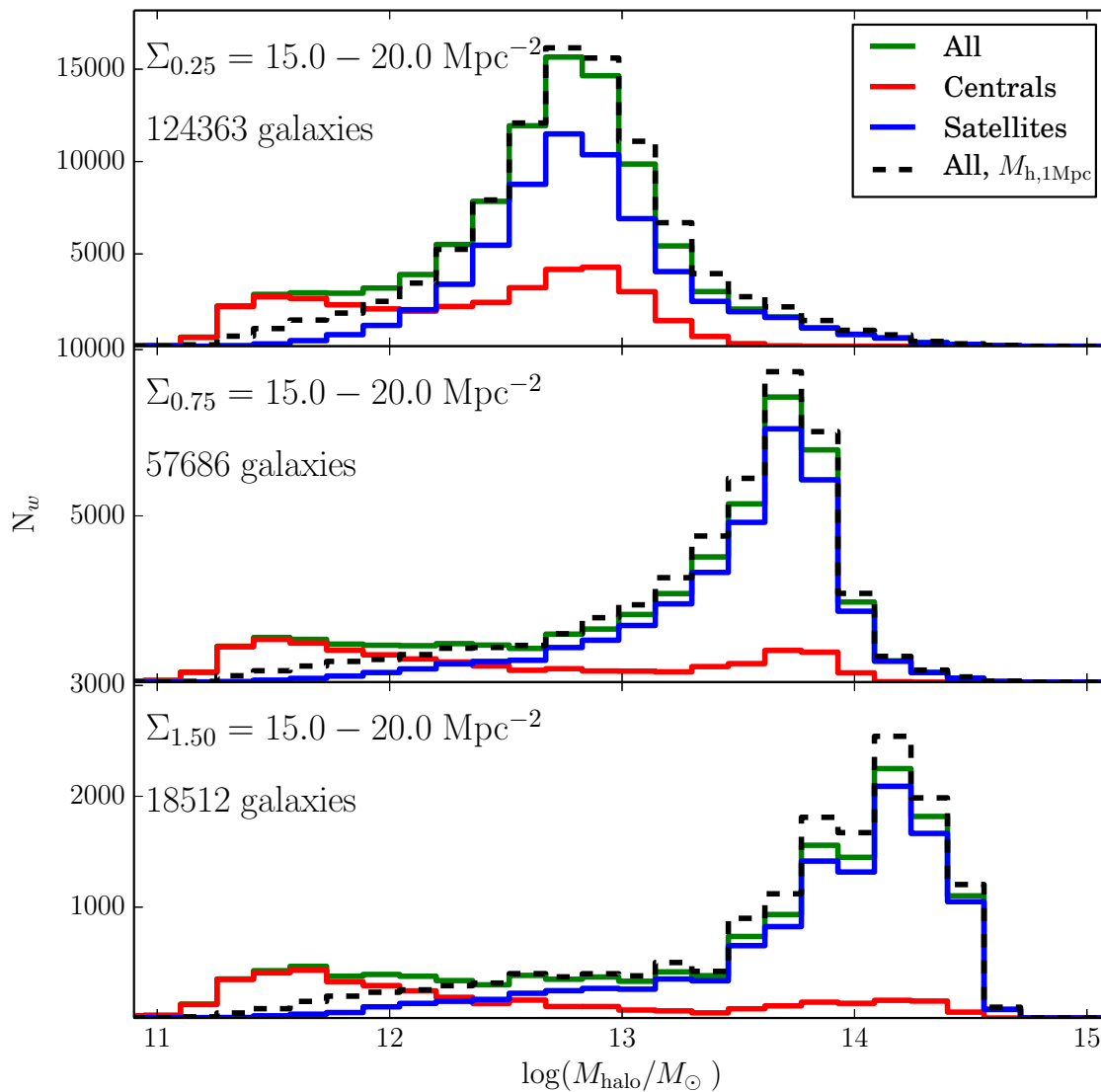


Figure 2.3: Weighted distributions of parent halo mass for each galaxy in a fixed bin of density ($15\text{--}20 \text{ Mpc}^{-2}$) on scales $\Sigma_{0.25}$ (top panel), $\Sigma_{0.75}$ (middle panel), and $\Sigma_{1.50}$ (bottom panel) at $z = 1.08$. The dashed line shows the weighted distribution of the most massive halo mass within 1 Mpc of each galaxy (see text).

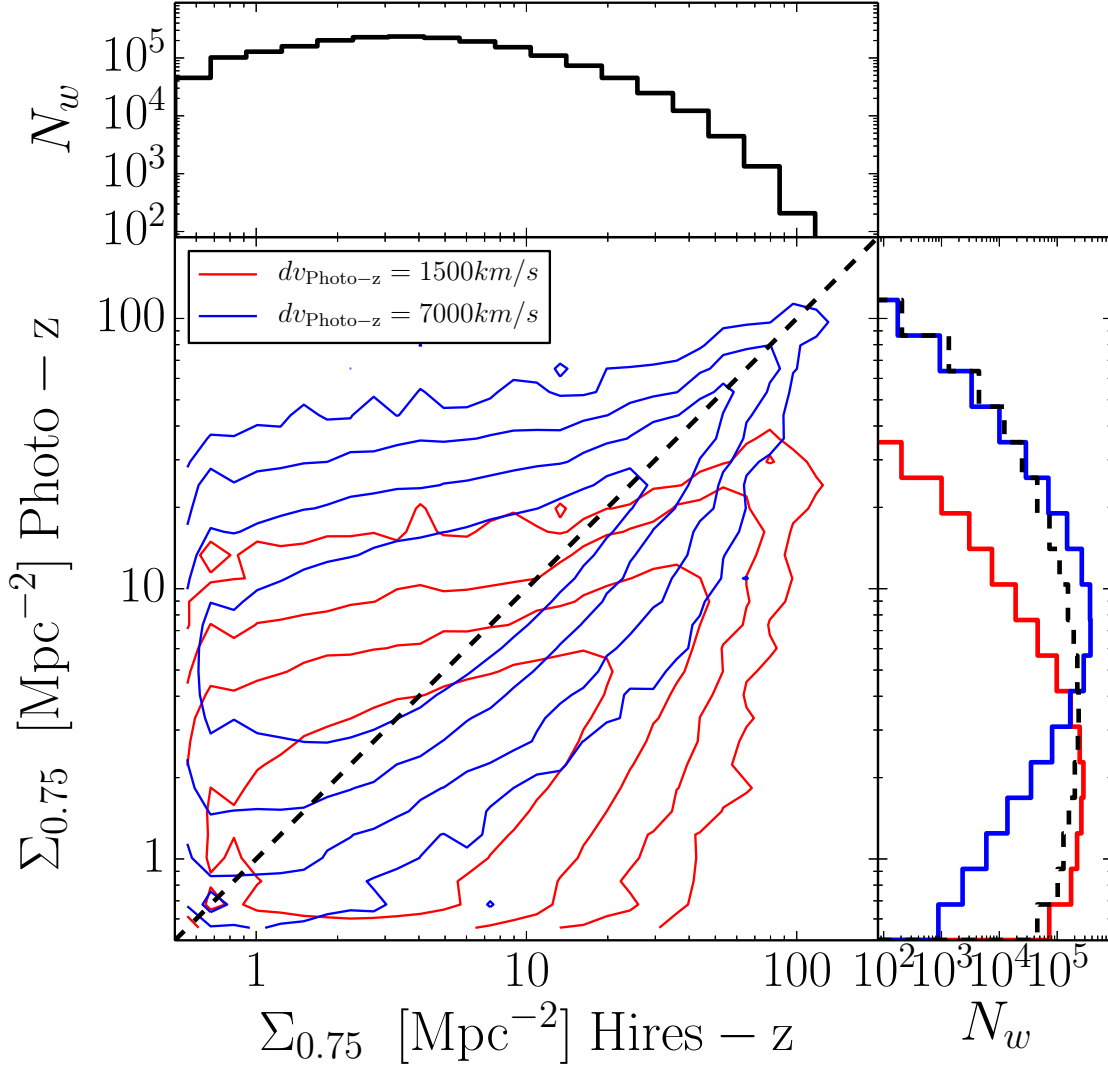


Figure 2.4: Main panel: Density on the 0.75 Mpc scale for the photo-z sample and different velocity cuts ($dv = \pm 1500 \text{ km s}^{-1}$ red and $dv = \pm 7000 \text{ km s}^{-1}$ blue) as a function of density in the same aperture (and $dv = \pm 1500 \text{ km s}^{-1}$) for the hires-z sample. The contours are logarithmically spaced with the outermost contours at 25 objects per bin and the innermost at 10^4 objects per bin. Upper panel: weighted distribution of density for the hires-z sample. Right panel: weighted distributions of density for the photo-z sample with the same velocity cuts as above. The distribution of density for the hires-z sample (dashed black) is repeated here for comparison.

following Angulo & White (2010). This simulation has a smaller cosmological volume but a particle resolution about 100 times better. The distribution of halo masses for centrals and satellites below $10^{12}M_{\odot}$ is unchanged, probably thanks to our conservative limit in stellar mass.

2.3.1 A multi-scale approach

As we already discussed in Sect. 2.3, the super-halo scale imprints a complex dependence on the halo mass vs density correlation for central galaxies. Here we show how the combination of two scales of density can be used to identify low mass galaxies at high density. In Figure 2.5 (top panels) the median halo mass dependence on density is shown for a pair of independent scales: $\Sigma_{0.00,0.75}$ and $\Sigma_{0.75,1.50}$. The smaller scale is chosen to cover $\sim 2 - 3$ times the virial radius of haloes more massive than $10^{13}M_{\odot}$, while the larger aperture highlights the second order effects on super-halo scales. The left hand panels include all galaxies while those in the middle and on the right include only centrals and satellites respectively. Over-plotted contours, where they exist, are computed from a smoothed map of the data using a Gaussian filter with $\sigma = 1.5$ pixels. Smoothing is required to wash out the local features while keeping the overall direction of change of the halo mass with density. Indeed, contours in the top left panel are typically aligned with the vertical axis, showing that halo mass correlates more strongly with smaller scale densities than with the larger ones.

A closer look shows that the contours are not fully aligned with the large scale-axis. There is a clear anti-correlation with large-scale density at fixed small-scale density, i.e. the median halo mass decreases when increasing the large scale density at *fixed* small scale density. The top middle panel shows that the median halo mass is not dependent on density for central galaxies except for the extremely high small-scale densities. Finally, the top right panel shows that the median halo mass for satellite galaxies depends almost entirely on the small-scale density, as seen in Figure 2.2.

In order to understand these patterns it is important to roughly sketch the densities experienced by galaxies living in the core or in the outskirts of their own halo. A galaxy living in the centre of its own halo has high densities within annuli up to the size of the halo and low densities beyond. A galaxy living just beyond the halo virial radius has an intermediate density on small scales (as the aperture encompasses a fraction of the halo) and a high density on the larger scale, since the nearby halo core is located in this annulus. If we consider that those galaxies beyond the halo boundary are considered centrals, we fully understand why the density does not correlate positively with halo mass on large scales.

For the bottom panels of Figure 2.5 we show instead the mass of the most massive halo within 1 Mpc of each galaxy, $M_{h,1\text{Mpc}}$. In contrast to the median mass of the parent halo, the mass of the most massive nearby halo correlates strongly with density for centrals (middle bottom panel). As already stressed in the text, the satellite galaxies are almost unaffected. The bottom left panel shows how the complete population behaves. The contours are now essentially vertical and the anti-correlation of halo mass with large-scale

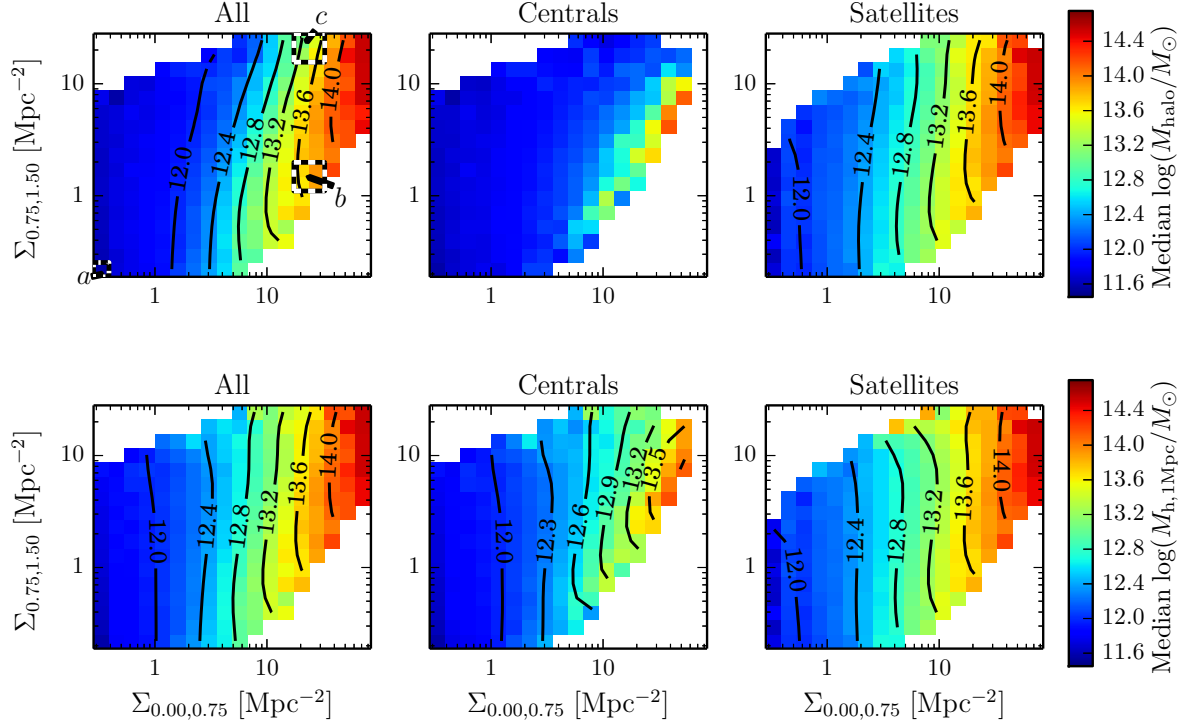


Figure 2.5: Top panels: halo mass dependence with density on scales $\Sigma_{0.00,0.75}$ and $\Sigma_{0.75,1.50}$ for all galaxies (left panels), central galaxies only (central panels) and satellite galaxies only (right panels) at $z = 1.08$. Bottom panels: as before but the nominal halo mass has been replaced with that of the most massive halo within a 3D physical sphere of 1Mpc radius ($M_{h,1\text{Mpc}}$). The labels a , b , and c in the top left panel highlight three bins (black and white squares) whose halo mass distributions are shown in Figure 2.6.

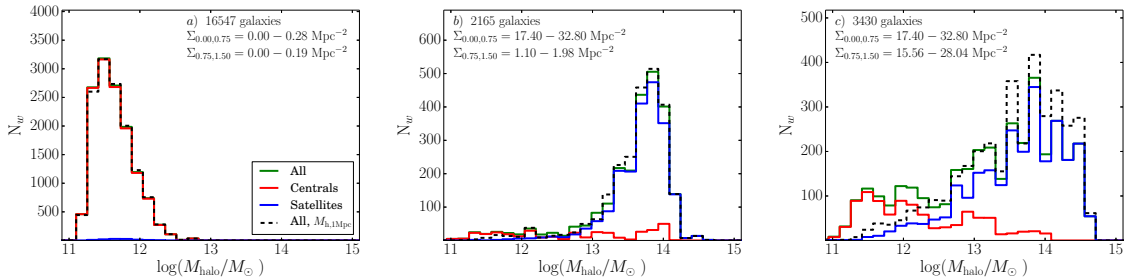


Figure 2.6: Halo mass distribution in three bins indicated using black and white squares and labelled a , b , and c in the top left panel of Figure 2.5.

density at fixed small-scale density disappears.

We select three representative regions (a , b , c) in the upper left panel in Figure 2.5 and we study the distributions of halo mass in these regions in Figure 2.6.

The left-hand panel (a) shows the distribution of halo masses in the lowest density bin on both scales. Almost all the galaxies are centrals (red solid) living in low mass haloes and the halo mass replacement has little effect on the overall distribution (blue solid) as the majority of them have no neighbors within 1 Mpc. With the Millennium-II simulation we get the same result and so this is robust against resolution effects. The centre and right-hand panels (b and c) are chosen to have the same high density on the inner 0.75 Mpc scale but very different densities in the outer annulus, highlighting the importance of the large-scale density. The galaxies whose large-scale density is low (panel b) live near the centre of their host halo, thus the sample is made almost entirely of satellites (blue solid) and the effect of centrals on the overall distribution is negligible. On the other hand, when $\Sigma_{0.75,1.50}$ is high (panel c), the contribution from centrals having halo masses smaller than $10^{12.5} M_{\odot}$ is 24%, causing a decrease in the median halo mass. This population of low halo mass centrals at high density can contain a significant population of “backsplash” galaxies, as discussed in Section 2.3. We see that the use of multiple scales can help identify such populations. Figure 2.5 also shows the distribution of $M_{h,1\text{Mpc}}$ (black dashed lines) for our three bins: in panel c , the fraction of centrals with halo masses smaller than $10^{12.5} M_{\odot}$ is reduced to 10%. In this case the halo mass distribution is skewed to higher halo mass becoming similar to that in panel b .

2.4 Mass rank as a method to disentangle centrals and satellites

It is also critical to describe whether a galaxy dominates its halo (and the local gravitational field) or if it is instead orbiting within a deeper potential well. This can be modeled (and is in SAMs) assuming a dichotomy between central and satellite galaxies. Central galaxies accrete gas by cooling, and merge with their satellites. In contrast, satellite galaxies orbit within the gravitational field, and move with respect to the intra-halo gas, thus experiencing tidal interaction and stripping effects. This has been both directly observed in nearby clusters (see e.g. Yagi et al., 2010; Fossati et al., 2012, 2016a; Boselli et al., 2016) and indirectly witnessed from statistical studies (Balogh et al., 2004; Baldry et al., 2006; Haines et al., 2015). Moreover, it has been claimed that, while the properties of all galaxies are shaped by intrinsic parameters, (e.g. stellar mass Peng et al. 2010; Kovač et al. 2014), satellites’ properties are also influenced by their environment (Peng et al., 2012; Quadri et al., 2012; Woo et al., 2013; Balogh et al., 2016). A reliable method to separate centrals from satellites in observations is therefore crucial.

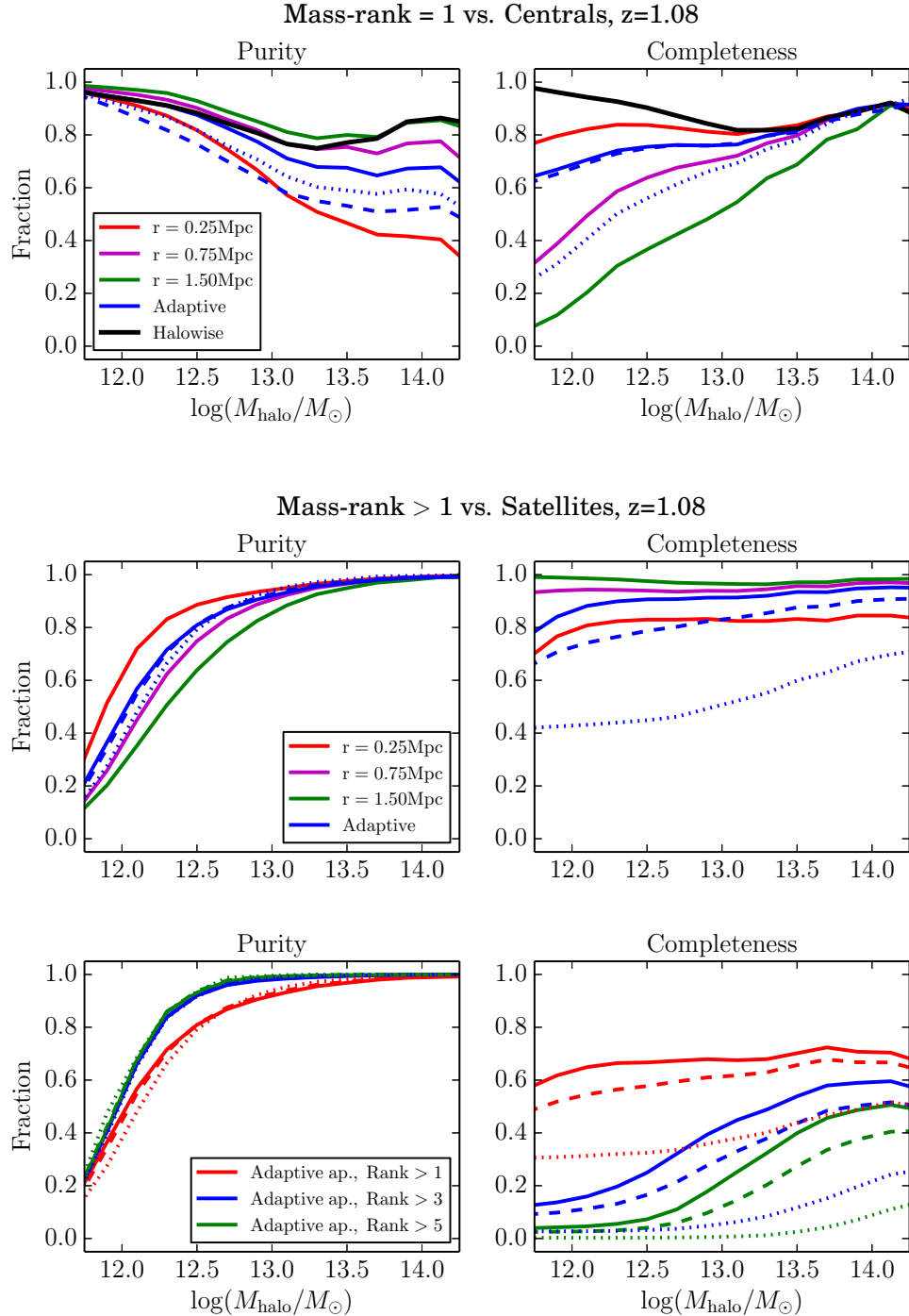


Figure 2.7: Top panels: purity and completeness for the selection of central galaxies based on stellar mass rank = 1 as a function of the halo mass. The rank is computed in various apertures ranging from 0.25 to 1.50 Mpc for the $z = 1.08$ bin. Solid lines refer to the hires- z , dashed lines to the lowres- z and dotted lines to the photo- z samples. Middle panels: same as before but for satellite galaxies selected by having stellar mass rank > 1. Bottom panels: comparison between different rank criteria for the selection of satellite galaxies using the adaptive aperture.

2.4.1 Identification of central galaxies

Central galaxies are usually the most massive galaxy in their halo (but not always, see Skibba et al. 2011). This follows from the fact that the other – satellite – galaxies in the halo were formed at the centre of less massive progenitor haloes. Therefore a sample of central galaxies can be identified by assuming that the most massive galaxy in a halo is also its central galaxy (e.g. Yang et al., 2008).

We compute the rank in stellar mass of each galaxy in several circular apertures. We examine both fixed radius apertures, and a radius that depends on stellar mass (accessible from observations). This approach resembles the Counts-in-Cylinders method (Reid & Spergel 2009, see also Trinh et al. 2013). However, it is worth stressing that previous applications of this method were focused on different science goals (e.g. the identification of 2 member groups in a specific survey). We present here a detailed analysis of how much a population of galaxies whose stellar mass rank is 1 compares to galaxies identified as centrals by the algorithms used in the models (see sec. 2.1).

We define two parameters to quantify the overlap between the two populations. The purity (P) is the number of centrals which are correctly identified over the number of selected galaxies; and the completeness (C) is the number of identified centrals over the total number of central galaxies.

In this section (and in Sections 2.4.2 and 2.4.3) the use of the weights for each galaxy has a negligible impact on both the qualitative and the quantitative results. The method is insensitive to the overestimation of the number of low mass galaxies because the galaxies which compete to be the most massive in an aperture have similar stellar masses, thus the same weight. Therefore we do not use the weights in this Section.

In the top panels of Figure 2.7 the purity and the completeness of identified centrals are plotted as a function of halo mass. Solid colored lines correspond different apertures for the hires-z sample ranging from 0.25 Mpc to 1.5 Mpc. Ideally one would like to maximize both P and C but a trade-off must be found. In table 2.1 the performances of different methods are given. Purity and completeness are given for haloes above and below $10^{13}M_{\odot}$ and for the complete sample.

We start by identifying the “halo-wise” mass rank of each galaxy by ranking in stellar mass all the galaxies belonging to the same halo. We obtain the black solid line in the top panels of figure 2.7. The purity and completeness of this sample describes the ideal overlap between mass rank 1 and central galaxies. The completeness is limited by the fact that the most massive galaxy is not always the central of its host halo. This is true especially at halo masses around $10^{13}M_{\odot}$ where this incompleteness reaches 20%. Due to the scatter in the stellar-mass halo-mass relation for central galaxies, haloes of masses $\sim 10^{12-13}M_{\odot}$ can all host galaxies of equivalent stellar mass which means that even in minor halo mergers (down to a mass ratio of $\sim 1 : 10$) a more massive galaxy can be supplied by the less massive halo. It will then become a satellite more massive than the central of the final halo. The purity and completeness estimates are always computed relative to the population of “true” central galaxies in the model – as such the halo-wise values provide an upper limit on completeness, and an “optimal” purity based on the assumption that we

perfectly know the content of each halo. However the most massive galaxy in any halo corresponds to a significant local potential, and as such one could also define a purity and completeness relative to this population. Such estimates of purity and completeness would clearly be significantly higher than those defined here (relative to the central population).

Looking at Figure 2.7, it is clear that fixed apertures (red, magenta, and green solid lines) struggle to balance the requirements for both high purity and completeness. The general trend is for an increasing purity and decreasing completeness as the aperture size is increased. However, for small apertures (0.25 Mpc) P goes down at the high halo mass end because the aperture covers only a fraction of the halo; if they are too large then C goes down in smaller haloes because one aperture covers multiple haloes.

From this evidence and based on the idea that a good correlation exists between stellar mass and halo virial radius (which is an analytic function of halo mass) for centrals, we define an “adaptive” aperture as follows:

$$r = \min(0.75, n \times 10^{(\alpha \log M_* + \beta)}) \text{ [Mpc]} \quad (2.3)$$

where M_* is the stellar mass of the galaxy, n is a multiplicative factor, and α and β are the parameters which describe the dependence of virial radius on stellar mass for centrals in the models³. From the models we get $\alpha = 0.25$, $\beta = -3.40$ at all redshifts and after extensive testing we define $n = 3$ in order to avoid very small apertures that would decrease the purity. In order to limit the size of the aperture to a scale that entirely covers the most massive haloes without extending beyond, we limit the aperture to a radius of 0.75 Mpc. From Figure 2.7 and from the values in table 2.1 it is evident that this is a great improvement for C at low halo masses relative to the fixed 0.75 Mpc aperture, while we lose 8% in purity at high halo masses. This is because we are using a small aperture for low mass galaxies (0.2 Mpc for $M_* = 10^{9.5} M_\odot$). Since some of them are satellites living in massive haloes, the apertures we use are too small to encompass the entire halo and those satellites can get high mass rankings reducing P .

2.4.2 Identification of satellite galaxies

The mass rank method can also be used to identify satellite galaxies, under the assumption that satellites are less massive than the central galaxy of their own halo, i.e. mass rank > 1 . In the middle panels of Figure 2.7 are plotted the purity and completeness (defined as in Section 2.4.1) of our identified satellite galaxies as a function of halo mass. The purity is limited - but only by 5% - by satellites that are more massive than the central galaxy of their host halo. The purity quickly drops at halo masses below $10^{12.5} M_\odot$, with little dependence on the aperture size. In Table 2.2 we present the values of P and C for satellite galaxies living in haloes less and more massive than $10^{13} M_\odot$, and for the complete sample. It is clear that the overlap between mass rank > 1 and satellites is strong among massive haloes, while in less massive haloes about half of the galaxies with mass rank

³The α and β parameters are obtained by fitting a linear relation ($r = 0.89$) in log-log space between the virial radius and the stellar mass for the central galaxies in the models.

Aperture	$\log M_h \leq 13$		$\log M_h > 13$		All	
	P	C	P	C	P	C
	$z = 1.08$					
0.25 Mpc	0.92	0.82	0.52	0.87	0.88	0.82
0.75 Mpc	0.94	0.40	0.75	0.78	0.92	0.42
1.50 Mpc	0.94	0.17	0.80	0.64	0.91	0.19
Adaptive	0.94	0.68	0.75	0.78	0.92	0.69
	$z = 2.07$					
0.25 Mpc	0.93	0.79	0.76	0.91	0.92	0.79
0.75 Mpc	0.95	0.38	0.86	0.83	0.94	0.40
1.50 Mpc	0.95	0.18	0.88	0.71	0.94	0.20
Adaptive	0.94	0.64	0.84	0.86	0.94	0.65

Table 2.1: Purity and completeness for the identification of central galaxies using stellar mass rank = 1 in four different apertures for haloes below and above $M_{\text{halo}} = 10^{13}M_{\odot}$, and for the full hires-z sample at $z = 1.08$ and $z = 2.07$.

Aperture	$\log M_h \leq 13$		$\log M_h > 13$		All	
	P	C	P	C	P	C
	$z = 1.08$					
0.25 Mpc	0.58	0.78	0.97	0.79	0.70	0.78
0.75 Mpc	0.33	0.92	0.96	0.93	0.45	0.93
1.50 Mpc	0.27	0.97	0.91	0.96	0.38	0.96
Adaptive	0.46	0.86	0.95	0.91	0.59	0.88
	$z = 2.07$					
0.25 Mpc	0.49	0.79	0.93	0.83	0.56	0.80
0.75 Mpc	0.28	0.92	0.90	0.92	0.33	0.93
1.50 Mpc	0.24	0.96	0.85	0.94	0.29	0.95
Adaptive	0.37	0.84	0.92	0.91	0.44	0.84

Table 2.2: Purity and completeness for the identification of satellite galaxies using stellar mass rank > 1 in four different apertures for haloes below and above $M_{\text{halo}} = 10^{13}M_{\odot}$, and for the full hires-z sample at $z = 1.08$ and $z = 2.07$.

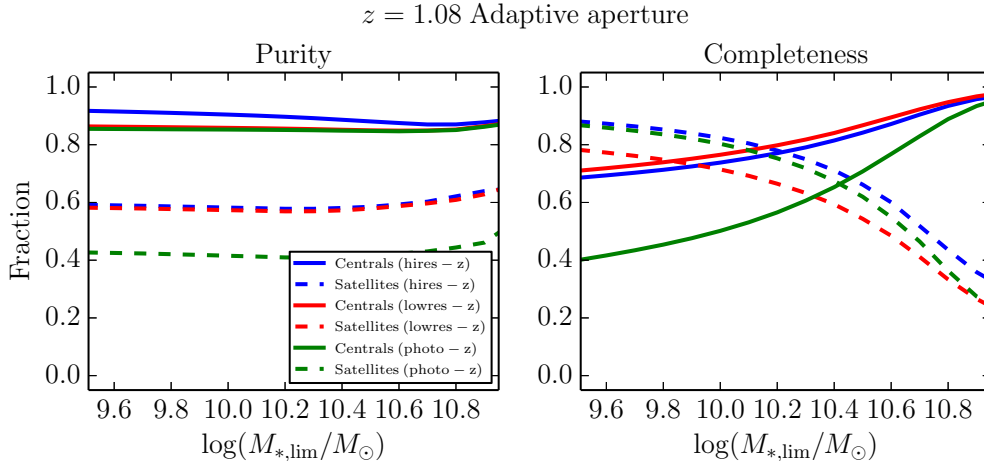


Figure 2.8: Purity and completeness for the identification of central (solid lines) and satellite (dashed lines) galaxies using stellar mass rank = 1 (> 1) in the adaptive aperture at $z = 1.08$ for the hires- z sample (blue lines), for the lowres- z sample (red lines) and for the photo- z sample (green lines).

> 1 are centrals which by chance have one (or more) more massive neighbors within the aperture but not within the same halo. It is hard to define a satellite in this halo mass regime, especially where the stellar mass of central galaxies approaches the mass limit: the mass of any satellites included in the sample must therefore be close to that of their central. This halo mass regime consists primarily of isolated galaxies and loose proto-groups (namely pairs or triplets). Completeness in contrast is remarkably high over the full range of halo masses, illustrating that our method is effective in picking up a complete population of satellites.

In the bottom panels of Figure 2.7 we explore the dependence of P and C on the stellar mass rank we required to identify a satellite within the adaptive aperture. Setting two more conservative limits (rank > 3 blue solid and > 5 green solid) we achieve a small improvement in the purity at low halo masses but with a dramatic degradation of the completeness. It is clear that with rank to be > 5 (> 3) we are implicitly selecting only galaxies that have at least five (three) companions within the aperture, all of them more massive. Moreover, especially at low/intermediate halo masses, the number of galaxies within a halo is often smaller than five (three). Thus many real satellites are missed.

Based all this evidence our preferred method to identify central (satellite) galaxies is to require a stellar mass rank = 1 (> 1) in the adaptive aperture. The purity and completeness values for this aperture are $P = 0.93$ and $C = 0.67$ for centrals and $P = 0.60$ $C = 0.90$ for satellites in the hires- z sample at $z = 1.08$. The use of the same aperture for both types has the advantage of making the two selections mutually exclusive. If two different apertures are used for selecting centrals and satellites, the fraction of interlopers has to be taken into account as one galaxy might be the most massive in one aperture but not in the other one. Finally it is worth stressing that both the purity and the completeness of the

full samples of centrals and satellites are completely independent of the measured density and any effort to calibrate halo mass. The key parameters are the scale over which the rank is computed and the assumption that central galaxies are typically more massive than nearby satellites. This assumption holds well in the G13 models and is typically assumed to be true in group reconstruction using observational data (e.g. Yang et al., 2007).

2.4.3 Dependence of Purity and Completeness on the stellar mass limit

To avoid model resolution biases in our definition of the environment, we probe down to a constant mass limit of $M_* = 10^{9.5} M_\odot$. This is deeper than most observational surveys at these redshifts. To examine more realistic survey depths, we now test how our selection methods perform as a function of the stellar mass limit $M_{*,\text{lim}}$. In Figure 2.8 we show P and C for the identification of both centrals and satellites as a function of $M_{*,\text{lim}}$ using the adaptive aperture. The purity is almost unaffected by the selection limit while, as expected, completeness is. Regarding the centrals, the overall purity is about 90% and does not depend on the aperture nor on the mass limit. Conversely C is a strong function of the minimum stellar mass. When low mass galaxies are removed, the sample of centrals with mass rank 1 becomes more and more complete. The completeness never reaches unity because, as discussed before, there are satellites which are more massive than the centrals of their own haloes.

As already discussed, the purity for the satellites is about 60% for all stellar mass limits. This happens because, close to the stellar mass limit and within 0.75 Mpc, two-halo pairs containing similar mass centrals are just as common as pairs of similar mass galaxies within one halo. For this reason there is an improvement using the adaptive aperture as it is smaller than 0.75 Mpc at low stellar masses and this helps in limiting the contamination from centrals. The completeness shows a well defined decreasing trend at increasing mass limits because the higher $M_{*,\text{lim}}$, the higher the chance that a satellite is more massive than the central of its halo. This, combined with the low number of massive satellites, makes the fraction drop below 40% at $M_{*,\text{lim}} > 10^{10.8} M_\odot$.

These results stand even when the stellar masses are convolved with a gaussian random error to mimic observational uncertainties. We tested the effect of errors up to a relatively large value of 0.5dex. The purity for centrals and the completeness in the identification of satellites decrease by less than 5%, while the purity for satellites and the completeness of centrals decrease by 10%. Moreover, the trends as a function of the mass uncertainty are smooth and the values given here are to be considered upper limits.

2.4.4 Dependence on Redshift Accuracy

The trends discussed so far have been drawn using the hires-z sample. In this section we analyze how they change using less accurate redshifts. Dashed lines in Figure 2.7 are for the lowres-z sample and dotted lines are for the photo-z sample using only the adaptive aperture. The general trends apply to the fixed apertures as well.

Concerning central galaxies, the purity is decreased by $\sim 10\text{--}15\%$, due to the smoothing of the density field introduced by lowres-z and photo-z. This happens because massive centrals are projected outside the cylinder of less massive satellites (the latter then scoring a mass rank 1, thus reducing the purity of the selection). The completeness on the other hand is not affected in the lowres-z sample because massive centrals are still identified as the most massive galaxies in their cylinders. The larger velocity cut we use for the photo-z sample has a positive effect on the purity but decreases the completeness. This is not unexpected because the larger velocity cut increases the volume of the cylinder where we compute the mass rank, therefore the final effect is similar to increasing the size of the aperture.

In the case of satellites the purity is not affected by the smoothing in the redshift direction because the population of rank > 1 galaxies is still mainly composed of satellites. Conversely the completeness is decreased by $\sim 10\%$, and $\sim 40\%$ for the lowres-z and photo-z respectively. As photo-z are much less accurate than spectroscopic redshifts it is worth noting why the performance of the method is still reasonably good. When the mass rank based method identifies a galaxy as a satellite, it does not mean we know it to be a satellite of a specific halo. Therefore the use of photo-z can project both the “true” central and one (or more) satellites outside their original halo. When this happens, the central/satellite status is preserved and a satellite galaxy is now identified as central in the original halo. If, as it is more likely, only satellites are projected outside the halo, the most massive is identified as a central, thus reducing the satellites’ completeness.

When the less accurate redshifts are used, we find no major impact on the trends of P and C on the stellar mass limit. The strongest effect is found on the completeness of the identification of satellites which follows the same trend described above.

Dependence of Purity and Completeness on the spectroscopic sampling rate

Here we examine the performances of our method in the case of variable sampling rate. Our approach is to progressively reduce the spectroscopic sampling rate from 100% to 0 in steps of 10% by randomly replacing the hires-z (or lowres-z) with photo-z. Figure 2.9 shows the purity and completeness in the adaptive aperture at each sampling rate. The main conclusions have been discussed above using pure spectroscopic (hi- and low-res) redshifts and photo-z. Here we only note that the decline in purity is roughly linear as a function of the sampling rate for both centrals and satellites and that the completeness for satellites decreases more significantly from full sampling rate to 50% rather than from this value to pure photo-z.

Regarding the completeness we note a mild increase for the identification of central galaxies with decreasing spectroscopic sampling rate. This is best explained by an example. If central galaxies of two haloes are closer in projected sky coordinates than the size of the adaptive aperture, only one of them will be identified as mass rank =1, when accurate redshifts are used. If only photo-z are available (sampling rate close to zero), there is a non zero probability that the two centrals are scattered apart in redshift space such that they no longer lie together in the cylinder where the mass rank is computed. In this case

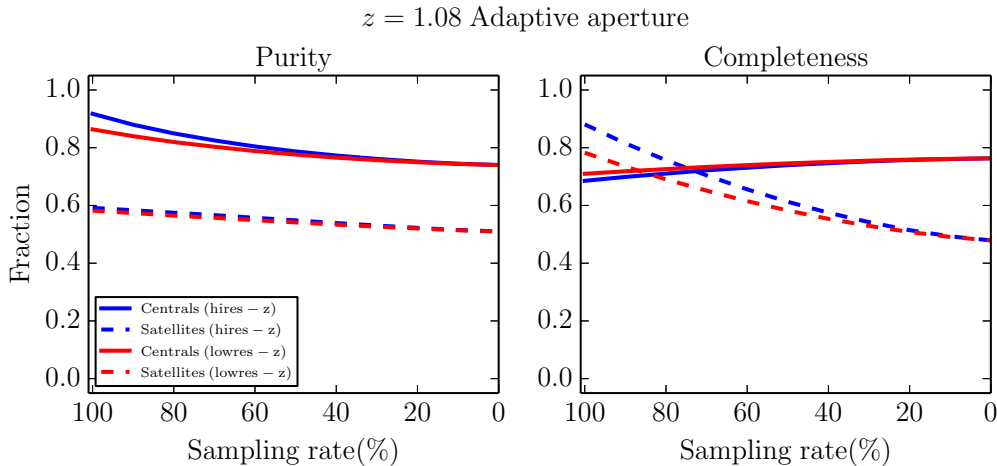


Figure 2.9: Purity and completeness for the identification of central (solid lines) and satellite (dashed lines) galaxies using stellar mass rank = 1 (> 1) in the adaptive aperture for incomplete hires- z (blue lines) and lowres- z (red lines) sampling at $z = 1.08$.

they are both identified as centrals. When this effect is integrated over the full galaxy population a decrease of $\sim 5 - 8\%$ in completeness is found. However this only occurs if a small velocity window is applied and this is only justified if the spectroscopic sampling rate is high. Conversely a larger velocity cut should be used to recover an unbiased density field at the expenses of purity and completeness in the mass rank identification of centrals and satellites.

Several other works have attempted a selection of central and satellite galaxies in real spectroscopic surveys. Among them Knobel et al. (2012) used a probability based method to assign a binary central/satellite classification to the I-band flux limited sample in the zCOSMOS survey. The spectroscopic sampling rate is about 50% in the redshift range 0.1 – 0.8. Despite the different identification method and the broad redshift range (which hampers the definition of a fixed stellar mass limit), their final results ($P = 0.81$ $C = 0.89$ and $P = 0.62$ $C = 0.45$ for centrals and satellites respectively) agree with our results at the same sampling rate within $\sim 5\%$ for the purity and $\sim 15\%$ for the completeness.

In conclusion, it is remarkable how the purity and the completeness both centrals and satellites are not strongly affected by low spectroscopic sampling rates nor by the survey detection threshold, this proving the robustness of the method and its usefulness in surveys with different designs.

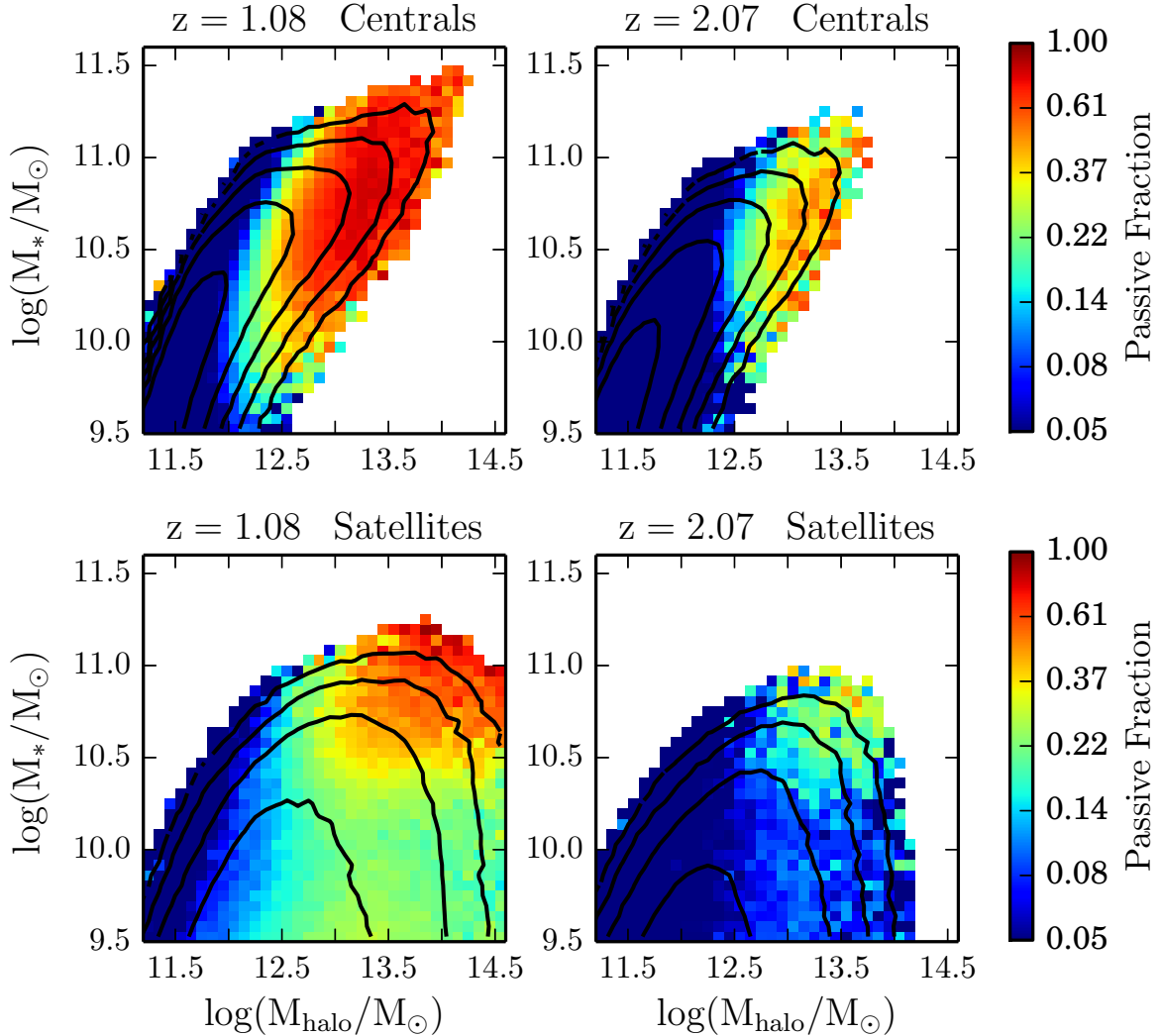


Figure 2.10: Fraction of passive galaxies (as defined in Section 2.1.1) as a function of halo mass and stellar mass for centrals (top panels) and satellites (bottom panels). Redshift increases from $z = 1.08$ (left panels) to $z = 2.07$ (right panels). The contours are drawn from the density of galaxies in the parameters space and are log-spaced with the outermost contour at 25 objects per bin and the innermost at 10^4 objects for centrals and $10^{3.4}$ for satellites.

2.5 Relation between environment and passive fraction

In this section, we examine if and how well the environmental trends predicted by the models can be recovered using quantities accessible from observations, e.g. density and mass rank. We focus our attention on a single physical quantity: the fraction of passive galaxies. Peng et al. (2010, 2012) and Woo et al. (2013) have shown that the passive fraction of satellite galaxies correlates strongly with a measurement of local density, labelled “environment”, while for centrals it is a function of their stellar mass (Peng et al., 2010, 2012) and halo mass (Woo et al., 2013).

2.5.1 The growth of a passive population in the models

First of all we investigate how the fraction of passive galaxies depends on stellar mass, halo mass and central/satellite status. The former basically describes the integrated star formation and merger history of a galaxy, while the latter two are strongly correlated to the regulation of its star formation in the models. Figure 2.10 shows the passive fraction in the $M_* - M_{\text{halo}}$ space for centrals (top panels) and satellites (bottom panels), at redshifts 1.08 (left) and 2.07 (right). The contours are drawn from the density of galaxies in the parameters space and are logarithmically spaced with the outermost contour at 25 objects per bin and the innermost at 10^4 objects for centrals and $10^{3.4}$ for satellites. Each bin has to contain at least 10 objects for the passive fraction to be computed, and the color coding is scaled logarithmically.

A common feature across the redshift bins is that centrals and satellites populate different regions of the parameters space. The centrals populate a sequence where the stellar mass linearly increases with halo mass (in log-log space). In contrast the satellites form a cloud that spans all halo masses such that $M_{\text{halo}}^{\text{sat}}(M_*) \geq M_{\text{halo}}^{\text{cen}}(M_*)$.

At halo masses above $10^{12.5} M_{\odot}$ a passive population of centrals starts to appear at $z \sim 2$, becoming dominant as the redshift decreases to 1. Those passive centrals move to higher halo masses without increasing their stellar mass enough to stay on the relation defined by the star forming centrals. The passive fraction increases to about 80% for centrals in haloes more massive than $10^{13} M_{\odot}$. De Lucia et al. (2012), using Wang et al. (2008) models (an early version of G13) at $z = 0$, showed that a strong correlation between bulge growth and passive fraction exists for massive centrals in SAMs. The physical reason is that for those galaxies the cold gas reservoir is exhausted (possibly by a merger induced starburst) and further cooling of the gas is prevented by the strong radio-mode AGN feedback. Although these trends do not perfectly reflect the observed data, they are qualitatively similar to those shown by Kimm et al. (2009) at $z = 0$ for different published SAMs. In their work the model by De Lucia & Blaizot (2007, another early version of G13) appears to be the closest to the observational constraints.

Also the passive fraction of satellite galaxies shows significant evolution. As time goes by (and redshift decreases) the satellite cloud extends to higher halo masses, and a population

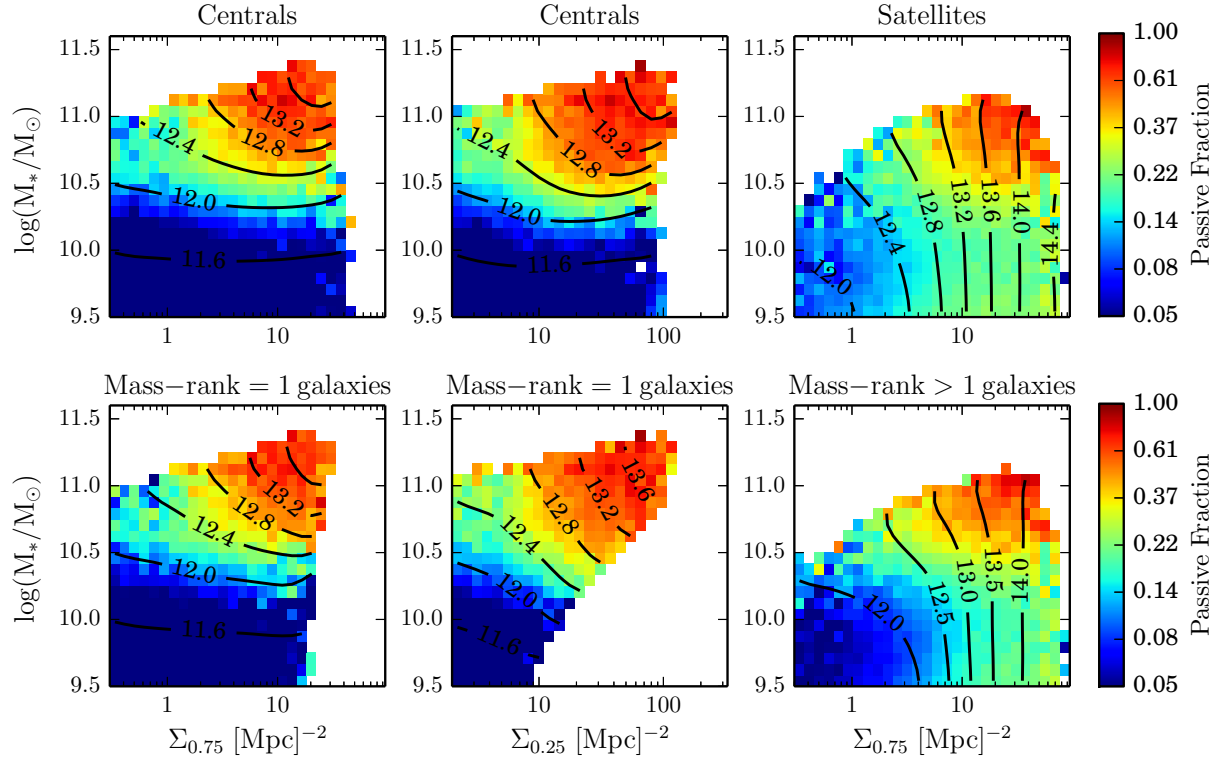


Figure 2.11: Fraction of passive galaxies as a function of density on the scale $\Sigma_{0.75}$ and stellar mass for central galaxies (left panels), on the scale $\Sigma_{0.25}$ for centrals (central panels) and on the scale $\Sigma_{0.75}$ for satellite galaxies (right panels), at $z = 1.08$. The central/satellite definition is the one provided by the SAMs in the top panels and the one defined by the mass rank in the adaptive aperture in the bottom panels. The contours are drawn from the median halo mass in the same bins.

of passive satellites appears at high stellar masses. Most of the passive satellites are likely to be turned passive by the stripping mechanisms acting in massive haloes. However, the highest passive fractions are found at both high halo mass and stellar mass. These galaxies were probably already passive when they were centrals and then merged with a more massive halo becoming passive satellites.

2.5.2 Recovering predicted trends with observational proxies

In this section we investigate if, and how well, the predicted trends of passive fraction as a function of halo mass and stellar mass can be recovered using only observable quantities. We make use of the density of galaxies in fixed apertures and the choice of centrals and satellites is performed both using the model definition and the observational mass rank method presented in Section 2.4. We recall that the densities, number density contours and the median halo mass values presented in this section are obtained after application

of the statistical weights described in Sections 2.1.1, and 2.2.

In Figure 2.11 we show the fraction of passive galaxies (at $z = 1.08$) as a function of density and stellar mass for centrals (left and middle panels) and satellites (right panels). The top row makes use of the separation between these two types as coded in the models, while the bottom row uses the mass rank in the adaptive aperture in order to divide the two types. The contours describe the median halo mass in the same bins of stellar mass and density. Again, each bin has to contain at least 10 objects for the passive fraction to be computed. A close examination of the direction of change for passive fraction relative to both the axes and to the direction of change for median halo mass, allows us to evaluate how well we can use the parameters to track the trends seen in the pure model space (see Figure 2.10).

Let us start with the centrals. We know from Figure 2.10 that the passive fraction increases primarily with halo mass, and that at fixed halo mass there is if anything a slight anti-correlation with stellar mass. Can we see this in the observational parameter space?

In the left panels in Figure 2.11 the density has been computed on scales of 0.75 Mpc, which covers a super-halo scale for all the haloes of mass below $10^{14}M_{\odot}$. To examine mostly intra-halo scales, we also examine the density computed on the smallest scale (0.25 Mpc, middle panels).

From the top panels, and without the halo mass contours, it would appear that the stellar mass is the main driver of the correlation with passive fraction. Indeed this confusion is caused by the wide range of density seen at low stellar mass: densities are reached which are just as large as those for the centrals of high mass haloes (even on 0.25 Mpc scales). as discussed in Section 2.3. However, when the halo mass contours are compared to the direction of increase of the passive fraction, it is evident that the halo mass is the main driver of the trend.

In the models, the low mass galaxies at high density show a passive fraction that is very similar to those at low density and comparable mass. However in the real Universe those galaxies may have already experienced physical processes driven by massive haloes, even if they are currently outside the virial radius – i.e. the “backsplash” population discussed by Balogh et al. (2000); Mamon et al. (2004); Ludlow et al. (2009); Bahé et al. (2013); Hirschmann et al. (2014). Indeed, observational data suggests they behave more like satellites (Wetzell et al., 2014; Hirschmann et al., 2014). One possibility is therefore to “clean” the sample of these high density, low mass objects. Fortunately, this happens as a direct consequence of making a mass rank 1 selection as in the bottom panels. The adoption of the adaptive aperture means that our mass rank 1 galaxies are the most massive within an aperture not larger than 0.75 Mpc but not smaller than 0.28 Mpc for galaxies in our stellar mass range (the lower limit is obtained by evaluating equation 2.3 for the lowest stellar mass in our sample). Galaxies at low mass and high 0.25 Mpc density are inevitably not the most massive within this aperture, and are excluded. However this correlation depends on both density and stellar mass because the halo mass for central galaxies depends on both these parameters. Another possibility (which is what we use when this framework is applied to an observational sample in chapter 3) is to treat “backsplash” galaxies as both centrals and satellites, in a probabilistic approach.

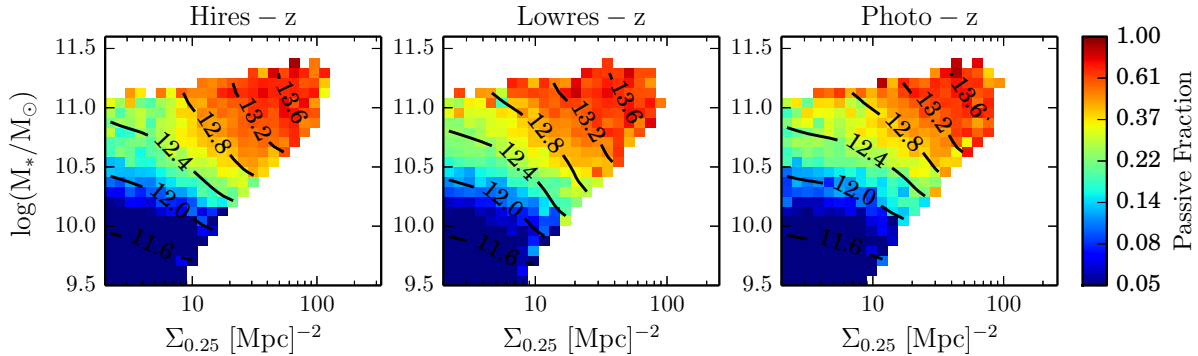


Figure 2.12: Fraction of passive galaxies as a function of density on the scale $\Sigma_{0.25}$ and stellar mass for mass rank 1 galaxies (in the adaptive aperture) using hires-z (left panel), lowres-z (central panel), and photo-z (right panel) at $z = 1.08$. The contours are drawn from the median halo mass in the same bins.

For satellites (which dominate in mass and number within the rich haloes), the correlation between halo mass and density is very good irrespective of the aperture used (the contours in the right panels of Figure 2.11 are essentially vertical). Therefore the passive fraction trends as a function of halo mass and stellar mass are easy to qualitatively recover using the density and either the satellite definition in the SAMs or the one coming from the mass rank. The low mass - high density central population removed by the mass rank method ends up in the cloud of satellites. While those galaxies dominate the low mass centrals at high density, they do not contribute much to the satellites at the same stellar mass and density. Density computed on either 0.25 or 0.75 Mpc work well in this regard.

A general conclusion is that a well calibrated halo mass dependence on the observed properties (stellar mass, density) is crucial in understanding which physical properties are shaping the trends (in this case the passive fraction) we observe. While the results can be already be achieved with the SAM definition of centrals and satellites, it is important to stress that the use of the observationally motivated mass rank method provides the same result.

Finally, Figure 2.12 shows how the passive fraction trends change if less accurate redshifts are used, as in our lowres-z and photo-z samples. We restrict ourselves to central galaxies defined with the mass rank method in the adaptive aperture and density computed on the 0.25 Mpc scale. Decreasing the quality of the redshift survey, the density - stellar mass correlation is less tight and the number of galaxies at the highest densities is reduced. The conclusions that can be drawn in this parameter space are unchanged. However, we stress that this conclusion comes with a number of caveats. First, the density dynamic range is reduced when photo-z are used on all scales, but less so for 0.25 Mpc. This small scale can only be used if the galaxy sampling is good enough, e.g. the stellar mass limit is low as in this work. Second, the use of the mass rank method “cleans” the sample of low mass centrals which are projected in high density regions due to the less accurate

photo- z , allowing us to obtain a trend similar to that for hires- z . Moreover, the density field is well reconstructed only with very good photometric redshifts. The photo- z accuracy typically depends on the number of photometric data points and their distribution across the rest-frame galaxy spectral energy distribution, generally being worse for fainter objects. Therefore, we warn the reader that the performance of photo- z in recovering the true density field should be carefully assessed for each individual sample, along with the significance of any particular result based on this approach.

2.6 Conclusions

In this chapter we have characterized the definition of “galaxy environment” by means of the projected density within fixed apertures at $z \sim 1-2$. We have tested our methods by applying them to the semi analytic models of galaxy formation presented by Guo et al. (2013b) and based on a new run of the Millennium simulation. We have focused on the correlation between observables (density, stellar mass rank) and properties provided only by the models (halo mass, central/satellite status). Then we have studied to what extent our tools can recover the environmental trends imprinted in the models in the context of the quenching of centrals and satellites, extending to higher redshift the results of Hirschmann et al. (2014). Our results can be summarized as follows:

1. The correlation between density and halo mass is not trivial and a variety of effects are on stage at the same time. We find that density poorly correlates with halo mass for centrals. This effect is caused by the well defined boundaries of haloes in the SAMs at high density: galaxies within those boundaries are satellites hosted by a high-mass halo, while those outside are central galaxies of low-mass haloes. It has been shown by Hirschmann et al. (2014) that density correlates with halo mass only for massive centrals. For all centrals at fixed density, the distribution of halo mass broadens so much that the density-halo mass correlation is lost. This is consistent with similar results by Woo et al. (2013). On the other hand density correlates well with halo mass for satellites, irrespective of the aperture used.
2. Central galaxies in the accretion regions of massive haloes can be highlighted with a simple but effective method. We replaced the nominal halo mass with that of the most massive halo within a physical (3D) distance of 1 Mpc. This traces the dominant DM mass nearby and we recover a correlation between density and this halo-mass for centrals which is similar to that for the satellites.
3. The stellar mass rank is an effective method to identify centrals and satellites. We have parameterized the performance of this method in terms of purity and completeness of the mass rank identification with respect to the SAM definition. We have tested various apertures where the rank is computed. For central galaxies we find that the larger the aperture, the higher is the purity but the lower is the completeness. In order to improve both the completeness at low halo masses and the purity in

massive haloes we have defined an adaptive aperture that depends on the stellar mass of the galaxy. This method is as good as a fixed 0.75 Mpc aperture in terms of purity but with an improvement of $\sim 30\%$ in completeness at halo masses below $10^{13}M_{\odot}$. The method is not strongly sensitive to the stellar mass limit or the spectroscopic sampling rate, though less so for the completeness of satellites. Our results for purity and completeness are remarkably consistent with Knobel et al. (2012), despite the different method and sample selection.

4. A strong M_{*} - M_{halo} correlation is predicted by the models for central galaxies. Passive centrals dominate above $M_{\text{halo}} = 10^{12.5}M_{\odot}$ due to strong AGN feedback, correlated to bulge growth (Wilman et al., 2013). However, the density-halo mass correlation for central galaxies is far from being linear or independent of stellar mass. Therefore the recovered trends do not only depend on density but also on stellar-mass. Within a purely observational parameter space, we are able to recover these trends.
5. The redshift accuracy does not negatively impact on this result. However, such a conclusion requires a combination of good photometric redshifts and deep survey limits as found also by Etherington & Thomas (2015).

In the next chapter we build on these results to characterize the environment of galaxies in the 3D-HST survey. This requires the following steps: first of all the sample selection in the models should be as close as possible to that in the data. The model galaxies need to be weighted to match the mass (and possibly also the magnitude and color) distributions. Then the quantification of densities needs to take into account the redshift accuracy of the survey under investigation. At this point the density distributions of real and model data can be compared. The models then provide calibrations of properties such as halo mass that will help identifying the physical processes driving observational trends.

Chapter 3

The environment of observed galaxies from 3D-HST and SDSS

This chapter is based on Fossati et al. (2016), submitted to ApJ

In this chapter we apply the methods and tools presented in chapter 2 to a high-redshift sample drawn from the 3D-HST survey (Brammer et al., 2012) and a low redshift sample drawn from the SDSS survey (York et al., 2000). Because our method has been developed and calibrated on an idealized mass complete sample, here we present how we adapt it to deal with the observational uncertainties and limitations of real datasets.

We assume a flat Λ CDM Universe with $\Omega_M = 0.3$, $\Omega_\Lambda = 0.7$, and $H_0 = 70 \text{ km s}^{-1} \text{ Mpc}^{-1}$.

3.1 The high redshift sample from 3D-HST

In this work we aim at a quantification and calibration of the local galaxy environment for galaxies in the five CANDELS/3D-HST fields (Grogin et al., 2011; Koekemoer et al., 2011; Brammer et al., 2012), namely COSMOS, GOODS-S, GOODS-N, AEGIS and UDS. The synergy of these two surveys represents the largest effort to obtain deep space-based near-infrared photometry and spectroscopy in those fields. For a description of the observations and reduction techniques we refer the reader to Skelton et al. (2014) and Momcheva et al. (2016) for the photometry and spectroscopy respectively. The CANDELS observations provide HST/WFC3 near infrared imaging in the F125W and F160W filters (J_{125} and H_{160} hereafter) for all the fields, while 3D-HST followed-up a large fraction of this area with the F140W filter (JH_{140} hereafter) and the WFC3/G141 grism for slit-less spectroscopy. The novelty of this approach is to obtain low resolution ($R \sim 100$) spectroscopy for the vast majority of the objects in the field. Taking advantage of the low background of the HST telescope, it is possible to reach a depth similar to traditional slit spectroscopy from 10m class telescopes on Earth.

The 3D-HST photometric catalog (Skelton et al., 2014) used H_{160} or JH_{140} as detection bands and its depth varies from field to field and across the same field due to the observing

strategy of CANDELS. However, even in the shallowest portions of each field, the 90% depth confidence level is $H_{160} \sim 25$ mag. Beyond this magnitude limit the star/galaxy classification (which is a key parameter for the environment quantification) becomes uncertain.

The 3D-HST spectroscopic release (Momcheva et al., 2016) provides reduced and extracted spectra down to $JH_{\text{IR}} = 26$ mag¹. The spectra are passed through the EAZY template fitting code (Brammer et al., 2008) along with the extensive ground and space based multiwavelength photometry. This results in “grism” redshifts, which are more accurate than photometric redshifts thanks to the wealth of stellar continuum and emission line features included in the spectra. However, only those brighter than $JH_{\text{IR}} = 24$ mag have been visually inspected, and have a `use_grism` flag that describes if the grism spectrum is used to compute the redshift. Incomplete masking of contaminating flux from nearby sources in the direction of the grism dispersion, residuals from spectra of bright stars, and corrupted photometric measurements can lead to this flag to be set to 0 (“bad”).

We include in the present analysis all galaxies brighter than $JH_{140} = 24$ mag, therefore limiting our footprint to those regions covered by grism and JH_{140} observations. We limit the redshift range to $0.5 < z < 3.0$. The lower limit roughly corresponds to the redshift where the H α line enters the grism coverage and the upper limit is chosen such that the number density of objects above the magnitude cut allows a reliable estimate of the environmental statistics. It also allows follow-up studies targeting the rest-frame optical features from ground based facilities in the J , H , and K bands (e.g. KMOS, Sharples et al. 2013 and MOSFIRE, McLean et al. 2012)

We exclude stars by requiring `star_flag` to be 0 or 2 (galaxies or uncertain classification). We do not use the `use_phot` flag because it is too conservative for our goals. Indeed this flag requires a minimum of 2 exposures in the F125W and F160W filters, and the object not being close to bright stars. The quantification of environment requires a catalog which is as complete as possible even at the expenses of more uncertain photometry (and photo- z) for the objects that do not meet those cuts. None the less a $JH_{140} = 24$ mag cut allows a reliable star/galaxy separation for 99% of the objects and is at least 1 mag brighter than the minimum depth of the mosaics, thus alleviating the negative effects of nearby stars on faint sources. The final sample is made of 18745 galaxies.

As a result of the analysis in Momcheva et al. (2016), each galaxy is assigned a “best” redshift. This is:

1. a spectroscopic redshift from a ladder of sources as described below.
2. a grism redshift if there is no spectroscopic redshift and `use_grism = 1`
3. a pure photometric redshift if there is no spectroscopic redshift and `use_grism = 0`.

¹The 3D-HST spectroscopic catalog is based on $JH_{\text{IR}} = J_{125} + JH_{140} + H_{160}$ magnitudes. We therefore quote limits in this band when referring to their catalog. However we perform the sample selection in JH_{140} to ensure that the footprint of our sample is entirely covered by G141 grism observations and direct imaging in F140W.

A `zbest_type` flag is assigned to each galaxy based on the conditions above. The best redshift is the quantity used to compute the environment for each galaxy in the 3D-HST fields.

Spectroscopic redshifts are taken from the compilation of Skelton et al. (2014) which we complement with newer data. For the COSMOS field we include the final data release of the zCOSMOS bright survey (Lilly et al., 2007). We find 253 new sources with reliable redshifts in the 3D-HST/COSMOS footprint mainly at $z < 1$. In COSMOS and GOODS-S we include 95 objects from the DR1 (Tasca et al., 2016) of the VIMOS Ultra Deep Survey (VUDS; Le Fèvre et al., 2015). This survey mainly targets galaxies at $z > 2$ therefore complementing zCOSMOS. We include 105 redshifts from the MOSFIRE Deep Evolution Field Survey (MOSDEF, Kriek et al., 2015) which provides deep rest frame optical spectra of galaxies selected from 3D-HST. For the UDS field we also include 164 redshifts from VIMOS spectroscopy in a narrow slice of redshift ($0.6 < z < 0.7$, Galametz et al. in prep.) Lastly we include 376 and 33 secure spectroscopic redshifts from KMOS^{3D} (Wisnioski et al., 2015) and VIRIAL (Mendel et al., 2015) respectively. Those large surveys use the multiplexing capabilities of the integral field spectrometer KMOS on the ESO Very Large Telescope to follow-up 3D-HST selected objects. The former is a mass selected survey of emission line galaxies, while the latter observed passive massive galaxies.

In the selected sample (covering the five fields), 20% of the galaxies have a spectroscopic redshift, 64% have a grism redshift, and only 16% have a pure photometric redshift. In the next section we explore the accuracy of the grism and photometric redshifts as a function of the galaxy brightness and the S/N of emission lines in the spectra.

Stellar masses and stellar population parameters are estimated using the FAST code (Kriek et al., 2009), coupled with Bruzual & Charlot (2003) stellar population synthesis models. Those models use a Chabrier (2003) initial mass function (IMF) and solar metallicity. The best redshift is used for each galaxy together with the available HST and ground based photometry. The star formation history is parametrized by an exponentially declining function and the Calzetti et al. (2000) dust attenuation law is adopted.

3.1.1 Redshift accuracy

A careful quantification of the grism and photometric redshift accuracy is paramount for a good calibration of the environmental statistics into physically motivated halo masses. In section 3.5 we will show how these masses are obtained from mock catalogs selected to match the number density and redshift uncertainty of 3D-HST galaxies.

The low-resolution spectra cover different spectral features as a function of galaxy properties and redshift. The most prominent features are emission lines, which are however limited to star forming objects. On the other hand stellar continuum features (Balmer break, absorption lines) are present in the spectra of all galaxies with a S/N that depends on the galaxy magnitude. Because all those features contribute in the redshift fitting procedure we explore their impact on the redshift accuracy in bins of S/N of the strongest emission line in the spectrum and JH_{140} total magnitude. Given the limited spectral coverage of the G141 grism, it is common to find only one prominent emission line feature

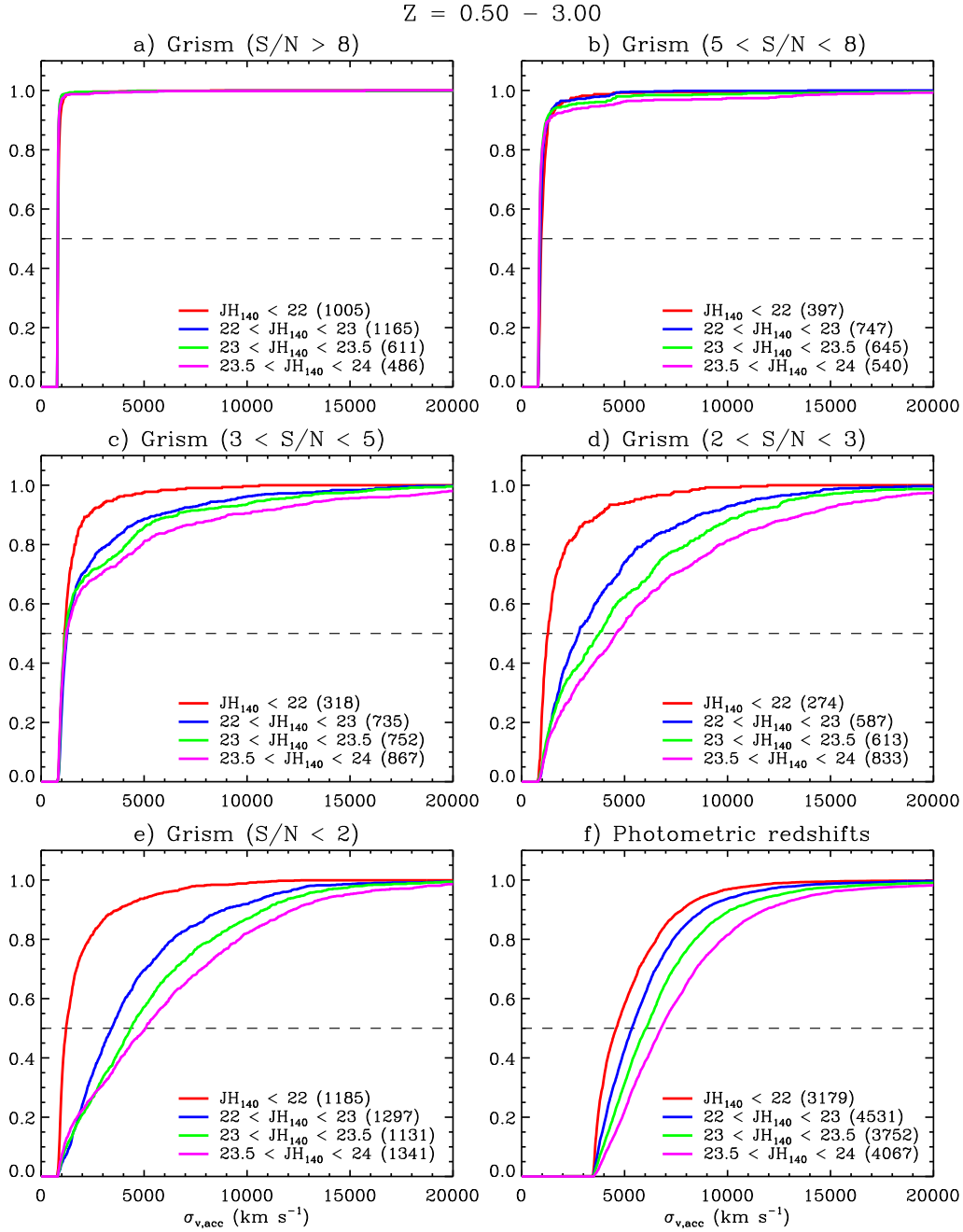


Figure 3.1: Cumulative histograms of the redshift accuracy ($\sigma_{v,\text{acc}}$ in km s^{-1}) for galaxies at $0.5 < z < 3.0$ and $JH_{140} < 24$ mag. Panels from a) to e) are for grism redshifts in bins of S/N of the strongest emission line in the spectra. In each panel the different lines are for different bins of JH_{140} total magnitude. The panel f) is for the pure photometric redshift uncertainty.

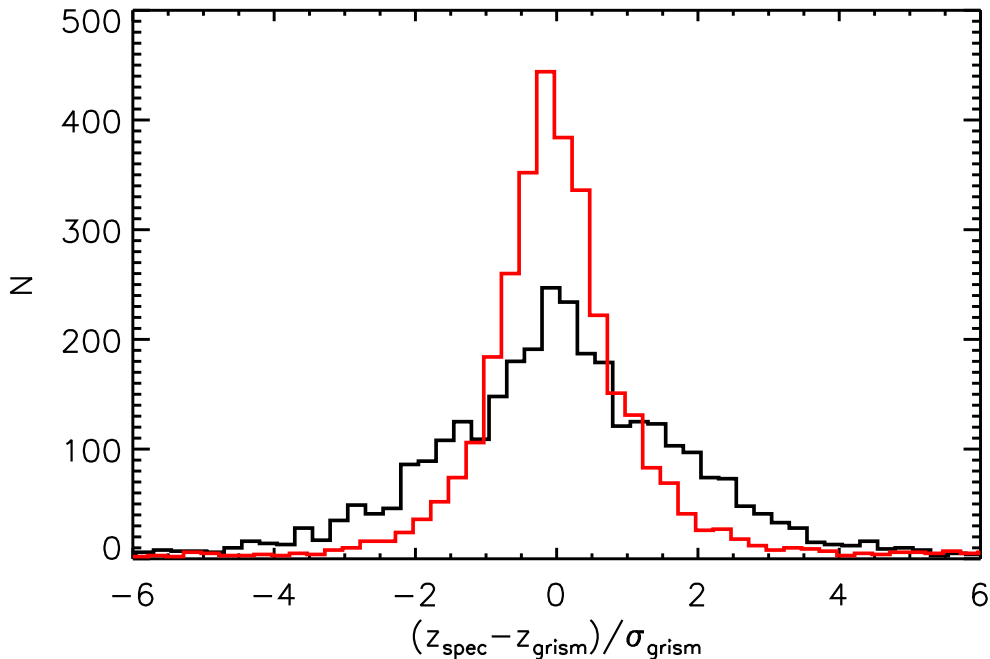


Figure 3.2: Black histogram: distribution of the difference of grism and spectroscopic redshifts divided by the grism formal uncertainty $(z_{\text{spec}} - z_{\text{grism}})/\sigma(z_{\text{grism}})$. The standard deviation of the distribution is larger than unity. Formal grism redshift uncertainties are therefore underestimated. Red histogram: distribution of the same quantity where an additional uncertainty of 800 km s^{-1} has been added in quadrature to the formal grism redshift uncertainty. The distribution has a standard deviation of unity.

in the spectrum (Momcheva et al., 2016); this justifies our approach of using the S/N of the strongest line.

Figure 3.1 shows the redshift accuracy ($\sigma_{v,\text{acc}}$) defined as 1σ of the probability density function (PDF) of grism redshifts, for bins of emission line S/N and JH_{140} magnitude. The bottom right panel (f) shows the accuracy of photometric redshifts for the same sources (fits obtained without the spectral information) highlighting the significant improvement on the redshift quality when the spectra are included.

A comparison of grism redshifts to spectroscopic redshifts shows that, for galaxies that have a spectroscopic redshift measurement, the quantity $(z_{\text{spec}} - z_{\text{grism}})/\sigma(z_{\text{grism}})$ does not have a standard deviation of unity (black histogram in Figure 3.2). This means that the formal uncertainty from the fitting process underestimates the total uncertainty. We derived that $\sim 800 \text{ km s}^{-1}$ should be added in quadrature to the formal uncertainty on the grism redshifts to obtain a scatter in $(z_{\text{spec}} - z_{\text{grism}})/\sigma(z_{\text{grism}})$ with a standard deviation of unity (red histogram in Figure 3.2). This “intrinsic grism” uncertainty can arise from morphological effects, i.e. the light weighted centroid of the gas emission can be offset from

that of the stars (see Nelson et al., 2016; Momcheva et al., 2016)

Focusing on the top panels of Figure 3.1, it is clear how an emission line detection narrows the redshift PDF to the intrinsic uncertainty, irrespective of the stellar continuum features. At S/N where the emission line becomes less dominant we start to witness a magnitude dependence of the redshift accuracy. Brighter galaxies have better continuum detections and therefore a more accurate redshift. Even when there is no line detection (Panel e), the typical redshift uncertainties are a factor 2-3 better than pure photometric redshifts. The inclusion of the spectra helps the determination of the redshifts even when the spectra are apparently featureless.

As a final note of caution we highlight that whenever the information in the spectra is limited, the final grism redshift accuracy depends largely on the photometric data, whose availability depends on the field. Indeed COSMOS and GOODS-S have been extensively observed with narrow or medium band filters (Taniguchi et al., 2007; Cardamone et al., 2010; Whitaker et al., 2011) resulting in better photometric redshifts compared to the other fields. However, as shown in section 3.5 these field-to-field variations have negligible effects on our calibration of halo mass.

3.2 Quantification of the environment

There are many ways to describe the environment in which a galaxy lives (see e.g. Haas et al., 2012; Muldrew et al., 2012; Etherington & Thomas, 2015). In this Chapter we apply to observational data the method presented in Chapter 2.

3.2.1 Density

We consider all 3D-HST galaxies selected in section 3.1 to be part both of the primary (galaxies for which the density is computed) and neighbor samples. We calculate the projected density $\Sigma_{r_{\text{ap}}}$ in a combination of circular apertures centered on the primary galaxies with radii r_{ap} . The apertures range from 0.25 to 1.00 Mpc in order to cover from intra-halo to super-halo scales.

For a given annulus defined by r_{ap} , the projected density is given by

$$\Sigma_{r_{\text{ap}}} = \frac{w_{r_{\text{ap}}}}{\pi \times r_{\text{ap}}^2} \quad (3.1)$$

where $w_{r_{\text{ap}}}$ is the sum of the weights of galaxies in the neighbors sample living at a projected distance on the sky $r < r_{\text{ap}}$ from the primary galaxy and within a relative rest-frame velocity $\pm dv$. For the 3D-HST galaxies with a grism or spectroscopic redshift the weights are set to unity (non weighted sum), while for galaxies with pure photometric redshifts we apply a statistical correction for the less accurate redshifts as described in section 3.2.2. The primary galaxy is not included in the sum therefore isolated galaxies have $\Sigma = 0$ in a given aperture.

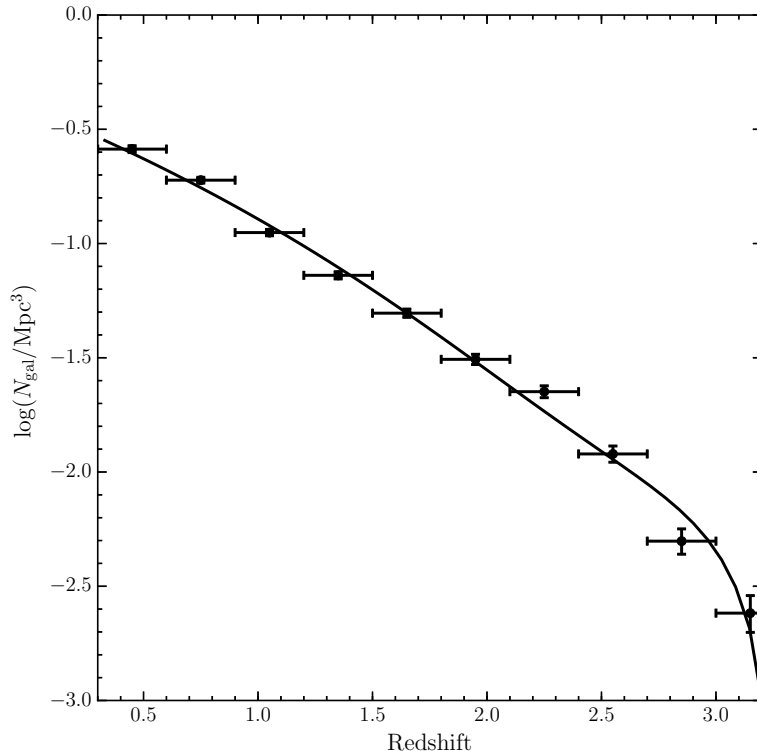


Figure 3.3: Volume density of 3D-HST galaxies as a function of redshift (black points with Poissonian uncertainties). The best third degree polynomial fit to the points is overplot as the black solid line.

We set the velocity cut at $dv = 1500 \text{ km s}^{-1}$. This value is deemed appropriate for surveys with complete spectroscopic redshift coverage (Muldrew et al., 2012) and for 3D-HST given the quality of grism redshifts shown in Figure 3.1. A small value of dv avoids the peaks in the environmental density to be smoothed by interlopers in projection along the redshift axis. On the other hand, if only less accurate redshifts are available a larger cut must be used to collect all the signal from overdense regions which is dispersed along the redshift axis (see Figure 2.4 in Chapter 2 and Etherington & Thomas, 2015).

Because Σ depends on the total number density of galaxies at a given redshift, it is not possible to compare its values at different redshifts. Therefore we define the overdensity δ which is given by

$$\delta r_{\text{ap}} = \frac{\Sigma_{r_{\text{ap}}} - \Sigma_{\text{mean}}(z)}{\Sigma_{\text{mean}}(z)} \quad (3.2)$$

where $\Sigma_{\text{mean}}(z)$ is the average surface density of galaxies at a given redshift.

Figure 3.3 shows the volume density of galaxies ($N_{\text{gal}}/\text{Mpc}^3$) in the whole survey in bins of redshift (black points with Poissonian uncertainties). The black solid line is the

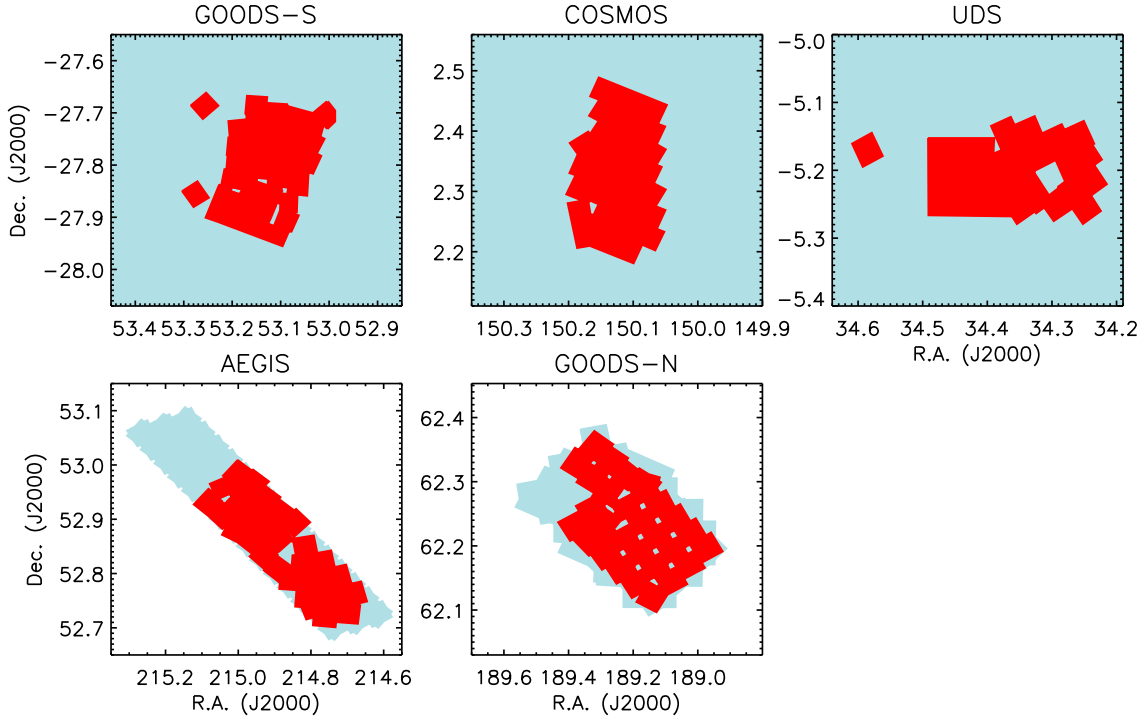


Figure 3.4: Footprints of the 3D-HST grism observations (red areas) in the five fields studied in this work and of the extended area catalogs (blue areas) used for the edge corrections. White areas are without photometric coverage.

best third degree polynomial fit to the data, which we use to parametrize the redshift dependence. This value is multiplied by the depth of the cylindrical aperture at redshift z to obtain the surface density $\Sigma_{\text{mean}}(z)$. We will mainly use the overdensity in terms of the logarithmic density contrast which is defined as $\log(1 + \delta r_{\text{ap}})$.

3.2.2 Edge corrections

The environment of primary galaxies at the edges of the 3D-HST footprint (see Figure 3.4, red areas) suffers from incomplete coverage of neighbors that results into an underestimated density in a given aperture. In large scale surveys (e.g. SDSS; Wilman et al., 2010) it is common practice to remove galaxies too close to the edges of the observed field. In the case of deep fields, however, the observed area is so small that the removal of such galaxies would reduce the statistics. One possible solution is to normalize the densities by the area of the circular aperture which is within the survey footprint in equation 3.1. Although this is a simple choice it assumes a constant density field and it neglects possible overdense structures just beyond the observed field. A more accurate solution consists of building up galaxy catalogs more extended in area than 3D-HST and then using those galaxies as

“pure neighbors” for the environment of the primary 3D-HST galaxies. Given the amount of publicly available data, this is possible in GOODS-S, COSMOS and UDS (see Figure 3.4, blue areas). In the next subsection we describe the data, depth and redshift quality of the catalogs we built in those fields. Then we present the method we developed and how it needs to be modified to perform the edge corrections in the other two fields GOODS-N and AEGIS.

Extended area catalogs for the GOODS-S, COSMOS and UDS fields

GOODS-S The GOODS-S field is part of a larger field known as the Extended Chandra Deep Field South (ECDFS, Lehmer et al., 2005). This field has been covered by the Multiwavelength Survey by Yale-Chile (MUSYC, Gawiser et al., 2006) in 32 broad and medium bands from the optical to the medium infrared wavelengths. The broadband data originates from various sources (Arnouts et al., 2001; Moy et al., 2003; Taylor et al., 2009) and a consistent reduction and analysis is performed by the MUSYC team (Cardamone et al., 2010). The source extraction is performed on a deep combined image of three optical filters (BVR) and reaches a depth of ~ 25.5 mag. Stars are removed from the catalog by using the `star_flag` parameter.

In order to select galaxies in a consistent way as for 3D-HST we need deep observations in a filter with a central wavelength as close as possible to that of WFC3/F140W ($1.4\mu\text{m}$). However, the near infrared observations from MUSYC are shallow and only reach a depth of $J = 22.4$ mag. We therefore match the MUSYC catalog with the Taiwan ECDFS Near-Infrared Survey (TENIS, Hsieh et al., 2012). This survey provides deep J and K_s images of the ECDFS area with limiting magnitudes of 24.5 and 23.9 respectively. Hereafter, where sky coordinates matching between different catalogs is required we select the closest match within a 1 arcsec radius. The comparison of J band magnitudes from the two surveys for sources above the sensitivity limit of the MUSYC data shows a remarkable agreement. We then match the MUSYC and 3D-HST/GOODS-S catalog, again by sky coordinates. Using the galaxies that are present in both surveys we fit a linear function between JH_{140} and J_{TENIS} magnitudes. Given the significant overlap between the filters we neglect color terms in the fit. The best bisector fit (Isobe et al., 1990) is $JH_{140} = 0.99 \times J_{\text{TENIS}} + 0.22$. Then we use this function to generate JH_{140} magnitudes for all objects in the MUSYC+TENIS catalog.

We evaluate the depth of the resulting catalog by inspecting the histogram of the number counts in the JH_{140} band. Since this is obtained from deep J_{TENIS} data (24.5 mag), the limiting factor will be the depth of the BVR selection band of MUSYC. The number counts increase linearly in log space up to $JH_{140} \sim 23.5$ and we therefore adopt this value for the selection. Since this limit is brighter than the one we set for the primary sample in 3D-HST, a fraction of the neighbors are missed. We correct for this by assigning to each MUSYC galaxy in eq. 3.1 a weight $w = 1.42$ that corresponds to the ratio of the cumulative luminosity function at $JH_{140} = 23.5$ and $JH_{140} = 24$ mag from the deeper 3D-HST catalog.

The most recent calculation of photometric redshifts in ECDFS is presented by Hsu

et al. (2014). These authors combined the MUSYC photometry with TENIS and HST/CANDELS (Guo et al., 2013b) in the GOODS-S area. We match our catalog with their catalog based on MUSYC ID and we find a match for each source. Hsu et al. (2014) also present a compilation of spectroscopic redshifts available in the literature which we use whenever available. Photo- z s are computed using *LePhare* (Arnouts et al., 1999; Ilbert et al., 2006) and their accuracy depends primarily on the availability and depth of multiwavelength photometry. The GOODS-S area has deep HST coverage from CANDELS, but those galaxies are already present in our primary 3D-HST catalog. Therefore we are primarily interested in sources outside the CANDELS/3D-HST area. In the ECDFS footprint which is not covered by HST more than 30 photometric bands are available and photo- z s are quite accurate²: $\sigma_{\text{NMAD}} \sim 3000$ (4000) km s^{-1} for galaxies with $H < 23$ ($H > 23$) respectively. Those values degrade where continuum spectral features (e.g. Balmer break) are redshifted outside the range observed with medium band filters ($z > 1.5$), although low number statistics hampers a robust determination of the photometric redshift quality.

Stellar masses are computed using the photometric data and the redshift information by choosing the same grid of templates used by Skelton et al. (2014) for the 3D-HST fields. We assess the quality of the stellar masses by comparing to those from Skelton et al. (2014), where MUSYC and 3D-HST overlap and we find a median offset of 0.01 dex and a scatter of 0.15 dex. The scatter is driven by the scatter in photometric redshifts in the two catalogs.

As a last step we remove from this catalog galaxies in the 3D-HST footprint and that satisfy the selection criteria for the primary environment sample, to obtain a pure catalog that we use only for the edge corrections.

COSMOS The entire COSMOS 2deg² field has been observed in 30 photometric bands from UV to medium infrared (including several medium bands) (Sanders et al., 2007; Taniguchi et al., 2007; Erben et al., 2009; Bielby et al., 2012). Photometric redshifts are computed using *LePhare* and are presented by Ilbert et al. (2009) for sources with $i^+ < 25$ mag. We include spectroscopic redshifts from zCOSMOS-bright (Lilly et al., 2007) where available.

The photometric redshift uncertainty is evaluated by Ilbert et al. (2009) comparing photo- z to spec- z and is $\sigma_{\text{NMAD}} \sim 2100$ (9000) km s^{-1} for galaxies with $i^+ < 22.5$ ($i^+ > 23$) respectively. The latter value must be taken with caution as it is calibrated using a small number of objects. We remake this comparison by using 3D-HST spec- z and grism- z as a reference (restricting our analysis to the 3D-HST/COSMOS field). We divide the sample into bright ($i^+ < 22.5$ mag) and faint ($i^+ \geq 22.5$ mag) for $0.5 < z \leq 1.5$ and irrespective of magnitude for $1.5 < z \leq 3.0$. We note that for faint sources the effective magnitude limit is that of the grism redshift extraction $JH_{140} < 24$ mag and the comparison is limited by the degraded accuracy of grism redshifts for faint sources with no emission line detection

²We measure the photo- z accuracy using the normalized median absolute deviation (NMAD): $\sigma_{\text{NMAD}} = 1.48 \times \text{median}(|\Delta z|/(1+z))$, where Δz is the difference between the spectroscopic and the photometric redshift.

(see Figure 3.1). The redshift accuracy is: $\sigma_{\text{NMAD}} \sim 3000$ (7500) km s^{-1} for the bright (faint) sample at low redshift and $\sigma_{\text{NMAD}} \sim 8500$ km s^{-1} for the high redshift sample. Those values are consistent with the determination by Ilbert et al. (2009) and the reduced accuracy at high redshift is due to the lack of narrow bands in the NIR.

To overcome this limitation the Newfirm Medium Band Survey (NMBS, Whitaker et al., 2011) observed the COSMOS field with 5 medium band filters in the J and H bands and a broadband filter in K . As a result the accuracy of photometric redshifts is significantly improved (see section 5 in Whitaker et al., 2011) and we use those photo- z where they are available.

Deep J band magnitudes are provided by the UltraVISTA survey (McCracken et al., 2012). After matching their catalog via sky coordinates we generate synthetic JH_{140} magnitudes as described in the previous section and using the best fit: $JH_{140} = 0.98 \times J_{\text{UltraVISTA}} + 0.31$. The depth of our catalog is limited by the depth of the i^+ selection band from Ilbert et al. (2009). The number counts increase linearly in log space until $JH_{140} \sim 23.0$ and we therefore adopt this value for the selection limit. As for the MUSYC catalog this limit is brighter than the one we set for the primary sample in 3D-HST therefore we assign to each galaxy in eq. 3.1 a weight ($w = 2.06$). Stars are removed from the catalog by using the `type` flag from Ilbert et al. (2009).

We compute stellar masses as described in the previous section. The agreement with stellar masses from Skelton et al. (2014) is remarkable, with a median offset of 0.02 dex and a scatter of 0.20 dex. Lastly we remove the primary 3D-HST sources from this edge correction sample.

UDS The 3D-HST UDS field is part of a larger field known as UKIDSS UDS. This field features deep near infrared J , H , and K observations with the UKIDSS telescope (Almaini et al. in prep) complemented by optical and medium infrared data (Furusawa et al., 2008; Ashby et al., 2013).

The UDS/DR8 catalog selection is performed in K band and the completeness limit is $K \sim 24.6$ mag. As for the previous fields we exclude stars and we compute synthetic JH_{140} magnitudes using the best fit relation: $JH_{140} = 0.98 \times J_{\text{UKIDSS}} + 0.19$. The depth of our catalog matches the limiting magnitude for the primary 3D-HST sample, thus we do not apply any statistical weight for the UKIDSS UDS galaxies when computing the density.

Photometric redshifts (W. Hartley private comm.) have a typical accuracy of $\sigma \sim 9000$ km s^{-1} due to the lack of narrow- or medium band photometry in this field. As for the other fields we compute stellar masses using the FAST code and we find a good agreement with the values from Skelton et al. (2014) for the 3D-HST/UDS field with an offset of -0.03 dex and a scatter of 0.22 dex. Again the last step is to remove the 3D-HST primary sources via positional matching with the Skelton et al. (2014) catalog.

Edge correction method for GOODS-S, COSMOS, and UDS

The availability of spectroscopic redshifts in the extended area catalogs is limited (from $\sim 5\%$ in COSMOS and UDS to $\sim 15\%$ in GOODS-S). We thus need to cope with the

limited accuracy of photometric redshifts for the galaxies in those fields. The photo- z accuracy, which varies from field to field and depends on the redshift of the objects, is such that most of the sources which are part of the same halo in real space would not be counted as neighbors of a primary galaxy, simply due to the redshift uncertainty. We showed in section 2.3 that increasing the depth of the velocity window would recover most of the real neighbors but at the expenses of a larger fraction of interlopers (galaxies which are not physically associated to the primary). Here we thus exploit a different method. We assume that galaxies which are close by on the sky and whose redshifts are consistent within the uncertainties are, with a high probability, physically associated (see e.g. Kovač et al., 2010; Cucciati et al., 2014). If one of them has a secure spectroscopic redshift, we assign this to the others.

Our method works as follows:

- For each galaxy with a photometric redshift we select all neighbors with a redshift within $dv_{\text{phot}} = \pm 10000 \text{ km s}^{-1}$. This value is chosen to recover most of the real neighbors given the average photo- z uncertainties.
- Among those neighbors, we select the closest (in spatial coordinates) which has a secure spectroscopic (or grism) redshift. Here we assume grism redshifts to have a negligible uncertainty compared to photo- z s.
- We replace the photo- z of each galaxy with this spec- z (or grism- z). Since the statistical validity of the assumption of physical association depends on the distance of the neighbor, for increasing distances we underestimate the true clustering. We correct for the bias by assigning a weight w_{ph} to each galaxy.

The weight is evaluated on a training sample made of galaxies in 3D-HST with $JH_{140} < 23$ mag. For each galaxy in the three fields we compute the “real” density (Σ_{real} in a 0.75Mpc radius and $dv = \pm 1500 \text{ km s}^{-1}$) using spec- z or grism- z from 3D-HST. For each galaxy we then take its photometric redshift, and follow the procedure described above, but, instead of choosing the closest neighbour with a secure redshift, we select a random neighbor in different bins of projected sky distance (from 0 to 3 Mpc in bins of 0.5 Mpc width). Then we compute densities with each of those distance replacements separately and the fractional bias (b_d) as:

$$b_d = \frac{\Sigma_d - \Sigma_{\text{real}}}{\Sigma_{\text{real}}} \quad (3.3)$$

where the d subscript denotes the replacement with a spec- z of a galaxy found at distance d . By using the 3D-HST data we make sure that there are always a large number of neighbors with a secure redshift, and we repeat this procedure 1000 times in order to uniformly sample the neighbors. Figure 3.5, left panel, shows b_d as a function of the real density in four bins of d . Clearly the larger d is, the more underestimated the real density will be, due to a decreasing fraction of correct redshift assignments smoothing out the density field.

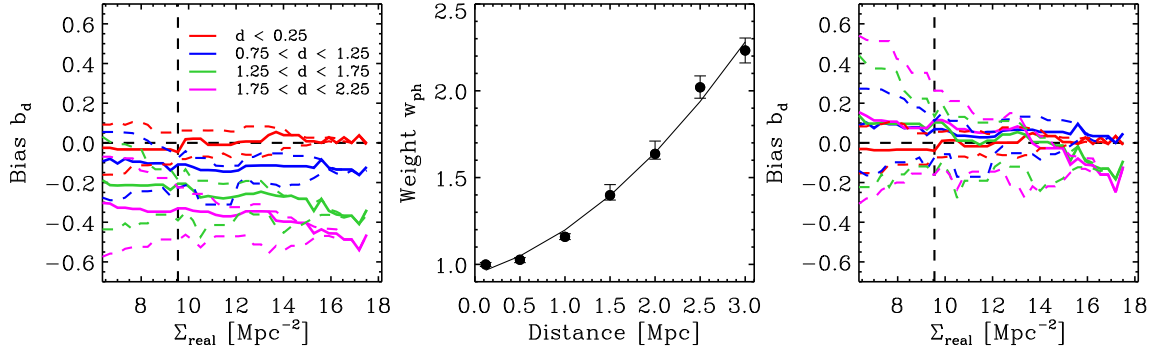


Figure 3.5: Left Panel: median bias b_d in the density field introduced when photo-z are replaced with spectroscopic redshifts of sources at $d < 0.25$ Mpc (Red), $d \sim 1.0$ Mpc (Blue), $d \sim 1.5$ Mpc (Green), and $d \sim 2.0$ Mpc (Magenta). Dashed lines mark the 10th – 90th percentiles of the distributions. The vertical dashed line marks the density above which the bias is computed and converted into a weight. Middle Panel: median weight as a function of the distance of the neighbor with a spectroscopic (or grism) redshift. The solid line is the best fit quadratic polynomial we use for the statistical correction (see Equation 3.4). Right Panel: median bias b_d color coded as in the left panel but after the statistical correction. The median values are consistent with no bias for all the distance bins.

We then derive the median weight $w_{\text{ph},d} = \text{med}((b_d + 1)^{-1})$ where the median is computed among all galaxies that have $\Sigma_{\text{real}} > 9.5 \text{Mpc}^{-2}$ (see the vertical dashed line in Figure 3.5, left panel). The density dependence of b_d is negligible at these densities, therefore by avoiding underdense regions (where the uncertainty on b_d is large) we obtain a robust determination of $w_{\text{ph},d}$. Figure 3.5, middle panel, shows $w_{\text{ph},d}$ versus d , which we fit with a quadratic relation obtaining:

$$w_{\text{ph},d} = 9.66 \times 10^{-2} \times d^2 + 0.155 \times d + 0.946 \quad (3.4)$$

with the additional constraint that $w_{\text{ph},d} \geq 1$ which corresponds to $w_{\text{ph},d} = 1$ for $d < 0.29$ Mpc. We tested that this relation, although obtained combining all fields, holds within the uncertainties when each field is considered separately. Lastly we show in Figure 3.5, right panel, how the systematic bias is removed when the weight is applied to all neighbors when computing the density. This is consistent with no bias within the uncertainties for all the distance bins.

Edge correction method for GOODS-N and AEGIS

The GOODS-N and AEGIS fields do not have deep and extended near-infrared public catalogs that can be used to derive the edge corrections as presented above, therefore we use a different method. As shown in Figure 3.4 (light blue shaded areas) the 3D-HST/CANDELS footprint slightly extends beyond the area covered by G141 grism observations (which is the main requirement for our primary sample). Therefore the 3D-HST/CANDELS catalog

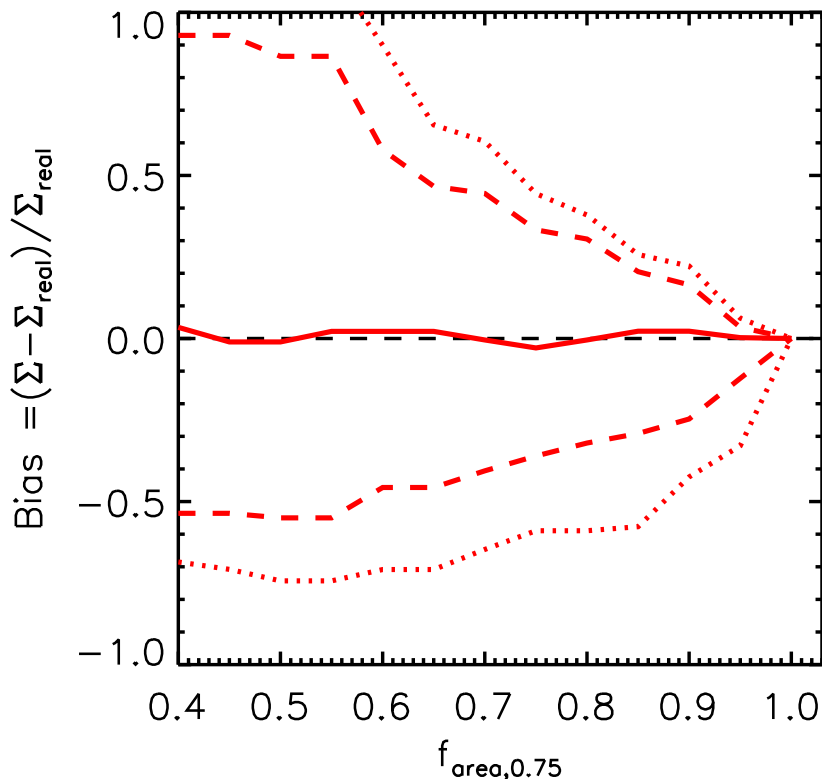


Figure 3.6: Bias (defined as in equation 3.3) between the density (Σ_{real}) in a 0.75Mpc aperture measured using the extended catalogs for COSMOS, GOODS-S, UDS and the density (Σ) measured using the fraction of the aperture in the 3D-HST footprint ($f_{\text{area},0.75}$) as a function of the latter quantity. The solid line is the median while dashed and dotted lines mark the 1σ and 2σ confidence intervals respectively. The bias between the two methods is zero, with a scatter for individual galaxies which increases by decreasing the fraction of the aperture in the 3D-HST footprint.

itself can be used to derive edge corrections which are critical to fill in the gaps between grism observations. We derive JH_{140} magnitudes from the J_{125} magnitudes using a linear function derived from the five 3D-HST fields ($JH_{140} = 1.000 \times J_{125} - 0.295$). Then we use 3D-HST photometric redshifts (or spec-z where available) and we apply the method described in section 3.2.2.

However, the 3D-HST/CANDELS photometric catalogs do not extend enough beyond the primary sample area to ensure the apertures used to compute the density are entirely within the photometric catalog footprint. For this reason we simply compute the densities using the area of the circular aperture within the photometric catalog. We test this method by comparing the density (Σ_{real}) in a 0.75Mpc aperture measured using the extended catalogs for COSMOS, GOODS-S, UDS and the density (Σ) measured correcting for the fraction of the aperture ($f_{\text{area},0.75}$) in the 3D-HST/CANDELS footprint. The result is

shown in Figure 3.6. We note that although the median (red solid line) is consistent with no bias, the area correction introduces a scatter (dotted and dashed lines) which increases by decreasing the fraction of the aperture in the footprint.

In conclusion, the environmental catalog released with this work will include all the primary galaxies in the five 3D-HST field. However in the rest of this work we only include galaxies for which $f_{\text{area},0.75} > 0.9$ for the GOODS-N and AEGIS fields. The total number of objects in the primary 3D-HST sample with a robust determination of the environmental density is therefore reduced to 17397 (93% of the original sample).

3.3 Overdensities in the 3D-HST deep fields

In order to explore correlations of galaxy evolution with environment we need to make sure the 3D-HST fields span a wide range of galaxy (over-)densities. Figures 3.7, 3.8, 3.9, 3.10, and 3.11 present the primary sample of 3D-HST galaxies in the five fields color coded by their overdensity in the 0.75 Mpc aperture in different redshift slices. The range of density probed is wide and spans from isolated galaxies to objects for which the local number of neighbors is up to ten times larger than the mean at that redshift.

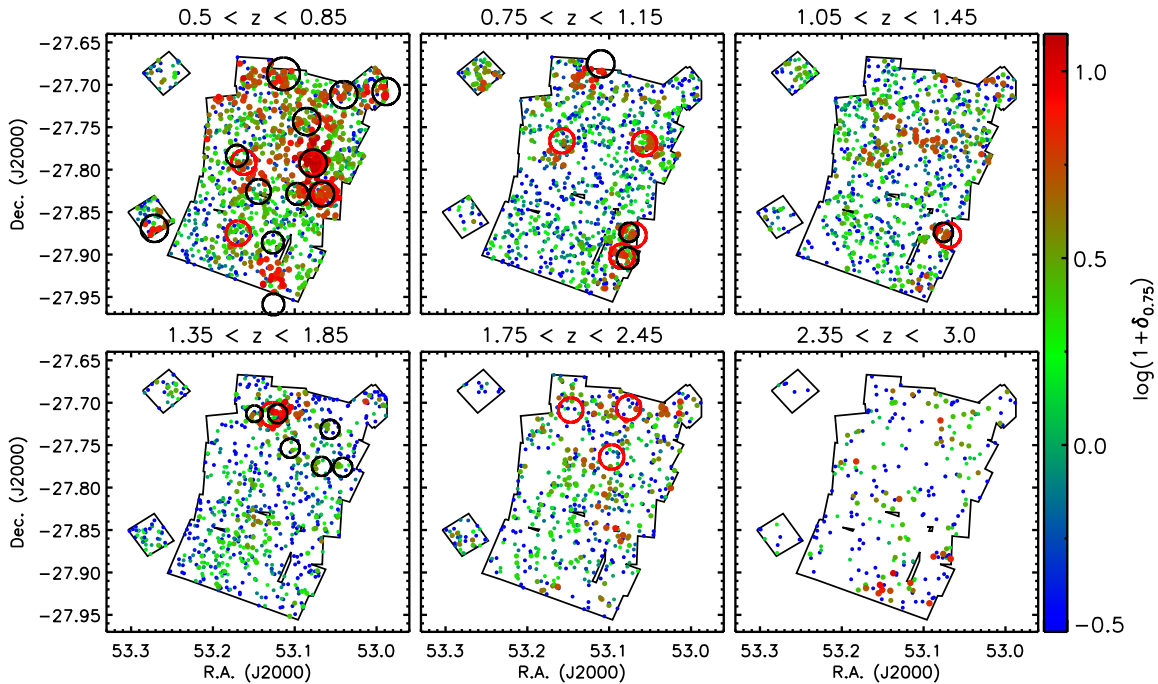


Figure 3.7: Gallery of the 3D-HST galaxies in the GOODS-S field in different redshift slices. Points are color coded by their overdensity in the 0.75 Mpc aperture. The size of the points also scales with overdensity. This figure clearly demonstrates the large dynamic range in environments found in the deep fields. Black circles mark the position of X-Ray extended emission from Finoguenov et al. (2015), the size of the circle giving the extension of the emission (R_{200}). Red circles mark the position of galaxy overdensities from Salimbeni et al. (2009) who used a smoothed 3D density technique from the GOODS-MUSIC catalog (the size of the circle is arbitrary and fixed).

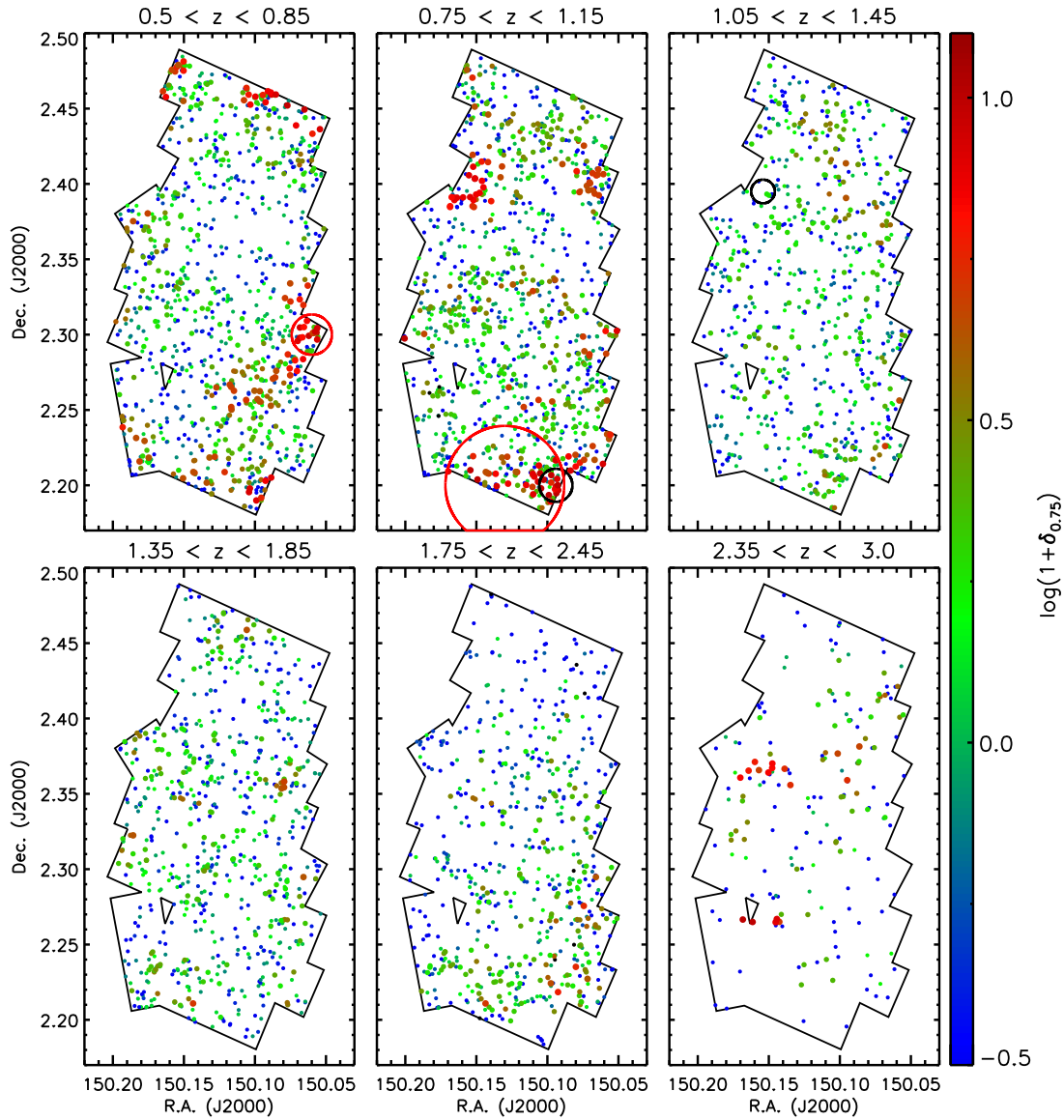


Figure 3.8: Same as Figure 3.7 but for the 3D-HST COSMOS field. The X-Ray extended emission circles (black) are from Finoguenov et al. (2007), and galaxy density based large scale structures (red) from Scoville et al. (2007) using pure photometric redshifts up to $z \sim 1$.

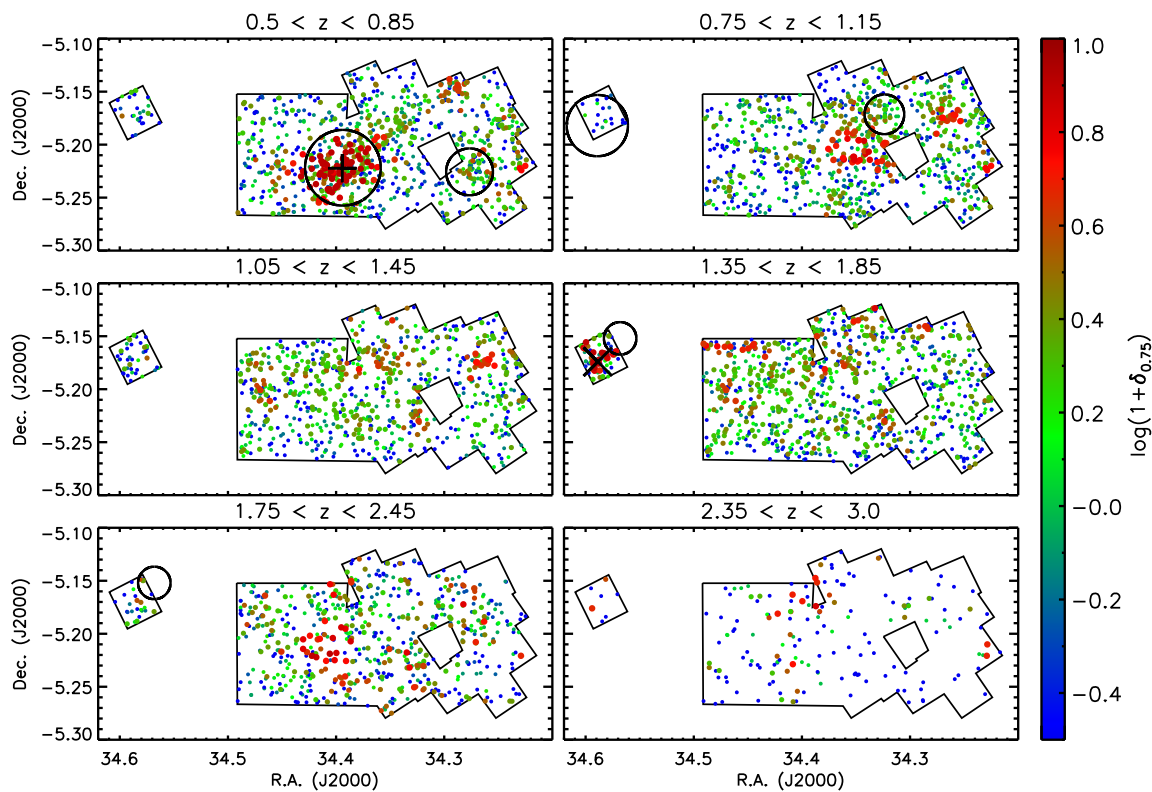


Figure 3.9: Same as Figure 3.7 but for the 3D-HST UDS field. The X-Ray extended emission circles (black) are from Finoguenov et al. (2010). The black + and \times symbols mark the center of known clusters at $z = 0.65$ (Geach et al. 2007, Galametz et al. in prep.) and $z = 1.62$ (Papovich et al., 2010; Tanaka et al., 2010) respectively.

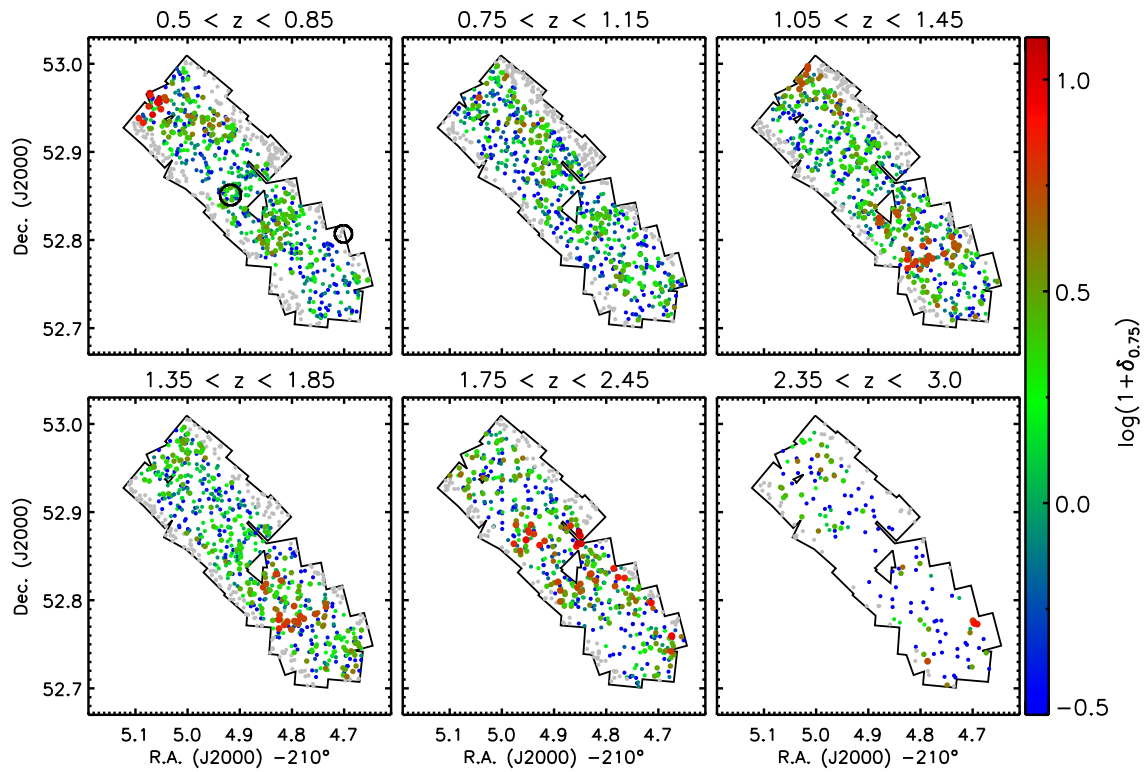


Figure 3.10: Same as Figure 3.7 but for the 3D-HST AEGIS field. The X-Ray extended emission circles (black) are from Erfanianfar et al. (2013).

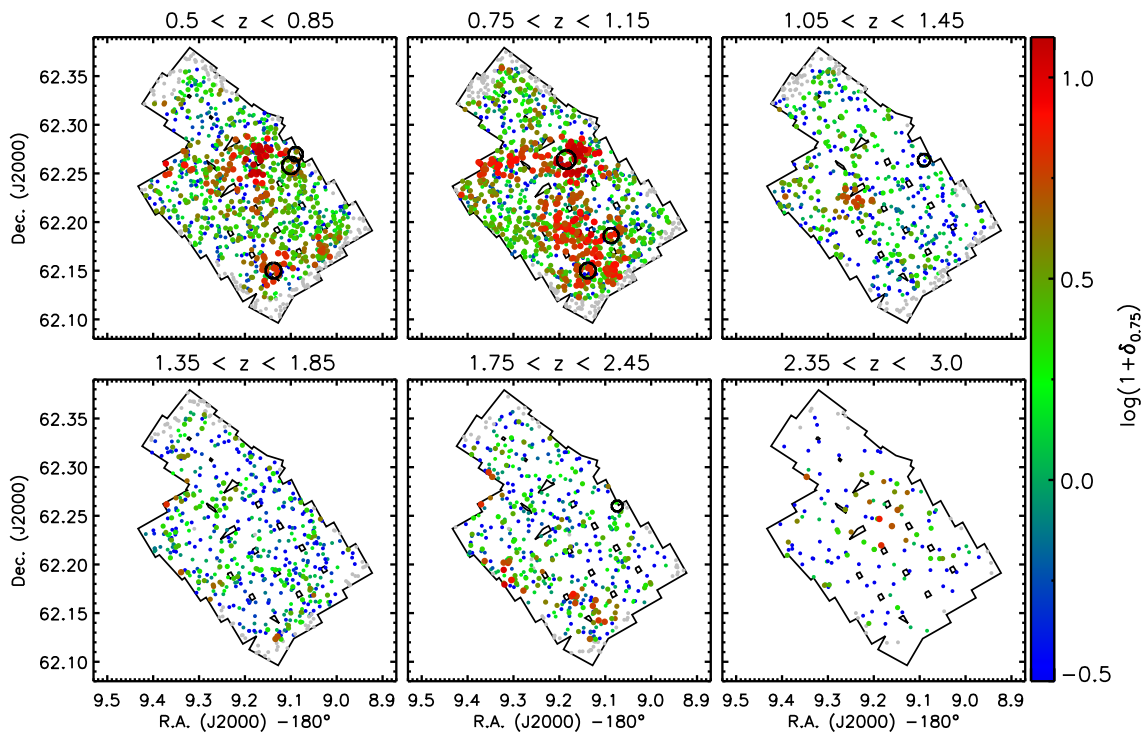


Figure 3.11: Same as Figure 3.7 but for the 3D-HST GOODS-N field. The X-Ray extended emission circles (black) are from A. Finoguenov (private comm.).

As a sanity check we overplot the position and extension of X-Ray extended emission from the hot intragroup (and intracluster) medium that fills massive haloes. The exquisite depth of X-Ray data in the deep fields (Finoguenov et al., 2007, 2010, 2015; Erfanianfar et al., 2013) allows the detection of the hot gas from haloes down to $M_{\text{halo}} \sim 10^{13} M_{\odot}$. We find a very satisfactory agreement between our overdensity fields and the X-Ray emission position. Indeed, most of the X-Ray groups are coincident with large overdensities in our maps. On the other hand not all the overdense structures identified in our work are detected in X-Ray. We speculate this is mainly due to the presence of more than one massive structure along the line of sight or that low mass groups are not yet virialized. Lastly we note that the redshift of the X-Ray emission is assigned based on the photometric or spectroscopic information available at the epoch of the publication of the catalog; these data might not have been as accurate as the density field reconstruction performed in this work. Our analysis has therefore the potential to spectroscopically confirm more X-Ray groups or improve the quality of previous redshift assignments.

Several other works have also analyzed, with different techniques, the presence of overdense structures in the deep fields. In the GOODS-S field we overplot on Figure 3.7 the position of overdensities from Salimbeni et al. (2009) derived from the GOODS-MUSIC catalog using a smoothed 3D density technique. These data have 15% spectroscopic redshifts and photometric redshifts for the remaining fraction. Because the smoothing technique is less able to constrain the size of the structure we plot circles with an arbitrary radius. The structures within the 3D-HST footprint (except those at $z > 2$) are confirmed with our data to be at least a factor of 2 – 3 denser than the mean. The differences in the samples and in the techniques used hamper a more quantitative comparison. Our data confirm with a high degree of significance the detection of two well known super-structures, one at redshift $z = 0.73$ (Gilli et al., 2003; Adami et al., 2005; Trevese et al., 2007) and one at redshift $z = 1.61$ first detected by Kurk et al. (2009). The latter is made by 5 peaks in the photo- z map (which correspond to putative positions for the X-Ray emission, see Table 1 in Finoguenov et al. (2015)). The main structure is robustly detected in our data while the other sub-structures are only mild ($\log(1 + \delta_{0.75}) \sim 0.5$) overdensities.

In the COSMOS field (see Figure 3.8) Scoville et al. (2007) applied an adaptive smoothing technique (similar to Salimbeni et al., 2009) to find large scale structures at $z < 1$. While their results do not constrain the size of the structure and are less sensitive to very compact overdensities we do find that their detections in the 3D-HST footprint correspond to high overdensities in our work.

Similarly in the UDS field we do detect a very massive cluster surrounded by filaments and less massive groups (upper left panel of Figure 3.9) at $z = 0.65$ (Galametz et al. in prep.). Another well known structure in this field is located at $z = 1.62$ (Papovich et al., 2010; Tanaka et al., 2010). Despite being only partially covered by the 3D-HST grism observations (isolated pointing on the left of the contiguous field) we do find it corresponds to a large overdensity of galaxies thanks to our accurate edge corrections using UKIDSS-UDS photometric data.

In summary we checked that our reconstruction of the density field in the 3D-HST deep fields recovers the previously known massive structures across the full redshift range

analyzed in this work.

3.4 The model galaxy sample

The goal of this work is to understand the environment of galaxies in the context of a hierarchical Universe. To reach this goal we need to calibrate physically motivated quantities using observed metrics of environment by means of semi-analytic models of galaxy formation (SAM). We make use of light cones from the latest release of the Munich model presented by Henriques et al. (2015). This model is based on the Millennium N-body simulation (Springel et al., 2005) which has a size of $500h^{-1}$ Mpc. The simulation outputs are scaled to cosmological initial conditions from the *Planck* mission (Planck Collaboration XVI, 2014): $\sigma_8 = 0.829$, $H_0 = 67.3 \text{ km s}^{-1} \text{ Mpc}^{-1}$, $\Omega_\Lambda = 0.685$, $\Omega_M = 0.315$. Although those values are slightly different from those used in our observational sample, the differences in cosmological parameters have a much smaller effect on mock galaxy properties than the uncertainties in galaxy formation physics (Wang et al., 2008; Fontanot et al., 2012; Guo et al., 2013a).

This model includes prescriptions for gas cooling, size evolution, star formation, stellar and active galactic nuclei feedback and metal enrichment as described by e.g. Croton et al. (2006); De Lucia & Blaizot (2007); Guo et al. (2011). The most significant updates concern the reincorporation timescales of galactic wind ejecta that, together with other tweaks in the free parameters, reproduce observational data on the abundance and color distributions of galaxies from $z = 0$ to $z = 3$ (Henriques et al., 2015). Our choice of this model is therefore driven by those new features which are critical for an accurate quantification of the environment.

We make use of the model in the form of 24 light cones, which are constructed by replicating the simulation box evaluated at multiple redshift snapshots. Before deriving environmental statistics from the light cones as described in section 3.2.1 we need to match the magnitude selection and redshift accuracy of the 3D-HST survey.

3.4.1 Sample selection

SAMs are based on N-body dark matter only simulations. Therefore (and opposite to observations) the galaxy stellar masses are accurate quantities, while magnitudes are uncertain and rely on radiative transfer and dust absorption recipes implemented in the models. On the other hand magnitudes are direct observables in a survey (like 3D-HST) therefore they are known with a high degree of accuracy.

To overcome these limitations (and the fact that JH_{140} magnitudes are not given in Henriques et al. (2015) cones) we employ a method that generates observed magnitudes for SAM galaxies by using observational constraints from 3D-HST. Each model galaxy is defined by its stellar mass ($M_{*,\text{mod}}$), $U - V$ rest frame color ($(U - V)_{\text{mod}}$) and redshift (z_{mod}). Similarly 3D-HST galaxies are defined by stellar mass ($M_{*,\text{obs}}$), $U - V$ rest frame color ($(U - V)_{\text{obs}}$), redshift (z_{obs}), and magnitude (JH_{obs}).

The method works as follows:

- For each bin of stellar mass (0.5 dex wide) and redshift (0.1 wide) we select all the model and 3D-HST galaxies.
- For each model galaxy in this bin we rank the $(U - V)_{\text{mod}}$ and we find the $(U - V)_{\text{obs}}$ that corresponds to the same ranking.
- We assign to the model galaxy a randomly selected stellar mass-to-light ratio $(M_*/L_{JH})_{\text{obs}}$ at $(U - V)_{\text{obs}} \pm 0.05$. Figure 3.12 shows an example of $(M_*/L_{JH})_{\text{obs}}$ as a function of $(U - V)_{\text{obs}}$ for galaxies at $0.5 < z < 0.6$ and $9.75 < \log(M_*) < 10.25$. By selecting a random $(M_*/L_{JH})_{\text{obs}}$ at fixed $(U - V)_{\text{obs}}$ we preserve the observed distribution of $(M_*/L_{JH})_{\text{obs}}$ in the mock sample.
- From $(M_*/L_{JH})_{\text{obs}}$, $M_{*,\text{mod}}$, and z_{mod} we compute JH_{mod} for the model galaxy.

This method generates JH_{140} magnitudes for all the model galaxies down to $10^8 M_\odot$. This is much deeper than the 3D-HST magnitude limit even at the lower end of our redshift range. We then select model galaxies down to a $JH_{\text{mod,lim}}$ magnitude that matches the total number density of the primary targets ($JH_{140} < 24$ mag) in the five 3D-HST fields to that in the 24 lightcones. This protects us from stellar mass function (SMF) mismatches between the models and the observations (although those differences are very small in Henriques et al. (2015)). We employ a $JH_{\text{mod,lim}} = 23.85$ mag, which is very close to 24 mag further supporting the quality of the SMF in the H15 models.

3.4.2 Matching the redshift accuracy

After the model sample is selected, the next goal is to assign to each galaxy a redshift accuracy that matches as closely as possible the one in 3D-HST. To do so, we should not only assign the correct fraction of spec-z, grism-z and photo-z as a function of observed magnitude but also assign an accuracy for the grism-z and photo-z as a function of physical properties such that the final distributions resemble those in Figure 3.1. We showed in section 3.1.1 that the grism redshift accuracy depends on the signal-to-noise of the strongest emission line and the galaxy magnitude. For the latter we use JH_{140} as derived above, while the former quantity needs to be parametrized in terms of other quantities available in the models.

Figure 3.13, left panel, shows how the emission line S/N depends both on the line flux and the JH_{140} magnitude for galaxies with a measured line flux. For each galaxy we take the flux (in units of $\text{erg cm}^{-2} \text{s}^{-1}$) of the strongest line and we define the line magnitude as $m_{\text{line}} = -2.5 \times \log(f_{\text{line}})$. At fixed line flux, brighter galaxies have more continuum, thus decreasing the line S/N . This relation is well reproduced by the following parametrization:

$$\log(S/N) = -0.33 \times (2 \times m_{\text{line}} - JH_{140}) + 19.85 \quad (3.5)$$

Figure 3.13, right panel, shows the line S/N obtained with this equation applied to 3D-HST galaxies. The small differences between the two panels are due to additional variables not

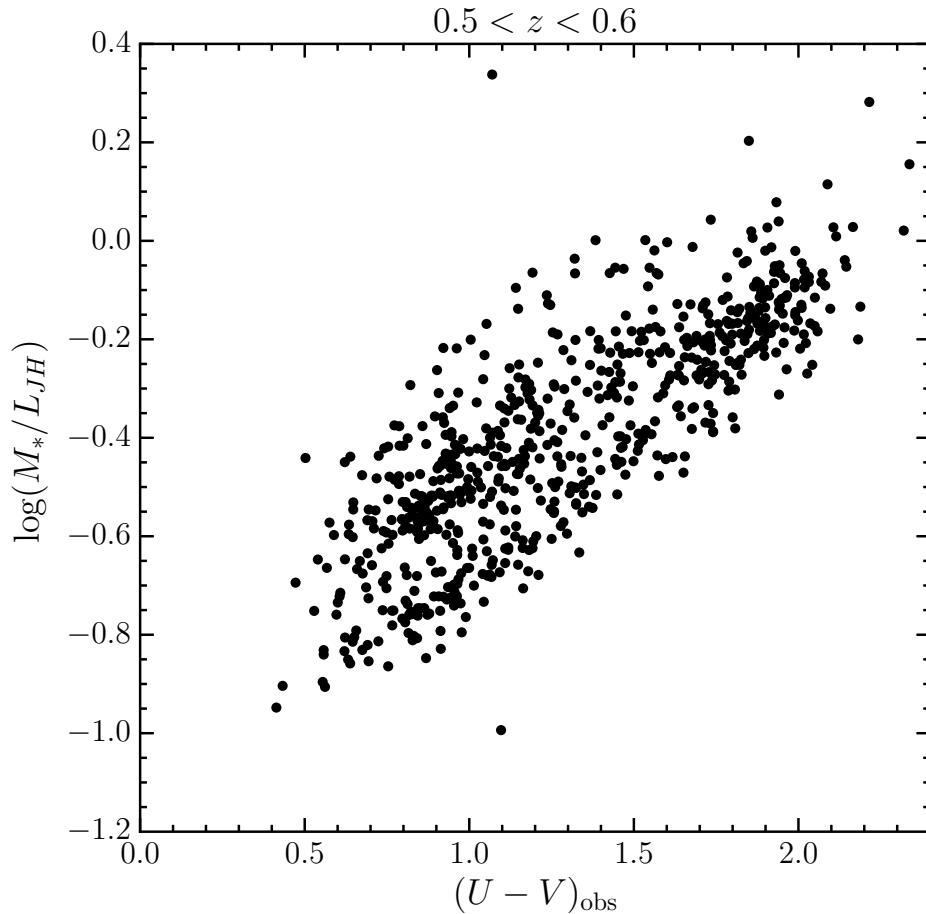


Figure 3.12: $(M_*/L_{JH})_{\text{obs}}$ as a function of $(U - V)_{\text{obs}}$ for 3D-HST galaxies at $0.5 < z < 0.6$ and $9.75 < \log(M_*) < 10.25$.

taken into account (e.g. dust extinction or grism throughput). We tested (by perturbing the S/N assigned to each model galaxy) that a more accurate parametrization of this relation is not required for the purposes of this work.

In order to obtain a synthetic line $(S/N)_{\text{mod}}$ for the model galaxies we first convert the star formation rate (SFR) of the model galaxies into an $H\alpha$ flux (or $H\beta$ flux where $H\alpha$ is redshifted outside the grism wavelength range) by inverting the relation given in Kennicutt (1998a). We then compute the line magnitude (m_{line}), which is used with JH_{mod} in equation 3.5 to obtain S/N_{mod} . The rank in $(S/N)_{\text{mod}}$ is then matched to that in the line S/N for 3D-HST selected galaxies (and not the absolute values).

Lastly we assign to each mock galaxy a random grism redshift accuracy such that the observed distributions shown in Figure 3.1 are reproduced for the mock sample. A photometric redshift accuracy is also generated using the same distributions (as a sole function of JH_{mod}).

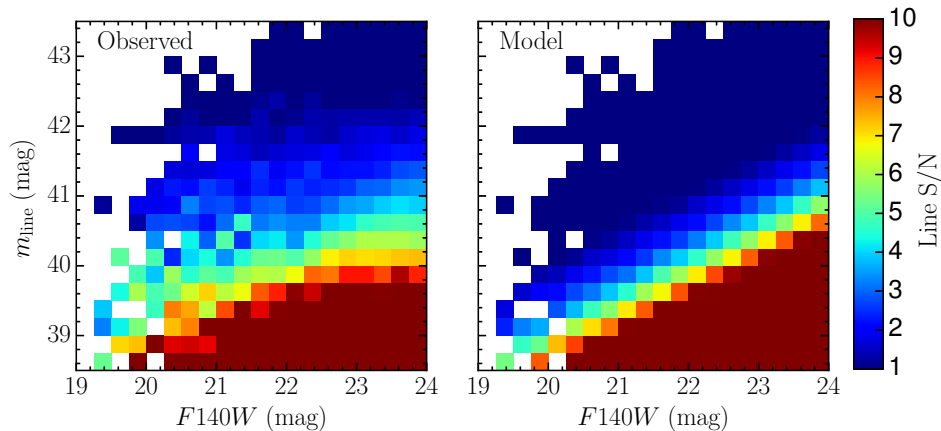


Figure 3.13: Left panel: emission line S/N for 3D-HST galaxies as a function of the JH_{140} magnitude and line magnitude. Right panel: emission line S/N obtained using the parametrization from equation 3.5.

Each model galaxy is then defined by three redshifts: a spectroscopic redshift which is derived from the geometric redshift (z_{GEO}) of the cones plus the peculiar velocity of the halo, a grism like redshift which is derived from the spec-z plus a random value drawn from a gaussian distribution with sigma equal to the grism redshift accuracy derived above, and a photometric redshift derived as the previous but using the photometric redshift accuracy.

The last step in this procedure requires that for each galaxy only one of these three redshifts is selected so to generate a “best” redshift that matches the one in the 3D-HST catalog. To do so we work in bins of JH_{140} magnitude. For each bin of magnitude the fraction of 3D-HST galaxies with spec-z, grism-z and photo-z is computed. Then in order of descending $(S/N)_{\text{mod}}$, the spec-z is taken for a number of galaxies matching the fraction in the observational catalog, a grism-z is taken for an appropriate number of galaxies and lastly a photo-z is taken for the galaxies with the lowest S/N_{mod} which mimic line non-detections in the grism data. We stress that since the grism redshift accuracy is a function of $(S/N)_{\text{mod}}$ the quality of grism redshifts for objects with marginal line detections is preserved in this method.

Once a catalog of model galaxies is selected and their redshift accuracy matches the 3D-HST catalog, we compute the environment parameters for those galaxies in the same way as was described in section 3.2.1. The only minor difference is that, as the number of model galaxies is very large, we can remove those objects closer than 1.0 Mpc to the edges of the cone, protecting us against edge biases.

3.5 Calibration of physical parameters

The local density of galaxies is not the only parameter that describes the environment in which a galaxy lives. Another important parameter is whether a galaxy is the domi-

nant within its dark matter halo (Central), or if it orbits within a deeper potential well (Satellite). In this section we describe how we use the mock catalog to assign a halo mass probability density function (PDF) and a probability of being central or satellite to 3D-HST galaxies. The method builds on the idea of finding all the galaxies in the mock lightcones that match each 3D-HST galaxy in redshift, density, mass-rank (described below), and stellar mass (within the observational uncertainties). The main advantage of using multiple parameters is to break degeneracies which are otherwise dominant if only one parameter is used (e.g. to account for the role of stellar mass at low density, where halo mass depends more significantly on stellar mass than density, as shown in section 2.5.2 and in Figure 2.11).

3.5.1 The stellar mass rank in fixed apertures

In Chapter 2 we explored how the rank in stellar mass of a galaxy in an appropriate aperture can be a good discriminator of the central/satellite status for a galaxy. This method, which complements the one usually used in local large scale surveys of galaxies based on halo finder algorithms, is more effective with the sparse sampling typical of high redshift surveys.

We recall that we define a galaxy to be central if it is the most massive (mass-rank = 1) within an adaptive aperture that depends only on the stellar mass. Otherwise, if it is not the most massive (mass-rank > 1), then it is classified as a satellite.

The adaptive aperture is motivated by the fact that ideally the aperture in which the mass-rank is computed should be as similar as possible to the halo virial radius to maximize the completeness of the central/satellite separation and reduce the fraction of spurious classifications. Based on the evidence of a good correlation between stellar mass and halo virial radius (see section 2.4.1), this aperture is defined as a cylinder with radius:

$$r_0 = 3 \times 10^{(\alpha \log M_* + \beta)} \text{ [Mpc]} \quad (3.6)$$

where M_* is the stellar mass, $\alpha = 0.25$, and $\beta = -3.40$ are the parameters which describe the dependence of the virial radius with stellar mass. We also limit the aperture to the range between 0.35 and 1.00 Mpc. The lower limit is set to avoid small apertures which would result in low mass galaxies being assigned mass-rank = 1 even if they are satellites of a large halo. The upper limit is approximately the radius of the largest haloes in the redshift range under study. The adaptive aperture radius (in Mpc) is therefore defined as:

$$r = \begin{cases} 0.35 & \text{if } r_0 < 0.35 \\ r_0 & \text{if } 0.35 \leq r_0 \leq 1.00 \\ 1.00 & \text{if } r_0 > 1.00 \end{cases} \quad (3.7)$$

In this Chapter we have to consider the variable redshift accuracy of 3D-HST galaxies. Therefore fixing the depth of the cylinder to $\pm 1500 \text{ km s}^{-1}$ does not optimize the central

versus satellite discrimination. We set the depth of the adaptive aperture cylinder (in km s^{-1}) to:

$$dv = \begin{cases} 1500 & \text{if } \sigma_{v,\text{acc}} < 1500 \\ \sigma_{v,\text{acc}} & \text{if } 1500 \leq \sigma_{v,\text{acc}} \leq 7500 \\ 7500 & \text{if } \sigma_{v,\text{acc}} > 7500 \end{cases} \quad (3.8)$$

where $\sigma_{v,\text{acc}}$ is the redshift accuracy of each primary galaxy. We have tested that this combination of upper and lower limits gives a pure yet sufficiently complete sample of central galaxies.

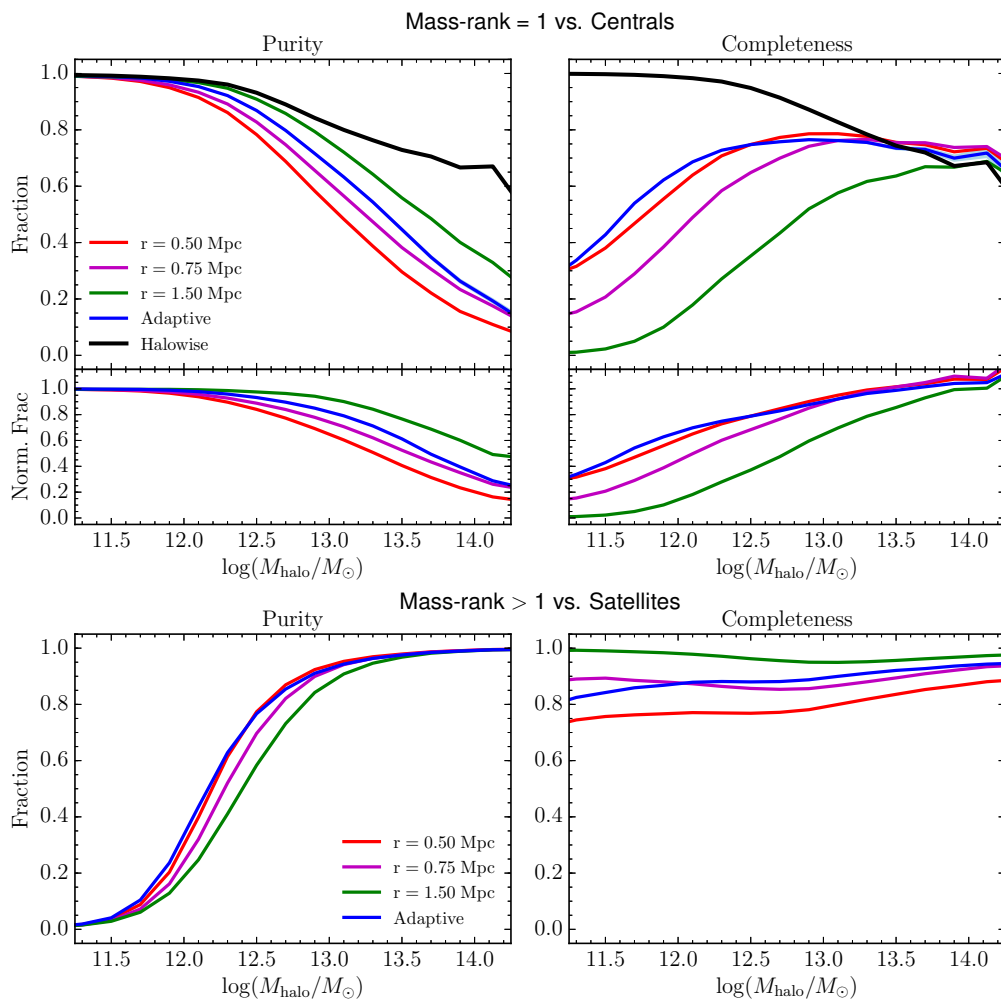


Figure 3.14: Top panels: purity and completeness for the selection of central galaxies based on stellar mass rank = 1 as a function of the halo mass. The rank is computed in various apertures ranging from 0.50 to 1.50 Mpc plus an ideal method based on the perfect knowledge of which galaxy belongs to each halo (Halowise, black solid). Middle Panels: purity and completeness for the selection of central galaxies normalized to the Halowise line described above. Bottom panels: same as top panels but for satellite galaxies selected by having stellar mass rank > 1 .

Figure 3.14 shows the performances of how much a population of galaxies whose stellar mass rank is 1 compares to galaxies identified as centrals by the algorithms used in the models. We define two parameters to quantify the overlap between the two populations. The purity (P) is the number of centrals which are correctly identified over the number of selected galaxies; and the completeness (C) is the number of identified centrals over the total number of central galaxies. The black solid line is not obtained with an aperture in position-redshift space but rather counting the mass rank of each galaxy with respect to all the other galaxies in the same halo. This is only possible in the models but sets a reference for our observationally motivated methods. We observe that the purity and completeness of this method drops at high halo masses; this is because the most massive galaxy is not always the central of its host halo. This is due to the scatter in the stellar-mass halo-mass relation which can lead to a merger of two haloes where the most massive galaxy resides in the least massive halo. Therefore this halo and the galaxy that it hosts are considered satellites by the models. The blue solid line is our fiducial adaptive aperture. It is clear that this aperture is the best compromise between a high purity (that can be obtained with a large aperture) and high completeness (which on the other hand can only be obtained with a small fixed aperture).

The middle panels of Figure 3.14 show the purity and completeness of the fixed and adaptive apertures normalized to the Halowise method. Indeed the most massive galaxy in any halo corresponds to a significant local potential, and as such one could also define a purity and completeness relative to this population. For the full population we then obtain a normalized purity of 98% while for haloes more massive than $10^{13.5}M_{\odot}$ this value is still 45% with the adaptive aperture. The normalized completeness is also satisfactory being close to 100% for massive haloes. This means that also in the regime of groups and clusters of galaxies we can identify all the centrals but with a $\sim 50\%$ contamination from satellites.

The bottom panels of Figure 3.14 show the purity and completeness of the fixed and adaptive apertures when we compare galaxies with a mass rank > 1 to satellites. At high halo masses ($M_{\text{halo}} > 10^{13.5}M_{\odot}$) the purity is 99% and the completeness is 93% and those values are hardly affected by the choice of the aperture. This means that the full population of satellite galaxies can be identified in this regime. On the other hand the purity quickly drops at halo masses below $10^{12.5}M_{\odot}$, with little dependence on the aperture size. This halo mass regime suffers from two sources of contamination. First in galaxy pairs (where the mass of the real central and satellite are very close) it is difficult to use the stellar mass (or any other method) to robustly define which galaxy is the central and which is the satellite. Second, low stellar (and halo) mass centrals outside the virial radius of massive haloes will most likely be assigned a mass-rank > 1 because they live in relatively high density regions. Therefore we would classify those galaxies as satellites, however because they are not part of the massive halo nearby they are considered centrals in the model classification.

In summary, the simple classification of centrals and satellites based on mass-rank only is subject to a variety of contaminating factors. It is therefore important to go beyond the dichotomic definition that each galaxy is a central or satellite using the mass-rank.

In the next section we combine multiple observables to derive a probability that each 3D-HST galaxy is central or satellite by matching observed galaxies to mock galaxies. This probabilistic approach naturally takes into account all the sources of impurity and is of fundamental importance to separate the effects of mass and environment on the quenching of galaxies.

3.5.2 Matching mock to real galaxies

In this section we describe how we match individual 3D-HST galaxies to the mock sample to access physical quantities inaccessible from observations only. Our method relies heavily on the fact that the distributions of stellar mass and density (and their bivariate distribution) are well matched between the mocks and the observations across the full redshift range. In what follows we use the density in a 0.75 Mpc aperture. This aperture is large enough to cover the full extent of massive haloes ($M_h > 10^{13.5} M_\odot$) at the redshift range under study. A good match between models and observations is found for other apertures as well. In the future, it should be possible to improve our method by combining density information on several scales by means of machine learning algorithms.

In the upper and right panels of Figure 3.15 we show the distributions of density and stellar mass respectively, while the main panel shows the 2D histogram of both quantities. The overall agreement is very satisfactory and relates to the agreement of the observed stellar mass functions to that from Henriques et al. (2015), and to our careful selection of objects. The match of the density distributions also confirms that the redshift assignment for mock galaxies is accurate enough to reproduce the observed density distributions.

To match observed galaxies to mock galaxies we also require an estimate of the uncertainty on both the density and the stellar mass. For the stellar mass we use a 0.15 dex error on $\log(M_*)$ (Conroy et al., 2009; Gallazzi & Bell, 2009; Mendel et al., 2014). For the density, the error budget is dominated by the redshift uncertainty of each galaxy and the fact that for a sample of galaxies with given JH_{140} and emission line S/N the redshift accuracy has a distribution with non zero width. This means that the redshift uncertainty of mock galaxies can only match the observational sample in a statistical sense. To test how the densities of individual galaxies are affected by the redshift uncertainty we repeat 50 times the process of assigning a redshift to mock galaxies described in subsection 3.4.2. Then we compute the density for each of those samples independently and we analyze the distribution of densities for each galaxy. We find that the distribution roughly follows a Poissonian distribution: $\sigma(\Sigma_{r_{\text{ap}}}) = \sqrt{w_{r_{\text{ap}}}} / (\pi \times r_{\text{ap}}^2)$

Based on this evidence we match each 3D-HST galaxy to the mock galaxies within ± 0.1 in redshift space and with stellar mass and density on the 0.75 Mpc scale within ± 1 sigma uncertainty on those quantities. Moreover, because the density peaks are subject to different degrees of smoothing for different redshift accuracies, the match is performed among model galaxies with a redshift accuracy within $\pm 2000 \text{ km s}^{-1}$ to that of the observed galaxy. Lastly we restrict the match for the most massive galaxies (mass-rank = 1) to the most massive mock galaxies. The rest of the population (mass-rank > 1) was matched to the same population in the mocks.

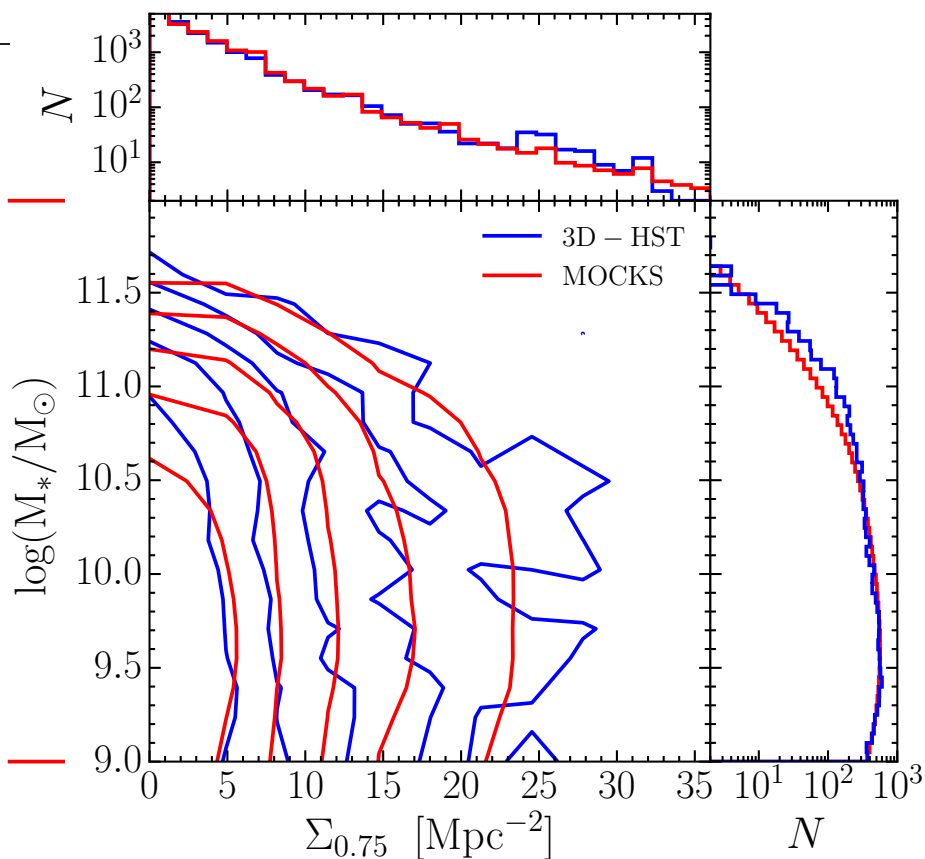


Figure 3.15: Main panel: bivariate distribution of density on the 0.75 Mpc scale and stellar mass for the 3D-HST sample (blue) and the mock sample (red). The mock contours have been scaled to account for the ratio of volumes between the lightcones and the data. The contours are logarithmically spaced with the outermost contour at 4 objects per bin and the innermost at 300 objects per bin. Upper panels: marginalized distributions of density on the 0.75 Mpc scale for the 3D-HST and the mock samples. The counts refer to the 3D-HST sample while the mock histogram has been normalized by the ratio of the volumes. Right-hand panel: same as above but marginalized over the stellar mass.

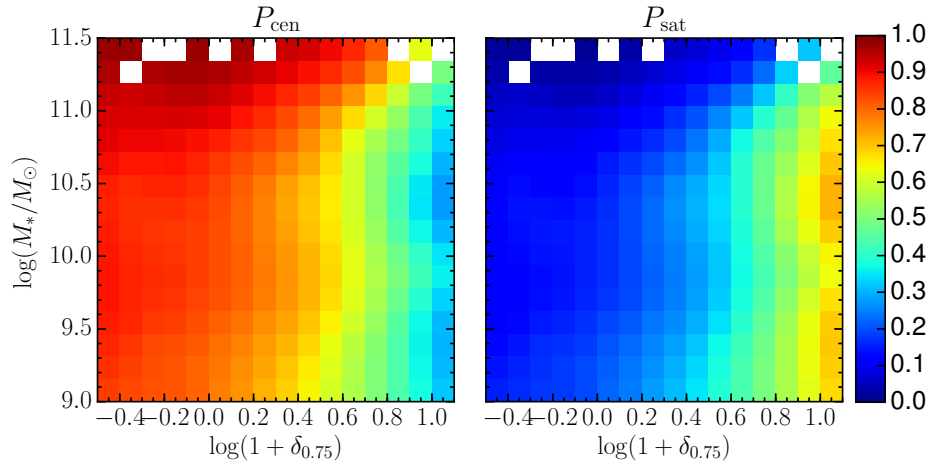


Figure 3.16: Average probability for a 3D-HST galaxy of being central (P_{cen} , left panel) or satellite (P_{sat} , right panel) in bins of density contrast in the 0.75 Mpc aperture and stellar mass.

A probabilistic determination of central versus satellite status

The central and satellite fractions of those matched mock galaxies are used to define a probability that the 3D-HST galaxy under consideration is central (P_{cen}) or satellite (P_{sat}).

Figure 3.16 shows the average values of those quantities in bins of logarithmic density contrast (see section 3.2.1) in the 0.75 Mpc aperture and stellar mass for all the 3D-HST galaxies included in our sample. The average value of P_{cen} decreases at increasing density and decreasing stellar mass, and the opposite trend occurs for P_{sat} . Indeed high mass haloes (high density regions) are dominated by the satellite population, but objects with high stellar masses are more likely to be centrals. Galaxies in low density environments ($\log(1 + \delta_{0.75}) < 0.2$) are almost entirely centrals. However in the analysis performed in the next sections we use the values of P_{cen} and P_{sat} computed for each galaxy instead of the average values (Kovač et al. 2014 performs instead an average correction as a function of galaxy density). This takes into full account possible second order dependencies on mass-rank, redshift, or redshift accuracy.

Lastly we study how P_{sat} varies as a function of the distance from the center of overdense structures, like massive groups or clusters of galaxies. To do so we take the haloes more massive than $10^{13.5} M_{\odot}$ in the mock lightcones. Then we select all galaxies in a redshift slice centered on the redshift of the central galaxy and with width ± 0.01 and we compute their positions with respect to the central galaxy. Lastly we normalize those positions to the virial radius of the halo and we remove the central galaxy.

Figure 3.17 shows the average value of P_{sat} as a function of normalized R.A. and Dec. offset from the center of the haloes. The black solid circles mark r_{vir} and $2 \times r_{\text{vir}}$. Figure 3.18 shows the average value of P_{sat} as a function of radial distance from the center of the haloes.

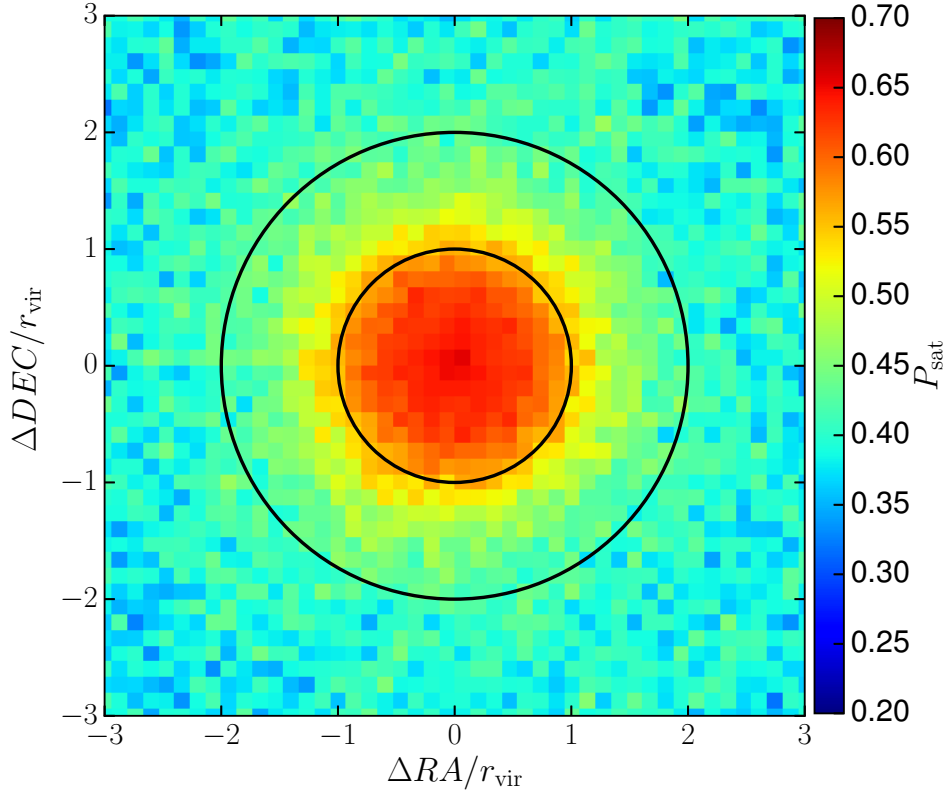


Figure 3.17: Average probability of being a satellite for mock galaxies as a function of RA and Dec offset from the center of haloes more massive than $10^{13.5} M_{\odot}$. The black solid circles mark r_{vir} and $2 \times r_{\text{vir}}$.

Our Bayesian definition tracks the SAM definition of satellites as a function of halo mass. However the real trend is smoothed due to both the transformation from real to redshift space, and the intrinsic uncertainty of our method to extract P_{sat} based on observational parameters.

Figure 3.18 shows that galaxies within r_{vir} have a $\sim 70\%$ probability of being satellites, while this fraction drops to $\sim 50\%$ between r_{vir} and $2 \times r_{\text{vir}}$. As discussed in Chapter 2 the galaxies in the infalling regions of a massive group or cluster might experience satellite specific processes prior to their first crossing of r_{vir} (Bahé et al., 2013). Another significant population can be that of “backsplash” galaxies, i.e. galaxies that have already crossed the halo and are centrals in the current simulation snapshot (see e.g. Balogh et al., 2000; Mamon et al., 2004; Wetzel et al., 2014). Our method naturally takes into account those galaxies by assigning them a roughly equal probability of being centrals or satellites.

Moreover, P_{sat} only drops to 40% at $\sim 5 \times r_{\text{vir}}$. This happens because massive structures

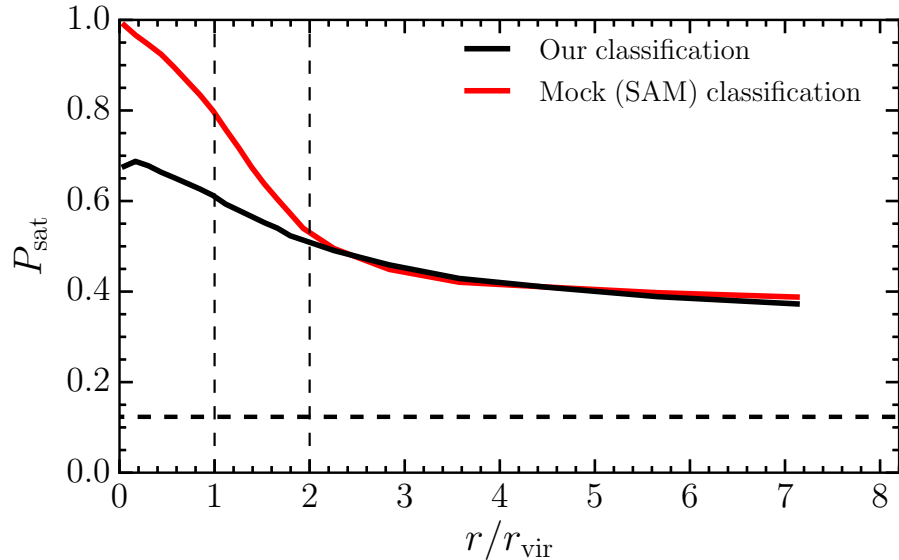


Figure 3.18: Average probability of being a satellite for mock galaxies using our Bayesian definition (black solid line) or the SAM definition of satellites (red solid line) as a function of radial distance from the center of haloes more massive than $10^{13.5}M_{\odot}$. The vertical dashed lines mark r_{vir} and $2 \times r_{\text{vir}}$. The horizontal dashed line is the value of P_{sat} for galaxies living in average density environments.

are embedded in filaments and surrounded by groups which will eventually merge with the cluster. Therefore, even at large distances from the center, the density is higher than the mean density. As a reference we show in Figure 3.17, bottom panel, the value of P_{sat} for galaxies living in average density environments (horizontal dashed line).

The halo mass calibration

We use the halo masses of matched central and satellite model galaxies to generate the halo mass PDFs given their type ($P_{M_h|\text{cen}}$ and $P_{M_h|\text{sat}}$ respectively). Figure 3.19 shows three examples of such PDFs for one object with high P_{cen} , one with high P_{sat} , and one object with an almost equal probability of being a central or a satellite. The vertical dashed lines mark the median halo mass for a given type. Although the total halo mass PDF can be double peaked (middle panel), the degeneracy between the two peaks is broken once the galaxy types are separated, making the median values well determined for each type independently.

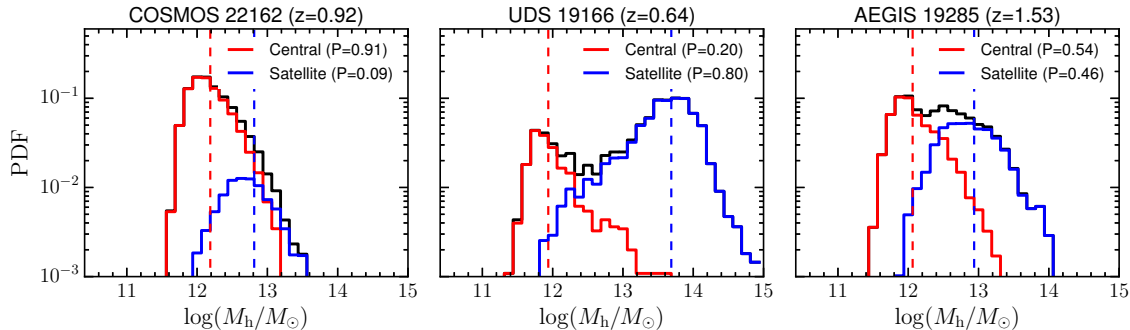


Figure 3.19: Example halo mass PDFs for three 3D-HST galaxies. The left panel shows a galaxy with a high probability of being a central, the middle panel one with a high probability of being a satellite, and the right panel an object with an almost equal probability of being a central or a satellite. The red and blue histograms show the halo mass probability given that the galaxy is a central ($P_{M_h|\text{cen}}$) or a satellite ($P_{M_h|\text{sat}}$), while the black histogram is the total halo mass PDF. The histograms are normalized such that the area under them gives P_{cen} and P_{sat} respectively. The vertical dashed lines mark the median halo mass for a given type.

3.5.3 Testing calibrations

We test the halo mass calibration by comparing the halo mass distributions of the mock sample to the 3D-HST sample. In both panels of Figure 3.20 we plot the halo mass histograms for centrals and satellites of the entire mock sample. The number counts are scaled by the ratio of the volume between the 24 lightcones and the five 3D-HST fields.

In the left panel of Figure 3.20 the dashed lines are the halo mass distributions of 3D-HST galaxies obtained by summing the full halo mass PDFs for centrals ($P_{M_h|\text{cen}}$, red dashed) and satellites ($P_{M_h|\text{sat}}$, blue dashed) weighted by P_{cen} and P_{sat} for each galaxy. The agreement with the mock sample distributions is remarkable. Although this is in principle expected because the halo mass PDFs for observed galaxies are generated from the mock sample, it should be noted that we perform the match in bins of redshift, redshift accuracy, stellar mass, density and mass-rank. The good agreement for the whole sample between the derived PDFs and the mock distributions (for centrals and satellites separately) should therefore be taken as an evidence that our method has not introduced any bias in the final PDFs.

In the right panel of Figure 3.20, the dashed lines are the halo mass distributions of 3D-HST galaxies obtained in a different way. We take the median value of the halo mass PDFs given that each galaxy is a central ($M_{h,50|\text{cen}}$) or a satellite ($M_{h,50|\text{sat}}$) as an estimate of the “best” halo mass, weighted by P_{cen} and P_{sat} . The agreement with the mock distributions is good. For central galaxies the shape and extent of the distribution is well preserved. For satellite galaxies the halo mass range is less extended than the one in the mocks. Values above $10^{14.2}M_{\odot}$ and below $10^{12}M_{\odot}$ indeed only contribute through the tails of the PDFs;

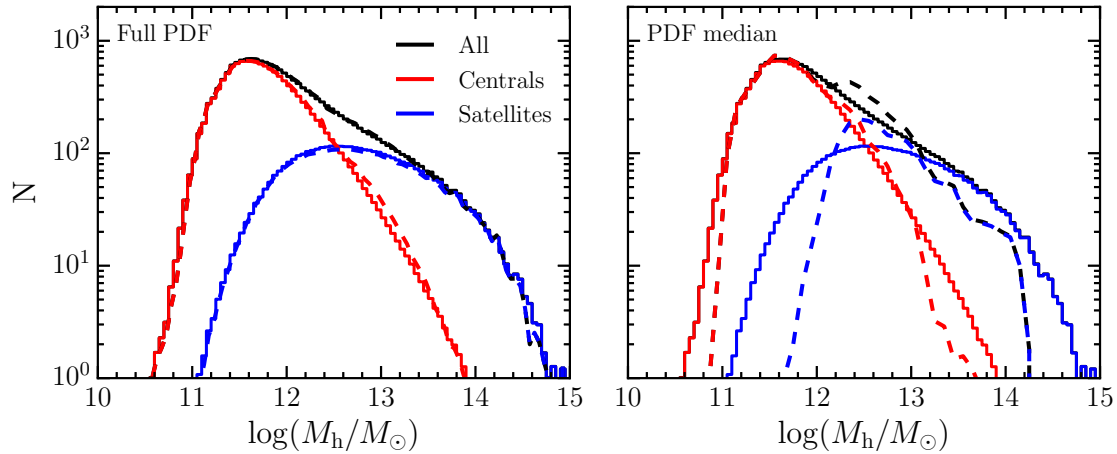


Figure 3.20: Comparison of the halo mass distributions for the mock galaxies (solid histograms) and 3D-HST galaxies (dashed lines). In the left panel the dashed lines are obtained by summing the full halo mass PDFs for centrals ($P_{M_h|\text{cen}}$, red) and satellites ($P_{M_h|\text{sat}}$, blue) weighted by P_{cen} and P_{sat} for each galaxy. In the right hand panel the dashed lines are obtained from the single value estimator (median value of the PDF given the type) weighted by the probability that a galaxy is of a given type. The black histograms and dashed lines are the sum of the colored.

therefore they do not appear when the median of the PDFs are used.

In the next section we make use of the full PDFs to derive constraints on the environmental quenching of satellite galaxies. However, the satisfactory agreement of the single value estimates of halo masses with the mock distributions makes them a valuable option in the science applications when the use of the full PDFs is not possible or feasible.

3.5.4 The environment catalog

The environmental properties of 3D-HST galaxies are made available at:
www.mpe.mpg.de/~mfossati/3dhst_environment/

Conditional halo mass PDFs given that each galaxy is a central or a satellite and covering the range $10 < \log(M_h/M_\odot) < 15$ with 100 uniform bins are also available as separate tables. Table 3.1 gives an example of the quantities provided in the catalog and the description of the columns follows:

- (1) 3D-HST field
- (2) 3D-HST photometric ID from Skelton et al. (2014)
- (3) fraction of the 0.75 Mpc aperture in the photometric catalog
- (4) density of galaxies in an aperture of 0.75 Mpc radius (see eq. 3.1)
- (5) overdensity of galaxies in an aperture of 0.75 Mpc radius (see eq. 3.2)

- (6) stellar mass rank in the adaptive aperture
- (7) and (8) probability that the galaxy is a central or a satellite
- (9), (10), and (11) 16th, 50th, and 84th percentile of the log halo mass cumulative PDF given that the galaxy is a central
- (12), (13), and (14) 16th, 50th, and 84th percentile of the log halo mass cumulative PDF given that the galaxy is a satellite

Field	ID	$f_{\text{area},0.75}$	$\Sigma_{0.75}$	$\delta_{0.75}$	M_{rank}	P_{CEN}	P_{SAT}	$M_{\text{h},16 \text{CEN}}$	$M_{\text{h},50 \text{CEN}}$	$M_{\text{h},84 \text{CEN}}$	$M_{\text{h},16 \text{SAT}}$	$M_{\text{h},50 \text{SAT}}$	$M_{\text{h},84 \text{SAT}}$
(1)	(2)	(3)	(4)	(5)	(6)	(7)	(8)	(9)	(10)	(11)	(12)	(13)	(14)
COSMOS	22162	1.00	3.96	1.160	1	0.911	0.089	11.968	12.195	12.524	12.428	12.753	13.134
UDS	19166	1.00	18.67	6.624	5	0.199	0.801	11.773	11.967	12.398	13.167	14.049	14.251
AEGIS	19285	1.00	2.83	1.200	4	0.544	0.456	11.867	12.087	12.510	12.536	12.917	13.352
.....													

Table 3.1: Example of the environmental catalog table made available with this work. Note: Halo mass values are given as $\log(M_{\text{h}}/M_{\odot})$.

3.6 The Local Universe sample from SDSS

3.6.1 Observational data

We repeat the environment calibration described in this Chapter on a sample of galaxies in the Local Universe selected from the SDSS (York et al., 2000) survey. We use the data from the SDSS DR8 database (Aihara et al., 2011) cross correlated with an updated version of the multi-scale density catalog from Wilman et al. (2010) (with densities computed according to equation 3.1; updated DR8 catalog as used by Phleps et al., 2014; Hirschmann et al., 2014).

SDSS DR8 includes 5 color *ugriz* imaging of 14555 square degrees. The spectroscopic part of the survey provides redshifts for 77% of objects brighter than a limit of $r = 17.77$ across 8032 square degrees. Our sample is derived from the spectroscopic database. Luminosities are computed by k-correcting and adding the distance modulus to the Petrosian r-band magnitude. k-corrections are performed using the K-CORRECT IDL tool (Blanton & Roweis, 2007).

We select as primary galaxies those with $M_r < -18$ mag and $0.015 < z < 0.08$. In contrast to the method we use at high redshift the sample of neighbors (galaxies used to calculate the density in equation 3.1) is restricted to $M_r < -20$ mag. This ensures a volume limited sample for the neighbors in this redshift range, while for the primary galaxies we correct for volume incompleteness using V_{\max} corrections. The primary sample numbers $\sim 3 \times 10^5$ galaxies. Stellar masses and star formation rates are obtained from the JHU-MPA³ catalogs updated to DR7 (Brinchmann et al., 2004; Kauffmann et al., 2003).

For this work we use the density computed on a fixed scale of 1 Mpc, with a velocity cut of $dv = \pm 1000 \text{ km s}^{-1}$. This scale is larger than what we use in the 3D-HST sample in order to take into account the growth of structure with cosmic time. We stress that our results do not significantly depend on the scale chosen because the halo mass calibration is performed self consistently and we only compare calibrated quantities across the two samples. We have further computed stellar mass ranks for each primary galaxy in the adaptive aperture as described in section 3.5.1.

One limitation of the SDSS spectroscopic strategy is that not all the spectroscopic targets can be actually observed because two fibers cannot be placed closer than 55" on the sky and each patch of the sky is only observed once (although with small overlaps between adjacent spectroscopic plates). As a result the spectroscopic catalog does not contain all the sources detected in the imaging. Spectroscopic completeness is taken into account in the computation of the densities as described by Wilman et al. (2010), and we take this incompleteness into account when we match to the mock galaxy sample.

3.6.2 The model sample

We generate a model galaxy sample that matches the stellar mass and density distributions of the SDSS observational catalog. To do so we take the SAM from Henriques et al. (2015)

³<http://www.mpa-garching.mpg.de/SDSS/DR7/>

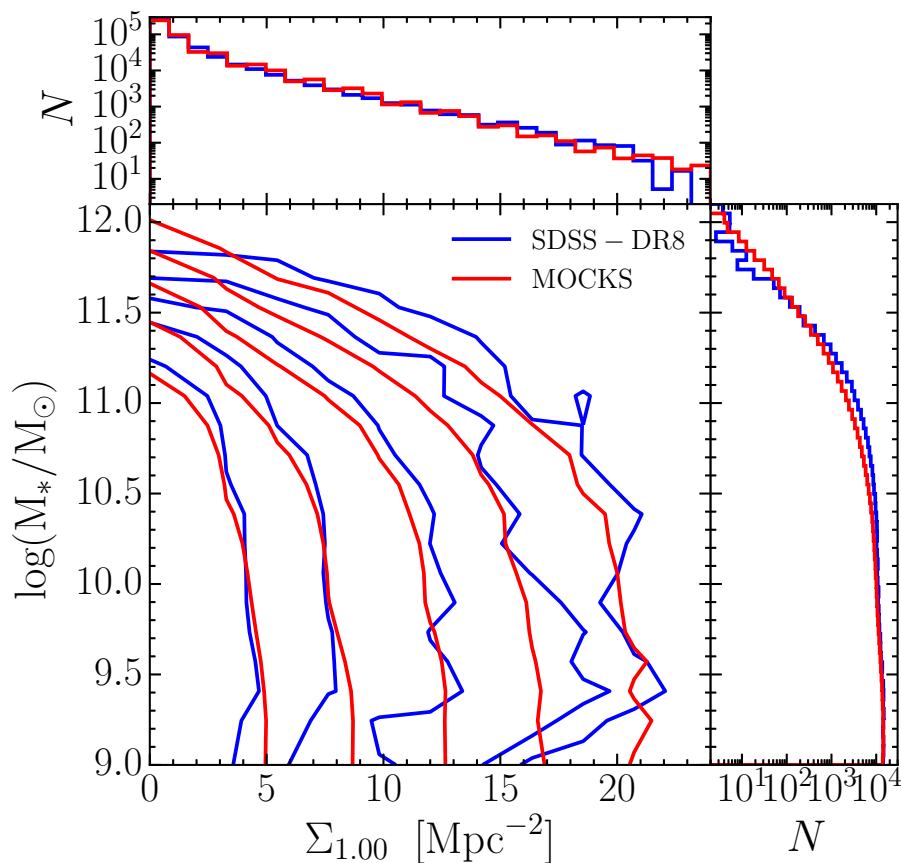


Figure 3.21: Main panel: bivariate distribution of density on the 1.00 Mpc scale and stellar mass for the SDSS sample (blue) and the mock sample (red). The mock contours have been scaled to account for the ratio of volumes between the simulation box and the data. The contours are logarithmically spaced with the outermost contour at 4 objects per bin and the innermost at 300 objects per bin. Upper panels: marginalized distributions of density on the 1.00 Mpc scale for the SDSS and the mock samples. The counts refer to the SDSS sample while the mock histogram has been normalized by the ratio of the volumes. Right-hand panel: same as above but marginalized over the stellar mass.

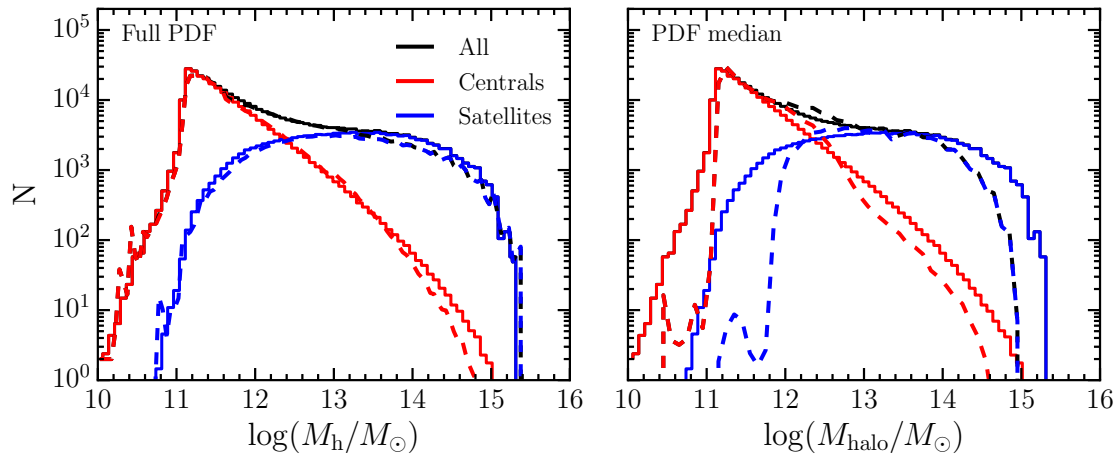


Figure 3.22: Comparison of the halo mass distributions for the mock galaxies (solid histograms) and SDSS galaxies (dashed lines). In the left panel the dashed lines are obtained by summing the full halo mass PDFs for centrals ($P_{M_h|\text{cen}}$, red) and satellites ($P_{M_h|\text{sat}}$, blue) weighted by P_{cen} and P_{sat} for each galaxy. In the right hand panel the dashed lines are obtained from the single value estimator (median value of the PDF given the type) weighted by the probability that a galaxy is of a given type. The black histograms and dashed lines are the sum of the colored.

at the $z = 0$ snapshot of the Millennium simulation. In this case we do not use lightcones but a three dimensional box because of the large area covered by SDSS and the single redshift bin. We also do not degrade the redshift accuracy of mock sample because the redshift of the galaxies in the SDSS sample is estimated from spectroscopic observations. Densities are computed by projecting one of the axes of the box into a redshift axis as described in chapter 2. We set an aperture size of 1 Mpc, a velocity cut $dv = \pm 1000 \text{ km s}^{-1}$, and we compute densities according to equation 3.1.

The model sample does not suffer from spectroscopic incompleteness; on the other hand the distribution of r -band magnitudes does not match perfectly the one obtained from the observations. To overcome both those issues at once we employ a method that iterates on the magnitude limits for the primary and the neighbors samples until the number density and the density distribution of the selected sample match the observational data. Before doing that we need to derive the total number of photometric galaxies in the SDSS DR8 footprint (more precisely in the area followed up by spectroscopy) that would have been observed if fiber collisions were not a limitation. We query the SDSS database for the number of galaxies in the spectroscopic database and the number of galaxies in the photometric database that would satisfy the criteria for spectroscopic follow-up. The ratio of those values is 0.769. Therefore the number density of mock galaxies needs to be $\rho_{\text{mod}} = 1.3 \times \rho_{\text{SDSS,sp}}$ where $\rho_{\text{SDSS,sp}}$ is the number density of primary galaxies in our observational catalog once we account for V_{max} corrections. The absolute magnitude cuts

we set in the models using this iterative method are $M_r < -17.6$ mag and $M_r < -19.0$ mag for the primary and the neighbor samples respectively. We note that these cuts are up to 1 mag deeper than those used in the SDSS sample. This difference arises in a non perfect match of the r -band luminosity function, while stellar mass functions are better matched between the SAM and the SDSS data. Figure 3.21 shows that, with this choice of magnitude limits, both the density and the stellar mass distributions are well matched. This is a critical step to trust our Bayesian approach to halo mass and central/satellite status.

As a last step we assign to each SDSS galaxy (and to model galaxies) a probability that it is central (P_{cen}) or satellite (P_{sat}) and the halo mass PDFs $P_{M_h|\text{cen}}$ and $P_{M_h|\text{sat}}$ as described in section 3.5. We verified in Figure 3.22 that the halo mass distributions of SDSS galaxies obtained either by summing the full halo mass PDFs for centrals and satellites (Left Panel) or using only the median value for each type (Right Panel) agree well with the halo mass of the full mock sample. As shown in section 3.5.3 this is a test of the quality of the halo mass calibration we performed.

3.7 Conclusions

In this work, we have characterized the environment of galaxies in the 3D-HST survey at $z = 0.5 - 3.0$. We used the projected density within fixed apertures coupled with a newly developed method for edge corrections to obtain a definitive measurement of the environment in five well studied deep-fields: GOODS-S, COSMOS, UDS, AEGIS, GOODS-N. Using a recent semi-analytic model of galaxy formation, we have assigned physical quantities describing the properties of dark matter haloes to observed galaxies. Our results can be summarized as follows:

1. The 3D-HST deep fields host galaxies in a wide range of environments, from under-dense regions to relatively massive clusters. This large variety is accurately quantified thanks to a homogeneous coverage of high quality redshifts provided by the 3D-HST grism observations.
2. Our reconstructed density field recovers the previously known massive structures (independently detected from the X-Ray emission of the intracluster/intragroup medium) across the full redshift range analyzed in this work.
3. As described in Chapter 2, a calibration of density into physically motivated quantities (e.g. halo mass, central/satellite status) requires a mock catalog tailored to match the properties of the 3D-HST survey. We developed such a catalog and performed a careful match to the observational sample. As a result, each 3D-HST galaxy is assigned a probability that it is a central or satellite galaxy with an associated probability distribution function of halo mass for each type. This Bayesian approach takes into account sources of contamination in the matching process.

4. Our method also naturally accounts for galaxies in the infalling region of a massive structure or the “backsplash” population of galaxies which would be classified as centrals in the mocks but that have experienced or are experiencing satellite specific processes. Those galaxies, because of their intermediate overdensity in a given aperture are likely to be assigned a roughly equal probability of being centrals or satellites.

The same method has been applied to a Local Universe sample from SDSS. In the next chapter we build on these results to investigate the mechanisms and timescales responsible of satellite quenching from the Local Universe up to $z \sim 2 - 2.5$.

Chapter 4

Satellite quenching efficiency and timescales at $0 < z < 2$

This chapter is based on Fossati et al. (2016), submitted to ApJ

In this chapter we explore the role of environment in quenching the star formation activity of galaxies over $0 < z < 2$ by combining the 3D-HST data at high redshift with the local SDSS sample.

It was first proposed by Baldry et al. (2006) that the fraction of passive galaxies depends both on stellar mass and environment in a separable manner. Peng et al. (2010), using the SDSS and zCOSMOS surveys, extended the independence of those processes to $z \sim 1$. More recently, Peng et al. (2012) interpreted these trends in the local Universe by suggesting that central galaxies are only subject to “mass quenching” while satellites suffer from the former plus an “environmental quenching”. Kovač et al. (2014) similarly found that satellite galaxies are the main drivers of environmental quenching up to $z \sim 0.7$ using zCOSMOS data.

Here, we extend these analysis to higher redshift by exploring the dependence of the fraction of passive galaxies on stellar mass, halo mass (or local density) and central/satellite status in order to derive the efficiency and timescale of environmental quenching.

4.1 Passive fractions as a function of halo mass

The populations of passive and star-forming galaxies are typically separated either by a specific star formation rate cut (e.g. Franx et al., 2008; Hirschmann et al., 2014; Fossati et al., 2015) or by a single color or color-color selection (e.g. Bell et al., 2004; Weiner et al., 2005; Whitaker et al., 2011; Muzzin et al., 2013; Mok et al., 2013). In this work, we use the latter method and select passive and star forming galaxies based on their position in the rest-frame UVJ color-color diagram (Williams et al., 2009). Following Whitaker et al. (2011), passive galaxies are selected to have:

$$(U - V) > 0.88 \times (V - J) + 0.59 \quad (4.1)$$

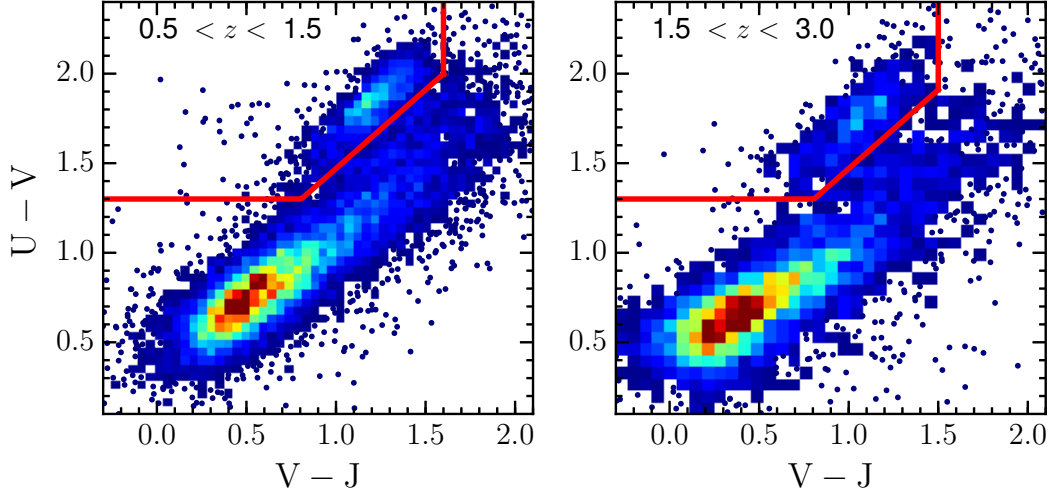


Figure 4.1: Rest-frame UVJ diagram for 3D-HST galaxies in two redshift bins. The color scale represents the density of points. Where the density is low we plot individual galaxies. The solid red line indicates the adopted separation between passive galaxies and star-forming galaxies.

$$(U - V) > 1.3, (V - J) < 1.6 \quad [0.5 < z < 1.5] \quad (4.2)$$

$$(U - V) > 1.3, (V - J) < 1.5 \quad [1.5 < z < 2.0] \quad (4.3)$$

where the colors are rest-frame and are taken from Momcheva et al. (2016). Figure 4.1 shows the distribution of 3D-HST galaxies in the rest frame UVJ color-color plane. The red solid line shows the adopted division between passive and star forming galaxies.

The fractions of passive centrals and satellites in bins of M_* and M_h are computed as the fraction of passive objects in a given stellar mass bin where each galaxy is weighted by its probability of being central or satellite and the probability of being in a given halo mass bin for its type. Algebraically:

$$f_{\text{pass|ty}} = \frac{\sum_i \left(\delta_{\text{pass},i} \times \delta_{M_*,i} \times P_{\text{ty},i} \times \int_{M_h} P_{M_h,i|\text{ty}} dM_h \right)}{\sum_i \left(\delta_{M_*,i} \times P_{\text{ty},i} \times \int_{M_h} P_{M_h,i|\text{ty}} dM_h \right)} \quad (4.4)$$

where ty refers to a given type (centrals or satellites), $\delta_{\text{pass},i}$ is 1 if a galaxy is UVJ passive and 0 otherwise, $\delta_{M_*,i}$ is 1 if a galaxy is in the stellar mass bin and 0 otherwise, $P_{\text{ty},i}$ is the probability that a galaxy is of a given type and $\int_{M_h} P_{M_h,i|\text{ty}} dM_h$ is the halo mass PDF given the type integrated over the halo mass bin limits.

The data points in Figure 4.2 show the passive fractions in two bins of halo mass (above and below $10^{13} M_\odot$) and in three independent redshift bins. The median (log) halo masses for satellites are 12.36, 13.53 at $z = 0.5 - 0.8$ for the lower and higher halo mass bin respectively; 12.41, 13.44 at $z = 0.8 - 1.2$; and 12.43, 13.34 at $z = 1.2 - 1.8$.

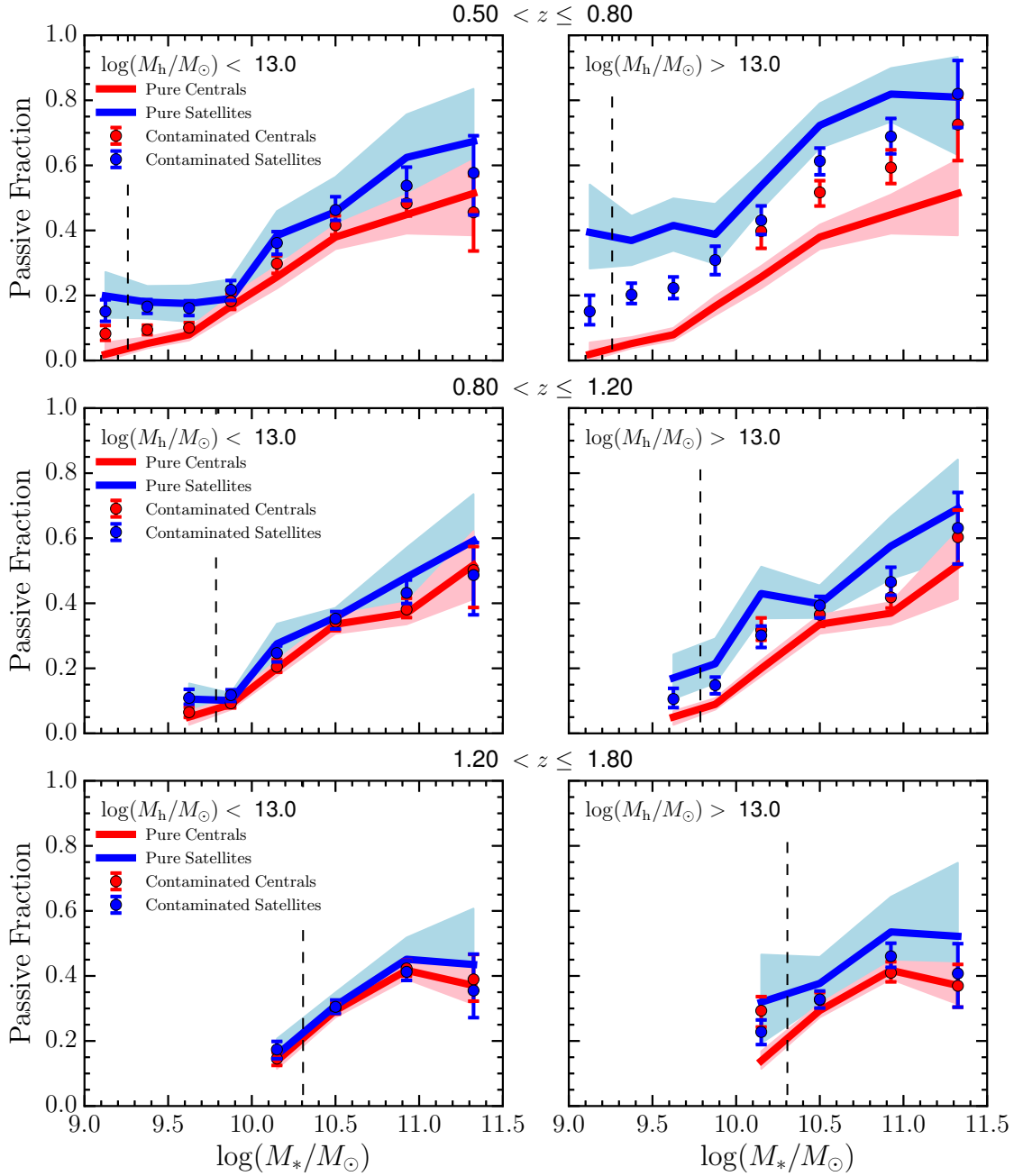


Figure 4.2: Passive fraction for central and satellite galaxies in bins of M_* and M_h in three independent redshift bins. The median (\log) halo masses for satellites are 12.36, 13.53 at $z = 0.5 - 0.8$ for the lower and higher halo mass bin respectively, 12.41, 13.44 at $z = 0.8 - 1.2$, and 12.43, 13.34 at $z = 1.2 - 1.8$. Datapoints show the observed passive fractions with uncertainties derived from Monte Carlo resampling of the mock sample. The thick red line is the passive fraction of a pure sample of central galaxies from the 3D-HST dataset. The thick blue line represents our modelled “pure” passive fraction of satellites (see text for the details of the modelling process). In both cases the shaded regions show the 1σ confidence intervals. The vertical dashed line marks the stellar mass limit of the volume limited sample.

The uncertainties on the data points cannot be easily evaluated assuming Binomial statistics because the number of galaxies contributing to each point is not a priori known. Indeed, $P_{\text{ty},i}$ and $\int_{M_h} P_{M_h,i|ty} dM_h$ act as weights and all galaxies with a stellar mass within the mass bin do contribute to the passive fraction. To assess the uncertainties we use the mock lightcones (where each mock galaxy has been assigned a P_{cen} and P_{sat} and halo mass PDFs as if they were observed galaxies). In a given stellar mass bin we assign each model galaxy to be either passive or active such that the fraction of passive galaxies matches the observed one. Then we randomly select a number of model galaxies equal to the number of observed galaxies in that bin and we compute the passive fraction of this subsample using equation 4.4. We repeat this procedure 50000 times to derive the 1σ errorbars shown in Figure 4.2. This method accounts for uncertainties in the estimate of $P_{\text{ty},i}$ and $\int_{M_h} P_{M_h,i|ty} dM_h$ as well as cosmic variance.

The vertical dashed lines mark the stellar mass completeness limit². Below this mass we limit the upper edge of the redshift slice such that all galaxies in the stellar mass bin are included in a mass complete sample. A stellar mass bin is included only if the covered volume is greater than 1/3 of the total volume of the redshift slice. This typically results in only one stellar mass bin below the completeness limit being included in the analysis.

In the highest halo mass bin of Figure 4.2 at $z = 0.5 - 0.8$, the satellite passive fraction (integrated over all galaxies) is higher than the central passive fraction, with a marginal significance. The same trend can be observed in the other halo mass and redshift bins, although the separation of the observed satellite and central passive fractions becomes more marginal.

In each redshift bin we also identify a sample of “pure” central galaxies ($P_{\text{cen}} > 0.8$, irrespective of overdensity or halo mass), which provides a reference for the passive fraction of galaxies subject only to mass-quenching. The passive fraction of this sample $f_{\text{pass|cen,pure}}(M_*)$ of centrals (which has an average $P_{\text{cen}} = 0.95$) is shown as the thick red line in both halo mass bins.

The separation of the observed satellite passive fraction from that of the pure sample of centrals is more significant (especially at $z < 1.2$). Indeed, the passive fractions derived using equation 4.4 can be strongly affected by impurities in the central/satellite classification and by cross-talk between the two halo mass bins, given that each galaxy can contribute to both bins and types (see equation 4.4). Any contribution of central galaxies to the satellite passive fraction, and vice versa, will reduce the observed difference between the two populations with respect to the “pure”, intrinsic difference.

²The mass limit is derived following Marchesini et al. (2009). In brief we use the 3D-HST photometric catalog (down to $JH_{140} = 25\text{mag}$) and we scale the stellar masses of the galaxies as if they were at the sample limit of $JH_{140}=24\text{ mag}$. The scatter of the points is indicative of the M/L variations in the population at a given redshift. We then take the upper 95th percentile of the distributions as a function of redshift as the stellar mass limit.

Parameter	Range	Nbins	Prior
$\log M_{\text{br,lo}}$	11,15	80	Uniform
$\log M_{\text{br,hi}}$	11,15	80	Uniform
$P_{\text{pass,hi}}$	0.0,1.0	100	Gaussian (if $P_{\text{pass,hi}} \leq f_{\text{pass cen,pure}}$) Uniform (if $P_{\text{pass,hi}} > f_{\text{pass cen,pure}}$)

Table 4.1: Table of the model parameters.

4.2 Recovering the “pure” passive fractions for satellite galaxies

In order to recover the “pure” passive fraction for satellite galaxies as a function of halo mass, we perform a parametric model fitting to our dataset.

We start by parametrizing the probability of a satellite galaxy being passive independently in each stellar mass bin as a function of log halo mass, using a broken function characterized by a constant value ($P_{\text{pass,lo}}$) below the lower break ($M_{\text{br,lo}}$) and another constant value ($P_{\text{pass,hi}}$) above the upper break ($M_{\text{br,hi}}$). In between the breaks, the passive fraction increases linearly. Algebraically, this 4-parameter function is defined as:

$$P_{\text{pass|sat}}(M_{\text{h}}) = \begin{cases} P_{\text{pass,lo}} & \text{if } M_{\text{h}} \leq M_{\text{br,lo}} \\ m \times (\log \frac{M_{\text{h}}}{M_{\text{br,lo}}}) + P_{\text{pass,lo}} & \text{if } M_{\text{br,lo}} < M_{\text{h}} \leq M_{\text{br,hi}} \\ P_{\text{pass,hi}} & \text{if } M_{\text{h}} > M_{\text{br,hi}} \end{cases} \quad (4.5)$$

where $m = (P_{\text{pass,hi}} - P_{\text{pass,lo}}) / (\log(M_{\text{br,hi}}) - \log(M_{\text{br,lo}}))$.

This function is chosen to allow for a great degree of flexibility. We make the assumption that satellite galaxies are not subject to environmental quenching below $M_{\text{br,lo}}$, and therefore treat $P_{\text{pass,lo}}$ as a nuisance parameter of the model with a Gaussian prior centered on the observed passive fraction of pure centrals $f_{\text{pass|cen,pure}}(M_*)$ and a sigma equal to its uncertainty. For $P_{\text{pass,hi}}$, instead we assume a semi-Gaussian prior with the same center and sigma as above, but only extending below the observed passive fraction of central galaxies (this implies that satellites are affected by the same mass-quenching as centrals). Above this value we assume a uniform prior. For the break masses we assume uniform priors. Table 4.1 summarizes the model parameters, their allowed range, and the number of bins in which the range is divided to compute the posterior.

The probability that each 3D-HST galaxy, i is passive is:

$$P_{\text{pass},i} = P_{\text{cen},i} \times P_{\text{pass|cen}} + P_{\text{sat},i} \times \int_{M_{\text{h}}} P_{M_{\text{h}}|i|\text{sat}} \times P_{\text{pass|sat}} dM_{\text{h}} \quad (4.6)$$

where $P_{\text{pass|sat}}$ is from equation 4.5 and $P_{\text{pass|cen}} = f_{\text{pass|cen,pure}}$.

The likelihood space that the star forming or passive activity of 3D-HST galaxies in a

stellar mass bin is reproduced by the model is computed as follows:

$$\mathcal{L} = \prod_i \begin{cases} P_{\text{pass},i} & \text{if } i \text{ is UVJ passive} \\ 1 - P_{\text{pass},i} & \text{if } i \text{ is not UVJ passive} \end{cases} \quad (4.7)$$

We compute the posterior on a regular grid covering the parameter space.

Figure 4.3 presents the constraints on the model parameters (marginalised over the nuisance parameter $P_{\text{pass|cen}}$) for a single stellar mass and redshift bin. The panels along the diagonal show the marginalised posterior distributions for each of the three parameters ($M_{\text{br,lo}}, M_{\text{br,hi}}, P_{\text{pass,hi}}$). The red solid lines show the median value of each parameter, and the black dashed lines show the 1σ confidence intervals. The off-diagonal panels show the marginalised posterior distributions for a pair of model parameters. The black contours show the 1σ , 1.5σ , and 2σ confidence intervals. The fits for the other stellar mass bins give qualitatively similar results.

We then sample the posterior distribution and we apply the model described in equation 4.5 to obtain the median value of $P_{\text{pass|sat}}$ and its 1σ uncertainty as a function of halo mass. Lastly, we assign the probability of being passive to mock satellites in each stellar mass bin according to their model halo mass, and we compute the average passive fraction in the two halo mass bins (above and below $10^{13}M_{\odot}$). This results in the thick blue ($f_{\text{pass|sat,pure}}(M_*)$) lines with 1σ confidence intervals plotted as shaded regions in Figure 4.2.

Figure 4.4 shows the median value (thick blue lines) of $P_{\text{pass|sat}}$ as a function of log halo mass and 1σ confidence intervals in each stellar mass bin. Despite the significant covariance of the model parameters, the shape of the passive fraction models for satellites is well determined. The horizontal black lines show the halo mass range that includes 90% of the satellites in each stellar mass bin.

The average passive fractions in the two halo mass bins above and below $10^{13}M_{\odot}$, presented as the thick blue lines in Figure 4.2, are shown for each stellar mass bin in Figure 4.4 by the black points. The red lines are the predictions from a quenching time independent of halo mass (see Section 4.5 for the details).

We verify that the separation seen in the pure passive fractions in Figure 4.2 is real. To do so we randomly shuffle the position in the UVJ diagram for galaxies in each stellar mass bin (irrespective of environmental properties) to break any correlation between passive fraction and environment. Then we compute the observed passive fractions of centrals and satellites, and for the pure sample of centrals and we perform again the model fitting procedure.

At $0.5 < z < 0.8$ we find that the pure satellite passive fraction is inconsistent with the null hypothesis (no satellite quenching) at a $\gtrsim 2\sigma$ level in each stellar bin at high halo mass and 7 out of 8 stellar mass bins at low halo mass. The combined probability of the null hypothesis is $P < 10^{-10}$ in either halo mass bin. The difference is smaller, but still very significant ($P \lesssim 10^{-5}$) at $0.8 < z < 1.2$. At $1.2 < z < 1.8$ the hypothesis of no satellite quenching is acceptable ($P \sim 0.4$) in the low halo mass bin, while it can be ruled out ($P \lesssim 10^{-5}$) at higher halo mass.

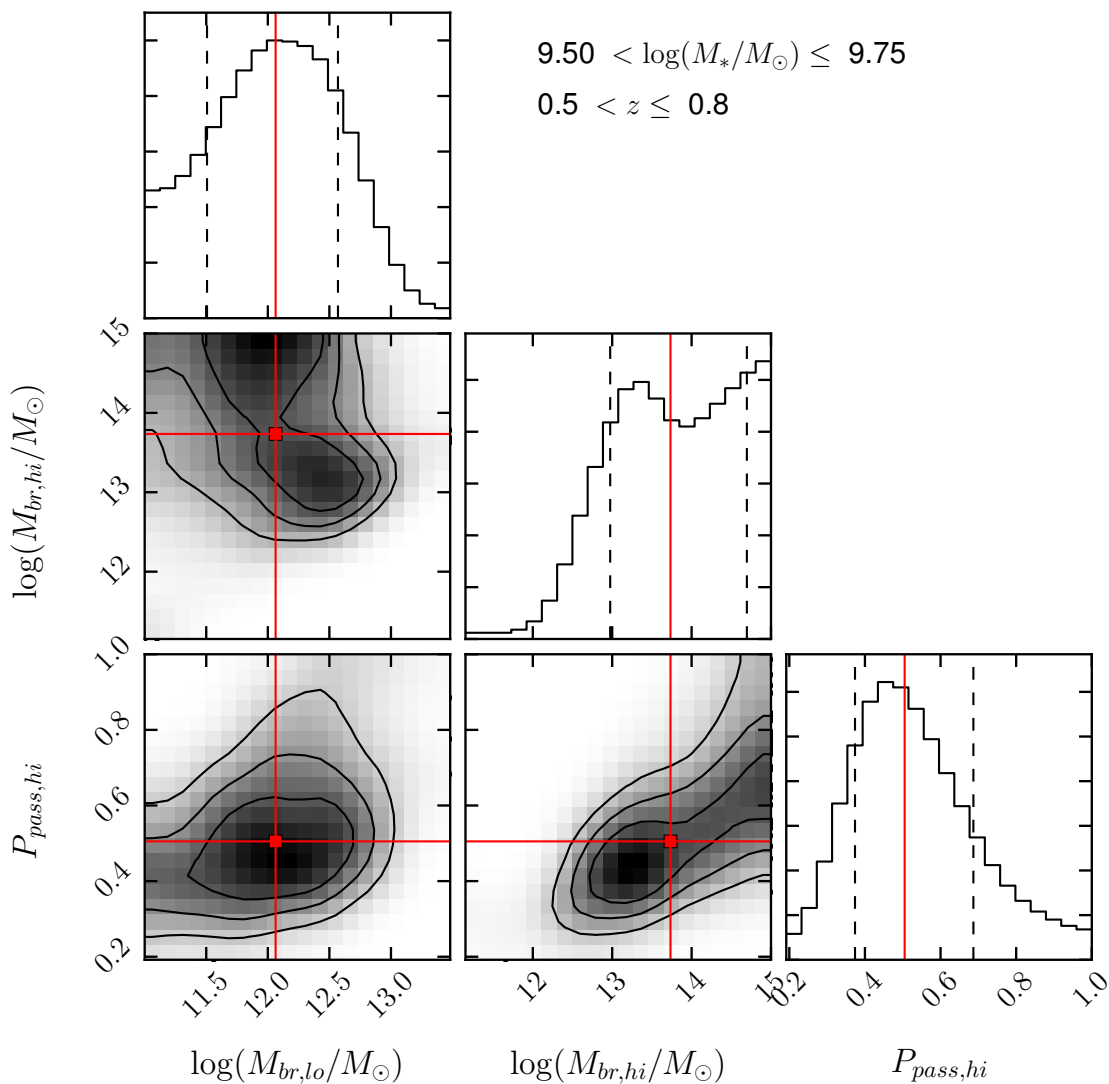


Figure 4.3: Marginalized likelihood distributions for individual model parameters (panels along the diagonal) and marginalized maps for pairs of parameters, for the stellar mass bin $9.50 < \log(M_*/M_\odot) \leq 9.75$ and redshift bin $0.5 < z \leq 0.8$. The red lines show the median value for each parameter (which may be distinct from the global maximum likelihood value). The vertical dashed lines in the histograms show the 1σ confidence intervals. The black contours in the two dimensional maps show the 1σ , 1.5σ , and 2σ confidence intervals.

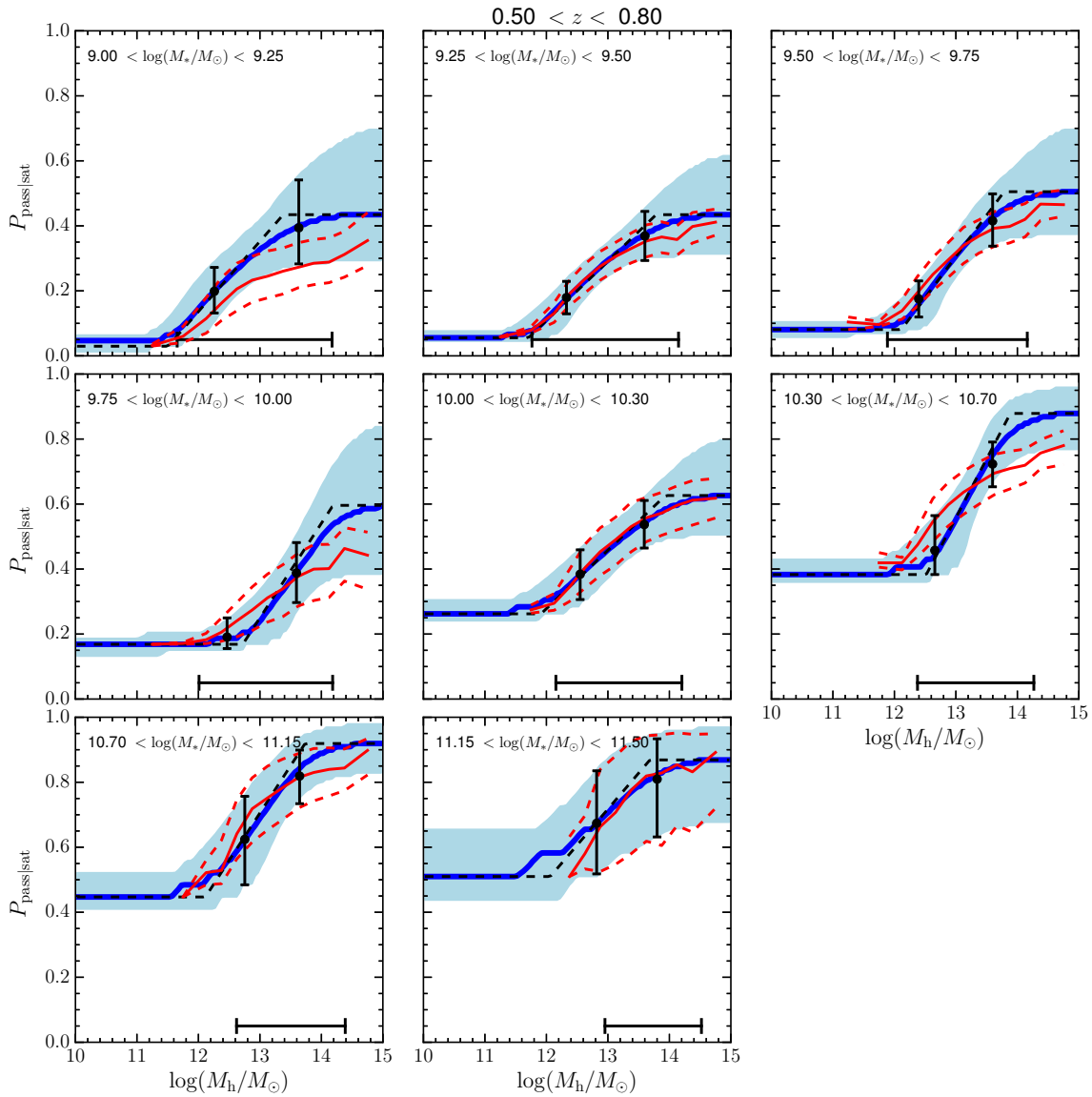


Figure 4.4: Median (thick blue lines) and 1σ confidence intervals (shaded areas) of the probability that a satellite galaxies is passive ($P_{\text{pass|sat}}$) as a function of halo mass from our fitting method in different stellar mass bins at $0.5 < z \leq 0.8$. The black dashed line is the best fit model with values obtained from the marginalised distributions in each parameter. The horizontal black lines show the halo mass range that includes 90% of the satellites in each stellar mass bin. The black points with errorbars show the average value of $P_{\text{pass|sat}}$ (and its 1σ uncertainty) for galaxies in haloes above and below $10^{13} M_\odot$. The red lines are the median prediction (solid) and 1σ confidence intervals (dashed lines) for $P_{\text{pass|sat}}$ under the assumption of a quenching timescale independent of halo mass. In most of the stellar mass bins this assumption well reproduces the best fit of $P_{\text{pass|sat}}$.

Van der Burg et al. (2013), Kovač et al. (2014), and Balogh et al. (2016) have found that the environment plays an important role in determining the star formation activity of satellites, at least up to $z \sim 1$. However these works have only probed relatively massive haloes ($M_{\text{halo}} \gtrsim 10^{13} M_{\odot}$). The depth of the 3D-HST sample allows us, for the first time, to extend these results to higher redshift, to lower mass galaxies and to lower mass haloes.

4.3 Passive fraction as a function of density

Halo mass is the parameter which most easily allows the interpretation of environmental effects across cosmic time. It also allows for easier and less biased comparisons across different works. Moreover it can be directly linked to models (either semi-analytic or hydrodynamical) allowing a better understanding of which physical processes are most relevant at different halo masses. Density, on the other hand, depends on the depth (and to some extent the observing strategy) of each survey. Detailed and quantitative comparisons are also made difficult by different approaches to density (e.g., Muldrew et al., 2012; Haas et al., 2012; Etherington & Thomas, 2015). However it is a parameter directly obtained from the observed redshift space coordinates of the population of galaxies under investigation. In this respect it is less sensitive to the quality and uncertainties in the calibration of halo mass.

We derive the passive fraction of galaxies in two bins of density and compare them to those obtained in Figure 4.2 using halo mass. The observed fractions of passive centrals and satellites in bins of M_* and density contrast $\log(1 + \delta_{0.75})$ are given by

$$f_{\text{pass|ty}} = \frac{\sum_i (\delta_{\text{pass},i} \times \delta_{M_*,i} \times \delta_{\log(1+\delta_{0.75}),i} \times P_{\text{ty},i})}{\sum_i (\delta_{M_*,i} \times \delta_{\log(1+\delta_{0.75}),i} \times P_{\text{ty},i})} \quad (4.8)$$

where ty refers to a given type (centrals or satellites), $\delta_{\text{pass},i}$ is 1 if a galaxy is UVJ passive and 0 otherwise, $\delta_{M_*,i}$ is 1 if a galaxy is in the stellar mass bin and 0 otherwise, $\delta_{\log(1+\delta_{0.75}),i}$ is 1 if a galaxy is in the density bin and 0 otherwise, and $P_{\text{ty},i}$ is the probability that a galaxy is of a given type. In this equation the only uncertain property for each object is its central/satellite status, while the cross talk between multiple density bins is not present (as it was for halo mass).

We therefore perform a simpler decontamination procedure. For each density, stellar mass and redshift bin, we assign to real centrals in the mocks a probability of being passive equal to the passive fraction of the pure sample of observed central galaxies $f_{\text{pass|cen,pure}}(M_*, \delta_{0.75})$, while the passive fraction of satellites $f_{\text{pass|sat,pure}}(M_*, \delta_{0.75})$ is a free parameter. Then we use equation 4.8 to compute the observed passive fractions for mock galaxies (therefore contaminating the “pure” values). We solve for $f_{\text{pass|sat,pure}}(M_*, \delta_{0.75})$ by maximising the likelihood that the contaminated passive fractions for mock galaxies match the observed passive fractions (jointly for centrals and satellites). This procedure is repeated 500 times in a Monte Carlo fashion in order to propagate the uncertainties on the datapoints to the “pure” (decontaminated) passive fractions.

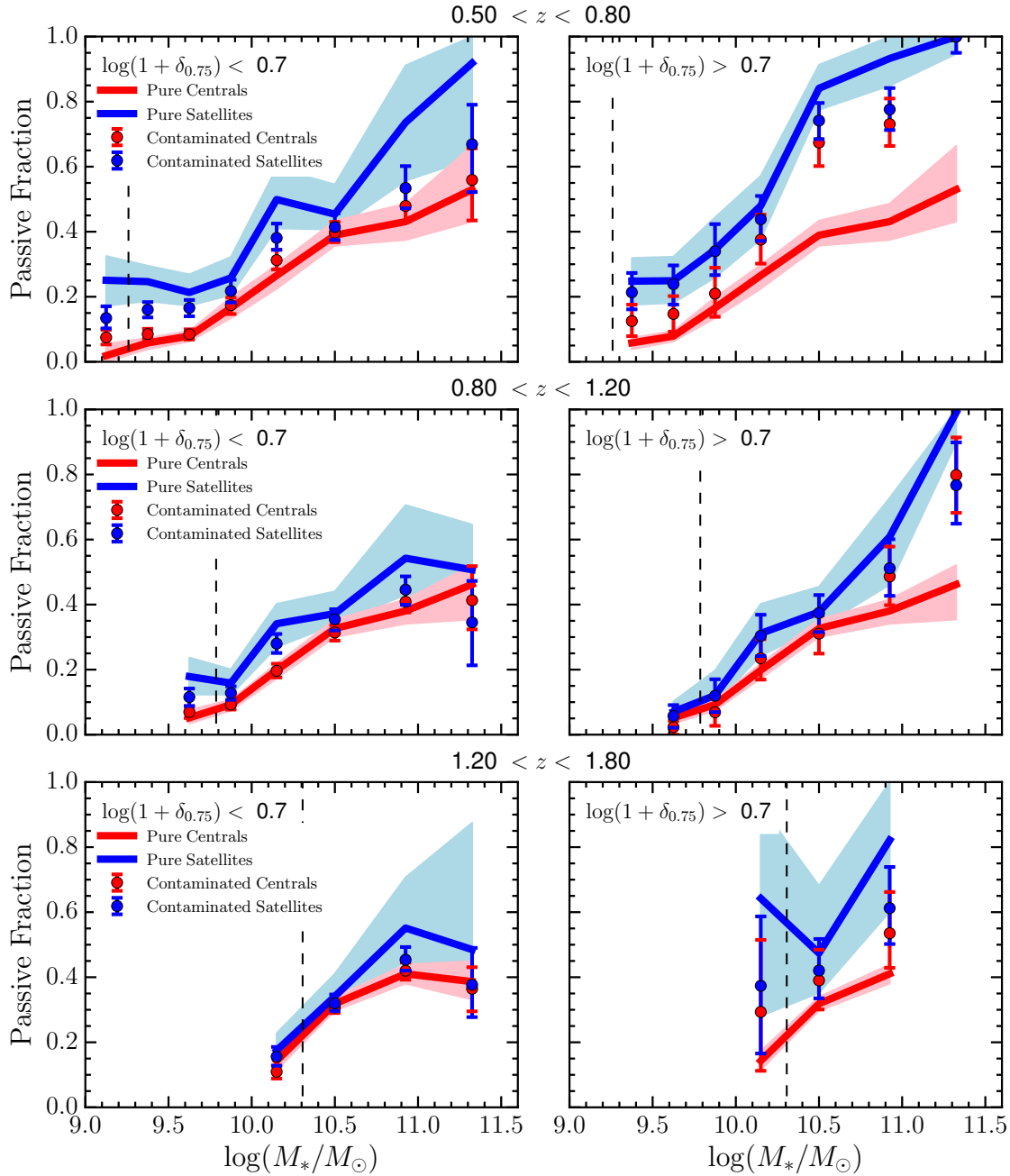


Figure 4.5: Passive fraction for central and satellite galaxies in bins of M_{star} , density contrast $\log(1 + \delta_{0.75})$, and redshift. Datapoints are the observed passive fractions with uncertainties derived from Monte Carlo resampling of the mock sample. Thick blue and red lines are the “pure” passive fractions with 1σ confidence intervals as shaded regions. The vertical dashed line marks the stellar mass of the volume limited sample.

The decontaminated values of the passive fraction for centrals and satellites shown in Figure 4.5 are qualitatively similar to those obtained in bins of halo mass in the same redshift slices (see Figure 4.2).

We conclude that the passive fraction dependence for satellite galaxies, when binned on local density, is similar to that in bins of halo mass, where density is a more directly observed quantity. In what follows we therefore use the halo mass as the main parameter describing the environment.

4.4 Satellite quenching efficiency

In order to further understand the increased passive fractions for satellite galaxies as a function of stellar and halo mass, we compute the “conversion fractions” as first introduced by van den Bosch et al. (2008). This parameter, sometimes called the satellite quenching efficiency, quantifies the fraction of galaxies that had their star formation activity quenched by environment specific processes since they accreted as satellites into a more massive halo (see also Kovač et al., 2014; Hirschmann et al., 2014; Balogh et al., 2016). It is defined as:

$$f_{\text{conv}}(M_*, M_h) = \frac{f_{\text{pass|sat,pure}}(M_*, M_h) - f_{\text{pass|cen,pure}}(M_*)}{1 - f_{\text{pass|cen,pure}}(M_*)} \quad (4.9)$$

where $f_{\text{pass|sat,pure}}(M_*, M_h)$ and $f_{\text{pass|cen,pure}}(M_*)$ are the corrected fractions of quenched centrals and satellites in a given bin of M_* and M_h obtained as described above.

In equation 4.9 we compare the sample of centrals at the same redshift as the satellites. This builds on the assumption that the passive fraction of central galaxies only depends on stellar mass and that the effects of mass and environment are independent and separable. The conversion fraction then represents the fraction of satellites which are quenched due to environmental processes above what would happen if those galaxies would have evolved as centrals of their haloes. A different approach would be to compare the passive fraction of satellites to that of centrals at the time of infall in order to measure the total fraction of satellites quenched since they were satellites (e.g., Wetzel et al., 2013; Hirschmann et al., 2014). However this measurement includes the contribution of mass-quenched satellite galaxies, which we instead remove under the assumption that the physical processes driving mass quenching do not vary in efficiency when a galaxy becomes a satellite.

We also caution the reader that equation 4.9 has to be taken as a simplification of reality as it does not take into account differential mass growth of centrals and satellites which can be caused by tidal phenomena in dense environments or different star formation histories.

Figure 4.6 shows the conversion fractions in the same bins of M_* , M_h and redshift as presented in Figure 4.2. Previous results from galaxy groups and clusters from Knobel et al. (2013), and Balogh et al. (2016) are plotted in our higher halo mass bin (colored points with errorbars). We also add the conversion fractions from Kovač et al. (2014) obtained from zCOSMOS data as a function of local galaxy overdensity. We plot their overdensity bins above the mean overdensity in our higher halo mass bin and the others in our lower

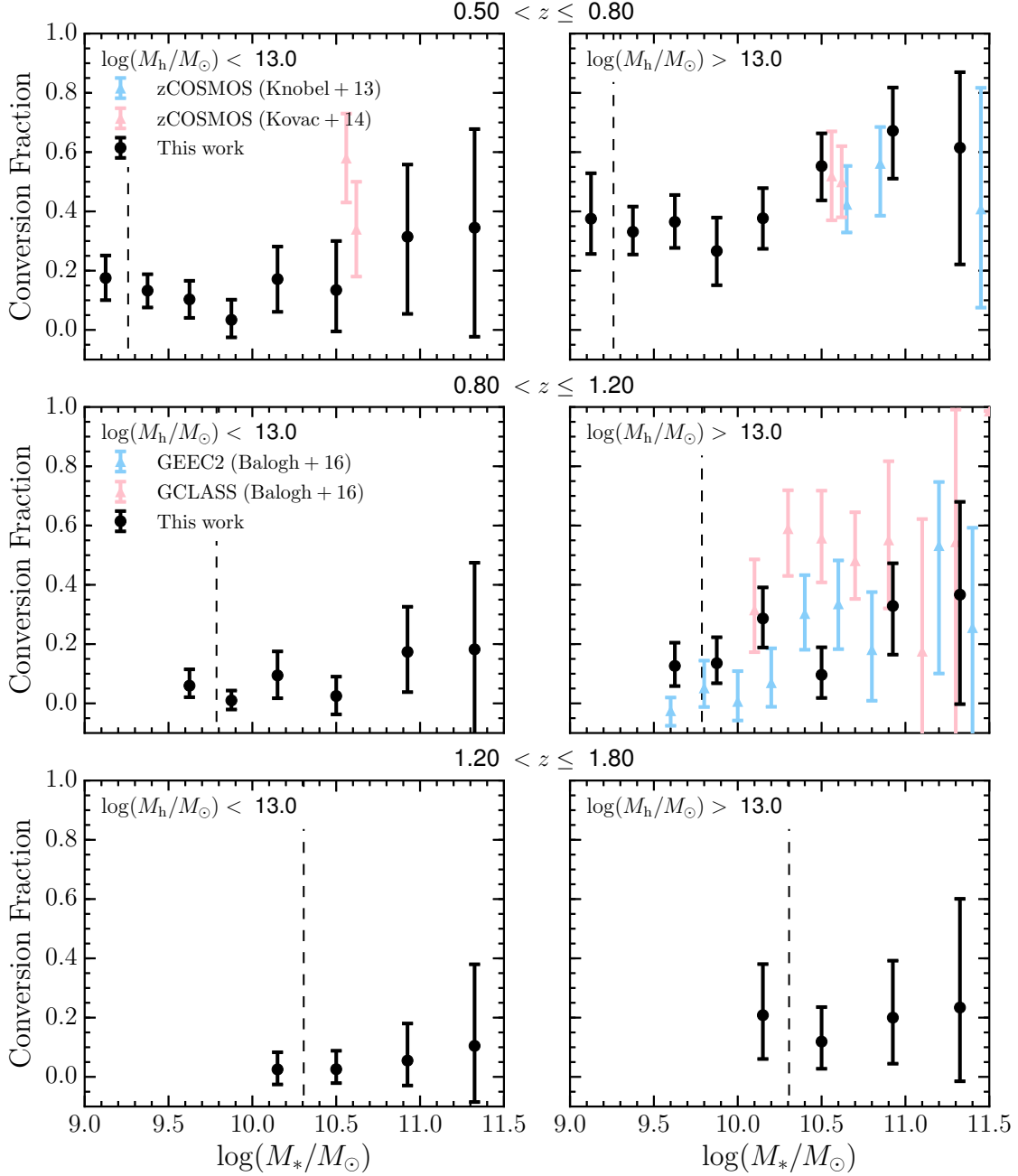


Figure 4.6: Conversion fractions for satellite galaxies in bins of M_* and M_h obtained from equation 4.9 in three independent redshift bins. Black points are from this work and the 1σ errorbars are propagated from the uncertainties on the passive fractions using a Monte Carlo technique. Colored points are from previous studies in the same redshift range. We note a good agreement with our measurements despite different passiveness criteria and environment estimates. The vertical dashed line marks the stellar mass limit of the volume limited sample.

halo mass bin following the overdensity to halo mass conversion given in Kovač et al. (2014). The agreement of our measurements with other works is remarkable considering that different techniques to define the environment (density and central/satellite status) and passiveness are used in different works.

The satellite quenching efficiency tends to increase with increasing stellar mass and to decrease with increasing redshift at fixed stellar mass. In the lower halo mass bin, we note the presence of similar trends as at higher halo masses although the uncertainties are larger due to the smaller number of satellites. In our probabilistic approach this is due to the lower P_{sat} in low density environments as shown in Figure 3.16. Moreover, f_{conv} is poorly constrained at $M_* > 10^{11} M_{\odot}$ due to small number statistics of high mass satellites in the 3D-HST fields.

4.5 Quenching timescales

A positive satellite conversion fraction can be interpreted in terms of a prematurely truncated star formation activity in satellite galaxies compared to field centrals of similar stellar mass. The timescales over which this transformation happens (T_{quench}) can be estimated by assuming that galaxies which have been satellites for longer times are more likely to be quenched (Balogh et al., 2000; McGee et al., 2009; Mok et al., 2014). This can be interpreted as happening (on average) a certain amount of time after satellite galaxies cease to accrete material (including gas) from the cosmic web (see Section 4.7).

Quenching timescales can be obtained if we know the distribution of T_{sat} for satellite galaxies, which we define as the time the galaxy has spent as a satellite of haloes of any mass since its first infall (e.g., Hirschmann et al., 2014). For each bin of M_* , M_h , and redshift we select all satellite galaxies in our mock lightcones which define the distribution of T_{sat} . Then we select as the quenching timescale the percentile of this distribution which corresponds to $1 - f_{\text{conv}}(M_*, M_h)$. This method builds on the assumption that the infall history of observed satellites is well reproduced by the SAM. Systematic uncertainties can arise in the analytic prescriptions used for the dynamical friction timescale of satellites whose parent halo has been tidally stripped in the N-body simulation below the minimum mass for its detection (the so-called “orphan galaxies”). When this time is too short, too many satellites merge with the central galaxy and are removed from the sample, and vice-versa when the time is too long. De Lucia et al. (2010) explored the dynamical friction timescale in multiple SAMs, finding a wide range of timescales. However a dramatically wrong dynamical friction recipe impacts the fraction of satellites, the stellar mass functions, and the density-mass bivariate distribution, which we found to be well matched between the mocks and the observations.

In principle low stellar mass galaxies ($M_* < 10^{10} M_{\odot}$) are more affected by the resolution limit of the simulation and their derived quenching timescales might be subject to a larger uncertainty compared to galaxies of higher stellar mass. We verified that this is not the case by comparing the distribution of T_{sat} in two redshift snapshots ($z = 1.04$ and $z = 2.07$) of Henriques et al. (2015) built on the Millennium-I and the Millennium-II simulations.

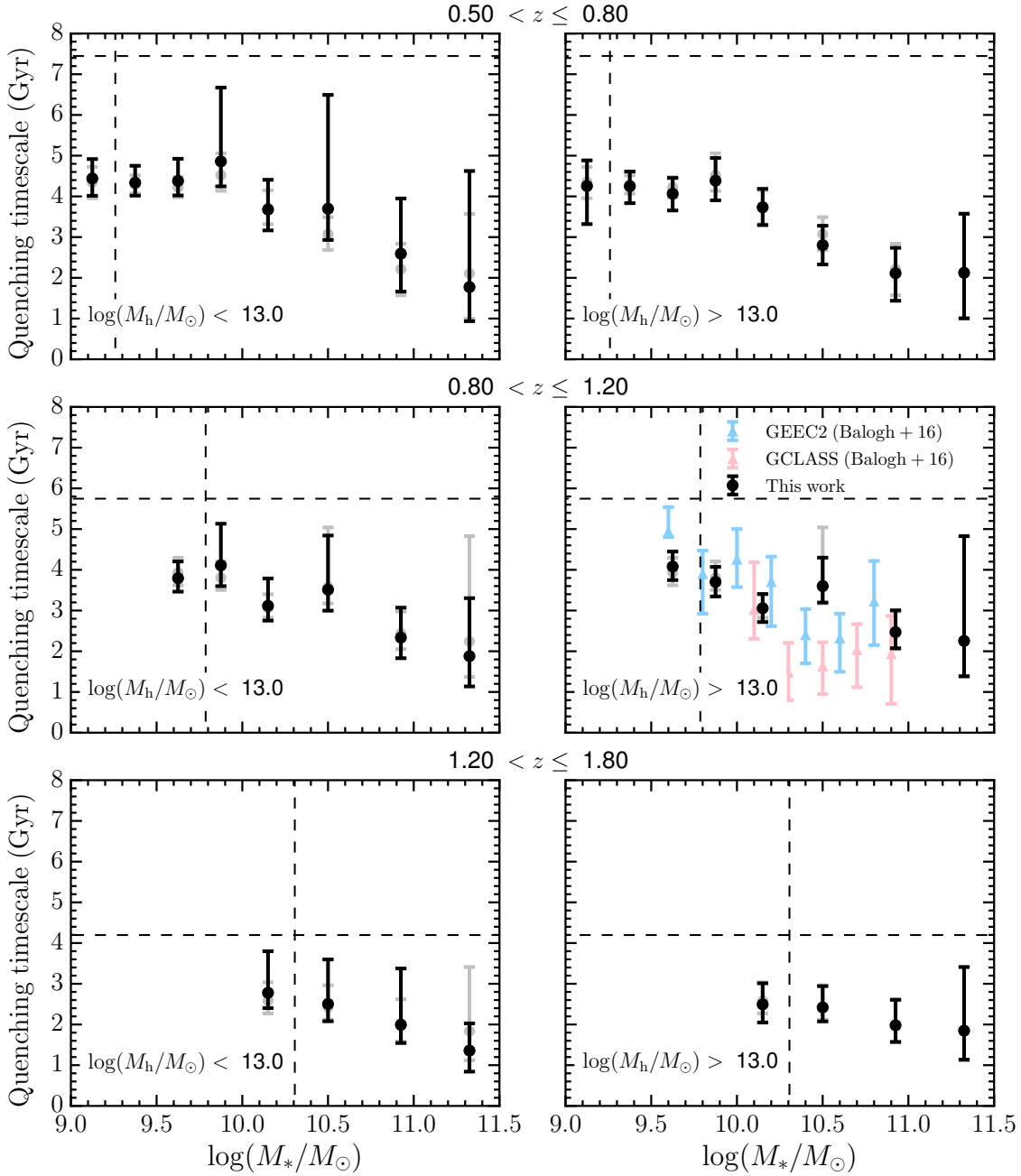


Figure 4.7: Quenching times for satellite galaxies in bins of M_* and M_h obtained from the distributions of T_{sat} from the mock sample. Quenching times are obtained under the assumption that the galaxies which have been satellites the longest are those which have been environmentally quenched. Black points are from this work, while colored points are from previous studies in the same redshift and halo mass range. The gray points are obtained from our sample without separating the dataset in two halo mass bins, and are therefore identical in the left and right panels. The vertical dashed line marks the stellar mass limit of the volume limited sample. The horizontal dashed line is the age of the Universe at the central redshift of each bin.

The latter is an N-body simulation started from the same initial conditions of the original Millennium run but with a higher mass resolution at the expense of a smaller volume. The higher resolution means that the sub-halos hosting low mass satellite galaxies, which can be tidally stripped, are explicitly tracked to lower mass and later times: while these are detected the recipe for dynamical friction is not invoked. We obtain consistent quenching timescales for Millennium-I and Millennium-II based mock catalogs, and therefore we conclude that the analytical treatment of orphan galaxies does not bias our results.

Figure 4.7 shows our derived quenching timescales (black points) in the same bins of M_* and M_h and redshift as presented in Figures 4.2 and 4.6. The observed trend of f_{conv} with stellar mass that is found in both redshift bins turns into a trend of T_{quench} . Quenching timescales increase to lower stellar mass in all redshift and halo mass bins, mainly a consequence of the decreasing conversion fraction. This parameter ranges from $\sim 4-5$ Gyr for low mass galaxies to < 2 Gyr for the most massive ones, and is in agreement with that found by Balogh et al. (2016).

Remarkably, the dependence of quenching timescale on halo mass is very weak. We overplot in each panel, as gray symbols, the quenching timescales obtained from our sample with the same procedure described above but without separating the data in two halo mass bins. In most of the stellar mass bins we find a good agreement, within the uncertainties, between the black and the gray points.

We add in Figure 4.4 an additional test of the result presented in Section 4.5 that the quenching time is largely independent of halo mass. We compute a single quenching time per stellar mass bin without binning the data in halo mass. Then we compute which fraction of mock galaxies have $T_{\text{sat}} > T_{\text{quench}}$ as a function of halo mass. This is converted in a probability of being passive as a function of halo mass which we show as solid red lines (with 1σ confidence intervals as dashed lines) in Figure 4.4. The agreement with the best fit values of $P_{\text{pass}|\text{sat}}$ is remarkable in most of the stellar mass bins, further supporting the result of a quenching timescale that is independent of halo mass.

The lack of a strong halo mass dependence is a consequence of the typically shorter time since infall for satellite galaxies in lower mass halos which largely cancels the lower conversion fraction in low mass halos, and suggests that the physical process responsible for the premature suppression of star formation in satellite galaxies (when the Universe was half of its present age) is largely independent of halo mass.

A mild redshift evolution is also seen when comparing the redshift bins: passive satellites at higher redshift are quenched on a shorter timescale.

4.6 Redshift evolution of the quenching timescales

Figure 4.8 shows the passive fraction, conversion fraction and quenching times as a function of stellar mass, and in two bins of halo mass for the $z = 0$ sample drawn from SDSS as described in Section 3.6. The pure passive fractions of central and satellite galaxies are derived using the same procedure we applied to the high redshift sample. For this sample, passive galaxies are selected using the specific star formation rate ($sSFR$) as a tracer. For

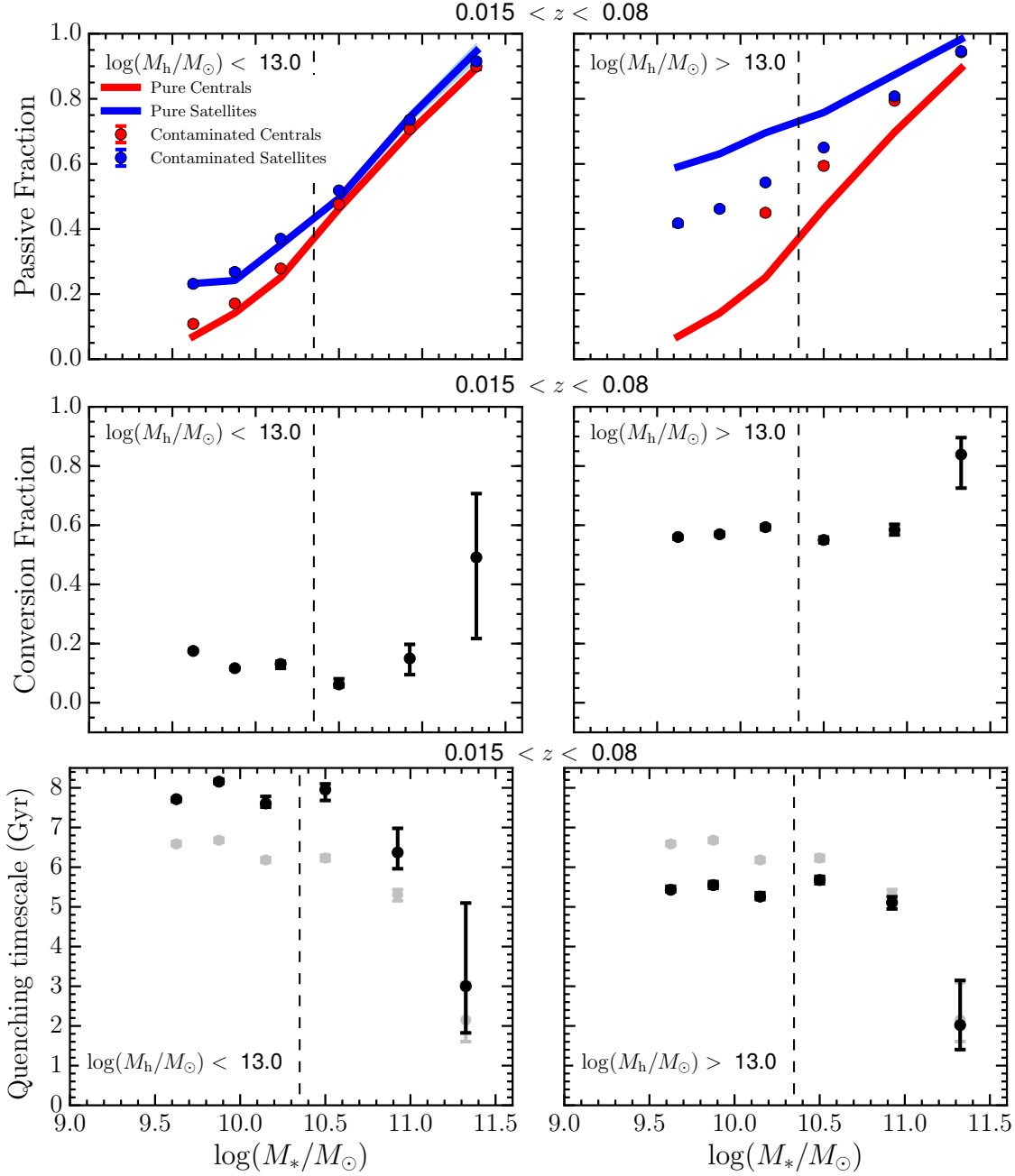


Figure 4.8: Top Panels: passive fraction for central and satellite galaxies in bins of M_* and M_{halo} for the SDSS sample. The median (\log) halo masses for satellites are 12.39, 13.77 for the lower and higher halo mass bin respectively. Points and lines are color coded as in Figure 4.2. Middle panels: conversion fractions for satellite galaxies in bins of M_* and M_h obtained from equation 4.9 for the SDSS sample. Bottom Panels: quenching times for satellite galaxies in bins of M_* and M_h for the SDSS sample.

consistency with previous studies (e.g. Hirschmann et al., 2014) we define passive galaxies those with $sSFR < 10^{-11}\text{yr}^{-1}$. We note that this corresponds to a ~ 1 dex offset from the main sequence of star forming galaxies at $z = 0$, which is consistent with the division of UVJ star forming from UVJ passive galaxies adopted in section 4.1. Moreover, V_{max} corrections are available for each galaxy, therefore we do not need to set a redshift cut that defines a volume limited sample. However we restrict to stellar masses above $10^{9.5}M_{\odot}$ to avoid including low mass galaxies with too large V_{max} corrections. The qualitative trends of conversion fraction and quenching timescales as a function of stellar mass are similar to the 3D-HST sample. Quenching times are longer at $z = 0$ than at higher redshift, and a halo mass dependence is observable (shorter T_{quench} in more massive haloes).

We now investigate the redshift evolution of conversion fractions and quenching times from $0 < z < 2$ by combining the 3D-HST sample with the SDSS sample, and discuss the physical mechanisms that can produce the observational evidence presented so far.

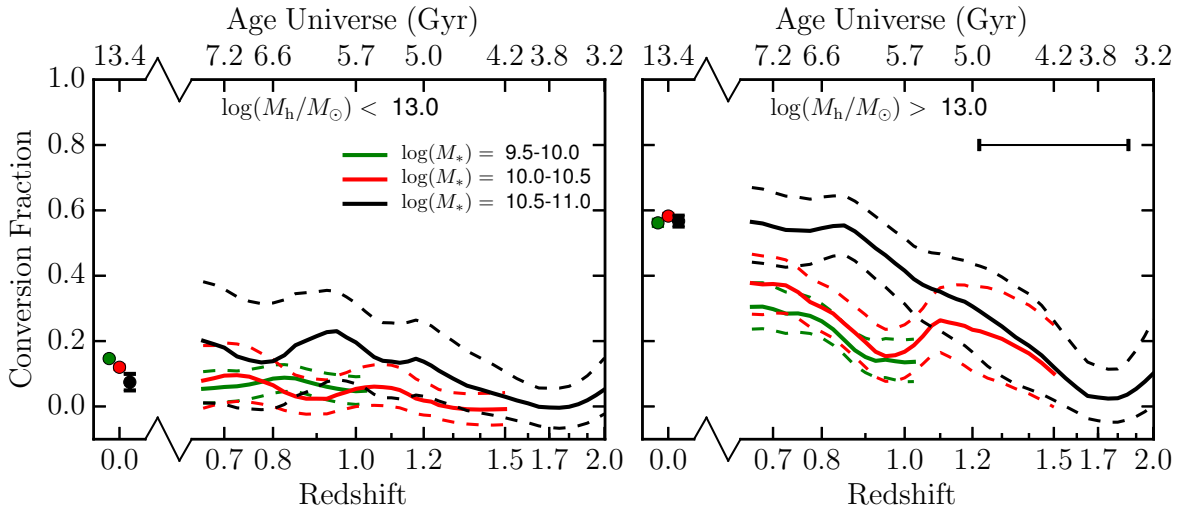


Figure 4.9: Conversion fractions for satellite galaxies as a function of redshift in bins of M_* and M_h (solid lines). Dashed lines mark the 1σ confidence levels. The horizontal error bar is the span of the redshift bins (for the 3D-HST sample) which is constant in $\Delta z/(1+z) = 0.2$ where Δz is the width of the redshift bin and z its center. Datapoints at $z = 0$ are from the SDSS sample and are offset along the x-axis for clarity if they overlap.

Figures 4.9 and 4.10 show the evolution of the conversion fraction and the quenching timescale from redshift 0 to 2. We now concentrate on three bins of stellar mass, each of 0.5 dex in width, and ranging from $10^{9.5}M_{\odot}$ to $10^{11}M_{\odot}$.

Given that f_{conv} (and consequently T_{quench}) are poorly constrained at $M_* > 10^{11}M_{\odot}$ due to the low number statistics of massive satellites, we exclude more massive galaxies from these plots. Similarly, galaxies at $M_* < 10^{9.5}M_{\odot}$ are only included in the mass limited sample at the lowest end of the redshift range under study, therefore the redshift evolution of f_{conv} , and T_{quench} cannot be derived for those low mass galaxies. A stellar mass bin appears in Figures 4.9 and 4.10 only if the stellar mass range above the mass limit is more

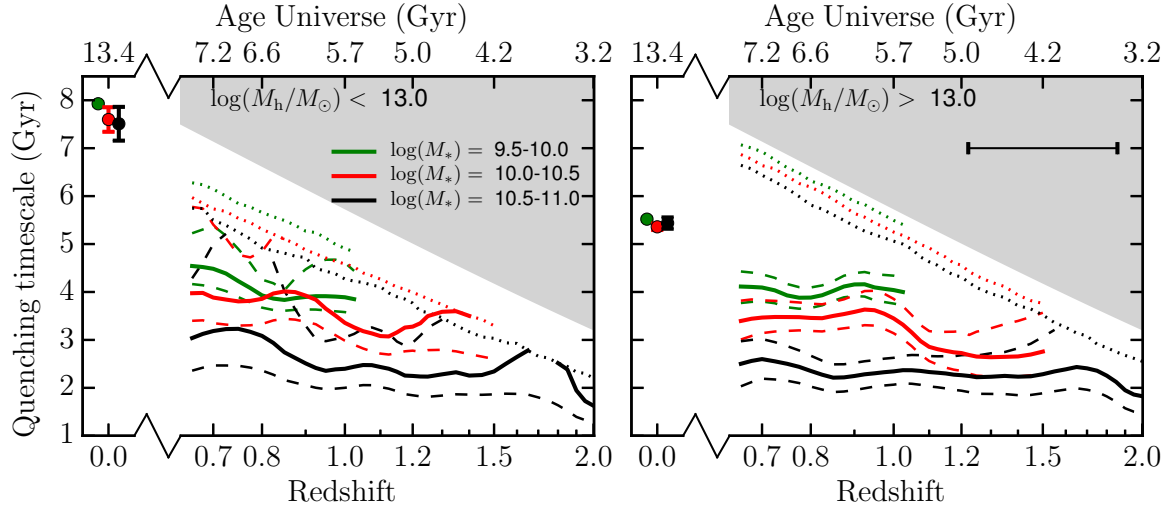


Figure 4.10: Quenching timescales for satellite galaxies as a function of redshift in bins of M_* and M_h (solid lines) for the 3D-HST sample. Dashed lines mark the 1σ confidence levels. The horizontal error bar is the span of the redshift bins (for the 3D-HST sample) which is constant in $\Delta z/(1+z) = 0.2$ where Δz is the width of the redshift bin and z its center. Datapoints at $z = 0$ are from the SDSS sample. The area where T_{quench} is larger than the Hubble time is shaded in grey. Dotted lines are obtained from the 99th percentile of T_{sat} in the mock sample and represent the look-back time at which the first 1% of the satellite population at a given redshift was accreted onto more massive halos as satellites. We define this limit as the maximum value of T_{quench} which would produce a meaningful environmentally quenched satellite population at any given redshift.

than half of the entire stellar mass extent of the bin.

The values (solid lines) and their associated uncertainties (dashed lines) are obtained by performing the procedure described in the previous sections in overlapping redshift bins defined such that $\Delta z/(1+z) = 0.2$ where Δz is the width of the redshift bin and z its center. This means we span larger volumes at higher redshift, modulating the decrease in sample density (Malmquist bias) and retaining sufficient sample statistics. It is also close to a constant bin in cosmic time. The x-axis of both figures is scaled such that the size of the redshift bins is constant and is shown as the horizontal error bar. We include only galaxies in a stellar mass complete sample for each redshift bin. In addition to the 3D-HST based constraints, we add constraints at $z = 0$, obtained using the same method to ensure homogeneity.

The evolution of f_{conv} as seen in Figure 4.6 is now clearly visible over the large redshift range probed by 3D-HST. The fraction of environmentally quenched satellite galaxies is a function of M_h , M_* and redshift. At fixed redshift f_{conv} is higher for higher mass galaxies and at fixed stellar mass it is higher in more massive haloes. More notably, the redshift evolution follows a decreasing trend with increasing redshift such that at $z \sim 1.5$ the excess of quenching of satellite galaxies becomes more marginal (at least for massive galaxies) as

first predicted by McGee et al. (2009) using halo accretion models. Several observational works reached a similar conclusion. Kodama et al. (2004), De Lucia et al. (2007), and Rudnick et al. (2009) found a significant build-up of the faint end of the red sequence (of passive galaxies) in cluster environments from $z \sim 1$ toward lower redshift. This implies an increase in the fraction of quenched satellites with decreasing redshift for low mass galaxies. Recently, Darvish et al. (2016) found that the environmental quenching efficiency tends to zero at $z > 1$, although their analysis is only based on local overdensity and does not separate centrals and satellites. With the 3D-HST dataset we cannot rule out that satellite quenching is still efficient for lower mass satellites at $z > 1.5$; deeper samples are required to robustly assess the satellite quenching efficiency at $z \sim 1.5 - 2.0$.

Moving to the present day Universe (SDSS data) does not significantly affect the fraction of environmentally quenched satellites despite the age of the Universe nearly doubling compared to the lowest redshift probed by the 3D-HST sample.

The redshift dependence of the quenching timescale originates from the combination of the evolution of f_{conv} and the distributions of infall times for satellite galaxies. The redshift evolution of f_{conv} in the high halo mass bin is well matched by the halo assembly history (at lower redshift they have been satellites on average for more time) and therefore T_{quench} is mostly independent of redshift. However, for lower mass galaxies a mild redshift evolution of T_{quench} might be present. However the slope is much shallower than the ageing of the Universe. For this reason, going to higher redshift, T_{quench} approaches the Hubble time and the satellite quenching efficiency decreases.

Despite the large uncertainty on the quenching times at low halo mass, their redshift evolution appears to be largely independent of halo mass. This means that the halo mass dependence of the conversion fractions may be mostly driven by an increase in the time spent as satellites in more massive haloes. At $z = 0$ a more significant difference is found between the quenching times in the two halo mass bins. In the next section we discuss which mechanism can produce these observational signatures.

4.7 Discussion

There is a growing consensus that the evolution of central galaxies is regulated by the balance between cosmological accretion, star formation and gas ejection processes in a so-called “equilibrium growth model” (e.g. Lilly et al., 2013). The reservoir of cold gas in each galaxy is replenished by accretion, and will fuel star formation. As the rate of cosmological accretion is correlated with the mass of the halo, this regulates mass growth via star formation. As a result the eventual stellar mass is also tightly correlated with halo mass, driving a tight relation between star formation rate and stellar mass for normal star forming galaxies (the main sequence - MS - of star forming galaxies, e.g. Noeske et al., 2007).

When galaxies fall into a more massive halo the accretion of new gas from the cosmic web is expected to cease: such gas will instead be accreted (and shock heated) when it reaches the parent halo (White & Frenk, 1991). More recently Dekel & Birnboim (2006)

estimate that this process occurs at a minimum halo mass $M_h \sim 10^{12} M_\odot$, which is largely independent of redshift. This roughly corresponds to the minimum halo mass at which satellites are detected in the 3D-HST survey (see Figure 3.20).

4.7.1 Identification of the main mechanism

There are several additional ways in which a satellite galaxy's gas and stellar content can be modified through interaction with its environment, including stripping of the hot or cold gas, and tidal interactions among galaxies or with the halo potential itself. An important combined effect is to remove (partially or completely) the gas reservoir leading to the quenching of star formation. However, as pointed out by McGee et al. (2014), and Balogh et al. (2016), it might not be necessary to invoke these mechanisms of environmental quenching to be effective. The high SFR typical of galaxies at high redshift, combined with outflows, can lead to exhaustion of the gas reservoir in the absence of cosmological accretion.

Our approach to link the conversion fractions to the distributions of time spent as satellite is based on the assumption that a galaxy starts to experience satellite specific processes at the time of its first infall into a larger halo and, in particular, that the cosmological accretion is shut off at that time.

We now examine whether a pure exhaustion of the gas reservoir can explain the quenching times we observe, or whether additional gas-removal mechanisms are required. First we appeal to the similarity of quenching times in the two halo mass bins shown in Figure 4.10 to support the pure gas exhaustion scenario. Other than at $z = 0$, the derived quenching times are indeed consistent within the uncertainties, therefore the main quenching mechanism has to be largely independent of halo mass.

Ram pressure stripping is often invoked as the main quenching mechanism for satellite galaxies in low redshift clusters (e.g., Poggianti et al., 2004; Gavazzi et al., 2013a; Boselli et al., 2014c). Its efficiency is a function of the intracluster medium (ICM) density and the velocity of galaxies in the halo. More massive haloes have a denser ICM and satellites move faster through it which exerts a stronger dynamical pressure on the gas leading to faster stripping (and shorter quenching times) in more massive haloes (Vollmer et al., 2001; Roediger & Hensler, 2005). Our 3D-HST dataset does not extend to the extreme high mass end of the halo mass function in which ram pressure effects have been clearly observed (e.g., Sun et al., 2007; Yagi et al., 2010; Merluzzi et al., 2013; Kenney et al., 2015; Fossati et al., 2016a), and so the lack of significantly shorter quenching times in the higher halo mass bin is consistent with the lack of stripping, and indeed of any strong halo-mass dependent gas-stripping process. However Balogh et al. (2016) find a small halo mass dependence of the quenching times comparing their GEEC2 group sample ($M_h \sim 10^{13.5} M_\odot$) to the GCLASS cluster sample ($M_h > 10^{14} M_\odot$). These evidences might indicate that dynamical stripping can play a minor role in more massive haloes even at $z \sim 1$.

At $z = 0$ instead, thanks to the large area covered by the SDSS dataset, a number of very massive haloes are included in the higher halo mass bin. This, combined with the presence of hot and dense ICM in massive haloes in the local Universe might be sufficient

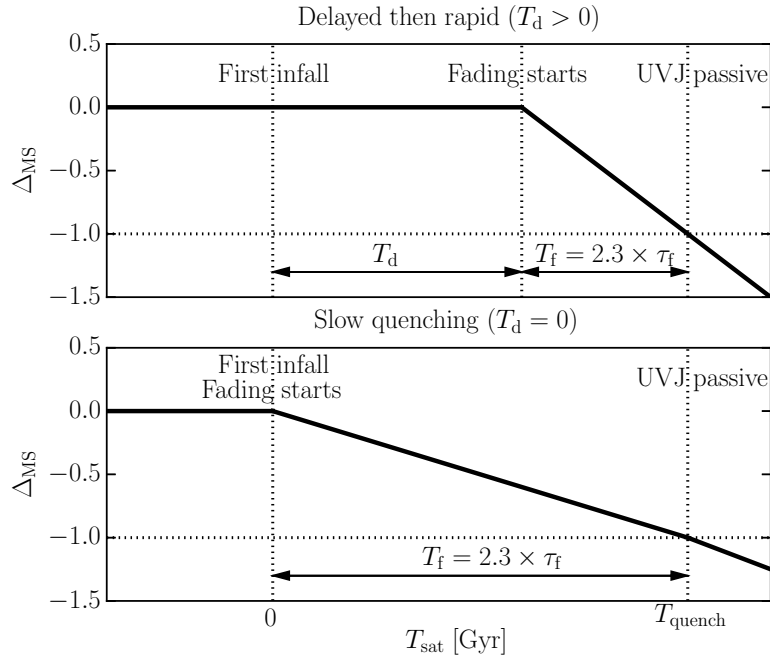


Figure 4.11: Schematic diagram of the evolution of the MS offset for two toy models of satellite quenching as a function of the time spent as a satellite. In both cases satellite quenching starts at the time of first infall for a galaxy at the main sequence mid-line value, which becomes UVJ passive after T_{quench} . In the “delayed then rapid” model (Top panel) the satellite galaxies evolves on the main sequence for a delay time T_d . Then their SFR drops exponentially with a characteristic timescale τ_f . In the “slow quenching” model (Bottom panel), $T_d = 0$ and the galaxy follows a slow(-er) exponential decline of the SFR immediately after its first infall into a more massive halo.

to explain the shorter quenching times in the high halo mass bin. Haines et al. (2015), and Paccagnella et al. (2016) found quenching timescales which are possibly shorter in massive clusters of galaxies ($\sim 2 - 5$ Gyr). However, a quantitative comparison is hampered by the different definitions of the quenching timescale.

4.7.2 Delayed then Rapid or Continuous Slow quenching?

Having ruled out gaseous stripping as the main driver of satellite quenching in the range of halo mass commonly probed by our samples ($M_h \lesssim 10^{14} M_\odot$), we now concentrate on how the gas exhaustion scenario can explain the observed values of T_{quench} .

To explain the quenching times at $z = 0$, Wetzell et al. (2013) presented a model dubbed the “delayed then rapid” quenching scenario, shown in the top panel of Figure 4.11. This model assumes that T_{quench} can be divided into two phases. During the first phase, usually called the “delay time” (T_d), the star formation activity of satellites on average follows the

MS of central galaxies. After this phase the star formation rate drops rapidly and satellite galaxies become passive on a short timescale called the “fading time”. Wetzel et al. (2013) estimated an exponential fading with a characteristic timescale $\tau_f \sim 0.3 - 0.8$ Gyr which depends on stellar mass at $z = 0$. At $z \sim 1$, Mok et al. (2014); Muzzin et al. (2014); and Balogh et al. (2016) estimated the fading time to be $\tau_f \sim 0.4 - 0.9$ Gyr, by identifying a “transition” population of galaxies likely to be transitioning from a star forming to a passive phase. These values suggest little redshift evolution of the fading timescale with cosmic time.

McGee et al. (2014) developed a physical interpretation of this model. These authors assumed that the long delay times are only possible if the satellite galaxy has maintained a multi-phase reservoir which can cool onto the galaxy and replenish the star forming gas (typically molecular) at roughly the same rate as the gas is lost to star formation (and potentially outflows). A constant molecular gas reservoir produces a nearly constant SFR according to the Kennicutt-Schmidt relation (Schmidt, 1959; Kennicutt, 1998b). Then the eventual depletion of this cold gas results in the rapid fading phase.

An alternative scenario would be that satellite galaxies retain only their molecular gas reservoirs after infall. In this case, if we assume a constant efficiency for star formation we should expect a star formation history which immediately departs from the MS, declining exponentially as the molecular gas is exhausted (“slow quenching” model shown in the bottom panel of Figure 4.11). By using our data we directly test those two toy models.

We use the star formation rates ($SFR(M_*, z)$) for 3D-HST galaxies presented in the Momcheva et al. (2016) catalog. By limiting to galaxies in the redshift range $0.5 < z < 1.5$, stellar mass range $9.5 < \log(M_*) < 11$ and a maximum offset below the main sequence of 0.5 dex, we make sure that the SFR estimates are reliable and, for 91% of the objects, are obtained from *Spitzer* $24\mu\text{m}$ observations combined with a UV monochromatic luminosity to take into account both dust obscured and unobscured star formation. For the remaining 9% SFR estimates are from an SED fitting procedure (see Whitaker et al., 2014; Momcheva et al., 2016).

There is growing evidence of curvature in the MS, which becomes shallower at higher stellar mass. Whitaker et al. (2014), Gavazzi et al. (2015), and Erfanianfar et al. (2016) interpreted this as a decline in star formation efficiency caused by the growth of bulges or bars in massive galaxies. To study the effects of environment above the internal processes driving the star formation efficiency at fixed stellar mass, we convert the SFR into an offset from this curved MS: $\Delta_{\text{MS,obs}} = \log(SFR(M_*, z)/SFR_{\text{MS}}(M_*, z))$ using the Wisnioski et al. (2015) parametrization of the MS from Whitaker et al. (2014).

In order to test the two models we again resort to the mock sample. For each central galaxy in the mocks we assign a random offset from the main sequence obtained from a pure sample ($P_{\text{cen}} > 0.8$) of observed centrals: $\Delta_{\text{MS,cen}}$. For satellite galaxies, instead, their Δ_{MS} is a function of their time spent as satellites (T_{sat}) as follows:

$$\Delta_{\text{MS}} = \begin{cases} < -1 & \text{if } T_{\text{sat}} > T_{\text{quench}} \\ \Delta_{\text{MS,cen}} & \text{if } T_{\text{sat}} \leq T_{\text{d}} \\ \Delta_{\text{MS,cen}} + \log(e^{-(T_{\text{sat}}-T_{\text{d}})/\tau_f}) & \text{if } T_{\text{sat}} > T_{\text{d}} \end{cases} \quad (4.10)$$

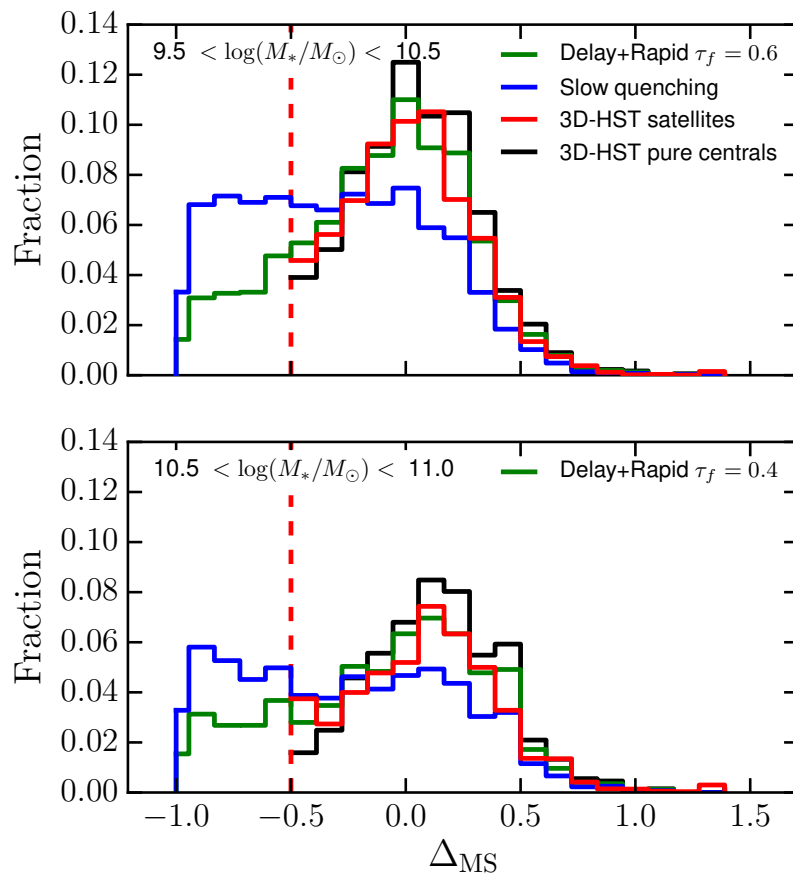


Figure 4.12: Logarithmic offset from the main sequence (Δ_{MS}) in two stellar mass bins for 3D-HST observed satellites at $0.5 < z < 1.5$ (red histogram) and for mock galaxies, in the same redshift range, assuming a “slow quenching” (blue histogram), or a “delayed then rapid” (green histogram) scenario (see text for the details of those two toy models). The histograms are normalized to the total number of 3D-HST satellites (including UVJ passive galaxies). The main sequence offset of a pure sample of observed central galaxies (black histogram) is shown for comparison. The red vertical dashed line is the limit below the main sequence at which SFR estimates for observed galaxies are based predominantly on accurate IR+UV measurements accounting for obscured and unobscured star formation.

where τ_f is computed for each galaxy independently such that the SFR drops 1 dex below the MS³ in $(T_{\text{quench}} - T_d)$ Gyr. As we already computed T_{quench} , the only free parameter remaining in this family of models is T_d . We define the “slow quenching” model for $T_d = 0$, and “delayed then rapid” those where $0 < T_d < T_{\text{quench}}$.

Figure 4.12 shows the distributions of Δ_{MS} for 3D-HST satellites in two stellar mass bins, obtained as usual by weighting all galaxies by P_{sat} , and for the two models obtained from the mock sample in the same way. The histograms are normalized to the total number of 3D-HST satellites in the same stellar mass bin (including UVJ passive galaxies). We stress that this comparison is meaningful because our models include the cross-talk between centrals and satellites.

In the “delayed then rapid” scenario, the value of the delay time that best reproduces the observed data is $T_d = T_{\text{quench}} - 1.4(0.9)$ Gyr for the $10^{9.5} - 10^{10.5}$ ($10^{10.5} - 10^{11}$) stellar mass bins respectively. This means the average satellite fades with an e -folding timescale of $\tau_f = 0.6(0.4)$ Gyr. Our values are consistent with those from Wetzel et al. (2013) at $z = 0$ and other independent estimates at high- z .

Conversely the “slow quenching” model predicts too many galaxies below the main sequence but which are not UVJ passive (“transition” galaxies). The fraction of 3D-HST satellites for which $\Delta_{\text{MS}} > -0.5$ is 65% (46%), which compares to 67% (47%) for the “delayed then rapid” model; instead it drops to 52% (39%) for the “slow quenching” model.

In conclusion the fading of the star formation activity must be a relatively rapid phenomenon which follows a long phase where satellite galaxies have a SFR which is indistinguishable from that of centrals. This is further supported by the evidence that the passive and star forming populations are well separated in color and SFR and that the “green valley” in between them is sparsely populated across different environments (Gavazzi et al., 2010; Boselli et al., 2014c; Schawinski et al., 2014; Mok et al., 2014).

4.7.3 The gas content of satellite galaxies

Finally, we discuss the implications of the quenching times on the gas content of satellites at the time of infall. Because satellite galaxies are not thought to accrete gas after infall, their continued star formation occurs at the expense of gas previously bound to the galaxy.

As previously discussed, McGee et al. (2014) explain the fading phase by the depletion of molecular gas. The depletion time of molecular gas ($T_{\text{depl,H}_2}$) has been derived by several authors (Saintonge et al., 2011; Tacconi et al., 2013; Boselli et al., 2014b; Genzel et al., 2015). There is general consensus that this timescale (which is an e -folding time) is ~ 1.5 Gyr at $z = 0$ and is ~ 0.75 Gyr at $z = 1$. Moreover it is independent of stellar mass. In this framework we might expect fading times shorter than (or similar to) $T_{\text{depl,H}_2}$, where shorter fading times are possible where a fraction of the gas is lost to outflows. Our fading times are indeed somewhat shorter than the molecular gas depletion times, consistent with this picture, but with a mass dependence which suggests a mass-dependent outflow rate.

³This is the value that defines the typical division between UVJ star forming and passive objects.

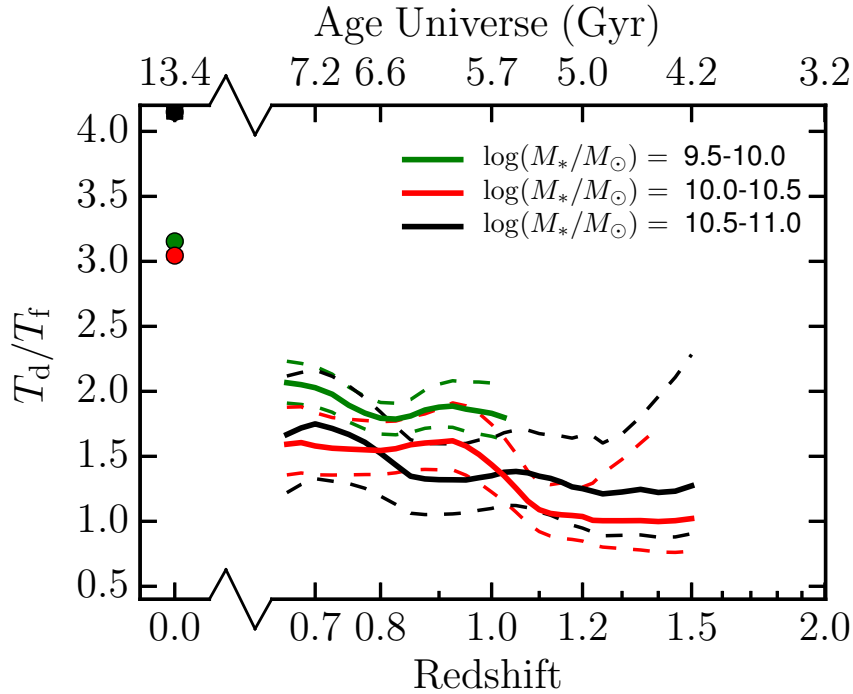


Figure 4.13: Ratio of the delay time (T_d) to the fading time (T_f) as a function of redshift in bins of stellar mass. The values of T_f at $z > 0.5$ are derived in Section 4.7.2, while those at $z = 0$ are taken from Wetzel et al. (2013). The uncertainties on the ratio propagate only the errors on the total quenching time.

In Figure 4.13 we show the ratio of the delay time to the fading time as a function of redshift in bins of stellar mass. Assuming that the fading phase is driven by depletion of molecular gas (in absence of further replenishment), this ratio informs us about the relative time spent refuelling the galaxy to keep it on the MS (from a gas reservoir initially in a warmer phase) to the time spent depleting the molecular gas. We note that the delay time is estimated via the quenching time (which is a function of stellar mass and redshift) while the fading time is computed only for 2 stellar mass bins at $0.5 < z < 1.5$, with $z = 0$ fading timescales taken from Wetzel et al. (2013). Errors in Figure 4.13 propagate only the errors on the total quenching time.

For all stellar mass bins this ratio is above unity, which we interpret to mean that gas in a non-molecular phase is required to supply fuel for star formation, and this gas is likely to exceed the molecular gas in mass. The longer delay times at $z = 0$ suggest that a smaller fraction of the gas mass is in molecular form. This model also implies that a significant fraction of the final stellar mass of satellite galaxies is built-up during the satellite phase.

A multi-phase gas reservoir is observed in the local Universe in the form of ionized, atomic, and molecular hydrogen. Atomic hydrogen cools, replenishing the molecular gas reservoir which is depleted by star formation. In the local Universe, using the scaling relations derived from the *Herschel* Reference Sample (Boselli et al., 2014b), the observed

mass of atomic hydrogen is found to be 2-3 times larger than the amount of molecular hydrogen for our most massive stellar mass bin. This ratio increases to ~ 8 for the lower mass objects, although with a large uncertainty. These numbers are consistent with the picture that much, if not all, of the reservoir required to maintain the satellite on the MS during the delay phase at $z \sim 0$ can be (initially) in an atomic phase. It is also plausible that much of the gas reservoir bound to higher redshift galaxies is contained in a non-molecular form, and that this can be retained and used for star formation when the galaxies become satellites.

Assuming that outflows are not only active during the fading phase but rather during the entire quenching time, the mass in the multi-phase gas reservoir needs to be even larger, although it is not straightforward to constrain by how much.

In conclusion our work supports a “delayed then rapid” quenching scenario for satellite galaxies regulated by star formation, depletion and cooling of a multi-phase gas reservoir.

4.8 Conclusions

In this chapter, we studied how the environment influences star formation in satellite galaxies. We combined data from SDSS at $z = 0$ with data from the 3D-HST survey at $z = 0.5 - 2.0$. Our results can be summarized as follows:

1. The 3D-HST sample provides us with a unique dataset to study the processes governing environmental quenching from $z \sim 2$ to the present day over a wide range of halo mass. As no galaxy has a perfectly defined environment, a Bayesian analysis allows us to recover “pure” passive fractions of central and satellite populations. We also estimated robust and realistic uncertainties through a Monte Carlo error propagation scheme that takes into account the use of probabilistic quantities.
2. By computing conversion fractions (i.e. the excess of quenched satellite galaxies compared to central galaxies at the same epoch and stellar mass) (van den Bosch et al., 2008), we find that satellite galaxies are efficiently environmentally quenched in haloes of any mass up to $z \sim 1.2 - 1.5$. Above these redshifts the fraction of passive satellites is roughly consistent with that of central galaxies.
3. Under the assumption that the earliest satellites to be accreted become passive first, we derive environmental quenching timescales. These are long ($\sim 2 - 5$ Gyr at $z \sim 0.7 - 1.5$; 5-7 Gyr at $z = 0$) and longer at lower stellar mass. As they become comparable to the Hubble time by $z \sim 1.5$, effective environmental quenching of satellites is not possible at earlier times. More remarkably, their halo mass dependence is negligible. By assuming that cosmological accretion stops when a galaxy becomes a satellite, we were able to interpret these evidences in a “gas exhaustion” scenario (i.e. the “overconsumption” model of McGee et al., 2014) where quenching happens because satellite galaxies eventually run out of their fuel which sustains further star formation.

4. We tested two toy models of satellite quenching: the “delayed then rapid” quenching scenario proposed by Wetzel et al. (2013) and a continuous “slow quenching” from the time of first infall. By comparing the observed SFR distribution for 3D-HST satellites to the predictions of these toy models we found that the scenario that best reproduces the data at $z \sim 0.5 - 1.5$ is “delayed then rapid”. Consistently with the results of Wetzel et al. (2013) at $z = 0$, we find that the fading of the star formation activity is a relatively rapid phenomenon ($\tau_f \sim 0.4 - 0.6$ Gyr, lower at higher mass) which follows a long phase where satellite galaxies have a SFR which is indistinguishable from that of centrals.
5. By linking the fading to the depletion of molecular gas we conclude that the “delayed then rapid” scenario is best explained, even at high redshift, by the presence of a significant multi-phase reservoir which can cool onto the galaxy and replenish the star forming gas at roughly the same rate as the gas is turned into stars.

Chapter 5

Environmental quenching caught in the act. A study of the archetypal galaxy ESO137-001

This chapter is adapted from Fossati et al. 2016, MNRAS, 455, 2028

In chapter 4 we have shown how galaxy color and star formation activity correlate both with local environment and stellar mass, and that environmental effects in overdense regions of the Universe are key drivers for satellite quenching.

In this respect, rich galaxy clusters are the best laboratories for investigating the processes that are responsible for quenching star formation, due to the combination of strong potential wells, high number density of galaxies, and the presence of the intracluster medium (ICM), a hot and dense plasma filling the intergalactic space. Several mechanisms have been proposed as the culprit for galaxy transformation within clusters (see Section 1.3.2), including tidal interactions between galaxies (sometimes called galaxy harassment) or with the cluster potential itself (Byrd & Valtonen, 1990; Henriksen & Byrd, 1996; Moore et al., 1998), and ram pressure stripping (Gunn & Gott, 1972).

Although more than one of these mechanisms likely play a role in the evolution of cluster galaxies at one time, a few pieces of observational evidence consistently point to ram pressure stripping as a widespread process, and one of crucial importance for the transformation of low mass galaxies that are being accreted on to clusters at recent times (Boselli et al., 2008). Observationally, the fingerprint of ram pressure is the removal of the galaxy gas content without inducing strong disturbances in the older stellar populations. Indeed, large radio surveys have found that the HI content of cluster (and to some extent group) galaxies is being reduced with respect to their field counterparts (Giovanelli & Haynes, 1985; Solanes et al., 2001; Cortese et al., 2011; Fabello et al., 2012; Catinella et al., 2013; Gavazzi et al., 2013b; Jaffé et al., 2015), an effect that has been also recently observed in the molecular phase (Fumagalli et al., 2009; Boselli et al., 2014a). This gas depletion, in turn, induces truncated profiles in young stellar populations compared to old ones (Koopmann et al., 2006; Boselli et al., 2006; Cortese et al., 2012b; Fossati et al., 2013).

In this chapter we aim to provide a detailed look at how this mechanism operates on small scales within individual galaxies, so as to gain insight into how gas removal occurs as a function of parameters such as galaxy mass or distance from the cluster centre. We also investigate the fate of the stripped gas, which could mix with the hotter ICM or cool again to form stars.

Ram pressure has been caught in the act by searching for UV and H α tails downstream of galaxies in fast motion through massive clusters like Coma or Virgo (Gavazzi et al., 2001; Yoshida et al., 2002; Cortese et al., 2006; Kenney et al., 2008; Smith et al., 2010; Yagi et al., 2010; Fossati et al., 2012). The amount of star formation in stripped tails has been the subject of several analyses, both from the observational (Yagi et al., 2010; Fumagalli et al., 2011; Arrigoni Battaia et al., 2012; Boissier et al., 2012; Fossati et al., 2012) and theoretical point of view (e.g. Kapferer et al., 2009; Tonnesen & Bryan, 2012). However, the efficiency of star formation and its dependence on the gas properties of the tails remain poorly understood.

5.1 The galaxy

A poster child for studies of ram pressure stripping is ESO137-001, a spiral galaxy near to the core of the Norma cluster. The Norma cluster, also known as A3627, has a dynamical mass of $M_{\text{dyn}} \sim 10^{15} M_{\odot}$ at a redshift $z_{\text{cl}} = 0.01625 \pm 0.00018$ (Woudt et al., 2008; Nishino et al., 2012).

Figure 5.1 shows the projected location of ESO137-001 and its X-Ray tail (white box) in the hot X-Ray emitting gas of the cluster. ESO137-001 is located at a projected distance of only ~ 267 kpc from the central cluster galaxy, and features a wealth of multiwavelength observations ranging from X-ray to radio wavelengths (Sun et al., 2006, 2007, 2010; Sivanandam et al., 2010; Jáchym et al., 2014).

All these observations clearly show that ESO137-001 is suffering from extreme ram pressure stripping, arguably during its first infall into the cluster environment. Indeed, while ESO137-001 can be classified as a normal spiral galaxy from its stellar continuum, X-ray and H α observations reveal the presence of a double tail that extends for ~ 80 kpc behind the galaxy disk, in the opposite direction from the cluster centre (Sun et al., 2006, 2007, 2010). These tails are believed to originate from the hydrodynamic interaction between the hot ICM and the cold interstellar medium (ISM), which is removed from the galactic disk (Sun et al., 2007; Jáchym et al., 2014; Fumagalli et al., 2014). Although stripped tails have been extensively studied in imaging in various nearby clusters, the number of spectroscopic studies in the optical has been limited in the past (e.g. Yagi et al., 2007; Yoshida et al., 2012; Merluzzi et al., 2013), due to the extended nature and the low surface brightness of the emitting regions.

To overcome the lack of extended spectroscopic follow-up of this galaxy, we have collected integral field spectroscopic observations of ESO137-001 following the deployment of Multi Unit Spectroscopic Explorer (MUSE; Bacon et al., 2010) at the ESO Very large Telescope. With its unique combination of high efficiency (~ 0.35 at 6800 Å), extended

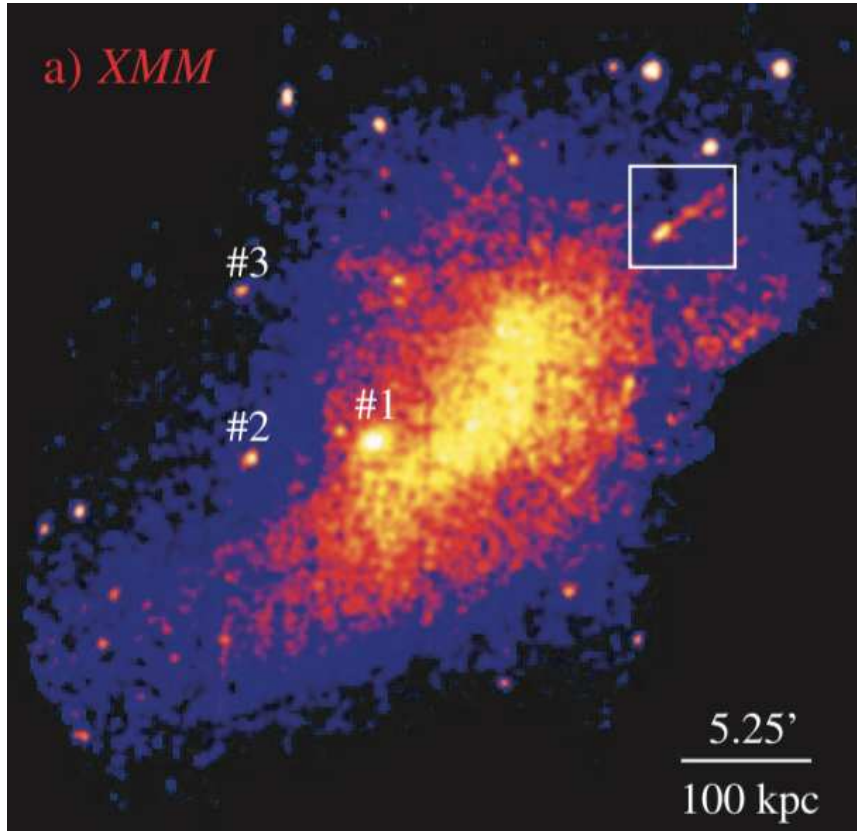


Figure 5.1: *XMM-Newton* 0.52 keV mosaic of the Norma cluster (A3627). A long X-ray tail from ESO137-001 is clearly visible, as indicated by the white box. The position of the brightest three cluster galaxies is highlighted by white numbers. Image taken from Sun et al. (2007).

wavelength coverage ($\sim 4800 - 9300 \text{ \AA}$ sampled at 1.25 \AA), and large field of view ($1 \text{ arcmin} \times 1 \text{ arcmin}$ in wide field mode, sampled with 0.2 arcsec pixels), MUSE is a unique instrument to map at optical wavelengths the kinematics and line ratios of the disk and tail of ESO137-001.

Adopting a standard Λ CDM cosmology with $h = 0.7$ and $\Omega_m = 0.3$, 1 arcsec corresponds to 0.32 kpc at the distance of ESO137-001.

5.2 Observations and data reduction

ESO137-001 was observed with MUSE during the science verification program 60.A-9349(A) on 2014 June 21. The left panel of Figure 5.2 shows the layout of the observations. Observations were acquired in photometric conditions and under good seeing ($0.7'' - 0.8''$), using the Wide Field Mode with nominal wavelength coverage ($4800-9300 \text{ \AA}$). The spectral resolution is $\sim 50 \text{ km s}^{-1}$ and roughly constant across the wavelength range. The disk and the

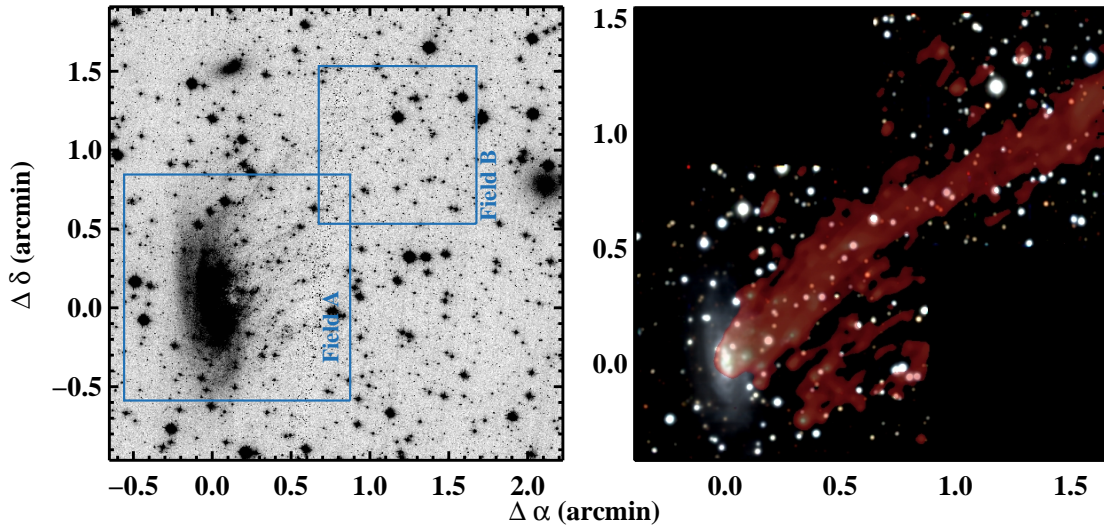


Figure 5.2: Left: archival HST/F475W image of ESO137-001 (PID11683; PI:MingSun) with, superposed, the MUSE field of view at the two locations targeted by our observations. In this figure, north is up and east is to the left. The coordinate system is centered on the nucleus of ESO137-001. Right: RGB color image obtained by collapsing the MUSE data cube in three wavelength intervals ($\lambda = 5000 - 6000 \text{ \AA}$ for the B channel, $\lambda = 6000 - 7000 \text{ \AA}$ for the G channel, and $\lambda = 7000 - 8000 \text{ \AA}$ for the R channel). A map of the $H\alpha$ emission line flux is superimposed in red. Image taken from Fumagalli et al. (2014).

inner tail of ESO137-001 (“Field A” in Figure 5.2) were observed with three exposures of 900 s each, with dithers of 13-16 arcsec and a rotation of 90 deg in the instrument position angle at each position. The main tail was targeted by a single 900 s exposure (“Field B” in Figure 5.2).

The raw data have been processed with the MUSE data reduction pipeline (v 0.18.1), which we supplemented with custom-made IDL codes to improve the quality of the illumination correction and of the sky subtraction. The pipeline removes instrumental signatures by performing bias subtraction, flat-field correction, wavelength calibration and flux calibration. As a result pixel-tables of non-interpolated detector fluxes are produced for each exposure.

We then apply a custom illumination correction to those pixel tables, which we obtain by comparing the brightness of multiple sky lines across the 1152 slits of the IFUs to compensate for variations in the spatial response of the different MUSE spectrographs.

After this step, we perform sky subtraction using in-house codes, as the very crowded nature of our field requires additional processing to avoid large negative residuals, as shown in Figure 5.3. In particular, because a significant fraction of our field is filled by the emission lines from the tail of ESO137-001 or by the continuum emission from the stellar disk and halo, we use exposures of empty sky regions to avoid the inclusion of spurious signal arising from the galaxy itself in the sky model. Specifically, we use a sky exposure of 60s, acquired

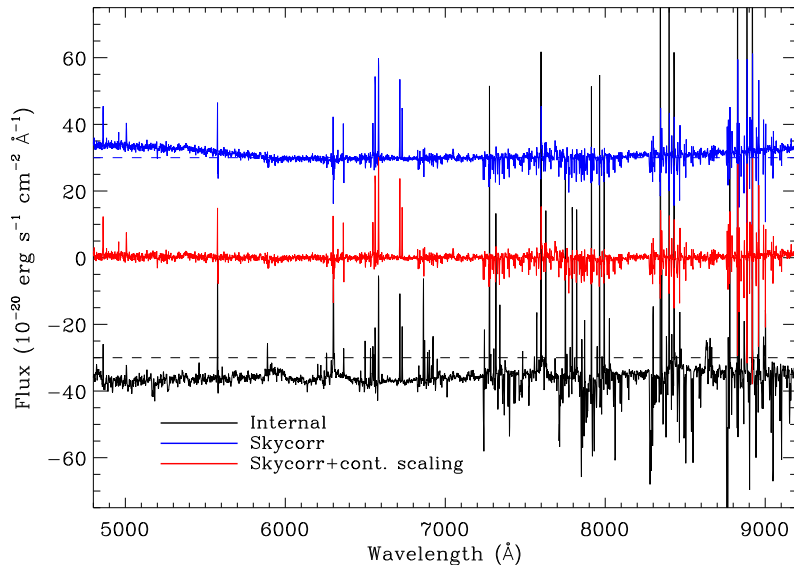


Figure 5.3: Sky residuals recorded in a 10-pixel square aperture within one science exposure that has been processed with different algorithm for sky subtraction. The black line shows the result of the MUSE pipeline in this crowded field. The blue line is obtained by subtracting a sky model derived from a second sky exposure together with the scaling computed with SKYCORR. Both spectra are visibly offset from the zero level, marked by the dashed lines. The red line shows the sky residual in the data cube, after including scaling in both the airglow lines and the continuum to match the level recorded in the science exposure. Large sky line residuals do not appear in the final processed cube (the group of lines at $\sim 6500\text{\AA}$, whose residuals do not change in the three spectra, are in fact emission lines from the Galaxy).

~ 1 hour apart from our science observations by the program 60.A-9303(A).

As a first step in the sky subtraction procedure, we generate a supersampled sky spectrum (hereafter the sky model) after processing the pixel table of the sky exposure with the same pipeline recipes used for our science exposures. This sky model, however, cannot be directly subtracted from the science exposures because of the time dependency of both the airglow line and continuum fluxes. To correct for this variation, we exploit the ESO tool SKYCORR (Noll et al., 2014) to compute a physically-motivated scaling of the airglow lines in the sky model to match the levels recorded in a model spectrum extracted from each of the science exposures. Empirically, we find that SKYCORR produces line models which yield small residuals after subtraction, as shown in Figure 5.3. At this stage, however, SKYCORR does not attempt any scaling of the sky continuum emission, mainly because the continuum emission from the sources cannot be easily separated from the sky continuum level. Thus, to set a zero-point for the sky continuum emission, we take advantage of the large field of view of MUSE which contains regions that are not affected by the galaxy’s

continuum flux. After subtracting the rescaled sky model from the science exposures, any residual deviation from a zero continuum level in these “empty” regions arises because of the different sky continuum level in the science and the sky exposures (see Figure 5.3). To remove this last signature, we fit two third-degree polynomials in regions free from sky lines above and below 6200 Å, that is the wavelength where the sky continuum reaches its peak. Finally, we use this polynomial fit to correct for the residuals due to varying sky continuum emission (Figure 5.3). During these steps, the sky model is subtracted from each pixel of the data cube by interpolating on the wavelength axis with a spline function. The appropriate uncertainties are added to the variance stored in the data cube (the “stat” extension).

After sky subtraction, we use the MUSE pipeline to combine the four individual exposures and reconstruct the final data cube on a regular grid of 0.2 arcsec in the spatial direction and 1.25 Å in the spectral direction. As a last step, we apply the heliocentric correction and we correct the observed flux as a function of wavelength to account for a substantial amount of Galactic extinction in the direction of ESO137-001. This correction is computed using the color excess from the dust map by Schlegel et al. (1998) with the recalibration of Schlafly & Finkbeiner (2011). We also assume a Galaxy extinction curve from Fitzpatrick (1999).

We verified the accuracy of the flux calibration by comparing the H α fluxes of selected HII regions to the measurements reported by Sun et al. (2007). We also test that the flux calibration is consistent across the entire wavelength range by checking that the spectra of stars in the field are well fitted by blackbody functions. Lastly, we compare the flux ratios of several emission lines derived in this work to those from Sun et al. (2010) for their HII regions ELO2 and ELO7, finding agreement within 5% for all the flux ratios compared.

5.3 Emission line measurements

To characterise the physical properties of the gas in the disk and the tail, we extract flux maps of the emission lines listed in Table 5.1. In this table, we also provide for each line an estimate of the noise, quantified as the 3σ limit per spaxel (spatial pixel) in the unsmoothed MUSE data cube. The noise is estimated as the standard deviation of fluxes in a wavelength interval of 30Å, close to the wavelength of the line of interest and clean of bright sky line residuals.

We assume a systemic redshift $z_{\text{sys}} = 0.01555 \pm 0.00015$ for ESO137-001. Maps of the line fluxes are obtained from the reduced datacube using the IDL custom code KUBEVIZ¹. Before the fit, the datacube is median filtered in the spatial direction with a kernel of 15×15 pixels (corresponding to 3" or 0.95 kpc at the distance of ESO137-001) to increase the signal-to-noise (S/N) per pixel without compromising the spatial resolution of the data. No spectral smoothing is performed.

In the galaxy disk, Balmer emission lines (H α and H β) are contaminated by stellar absorption. Direct fitting of the emission lines would thus underestimate the fluxes. To

¹www.mpe.mpg.de/~mfossati/kubeviz/

Line	λ_r (Å)	μ_{\min} (erg s ⁻¹ cm ⁻² Å ⁻¹ arcsec ⁻²)
H β	4861.33	8.2 – 11.7 × 10 ⁻¹⁸
[O III]	4958.91	7.7 – 10.7 × 10 ⁻¹⁸
[O III]	5006.84	7.5 – 10.5 × 10 ⁻¹⁸
[N II]	5754.64	6.2 – 8.7 × 10 ⁻¹⁸
[O I]	6300.30	4.6 – 6.3 × 10 ⁻¹⁸
[O I]	6363.78	5.0 – 6.7 × 10 ⁻¹⁸
[N II]	6548.05	4.1 – 5.6 × 10 ⁻¹⁸
H α	6562.82	4.1 – 5.6 × 10 ⁻¹⁸
[N II]	6583.45	4.1 – 5.5 × 10 ⁻¹⁸
[S II]	6716.44	4.9 – 6.4 × 10 ⁻¹⁸
[S II]	6730.81	5.0 – 6.6 × 10 ⁻¹⁸
[S III]	9068.60	4.8 – 6.9 × 10 ⁻¹⁸

Table 5.1: Emission lines considered in this study. The columns of the table are: (1) name of the emission line; (2) wavelength in air; (3) characteristic surface brightness limit at 3σ C.L. computed in each spaxel after correcting for Galactic extinction. The two values refer to pointing A and B respectively.

solve this problem, we first model and subtract the underlying galaxy stellar continuum using the GANDALF code (Sarzi et al., 2006) for spaxels in a rectangular area that covers the stellar disk (see the inset in Figure 5.5) and with $S/N > 5$ per velocity channel in the continuum. GANDALF works in combination with the Penalized Pixel-Fitting code (PPXF) (Cappellari & Emsellem, 2004) to simultaneously model the stellar continuum and the emission lines in individual spaxels. The stellar continuum is modeled with a superposition of stellar templates convolved by the stellar line-of-sight velocity distribution, whereas the gas emission and kinematics are derived assuming a Gaussian line profile. To construct the stellar templates, we use the MILES library (Vazdekis et al., 2010).

Having obtained a data cube free from underlying stellar absorption, we use KUBEVIZ to fit the emission lines. This code uses “linesets”, defined as groups of lines that are fitted simultaneously. Each lineset (e.g. H α and [NII] $\lambda\lambda 6548, 6584$) is described by a combination of 1D Gaussian functions where the relative velocity separation of the lines is kept fixed according to the wavelengths listed in Table 5.1. To facilitate the convergence of the fit for the faintest lines, we impose a prior on the velocity and the intrinsic line width σ of each lineset, which is fixed to that obtained fitting the H α and [NII] lines. We have explicitly verified on the master spectra described in section 5.5 that this assumption holds well both in the disk and across the tail. Furthermore, the flux ratio of the two [NII] and [OIII] lines are kept constant in the fit to the ratios in Storey & Zeippen (2000). The continuum level is evaluated inside two symmetric windows around each lineset. Figure 5.4 shows emission line maps obtained from our fits of the datacube at selected wavelengths. We note that, at the redshift of ESO137-001, [SII] $\lambda 6731$ falls onto a bright sky line at

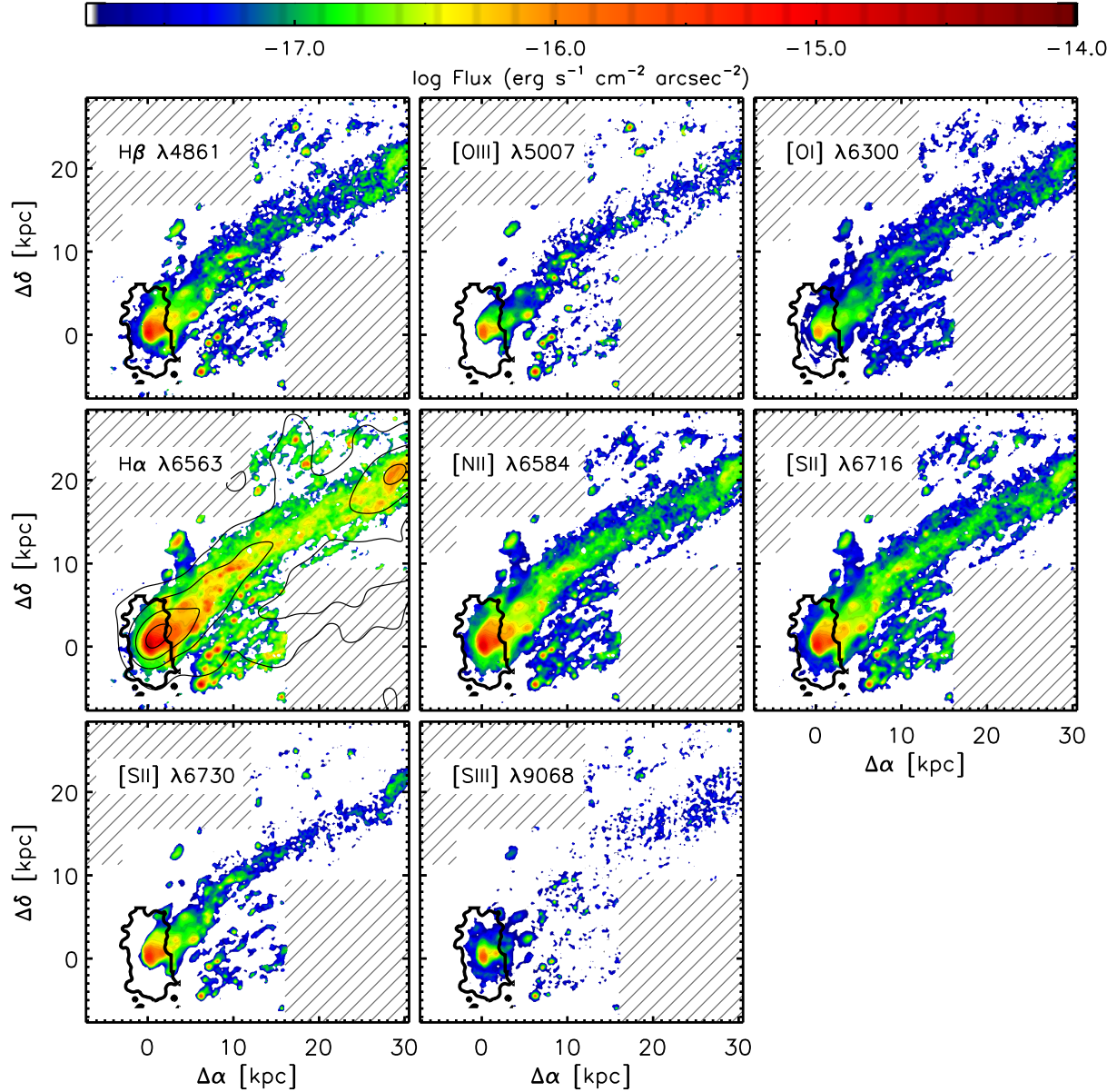


Figure 5.4: Emission line maps of ESO137-001. The panels are sorted by the wavelength of the line from left to right and top to bottom. The black solid contour marks the isophote of the galactic disk at $22 \text{ mag arcsec}^{-2}$ measured on an r -band image obtained from the datacube. The thinner solid contours in the $H\alpha$ panel show the location of the X-ray emitting gas from *Chandra* observations (Sun et al., 2010), highlighting the primary and secondary tails. Areas not covered by MUSE observations are shaded in grey.

$\lambda 6834$ and thus the strong residual hampers a reliable estimate of the flux for this line (see Figure 5.9). Therefore, we are forced to exclude [SII] from most of the following analysis.

During the fit, KUBEVIZ takes into account the noise from the “stat” data cube, thus optimally suppressing sky line residuals. However, the adopted variance underestimates the real error, most notably because it does not account for correlated noise introduced by resampling and smoothing. We therefore renormalize the final errors on the line fluxes assuming a $\chi^2 = 1$ per degree of freedom. In the end, we mask spaxels where the S/N in the $H\alpha$ line is < 3 . Further masking is applied to the spaxels for which the line centroids or the line widths are extreme outliers compared to the median value of their distributions, or the errors on these quantities exceed 50 km s^{-1} .

5.4 Kinematics

The analysis of the gas and stellar kinematics offers unique insight into how ram-pressure stripping occurs in ESO137-001. Here we briefly summarize the results of the kinematic analysis first presented in Fumagalli et al. (2014) and later updated with the improved data reduction scheme presented here. The projected position of the galaxy in the cluster and the direction of the tail suggest that ESO137-001 is moving towards the centre of the Norma cluster on a projected orbit with position angle of ~ -50 deg.

Figure 5.5 shows the velocity map, as traced by the $H\alpha$ emission line and its associated uncertainty. The gas radial velocity reveals no clear gradient along the tail, implying that the motion occurs in the plane of the sky. Conversely, a clear velocity gradient is seen in the direction parallel to the galaxy major axis, perpendicular to the tail. This velocity pattern was already observed by Sun et al. (2010) who studied selected HII regions with Gemini/GMOS spectroscopy. Our observations confirm that ESO137-001 is approaching the cluster centre on a nearly radial orbit, with no significant tangential velocity component. The stripped gas retains a remarkable degree of coherence in velocity to ~ 20 kpc downstream, which is originally imprinted by the rotation curve of the stellar disk. The map of the stellar kinematics is shown in the inset of Figure 5.5 is in remarkable agreement with the ionized gas map within the stellar disk. Higher radial velocities $80 - 120 \text{ km s}^{-1}$ are visible in the stripped gas in the southern secondary tail, which is likely to originate from material that detached from the southernmost part of the disk of ESO137-001, where stars rotate at comparable velocity. A hint of the same effect, but with reversed sign, is visible in the northern part of the primary tail where the stripped gas is blue-shifted compared to systemic velocity, in agreement with the velocity field of the stellar disk.

Figure 5.6 shows the velocity dispersion map, as traced by the $H\alpha$ emission line and its associated uncertainty. On scales of ~ 20 kpc from the galaxy centre, the $H\alpha$ emitting gas exhibits low turbulence. The bulk of the gas has a velocity dispersion $\sigma \sim 25 - 50 \text{ km s}^{-1}$, in qualitative agreement with the narrow CO line profiles shown by Jáchym et al. (2014). Two notable exceptions are the bright $H\alpha$ knots (which we identify as HII regions in section 5.5.1), where the velocity dispersion is lower ($\sigma \lesssim 25 \text{ km s}^{-1}$) as expected from a colder medium that hosts on-going star formation; and the front of the tail where the

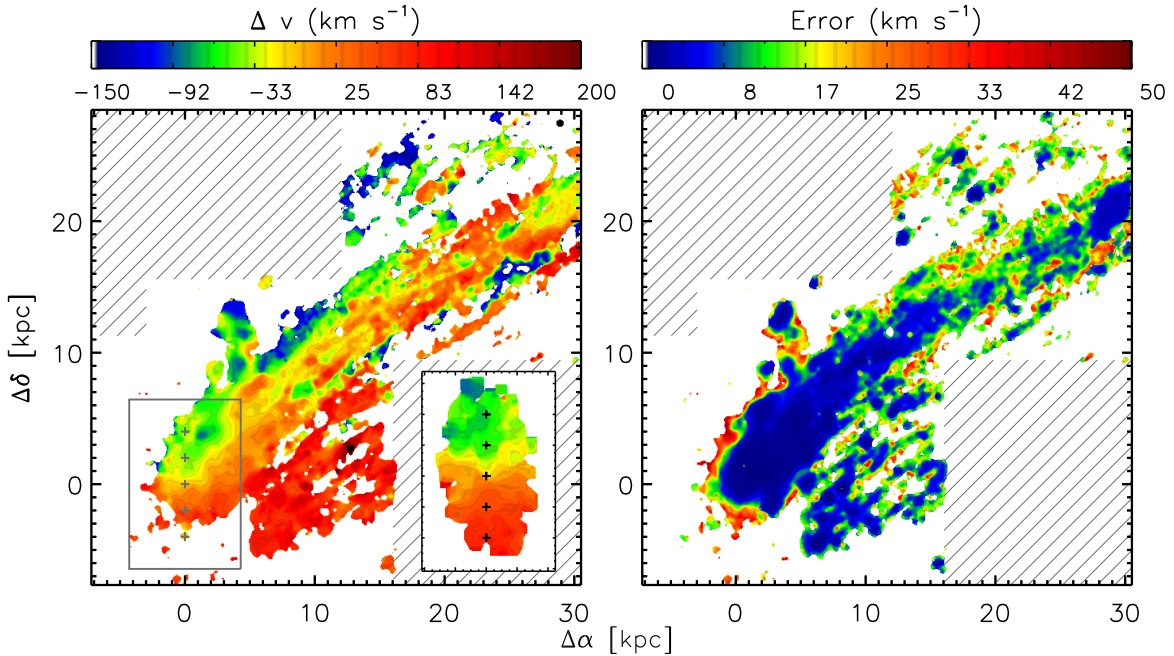


Figure 5.5: Left: velocity map of the H α line relative to the galaxy systemic velocity. In the inset, we show the stellar kinematics, on the same color scale adopted for the gas velocity map. To facilitate the comparison, we show the position of the inset in the main panel (grey box), and we use crosses as a ruler with steps of 2 kpc. Right: the error map of the fitted centroids. Areas not covered by MUSE observations are shaded in grey.

dispersion is high ($\sigma > 100 \text{ km s}^{-1}$) albeit with a large uncertainty. We investigate in more detail the ionization conditions in this region in section 5.5.3.

Beyond $\sim 20 \text{ kpc}$ from the galaxy position, a higher degree of velocity dispersion can be seen, with typical values above $\sim 50 \text{ km s}^{-1}$ and peaks exceeding 100 km s^{-1} . We need to be more cautious in interpreting kinematics within Field B, due to the lower S/N of our observations. Nevertheless, a progressively higher velocity dispersion moving far from the ESO137-001 disk along the tail was also noted by Jáchym et al. (2014) who found larger line widths in their CO observations at similar distances from the disk. We also tested that Gaussian fits to coarsely binned data with higher S/N show consistent velocity dispersion measurements within the uncertainties.

5.5 Emission line diagnostics

Several physical processes, including photoionisation, shocks, and thermal energy in mixing layers, are likely to contribute to the emission lines we see in the spectra of the main body of ESO137-001 and its tail.

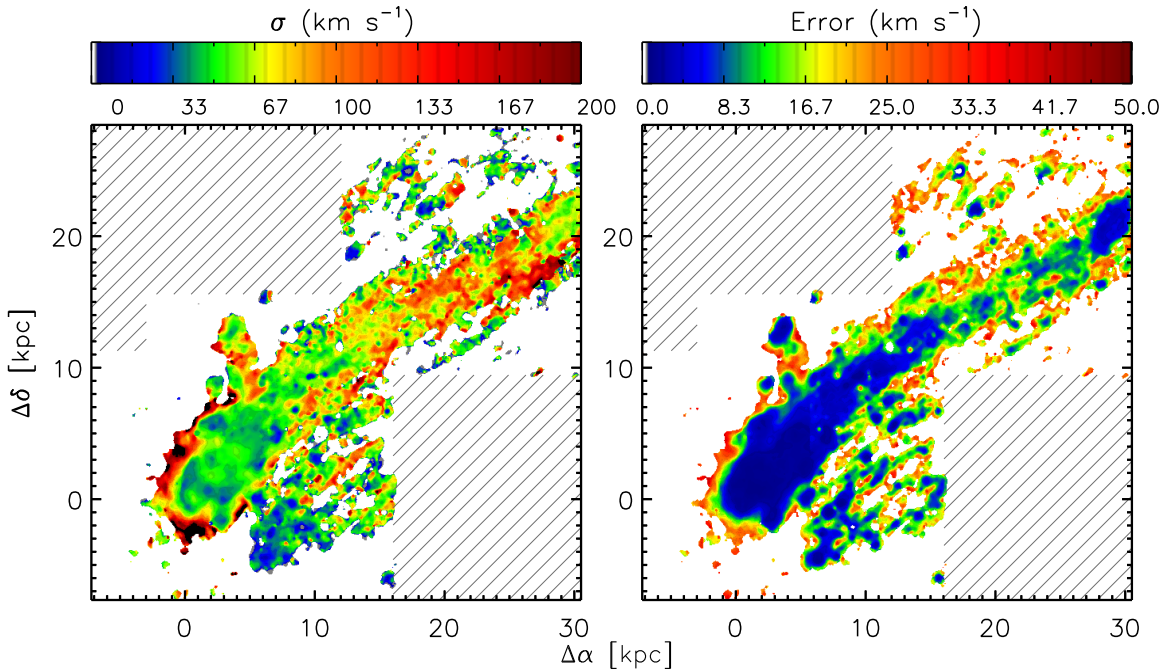


Figure 5.6: Left: velocity dispersion map of the $H\alpha$ line. Values have been corrected for instrumental resolution. Right: the error map of the fitted line widths, in velocity units. Areas not covered by MUSE observations are shaded in grey.

5.5.1 Line ratio maps

In this section, we exploit the integral field capabilities of MUSE to investigate the spatial variations of physical properties inferred from strong emission line diagnostics computed for each pixel. Next, we will coadd the spectra of several characteristic regions of the ESO137-001 system to achieve higher S/N in the fainter lines.

The ratio of collisionally excited lines like $[OIII]\lambda 5007$, $[NII]\lambda 6584$ to hydrogen recombination lines ($H\alpha$, $H\beta$) is traditionally used as indicator of the ionization properties of the gas. More specifically, the combination of pairs of these line ratios is used to construct BPT diagrams (Baldwin et al., 1981), so as to distinguish different sources of ionization, e.g. photoionization in star forming galaxies or active galactic nuclei, and shocks. These line ratios are typically chosen such that both lines fall inside a small window of wavelength to minimize the effects of dust extinction.

The top panels of Figure 5.7 show 2D maps of the $[OIII]\lambda 5007/H\beta$, $[NII]\lambda 6584/H\alpha$, and $[OI]\lambda 6300/H\alpha$ ratios, computed for all the spaxels in which both of the lines of interest are detected with $S/N > 3$. Significant spatial variations in these three line ratios can be seen in the data. Most of the large scale trends visible in this figure are real, but we caution that two effects should be taken into account when interpreting the maps. First, in the outer tail, the depth of the observations is shallower due to shorter exposure time. Second, in the front region, the smoothing applied to the datacube can artificially enhance

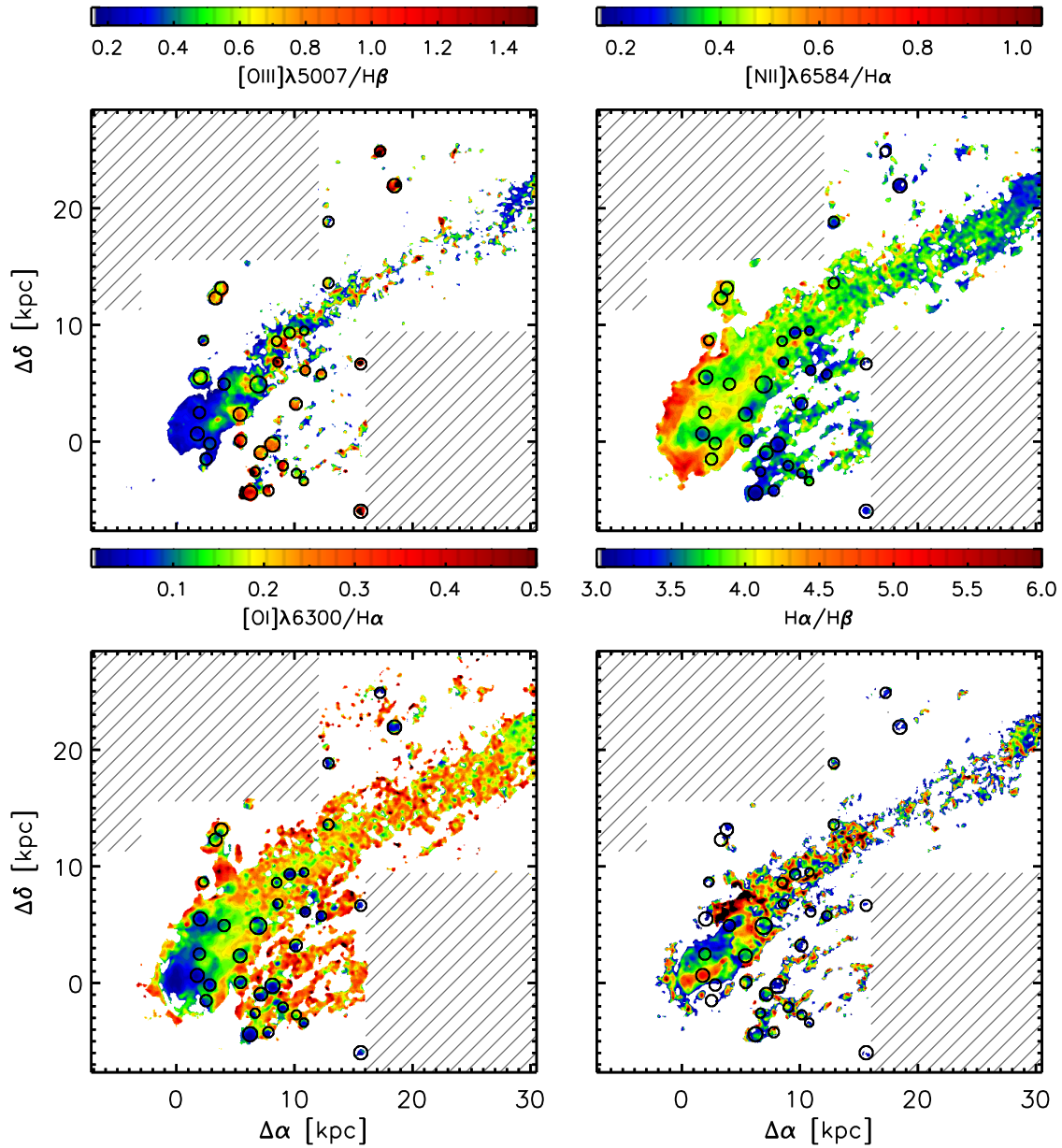


Figure 5.7: Maps of the $[\text{OIII}]\lambda 5007/\text{H}\beta$, $[\text{NII}]\lambda 6584/\text{H}\alpha$, $[\text{OI}]\lambda 6300/\text{H}\alpha$, and $\text{H}\alpha/\text{H}\beta$ line ratios. Areas not covered by MUSE observations are shaded in grey. The compact knots associated with HII regions along the tail are highlighted with black circles in all the panels.

discontinuities in line ratios and affect their gradients.

Inspecting the $H\alpha$ map (left central panel in Figure 5.4), compact knots along the tail can be identified as high surface brightness regions. To isolate these knots, we run SExtractor v2.19.5 (Bertin & Arnouts, 1996) on the $H\alpha$ map. Among the detected objects ($S/N > 5$) we selected those with a classification consistent with point-like sources ($CLASS_STAR > 0.9$) and low ellipticity ($e < 0.2$). 33 such knots are identified in our data. Out of these 27 correspond to the HII regions analyzed in Sun et al. (2007, 2010). The remaining six regions lie close to foreground stars, making their selection more difficult in the narrow band imaging data of Sun et al. (2007). In Figure 5.7, we have highlighted the position the compact knots with black circles. These regions are mainly characterized by high values of $[OIII]\lambda 5007/H\beta$ ($\gtrsim 0.7$) as well as low values of $[NII]\lambda 6584/H\alpha$ ($\lesssim 0.3$) and $[OI]\lambda 6300/H\alpha$ ($\lesssim 0.1$) ratios. According to the BPT classification (see also Figure 5.11), all these regions occupy the parameter space populated by HII regions photoionized by OB stars.

Focusing next on the galaxy nucleus, at the origin of the coordinate system in Figure 5.7, we see modest ratios for $[OIII]\lambda 5007/H\beta$, $[NII]\lambda 6584/H\alpha$ and $[OI]\lambda 6300/H\alpha$, which is again consistent with ionization from a soft spectral energy distribution. Thus, in agreement with the X-ray analysis of Sun et al. (2010), we conclude that the nuclear emission of ESO137-001 is powered by star formation activity and that this galaxy does not host a strong AGN.

Looking at the galaxy front next, where the ISM collides with the hot plasma from the cluster, we see enhanced $[NII]\lambda 6584/H\alpha$ ($\gtrsim 0.6$) as well as low $[OIII]\lambda 5007/H\beta$ ($\lesssim 0.3$), with a hint of elevated $[OI]\lambda 6300/H\alpha$. These ratios are suggestive of shocks playing a role in the gas excitation (Allen et al., 2008; Rich et al., 2011). Throughout the primary tail $[NII]\lambda 6584/H\alpha$ remains elevated (~ 0.4) decreasing only towards the end of the tail, in proximity of the extended $H\alpha$ blob that is known to harbor a large molecular complex (Jáchym et al., 2014). We also find enhanced $[OI]\lambda 6300/H\alpha$ ($\gtrsim 0.2$) in the tail, while the $[OI]$ line is weaker in the galactic disk. This piece of evidence, combined with the high gas turbulence (see Figure 5.6), points to shock heating as an important mechanism to excite the gas in the tail.

Differently from the primary tail, the southern secondary tail shows a strong $[OI]$ emission, but a lower $[NII]\lambda 6584/H\alpha$, which is on average ~ 0.2 after removing the HII regions. These line ratios are more difficult to reconcile with emission lines from ordinary shock models. We note however that the presence of several bright HII regions embedded in this tail can produce mixed types of spectra, with a superposition of emission lines that originate from different emission mechanisms in distinct gas phases. More generally, we are witnessing a complex interaction between multiple gas phases as the warm ISM from the galaxy, ionized by past and ongoing star formation, mixes and interacts with the hot ICM. Thus, photoionisation from stars, shocks, and even thermal conduction and the presence of magnetic fields (see e.g. Ferland et al., 2008, 2009), are likely contributing to a varying degree to the peculiar line ratios seen in ESO137-001.

We conclude this section by briefly commenting on the $H\alpha/H\beta$ ratio, shown in the forth panel of Figure 5.7. This ratio is commonly used in the low density limit to infer

the dust extinction, assuming an intrinsic ratio of 2.86 from case B recombination at $T = 10^4$ K (Osterbrock, 1989). As the observed emission, especially in the tail, may not simply arise from photoionized gas at the temperature of typical HII regions (see Sect. 5.5.2), we refrain from deriving a spatially-resolved map for the extinction. We only note that ratios are generally $H\alpha/H\beta \gtrsim 3$, which is suggestive of the presence of dust both in the disk and tail of ESO137-001. Cortese et al. (2010a,b) indeed observed dust stripping from galaxies in cluster environments, supporting the idea that gas and dust are subject to similar perturbations.

5.5.2 Composite spectra

Having examined qualitatively the spatial variation of the different line ratios, in this section we exploit the ability to rebin IFU data in regions of interest. We generate high S/N composite spectra for a quantitative analysis of even weak emission lines. We focus on five characteristic regions, which exhibit different line ratios in Figure 5.7. These are: 1) the galaxy disk, including the nucleus; 2) the front region, defined as the area with enhanced [NII]/ $H\alpha$ ratio in the south-east of the galaxy disk; 3) the compact knots along the tail, which we have identified as HII regions; 4) the diffuse gas within the primary tail; 5) the $H\alpha$ “blob” in the outer tail.

The locations of these different regions are shown in Figure 5.8, while Figure 5.9 shows the composite spectra obtained by co-adding all spaxels in the selected apertures with a mean. Before generating the composite spectra, we remove the galaxy rotation component using the kinematic maps derived in section 5.4. For the regions 1 and 2, we further use the GANDALF code to remove the stellar continuum spectrum from the composite spectrum, as described above. The composite spectrum of the HII regions is instead obtained by averaging the individual spectra with inverse variance weights derived from the bootstrap noise spectra described below.

Figure 5.9 reveals that the wavelength at which all the emission lines peak is consistent with the galaxy’s redshift regardless of the transition under consideration. The largest offsets occur predominantly in the regions where the lines are fainter, but these are generally consistent with zero given the uncertainties on the line centroid. This empirical evidence justifies our previous assumption to peg the centroid of different emission lines to the one of $H\alpha$ when deriving the flux maps in the full data cube.

Furthermore, as already discussed above, this figure readily shows that the flux ratios change as a function of the spatial position in the disk of the galaxy and in the tail, which is suggestive of various excitation mechanisms at work in different regions. For instance, the front region has the highest [NII] to $H\alpha$ ratio, while [OIII] λ 5007 is most strongly detected in the bright $H\alpha$ knots along the tail. Furthermore, [OI] λ 6300 emission is visibly stronger throughout the tail than in the main galaxy body.

This visual assessment of the data is more quantitatively supported by the integrated fluxes, listed in Table 5.2. The uncertainties on the line fluxes are computed from 100 bootstrap realizations of the median spectra. More specifically, the fitting procedure is repeated for each bootstrap realization, and we assume the 1σ confidence level of the

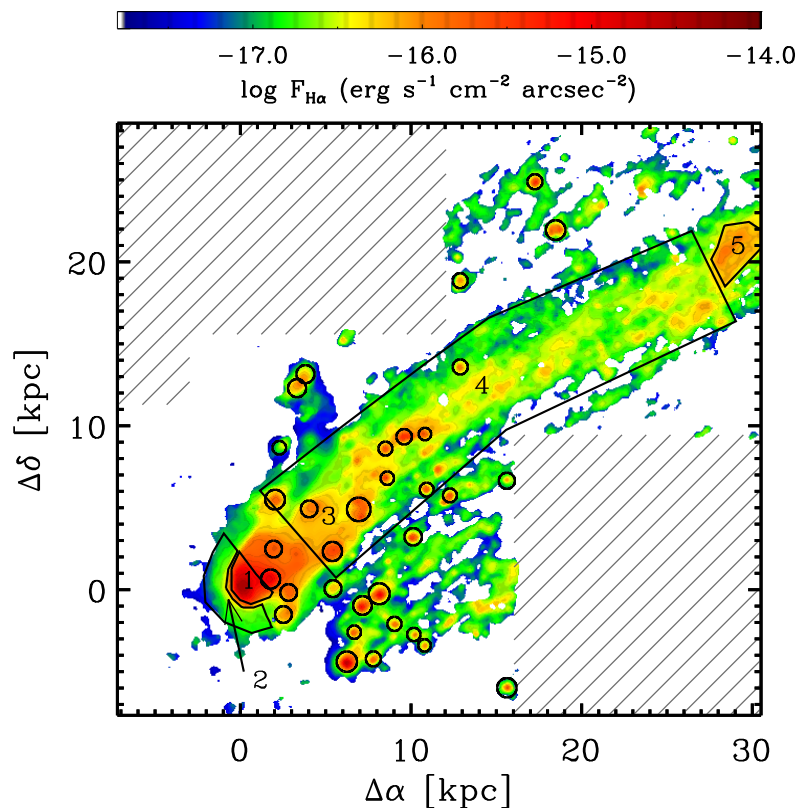


Figure 5.8: $H\alpha$ map of ESO137-001. Black apertures represent selected regions used to create composite spectra as described in the text. Specifically, circular apertures identify HII regions (3), while polygons identify (from left to right): the front region (2); the main body of the galaxy (1); the diffuse gas within the tail (4); the blob in the outer tail (5). Areas not covered by MUSE observations are shaded in grey.

measured line fluxes as the formal uncertainty. This approach, however, does not take into account the correlated noise contribution, which is estimated to be a factor ~ 2 for IFU observations where a similar number of pixels is combined (e.g. Förster Schreiber et al., 2009). For undetected lines, we quote the 3σ confidence level obtained from the standard deviation of the continuum values on both sides of each line.

In the next section, we will attempt to characterize the density, temperature, and metallicity of the gas, by means of emission line diagnostics leveraging a combination of spatially resolved maps and composite spectra.

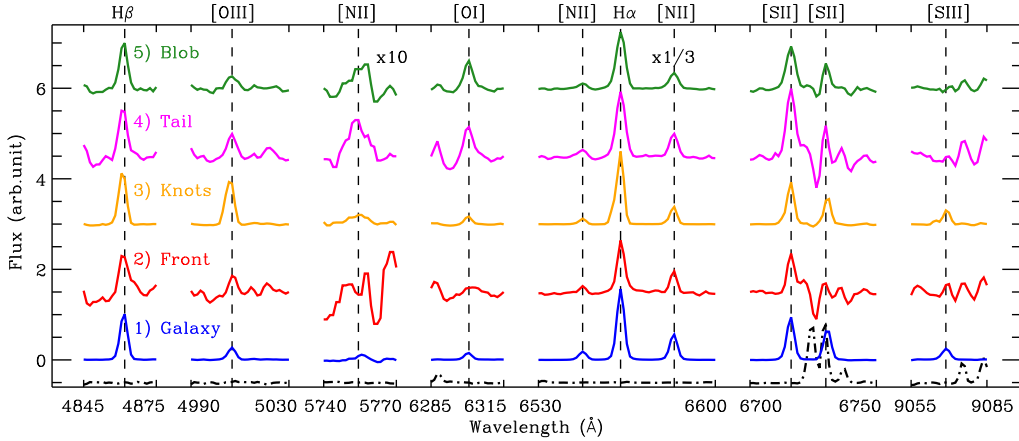


Figure 5.9: Coadded rest frame spectra of the five regions of ESO137-001 shown in Figure 5.8. The spectra are normalized to the $H\beta$ intensity and shifted along the vertical axis to facilitate the comparison. Only the emission lines relevant to this study are shown. In case of [OIII], and [OI] doublets only the strongest line is shown. For visualization purposes, the $H\alpha$ and [NII] complex have been scaled by a factor of three, while the [NII] λ 5755 is enhanced a factor of 10. The lowermost spectrum (dash-dotted line) is a night sky spectrum (not in scale) extracted from the datacube.

5.5.3 Properties of the diffuse gaseous tails

Density

The electron density in the ionized gas can be measured, for instance, through collisional de-excitation in doublets of the same ion from different levels with comparable excitation energy. One such doublet is [SII] λ 6716/ λ 6731. Unfortunately, the intensity ratio is only weakly sensitive to the density for $n_e < 10^2 \text{ cm}^{-3}$, where collisional excitation is generally followed by photon emission. Moreover, in the case of ESO137-001, one of the [SII] lines falls onto a bright skyline, severely compromising the derived fluxes especially in the low surface brightness regions of the tail. For these reasons, we are forced to resort to other estimators for the gas density.

A crude order of magnitude estimate for the electron density can be obtained from the observed $H\alpha$ luminosity, together with an estimate of the volume. More specifically, in equilibrium, the $H\alpha$ luminosity in a given spatial region can be written as

$$L_{H\alpha} = n_e n_p \alpha_{H\alpha}^{\text{eff}} V f h \nu_{H\alpha} \quad (5.1)$$

where n_e is the number density of electrons, n_p is the number density of protons (hydrogen ions), $\alpha_{H\alpha}^{\text{eff}}$ is the $H\alpha$ effective recombination coefficient, V is the volume of the emitting region, f is the filling factor, h is the Planck's constant and $\nu_{H\alpha}$ is the frequency of the $H\alpha$ transition.

For the geometry of the tail, we assume a cylinder with line-of-sight depth equal to the diameter in the plane of the sky. The diameter, as measured on the $H\alpha$ image, is

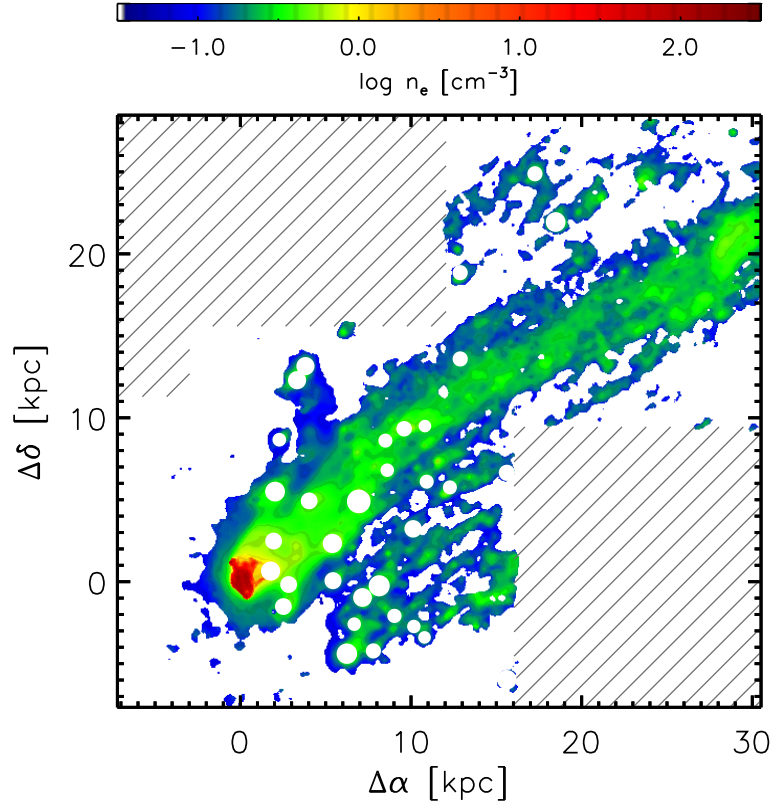


Figure 5.10: Map of the mean electron density obtained from the $H\alpha$ surface brightness and a cylindrical volume from the tail. A filling factor $f = 0.05$ is assumed. Areas not covered by MUSE observations are shaded in grey. The HII regions along the tail are excluded from the map.

$D \sim 0.3$ arcmin throughout the entire length of the tail, or about $D \sim 5.5$ kpc at the distance of ESO137-001. This value is $\sim 50\%$ larger than the diameter used by Sun et al. (2007), as the superior depth of the MUSE observations allows us to also detect the lower surface brightness components of the tail. In our calculation, we consider single spaxel with area A as individual regions. The filling factor is instead unconstrained. However, there is indication that the warm ionized gas in the tail can be very clumpy, as shown for instance in hydrodynamic simulations of ram-pressure stripping (e.g. Tonnesen et al., 2011). Thus, we assume $f = 0.05$, as in Sun et al. (2007). Finally, we assume that the gas is fully ionized ($n_e = n_p$) and $\alpha_{H\alpha}^{\text{eff}} = 1.17 \times 10^{-13} \text{ cm}^3 \text{ s}^{-1}$ (Osterbrock & Ferland, 2006). As previously noted, the excitation mechanisms of the tail are unknown and the value of the recombination coefficient is uncertain. Moreover, the assumption of a cylindrical volume implies that the line-of-sight depth of the cylinder depends on the spatial position. However our calculation aims to provide only a order of magnitude estimate for the gas density and other quantities, such as the filling factor, are likely to dominate the error

budget in this calculation. Under these assumptions, manipulating equation 5.1 we obtain

$$n_e = \sqrt{\frac{L_{\text{H}\alpha}}{\alpha_{\text{H}\alpha}^{\text{eff}} A D f h \nu_{\text{H}\alpha}}} \quad (5.2)$$

Figure 5.10 shows the resulting map for the gas density obtained following equation 5.2, where HII regions have been excluded from the calculation. From the map, we find that the average density in the tail, although uncertain, is of the order of 0.3 cm^{-3} , in agreement with the estimate of Sun et al. (2007). Very similar densities are found by Yagi et al. (2007) and Fossati et al. (2012) in ram pressure stripped tails in the Coma cluster, once a common filling factor is assumed. As a cross check, we also examine the composite spectrum of the tail, where the improved S/N also allows us to estimate the density with the direct method. In this case, we find an upper limit at $n_e \leq 1 \text{ cm}^{-3}$ typical for the low density regime, which is again consistent with our spatially-resolved measurement.

In the nucleus, the S/N of both [SII] lines is high (see Figure 5.9) and the density is in the intermediate regime where the doublet line ratio becomes a useful diagnostic of the n_e . We can therefore use the direct method, obtaining $n_e \sim 10^2 \text{ cm}^{-3}$.

With an estimate for the density, we then compute the recombination time-scale for the ionized gas:

$$\tau_r = \frac{1}{n_e \alpha_A} \sim \frac{10^5}{n_e} \text{yr} \quad (5.3)$$

where α_A is the total recombination coefficient. At the high densities of the nucleus, the gas would recombine in less than 10^3 yr , and the observed emission arises from on-going star formation that keeps the gas ionized. On the other hand, the gas in the tail can remain ionized up to $\sim 1 \text{ Myr}$ following ionization. It is therefore interesting to consider whether the gas is being stripped as ionized and recombines in the tail, or whether other ionization mechanisms are needed to power the observed emission. The orbital study of Jáchym et al. (2014) suggests an infall velocity of 3000 km s^{-1} , which means that material at $\sim 30 \text{ kpc}$ has been stripped at least 10 Myr ago, assuming instantaneous acceleration of the gas. Thus, according to our crude estimate, only the inner part of the tail could be recombining after being stripped in a ionized phase. Other excitation mechanisms are at work in the full extent of the tail, as shown by simulations (Tonnesen & Bryan, 2010). Clearly, the uncertainties on the density and thus in the recombination timescale hamper firm conclusions. Arguably, both recombination of stripped gas in the ionized phase and from gas excited in situ within the tail are powering the observed emission.

Electron temperature

The high S/N of the composite spectra allows the detection of emission lines that are suitable to measure the electron temperature of the gas in the galaxy and its tail. In principle, a few transitions like [OIII], [NII], and [SIII] could be used for this purpose, as emission lines from levels with different excitation energies fall into the optical window.

However, given the wavelength coverage of our MUSE data, we are restricted to the use of [NII] for this calculation.

The electron temperature (T_e) can be derived following Osterbrock & Ferland (2006), their equation (5.5):

$$R_{[\text{NII}]} = \frac{8.23 e^{(2.5 \times 10^4 / T_e)}}{1 + 4.4 \times 10^{-3} n_e / T_e^{1/2}} \quad (5.4)$$

where $R_{[\text{NII}]} = [\text{NII}]\lambda 6584, 6548 / [\text{NII}]\lambda 5755$. We assume the density dependence in the denominator is negligible. The error introduced in making this assumption is 0.4% (for $T_e \sim 10^4 \text{K}$) in the nucleus where $n_e \sim 10^2 \text{cm}^{-3}$, and smaller elsewhere. Under this assumption, T_e is given by:

$$T_e = \frac{2.5 \times 10^4 \text{ K}}{\ln(0.121 \times R_{[\text{NII}]})} \quad (5.5)$$

In this calculation we use observed line ratios not corrected for dust extinction, primarily because of our inability to derive the extinction curve especially in the tail and blob, where the ionization mechanisms are more uncertain. The values of T_e must therefore be taken as lower limits, given that $R_{[\text{NII}]}$ may in fact be lower than the value we measure. However, we checked that in the disk of the galaxy, where there is substantial extinction ($A_V \sim 1.44 \text{mag}$) the temperature would increase by only $\sim 6\%$.

Clearly, the accuracy of this direct method is limited by the detection of the faint [NII] $\lambda 5755$ line. In our composite spectra, we obtain marginal detections in all the regions, except the front. Fortunately, the wavelength where this line falls is clean from skylines and we can attempt a measurement of the temperature even in a moderate S/N regime. Robust fits are obtained by fixing the line width and centroid for all the [NII] lines, therefore avoiding spurious solutions for the faint [NII] $\lambda 5755$ line. Bootstrap errors are used to derive the uncertainties for the electron temperatures. T_e are then $(0.96 \pm 0.19) \times 10^4 \text{ K}$ in the galactic disk, $(1.8 \pm 0.3) \times 10^4 \text{ K}$ in the stacked HII regions and $(2.1 \pm 0.9) \times 10^4 \text{ K}$, $(2.0 \pm 0.5) \times 10^4 \text{ K}$ for the tail and the blob respectively. At face value, this measurement suggests that the gas in ESO137-001 has temperatures commonly seen in photoionized regions, perhaps with a hint of a lower value in the galactic disk compared to the tail or the HII regions. However, given the large uncertainties on the line flux and to lesser extent on the wavelength-dependent dust extinction, these values must be taken with caution. Deeper observations are thus required to confirm this result with higher S/N detection of the weak [NII] $\lambda 5755$.

BPT diagnostics

In section 5.5.1, we have shown two dimensional maps of various line ratios. We now use the higher S/N composite spectra to study emission line ratios from the detections of $\text{H}\beta$, [OIII], [OI], [NII] and $\text{H}\alpha$ in the 5 characteristic regions of ESO137-001, defined in Figure 5.8. Figure 5.11 shows the BPT diagrams for these composite spectra, using the same color coding as in Figure 5.9. The 30 individual HII regions with detections in all the line ratios are also shown as small grey points. The error bars for the HII regions reflect the

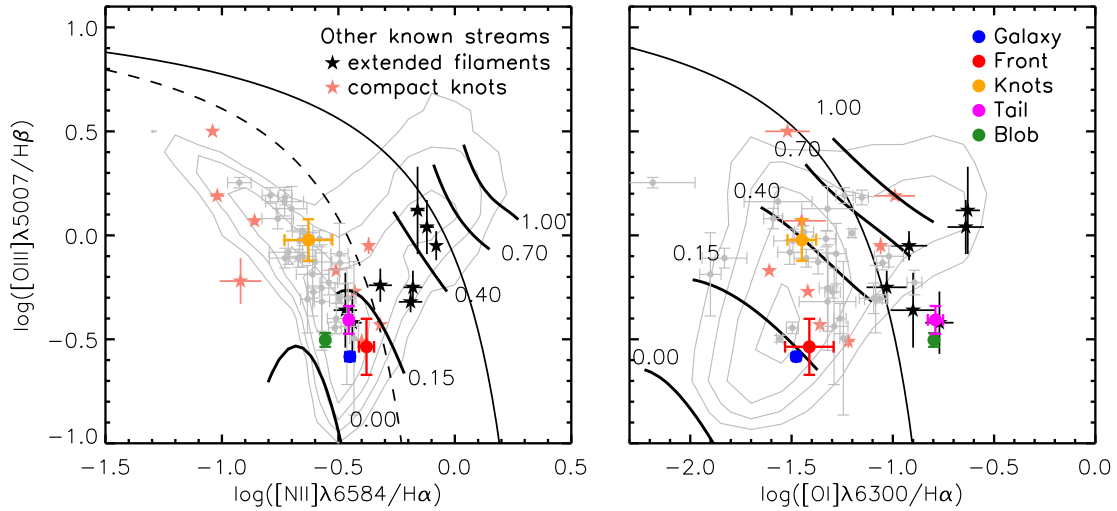


Figure 5.11: BPT diagrams for the composite spectra extracted from the 5 characteristic regions of ESO137-001. Data points are color coded as in Figure 5.9. Individual knots with robust detections in all the line ratios are also shown with small grey circles. The error bars shown for the composite knot spectrum reflect the sample variance, while the errors on the mean line ratios are of the size of the datapoint. Black (pink) stars are extended filaments (compact knots) from Yagi et al. (2007), Yoshida et al. (2012), and Merluzzi et al. (2013). The grey contours are obtained from the nuclear spectra of a random sample of Sloan Digital Sky Survey (SDSS) galaxies at $0.03 < z < 0.1$. The solid black line is the extreme starburst separation between photoionisation and AGN/shock heating from Kewley et al. (2001). The dashed black line is the empirical division from Kauffmann et al. (2003) based on SDSS data. Thick solid lines highlight different fractions (from 0 to 1) of $\text{H}\alpha$ flux contributed by shocks from models by Rich et al. (2011).

sample variance, while errors on the mean line ratios are of the size of the datapoint. The grey contours are obtained from the nuclear spectra of a random sample of SDSS galaxies selected from the DR12 (Alam et al., 2015) database at $0.03 < z < 0.1$, while the solid black line is the extreme starburst separation between photoionisation and AGN/shock heating from Kewley et al. (2001). The dashed black line is the empirical division from Kauffmann et al. (2003) based on SDSS data. The thick solid lines highlight different fractions (from 0 to 1) of $\text{H}\alpha$ flux contributed by shocks from models by Rich et al. (2011). Moreover, in Figure 5.11 we show the line ratios obtained from the literature for extended ionized gas filaments (black stars) and compact star forming knots (pink stars). Yagi et al. (2007) observed the tail behind D100, a galaxy in the Coma cluster. We average the line ratios of their slits along the tail, weighting by the $\text{H}\alpha$ flux. Yoshida et al. (2012) observed several knots and extended diffuse emission filaments behind two galaxies infalling into the Coma cluster (IC4040 and RB199). Lastly, Merluzzi et al. (2013) observed a ram pressure

stripped galaxy in the Shapley Supercluster, and we show the line ratios of their extra planar ionized gas regions.

From the left panel, it is clear that all the HII regions in the tail as well as the central galaxy reside in the locus occupied by gas photoionized by stars. These HII regions span a broad range of values in $[\text{OIII}]\lambda 5007/\text{H}\beta$, which is indicative of different ionization parameters. This result is consistent with the line ratios of HII regions observed in the tails of other ram pressure stripped galaxies from the literature (pink stars in Figure 5.11). Thus, despite the extreme ram pressure stripping suffered by ESO137-001, the star formation properties of the galaxy disk and of the HII regions embedded in the tail appear typical. Indeed, the stacked spectrum of the galactic disk is well within the region where most of local galaxy nuclei are found. It should be noted, however, that this analysis is restricted to the most bound parts of the ESO137-001 disk, as the star formation activity is completely truncated in the outer parts of the disk, where ram pressure has already removed the galaxy ISM and no $\text{H}\alpha$ emission is found.

The galaxy front stands out as the region with the strongest $[\text{NII}]$ contribution, which is however weak compared to the emission expected for a LINER or gas that is purely shock heated. This evidence, combined with the weak $[\text{OI}]$ complicates the interpretation of which excitation mechanism is responsible for the gas emission. Indeed at most 15% of the excitation can be contributed by shocks in the front, according to the models by Rich et al. (2011). Moreover, the gas is kinematically cold in this region, perhaps surprising in presence of strong shocks moving through the gas. We therefore conclude that this region is mainly ionized, with an elevated $[\text{NII}]/\text{H}\alpha$ ratio but a faint $[\text{OIII}]$ emission indicative of a weak ionization parameter. As discussed above, however, we cannot rule out the contribution of shocks, as the separation between a putative thin shock-dominated region and the bulk of the photoionized ISM in the ESO137-001 disk is poorly resolved in our observations. Moreover, composite spectra from extended regions are light weighted, and thus the measured fluxes near density discontinuities tend to be biased towards the brightest regions.

On the other hand, the tail and the bright blob in the outer tail show a contribution from very strong $[\text{OI}]$ emitting gas, much beyond the locus typical for local galaxies. This evidence is consistent with the strength of $[\text{OI}]$ in all the other ram pressure stripped tails observations collected from the literature. However, the $[\text{NII}]/\text{H}\alpha$ ratio is weaker compared to most of the other tails, a fact that is difficult to reconcile with ordinary shock-heating models. We note that the tail of ESO137-001 hosts several HII regions, especially in the secondary tail where lower values of $[\text{NII}]/\text{H}\alpha$ can be found. In this case, we are tempted to conclude that such peculiar line ratios in the tail arise from a combination of recombination from photoionized gas, (including gas that was stripped as ionized from the galaxy or that is ionized in situ by the HII regions), plus a shock contribution from the turbulence of the gas itself. This scenario is further supported by the high velocity dispersion of the gas along the tail (Fumagalli et al., 2014; Jáchym et al., 2014).

Line	λ_r (Å)	Δ_v (km s ⁻¹)	Region 1 (Disk)	Region 2 (Front)	Region 3 (Knots)	Region 4 (Tail)	Region 5 (Blob)
H β	4861.33	0	1.000±0.022	1.000±0.065	1.000±0.013	1.000±0.064	1.000±0.020
[O III]	4958.91	<9 (3)	0.095±0.006	<0.189	0.322±0.066	0.111±0.058	<0.141
[O III]	5006.84	<10 (4)	0.261±0.007	0.252±0.102	0.952±0.174	0.392±0.060	0.314±0.023
[N II]	5754.64	<58 (3)	0.016±0.009	<0.135	0.034±0.008	0.065±0.045	0.047±0.019
[O I]	6300.30	<24 (3)	0.151±0.005	<0.173	0.145±0.010	0.694±0.060	0.636±0.018
[O I]	6363.78	<19 (1)	0.050±0.005	<0.147	<0.051	<0.138	0.269±0.026
[N II]	6548.05	<22 (3)	0.501±0.017	0.322±0.025	0.287±0.056	0.467±0.024	0.357±0.010
H α	6562.82	<20 (1)	4.529±0.092	2.998±0.038	3.954±0.140	4.267±0.040	3.984±0.019
[N II]	6583.45	<24 (3)	1.604±0.065	1.190±0.036	0.928±0.106	1.499±0.032	1.107±0.013
[S II]	6716.44	<23 (5)	0.921±0.022	<0.174	0.745±0.039	1.629±0.116	1.056±0.015
[S II]	6730.81	<20 (5)	0.651±0.016	<0.219	0.470±0.037	<0.297	0.422±0.030
[S III]	9068.60	<16 (2)	0.249±0.010	0.210±0.055	0.241±0.030	<0.216	<0.108
A_V			1.44±0.09	-	1.02±0.25	-	-

Table 5.2: Fluxes measured in the composite spectra of the five regions shown in Figure 5.9. The values are normalized to the H β flux and are not corrected for dust extinction. We also report the dust extinction in units of A_V , measured from the Balmer decrement for the regions dominated by photoionisation. Δ_v is the absolute value of the largest offset peak centre relative to H β . The value in parenthesis indicates the region where this occurs.

5.5.4 Properties of the HII regions

In this section we estimate the density, metallicity and ionization parameters for regions where the gas is mainly photoionized by young stars, namely the HII regions embedded in the tail and the body of the ESO137-001 galaxy.

As a first step, we correct the emission line spectra for dust extinction using the Balmer decrement. Having restricted our analysis to purely photoionized regions, and with a temperature of $T \sim 10^4$ K, we can assume a theoretical $H\alpha/H\beta$ ratio from case B recombination. This value depends only weakly on density and temperature and is 2.86 in the low density limit at $T = 10^4 K$ (Osterbrock, 1989). In case of density and temperature variations, the variation in the theoretical $H\alpha/H\beta$ ratio is minimal. Therefore the variations in the observed ratios can be mainly attributed to variations in the dust content. We compute the Balmer decrement as:

$$C(H\beta) = \frac{\log(2.86) - \log\left[\frac{F(H\alpha)}{F(H\beta)}\right]_{\text{obs}}}{f(H\alpha)} \quad (5.6)$$

where $f(H\alpha) = -0.297$ is the selective extinction of H α relative to H β from the Galactic extinction law of Cardelli et al. (1989), which we also use for the correction of all the observed emission lines. Under these assumptions, we express the attenuation in units of $A_V = 2.5 \times 0.86 \times C(H\beta)$. A map of the extinction of the HII regions is given in the bottom panel of Figure 5.12. The extinction is on average 1 mag, with substantial scatter from region to region, suggestive of varying dust content within the body and tail of this galaxy (and perhaps along the line of sight to it). No clear trends are visible with the position

along the tail.

The density for the HII regions in the tail, can be estimated following eq. 5.1 but adopting a spherical geometry in which the volume is $V = 4\pi R^3/3$. In our observations, we cannot resolve the size of the individual HII regions and we assume a constant radius $R = 20$ pc (see Gutiérrez & Beckman, 2010). Also for the HII regions, the filling factor is unknown and likely to be a function of radius (Cedr es et al., 2013). In this case, we assume $f = 1$ meaning that our estimates provide a lower limit for the local density of these HII regions. Although the uncertainty on the density is very large, we find $n_e \gtrsim 10^2 \text{ cm}^{-3}$, at least two orders of magnitude denser than the diffuse gas in the tail.

With the dust corrected spectra, we can infer the chemical abundance of the HII regions using photoionisation modeling. The metallicity is of great importance to understand how the star formation proceeds in stripped tails, and how much of the stripped gas pollutes the intracluster environment. Another interesting parameter, a by-product of the metallicity analysis, is the ionization parameter (q), defined as the flux of ionizing photons per unit gas density.

In order to derive the gas phase metallicity (O/H) and ionization parameter of the gas, we use the IZI (Blanc et al., 2015) code to fit the observed nebular emission lines in our spectra against photoionisation models. For this analysis, we use the input models from Kewley et al. (2001), who derive line fluxes from the MAPPINGS-III code with input stellar spectra computed using the STARBURST99 code (Leitherer et al., 1999). Those models are computed for a gas density $n_e = 350 \text{ cm}^{-3}$, a constant star formation rate, and they assume a Salpeter (Salpeter, 1955) initial mass function (IMF). The IZI code uses Bayesian statistics to derive the joint marginalized probability density function (PDF) for O/H and q . Here, we run the code with flat priors, with the exception of a handful of problematic cases. Indeed, during the analysis we identify 4 HII regions for which the posterior PDF has multiple peaks for at least one of the parameters of interest. In these few cases, we impose a Gaussian prior on q which is motivated by the excellent linear correlation ($r = 0.91$) between q and the $[OIII]\lambda 5007/H\beta$ ratio observed in the remaining HII regions where the PDFs are well behaved. We checked that the results do not change if we assume models with density $n_e = 10 \text{ cm}^{-3}$, as data constrain only the ionization parameter with a degeneracy between density and intensity of the ionizing radiation.

Maps of O/H and q are shown in the top panels of Figure 5.12. We start by noting that the metallicity in the body of the galaxy is $\log(O/H) + 12 \sim 8.65$, which is consistent with the determination $\log(O/H) + 12 \sim 8.7$ by Sun et al. (2007), obtained using different data but the same suite of models. This agreement confirms the lack of systematic biases due to flux calibrations in the analysis. The uncertainty on the metallicity of individual HII regions is 0.1dex as obtained from the widths of the posterior distributions. However, the use a specific grid of models introduces an additional systematic uncertainty, which we estimate around 0.15dex error by repeating the analysis with different models. Therefore the metallicity is known with a quite large uncertainty.

The spatial variations we find in Figure 5.12 are small and consistent with constant metallicity throughout the tail with an average value of $\log(O/H) + 12 \sim 8.55 \pm 0.06$, which is 0.75 times the value assumed for the Solar metallicity. A similar behavior is seen for

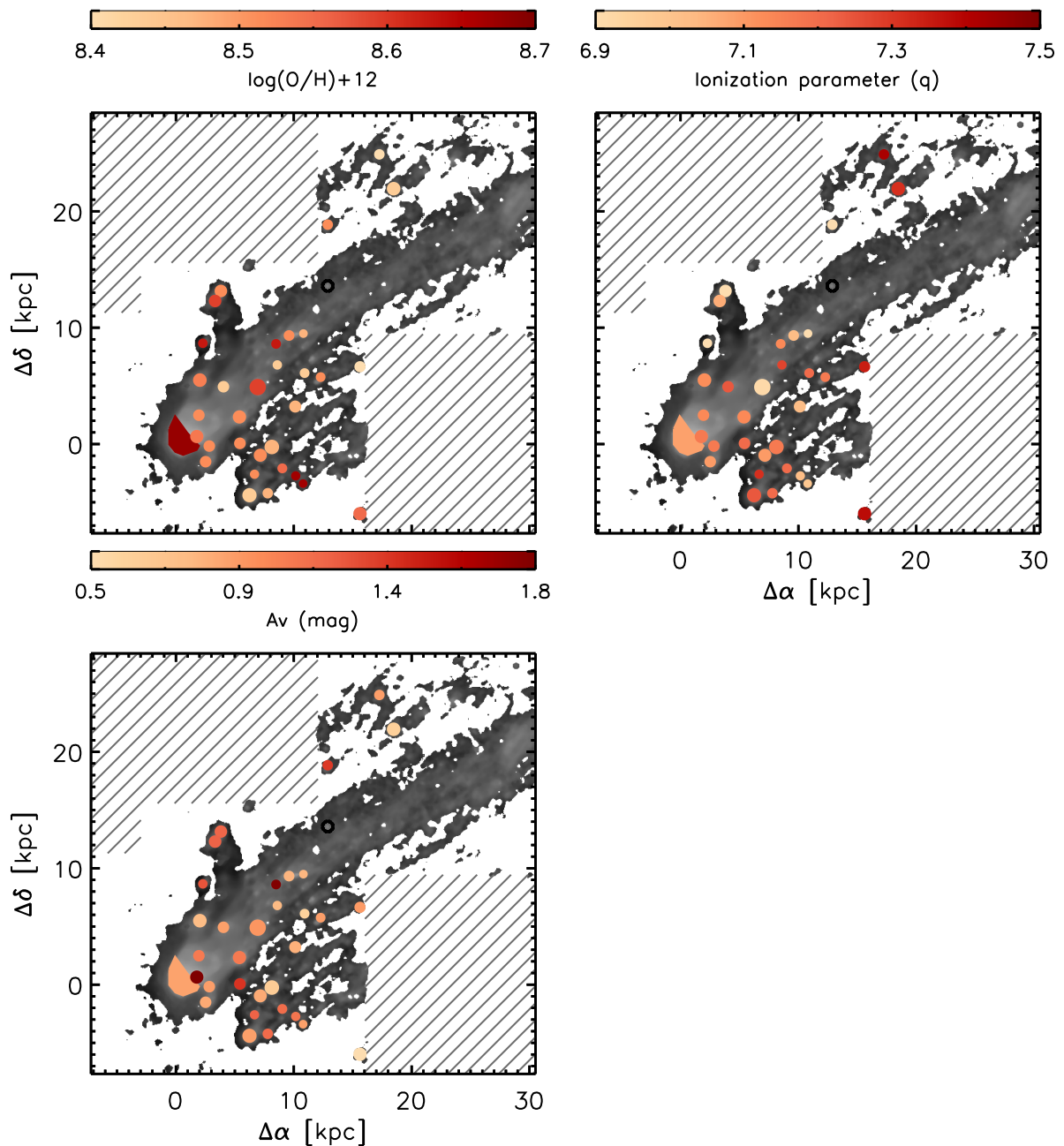


Figure 5.12: Top: maps of the gas phase metallicity and ionization parameter for the HII regions and the disk of ESO137-001 obtained from nebular emission lines fitting with the IZI code. Bottom: map of the dust extinction in the same regions, computed from the Balmer decrement. One HII region with insufficient S/N in $\text{H}\beta$ is shown as an empty black circle. The $\text{H}\alpha$ diffuse emission is shown in grey scale as a reference for the position of the HII regions along the tail.

the ionization parameter, although uncertainties in individual measurements hamper firm conclusions on a spatial variation, if any is present.

Lastly, we convert the H α de-reddened flux into a SFR using the Kennicutt (1998a) calibration. The total SFR of the selected HII regions is $SFR = 0.62 \pm 0.03 M_{\odot} \text{ yr}^{-1}$, in excellent agreement with the value $SFR = 0.59 M_{\odot} \text{ yr}^{-1}$ found by Sun et al. (2007) using the same SFR calibration and a Salpeter IMF. This confirms once again the quality of the absolute flux calibration of the MUSE observations. We caution however that, because of the low intrinsic SFR of individual HII regions, a full treatment of the stochastic IMF sampling is likely required for a more precise measurement of the SFR (da Silva et al., 2014).

While there is no systematic trend of the physical properties of these HII regions with respect to their spatial location, the distribution of HII regions is in itself peculiar and traces the imprint of the formation mechanism. One third of the HII regions are found in leading edge of the secondary tail and they are among the brightest that we have observed in ESO137-001. Other HII regions are distributed along the main tail and only a few of them are found at a distance greater than 15 kpc from the galactic disk. Moreover, most of the HII regions are located in the inner part of the tail, where the velocity dispersion of the gas on scales larger than individual HII regions is low ($\sigma \sim 25 - 50 \text{ km s}^{-1}$). In fact, the most distant HII regions are not found in the primary tail, where we observe an increased velocity dispersion. Rather, they reside in the diffuse gas in the northern part of our field of view, where the velocity dispersion is indeed low. If HII regions were formed in the galactic disk and stripped downstream by ram pressure, then they would be expected to lie anywhere in the tail. However, if instead the HII regions are formed in situ within the tail, then they are preferentially expected to reside where the gas is less turbulent, and the gas can cool and self-shield to form molecules.

This argument is complicated by age effects, as the stripped HII regions would progressively fade as the gas is accelerated to larger distances from the galaxy body. Further, some of the HII regions may not survive the violent stripping and hydrodynamic interactions with the hot ICM. However, another piece of evidence in favor of in situ formation, at least for some HII regions, comes from the analysis of Sun et al. (2007), who reported young ages $< 8 \text{ Myr}$ for all the HII regions considered. If they were formed in the galaxy, then a clearer age gradient would be expected, as the galaxy moves in the cluster potential and the HII regions trail behind it. As we noted, also Sun et al. (2007) caution that older HII regions may have faded in the outer tail, below the depth of our observations.

5.6 Conclusions

In this chapter, we have presented the analysis of the physical properties of the disk and stripped tail of ESO137-001, a galaxy that is infalling into the nearby Norma cluster at high velocity. Leveraging the sensitivity and spatial resolution of MUSE observations, we have studied for the first time 2D maps of kinematics and emission line ratios within a poster child of violent ram-pressure stripping. Our results can be summarized as follows:

- The kinematic maps revealed that the stripped gas retains the imprint of the disk rotational velocity up to ~ 20 kpc downstream, with low velocity dispersion. Further on along the tail, the gas velocity dispersion increases above 100 km s^{-1} . Moreover, we observed an ordered velocity field for the stellar disk, which convincingly points to ram pressure as the mechanism for gas removal.
- Considering the tail, the analysis of line ratios shows high values of $[\text{NII}]/\text{H}\alpha$ and $[\text{OI}]/\text{H}\alpha$. Thus, photoionisation alone cannot be responsible for the observed emission, and the contributions of other mechanisms is required. A contribution from shocks is likely, also given the turbulent nature of the gas in the outer tail, but we cannot exclude other excitation mechanisms. At the same time, line ratios are not as strong as commonly seen in pure shock heating models, and the gas temperature of $(2.1 \pm 0.9) \times 10^4 \text{ K}$ is similar to what found in photoionized gas. Part of the emission, particularly at close separations from the galaxy, may originate from recombination of photoionized gas stripped from the main body of the galaxy. The electron density in the tail is indeed low, $n_e \sim 0.3 \text{ cm}^{-3}$, and thus the recombination timescale is long enough to keep the gas ionized up to a few kpc downstream.
- The bulk of the front region where the galaxy ISM first collides with the hot ICM is not dominated by strong shocks, as $[\text{OI}]$ is only weakly or mostly undetected in our observations. Line ratios are mostly consistent with photoionized gas, although with a higher $[\text{NII}]/\text{H}\alpha$ ratio compared to the main body of the galaxy. We caution, however, that the front region is poorly resolved in our observations, and the separation with the bulk of the galaxy ISM is ambiguous.
- A large number of bright compact knots have been identified in the tail. These regions stand out because of their high $[\text{OIII}]/\text{H}\beta$ and low $[\text{NII}]/\text{H}\alpha$ and $[\text{OI}]/\text{H}\alpha$ ratios, fully consistent with the locus occupied by HII regions in the BPT diagram. These HII regions have densities $n_e \gtrsim 10^2 \text{ cm}^{-3}$ and temperatures $(1.8 \pm 0.3) \times 10^4 \text{ K}$. Thus, despite residing in ram-pressure stripped tails, they exhibit usual properties, commonly observed in HII regions. By comparing the line ratios to a grid of photoionisation models, we found a metallicity close to the solar value (~ 0.7 solar), albeit with substantial scatter.
- By comparing the spatial position of the HII regions to the kinematic maps presented in section 5.4, we found the HII regions are preferentially located in regions where the gas is dynamically cool, with a velocity dispersion less than $25 - 50 \text{ km s}^{-1}$. Indeed no HII regions are found in the outer part of the tail where Jáchym et al. (2014) found a high degree of turbulence. Moreover, the young ages of these regions as well as the lack of any trend in the physical properties as the function of their position suggest that these HII regions have formed in situ from the stripped gas in the tail, as also concluded by previous studies of this and similar systems (Sun et al., 2007; Arrigoni Battaia et al., 2012; Fossati et al., 2012). However, we can not fully exclude

selection biases that prevent us from detecting older HII regions stripped from the main body.

Our analysis represents the first attempt to characterize the rich physics of the ESO137-001 tail. In this work, we have primarily focused on the most common emission line diagnostics for shocks and photoionized gas. However, other processes such as thermal conduction the presence of magnetic fields may play a role in the excitation of the tail. Deeper observations of the full extent of the tail that have been recently obtained with MUSE (PI M.Sun), together with detailed radiative transfer models, will allow future explorations of other diagnostics (including weak lines) that are necessary to gain a more complete understanding of the physics at work in ram-pressure stripped tails.

Chapter 6

Conclusions

The aim of this thesis was to accurately quantify the environment of galaxies across 10 billion years of cosmic time, and to investigate the role of environmental processes in suppressing the star formation activity of satellite galaxies.

We reconstruct the density field by counting the number of neighbors around each galaxy. In this case the choice of environmental metrics is important. Very different techniques have been used in the literature to define environment (see Cooper et al., 2005; Muldrew et al., 2012; Etherington & Thomas, 2015, and references therein), with the choice typically driven by the specific goals and features of each dataset, thus hampering unbiased comparisons of the results.

In chapter 2, we started to address this issue by characterizing the environment in an ideal survey at $z \sim 1 - 2$, using a sample drawn from the semi-analytic model of galaxy formation (SAM) presented by Guo et al. (2013b). First we reconstructed the local density field by counting the number of neighbors in cylinders described by a fixed spatial aperture and depth in redshift space. By varying the size of the aperture we investigated how the density correlates with halo mass, which is a more physically motivated quantity.

The correlation between density and halo mass is not straightforward and subject to a variety of effects. We find that the local density poorly correlates with halo mass for central galaxies (those living at the bottom of the local potential well) using an aperture that corresponds to the virial radius of relatively massive haloes ($M_h \sim 10^{13.5} M_\odot$). This effect is caused by the well defined boundaries of haloes in the SAMs: galaxies within the virial radius are satellites hosted by a high-mass halo, while those outside the virial radius are central galaxies of low-mass haloes. The significant contamination from centrals beyond the virial radius of massive haloes is such that, at fixed density, the distribution of halo mass for centrals broadens so much that a correlation between density and median halo mass is lost. When the aperture used is smaller (probing scales inside the halo, and reducing the contamination mentioned above) a better correlation is recovered. On the other hand density correlates well with halo mass for satellites, irrespective of the aperture used.

We studied the impact of the average redshift accuracy of the sample on the recon-

struction of the density field. We find that the depth of the cylinder (in redshift space) should be increased for poorer redshift accuracy. A depth comparable to (or slightly larger than) the typical redshift accuracy, ensures that galaxies that are scattered along the line of sight by the uncertain redshifts are captured within the cylinder. Similar conclusions have been reached by Etherington & Thomas (2015).

In order to identify central and satellite galaxies using observational quantities we devised a method that uses the rank in stellar mass in a cylinder, under the assumption that the most massive galaxies are more likely to be centrals. We parametrized the performance of this method in terms of purity and completeness of the mass rank identification with respect to the SAM definition of centrals and satellites. We tested various spatial apertures within which the rank is computed. For central galaxies we found that the larger the aperture, the higher is the purity but the lower is the completeness. In order to improve both the completeness at low halo masses and the purity in massive haloes we have defined an adaptive aperture that depends on the stellar mass of the galaxy. This method is as good as a fixed aperture with radius 0.75 Mpc in terms of purity but with an improvement of $\sim 30\%$ in completeness at halo masses below $10^{13} M_{\odot}$. The method is not strongly sensitive to the stellar mass limit or the spectroscopic sampling rate of the dataset. Our results for purity and completeness are remarkably consistent with Knobel et al. (2012), despite the different method and sample selection.

A final test of our method is performed by recovering known trends (fraction of passive galaxies as a function of halo mass and stellar mass) predicted by the models. The fraction of passive centrals in the models increases as a function of halo mass, while it is almost independent of stellar mass. On the other hand the fraction of passive satellites increases with both stellar and halo mass. We have been able to recover these trends in a purely observable parameter space using the local galaxy density, stellar mass and stellar mass rank in the adaptive aperture. Because the density-halo mass correlation for central galaxies is far from being linear or independent of stellar mass, the passive fraction depends both on density and stellar mass for central galaxies (defined using the mass-rank). For satellite galaxies, instead, the correlation between halo mass and density is very good, therefore the passive fraction trends as a function of stellar and halo mass are easy to qualitatively recover using the density and the mass rank. A lower redshift accuracy does not negatively impact on this result. However, such a conclusion requires a combination of good photometric redshifts and deep survey limits as found also by Etherington & Thomas (2015). In conclusion, an accurate calibration of the halo mass can be achieved by jointly taking into account the local density and the stellar mass, with the extra constraint given by the mass-rank to define centrals and satellites. These results are presented in Fossati et al. (2015).

In chapter 3, we then applied our methods and tools to a real high-redshift sample drawn from the 3D-HST survey (Brammer et al., 2012) and a low redshift sample drawn from the SDSS survey (York et al., 2000). The 3D-HST survey combines imaging observations from CANDELS with deep slit-less spectroscopic observations in five well studied deep fields, namely COSMOS, GOODS-S, GOODS-N, AEGIS and UDS. The CANDELS observations

provide HST/WFC3 near infrared imaging in the F125W and F160W filters for all the fields, while 3D-HST followed-up a large fraction of this area with the F140W filter and the WFC3/G141 grism for slit-less spectroscopy. These spectroscopic observations provide high-quality redshifts ($\Delta z/(1+z) \sim 0.003$) for the vast majority of the objects in the field, dramatically improving upon the accuracy of photometric redshifts ($\Delta z/(1+z) \sim 0.015$).

We selected a magnitude limited sample ($F140W < 24$ mag) of galaxies in those fields and we computed the local density of galaxies in fixed apertures. Accurate edge corrections are applied using ground-based photometric catalogs which are more extended than the 3D-HST field where available, otherwise using simple aperture corrections. We take into account the reduced accuracy of photometric redshifts (in those extended catalogs) when the edge corrections are applied to the density measurements. Our reconstructed density field recovers the previously known massive structures (independently detected from the X-Ray emission of the intracluster/intragroup medium) across the full redshift range analyzed in this work.

As described above, a calibration of physically motivated quantities (e.g. halo mass, central/satellite status) from the local density and mass rank requires a mock catalog tailored to match the properties of the 3D-HST survey. We developed such a catalog and performed a careful match to the observational sample. First, we generated synthetic F140W magnitudes for a catalog of galaxies selected from the Henriques et al. (2015) SAM, and we applied a magnitude cut such that the volume density of 3D-HST galaxies is matched. Second, we degraded the redshift accuracy of mock galaxies such that the redshift accuracy of 3D-HST galaxies is matched. This was done as a function of mock galaxy brightness and predicted emission line S/N , which are the quantities driving the redshift accuracy of 3D-HST galaxies. As a result, the joint stellar mass and local density distributions of mock galaxies are remarkably similar to those of the 3D-HST sample.

Lastly we linked observed galaxies to multiple mock galaxies by matching in stellar mass, density in a fixed aperture, redshift, and stellar mass rank in the adaptive aperture described above. From this match we assigned to each 3D-HST galaxy a probability of being a central or a satellite (P_{cen} or P_{sat} , from the fraction of matching centrals in the mock sample) and probability density functions for the halo mass. This Bayesian approach fully takes into account sources of contamination (“interlopers”) via the matching process. We applied the same method to a $z = 0$ sample from SDSS, such that the physical processes driving the evolution of galaxies as a function of their environment can be studied over ~ 10 Gyr of cosmic time with a homogeneous technique.

In chapter 4, we made use of these two datasets to study the processes governing environmental quenching from $z \sim 2$ to the present day over a wide range of stellar and halo mass. We assumed a separability of mass-quenching and environmental-quenching as predicted (and observed up to $z \sim 1$) by Peng et al. (2010, 2012), and Kovač et al. (2014).

First we computed the fraction of passive galaxies (from the UVJ diagram in the 3D-HST sample and from a SFR cut in the SDSS sample) as a function of stellar and halo mass, for central and satellite galaxies. As no galaxy has a perfectly defined environment, the passive fractions we derived can be strongly affected by impurities in the central/satellite

classification and by cross-talk between the halo mass bins, given that each galaxy can contribute to each bin and both types. We then identify a sample of “pure” central galaxies, defined by $P_{\text{cen}} > 0.8$, and with an average $P_{\text{cen}} = 0.95$, which provides a reference for the passive fraction of galaxies subject only to mass-quenching.

In order to recover the passive fraction of “pure” satellites we instead used a parametric model, which we fit to the data in bins of stellar mass and redshift. We also estimated robust and realistic uncertainties through a Monte Carlo error propagation scheme that takes into account the use of probabilistic quantities.

By computing conversion fractions (i.e. the excess of quenched satellite galaxies compared to central galaxies at the same epoch and stellar mass, van den Bosch et al. 2008), we found that, within the range of our dataset, satellite galaxies are environmentally quenched in haloes of any mass up to $z \sim 1.2 - 1.5$. Above these redshifts the fraction of passive satellites is roughly consistent with that of central galaxies.

Under the assumption that the earliest satellites to be accreted become passive first, we derived environmental quenching timescales. These are long, and quenching started $\sim 2 - 5$ Gyr before the galaxies are observed at $z \sim 0.7 - 1.5$. Those times are even longer (5-7 Gyr) for galaxies observed at $z = 0$. The upper end of those ranges is reached by low mass galaxies, and the quenching timescale smoothly declines towards more massive galaxies. As they become comparable to the Hubble time by $z \sim 1.5$, effective environmental quenching of satellites is not possible at earlier times. More remarkably, a halo mass dependence is not detectable in our sample. By assuming that cosmological accretion stops when a galaxy becomes a satellite, we were able to interpret this evidence in a “gas exhaustion” scenario (i.e. the “overconsumption” model of McGee et al., 2014) where quenching happens because satellite galaxies eventually run out of the fuel which sustains further star formation.

We tested two toy models of satellite quenching: the “delayed then rapid” quenching scenario proposed by Wetzel et al. (2013) and a continuous “slow quenching” from the time of first infall. By comparing the observed SFR distribution for 3D-HST satellites to the predictions of these toy models we found that the scenario that best reproduces the data at $z \sim 0.5 - 1.5$ is “delayed then rapid”. Consistently with the results of Wetzel et al. (2013) at $z = 0$, we find that the fading of the star formation activity is a relatively rapid phenomenon ($\tau_f \sim 0.4 - 0.6$ Gyr, shorter to higher mass) which follows a long phase where satellite galaxies have a SFR which is indistinguishable from that of centrals at fixed stellar mass. By linking the fading to the depletion of molecular gas we concluded that the “delayed then rapid” scenario is best explained, even at high redshift, by the presence of a significant multi-phase reservoir which can cool onto the galaxy and replenish the star forming gas at roughly the same rate as the gas is turned into stars. These results are presented in Fossati et al. (2016), submitted to ApJ.

During the development of this thesis, the Multi Unit Spectroscopic Explorer (MUSE; Bacon et al., 2010) saw the first light at the ESO Very Large Telescope (VLT). With its unique combination of high efficiency, extended wavelength coverage, and large field of view ($1 \text{ arcmin} \times 1 \text{ arcmin}$), MUSE is a unique instrument to produce resolved spectroscopic

observations of local galaxies. Indeed, at high-redshift, studies of individual galaxies at the spatial resolution of ~ 1 kpc, needed to probe the physics of their environmental transformations, are only feasible in the best observing conditions with adaptive optics assisted instruments (e.g. SINFONI at the VLT). However these observations require a huge investment of observing time, and are limited by the small field of view. On the other hand, a wealth of multi-frequency data is available for galaxies in the local Universe, and therefore it is possible to identify galaxies undergoing environmental quenching (e.g. due to gaseous stripping or gravitational effects). The study of these objects improves our understanding of the physics of environmental processes which are important both at low- and high-redshift.

Taking advantage of the MUSE instrument we observed ESO137-001, a spiral galaxy infalling at high velocity into the Norma cluster ($M_h \sim 10^{15} M_\odot$, Woudt et al., 2008; Nishino et al., 2012). Previous multi-frequency observations (Sun et al., 2007, 2010; Jáchym et al., 2014) revealed an extended one sided tail of gas, which is being stripped from the galaxy disk. This tail is detected in ionized gas ($H\alpha$), hot gas (soft X-Ray), and in molecular gas. These data made ESO137-001 a poster child for studies of ram-pressure stripping. Leveraging the depth and unprecedented spatial resolution of MUSE, we have studied for the first time 2D maps of kinematics and emission line ratios within the galaxy and the stripped tail, which we presented in chapter 5.

The kinematic maps revealed that the stripped gas retains the imprint of the disk rotational velocity up to ~ 20 kpc downstream, with low velocity dispersion. Further on along the tail, the gas velocity dispersion increases significantly. Moreover, we observed an ordered velocity field for the stellar disk, which convincingly points to ram pressure as the mechanism for gas removal. Considering the tail we found that photoionisation by massive young stars cannot power the observed emission alone, and a contribution from shocks is likely, also given the turbulent nature of the gas in the tail. A large number of bright regions of star formation (HII regions) have been identified in the tail. They exhibit properties (density, brightness, metallicity), commonly observed in normal HII regions in galaxy disks. From their spatial location in the tail we conclude that these HII regions have formed in situ from the stripped gas, as also found by previous studies of this and similar systems (Sun et al., 2007; Arrigoni Battaia et al., 2012; Fossati et al., 2012). These results are presented in Fossati et al. (2016a), and in Fumagalli, Fossati et al. (2014).

6.1 Future prospects

The legacy value of the environment catalogs for 3D-HST and SDSS is potentially very large. Combining the 3D-HST environment catalog with large samples of galaxies from integral field spectroscopic surveys is a powerful tool to investigate the detailed effects of environment on the kinematic and photometric properties of stars and gas in galaxies. One of the largest efforts to map high redshift ($0.7 < z < 2.7$) galaxies is the KMOS^{3D} survey (Wisnioski et al., 2015). This survey is making use of 75 nights of guaranteed time observations to target a mass selected sample of ~ 600 galaxies selected from 3D-HST,

providing maps of the flux and kinematics of ionized gas from the $H\alpha$ + $[NII]$ line complex.

I am part of the KMOS GTO team and have been heavily involved in the observing strategy of KMOS^{3D}, and in developing advanced data reduction techniques. With other members of KMOS^{3D}, we pushed for reduction of systematic noise in the reduced data. This, combined with a strategy that prioritizes depth rather than sample size, allows us to reach lower $H\alpha$ surface brightness limits than other surveys at the same redshift. We also produced accurate bootstrap realizations to calculate errors and signal to noise.

Early results from KMOS^{3D} include the large fraction of disk dominated galaxies at $z \sim 1 - 2$ (Wisnioski et al., 2015), the ubiquitous presence of AGN driven outflows in massive galaxies (Genzel et al., 2014), the study of metallicity and metallicity gradients in the galaxy population (Wuyts, E., et al. 2014, 2016), and the evidence that high- z disks are strongly baryon dominated (Wuyts, S., et al. 2016), with a specific angular momentum consistent with that of the dark matter halo (Burkert et al., 2016). The analysis of the disk rotation curves shows that they indeed exhibit a decline with increasing radius beyond a characteristic turnover radius (Lang et al. in prep).

My role in KMOS^{3D} over the next months will be the analysis of the effects of environment. One of the signatures of cold gas stripping in dense environments is the truncation of ionized gas disks compared to the stellar disk (Koopmann et al., 2006; Fossati et al., 2013). With KMOS^{3D} we can extend this study to high redshift. Although the results presented in this thesis point towards gas consumption as the main driver of environmental effects, it is likely that a small population of galaxies experience dynamical stripping (Balogh et al., 2016) (mostly in massive clusters but also galaxies infalling on radial orbits in less massive groups), and we can directly test this hypothesis with KMOS^{3D} data. Similarly we can investigate the halo mass dependence of the disk fraction or the gas turbulence in the disk using kinematical maps from KMOS^{3D}. We can also study, by stacking centrals and satellites, if the rotation curves exhibit a different shape in satellite galaxies compared to centrals, which would imply a different baryon domination possibly caused by dynamical stripping of the gaseous component or tidal stripping of the dark matter halo. Finally, using the outflows classification from Genzel et al. (2014) we can test if the fraction of massive galaxies showing strong AGN driven outflows depends on the environment. It is possible that the gas ejected by outflows at large galactocentric radii can more easily be removed by stripping processes if the galaxy is orbiting in a more massive halo (Bahé & McCarthy, 2015; Boselli et al., 2015).

Our study of ESO137-001 demonstrates the feasibility of detailed analyses of the properties of diffuse low-surface brightness material with integral field spectrographs on 8-10 m class telescopes. By targeting galaxies like ESO137-001, future observations will be able to provide key information on how gas is ablated from galaxies that are infalling into clusters of different richness and along different orbits. Moreover, by examining spatially resolved line ratios, these studies will inform us about which mechanisms power the observed emission. I have successfully proposed such a project which will observe a mass complete sample of 85 galaxies in the Virgo cluster with MUSE. We will investigate how many galaxies exhibit signatures of stripping, or if other mechanisms (e.g. tidal interac-

tions) can explain the observations.

Our results can also be used to improve our understanding of the galaxy formation physics implemented in SAMs. Hirschmann et al. (2014) showed that by comparing the quenching times derived for observed SDSS galaxies to those estimated in the same way for mock galaxies (using the same technique of computing passive fractions, conversion fractions and lastly the quenching timescale) can improve our understanding of the physical recipes implemented in different SAMs. These authors found that the SAM presented by Guo et al. (2011) quenches satellite galaxies too rapidly compared to observations, suggesting that environmental effects are too efficient in the SAM. Repeating the same exercise at higher redshift would provide a larger baseline in cosmic time to constraint the free parameters regulating environmental quenching in the SAM recipes. Combined with the constraint that the stellar mass and density distributions of mock galaxies should match that of the observed samples, the SAM parameters can be iteratively modified to achieve a match between quenching times for mock satellites and those estimated from the observations.

In the future, the advent of the *James Webb Space Telescope*, *WFIRST* and *Euclid* space missions, as well as highly multiplexed spectroscopic instruments from the ground (e.g., *MOONS* at VLT; *PFS* at Subaru), will provide excellent redshift estimates for highly complete samples extending to fainter objects or to much larger areas, to which similar techniques to calibrate the environment can be applied. Our work on the 3D-HST sample and these future missions have a large potential for improving our understanding of how the evolution of galaxies is affected by the environment over a wide baseline of redshift and stellar mass. Lastly, the tools that we used to describe the environment can be refined by combining densities evaluated on different independent scales to better separate centrals and satellites and derive narrower halo mass PDFs. However, the combination of several scales requires non-parametric methods to link observed galaxies to mock galaxies. This can be achieved by machine learning algorithms based on artificial neural network, which can be trained on a subsample of the mock sample.

The result presented in this thesis that satellite galaxies retain a large multi-phase gaseous reservoir upon accretion into a massive halo will be tested by new and revolutionary observing facilities in the near future. The *Square Kilometer Array (SKA)* and the *Atacama Large Millimeter Array (ALMA)* will provide data for the atomic and molecular gas for large samples of galaxies extending to lower stellar mass and higher redshift, thus revolutionizing our understanding of how galaxies evolve and quench as a function of their environment.

Bibliography

- Abell, G. O. 1965, *ARA&A*, 3, 1
- Adami, C., Mazure, A., Ilbert, O., et al. 2005, *A&A*, 443, 805
- Aihara, H., Allende Prieto, C., An, D., et al. 2011, *ApJS*, 193, 29
- Alam, S., Albareti, F. D., Allende Prieto, C., et al. 2015, *ApJS*, 219, 12
- Allen, M. G., Groves, B. A., Dopita, M. A., Sutherland, R. S., & Kewley, L. J. 2008, *ApJS*, 178, 20
- Angulo, R. E., & White, S. D. M. 2010, *MNRAS*, 405, 143
- Arnouts, S., Cristiani, S., Moscardini, L., et al. 1999, *MNRAS*, 310, 540
- Arnouts, S., Vandame, B., Benoist, C., et al. 2001, *A&A*, 379, 740
- Arrigoni Battaia, F., Gavazzi, G., Fumagalli, M., et al. 2012, *A&A*, 543, A112
- Ashby, M. L. N., Willner, S. P., Fazio, G. G., et al. 2013, *ApJ*, 769, 80
- Bacon, R., Accardo, M., Adjali, L., et al. 2010, in *Proc. SPIE*, Vol. 7735, *Ground-based and Airborne Instrumentation for Astronomy III*, 773508
- Bahé, Y. M., & McCarthy, I. G. 2015, *MNRAS*, 447, 969
- Bahé, Y. M., McCarthy, I. G., Balogh, M. L., & Font, A. S. 2013, *MNRAS*, 430, 3017
- Baldry, I. K., Balogh, M. L., Bower, R. G., et al. 2006, *MNRAS*, 373, 469
- Baldry, I. K., Glazebrook, K., Brinkmann, J., et al. 2004, *ApJ*, 600, 681
- Baldwin, J. A., Phillips, M. M., & Terlevich, R. 1981, *PASP*, 93, 5
- Balogh, M., Eke, V., Miller, C., et al. 2004, *MNRAS*, 348, 1355
- Balogh, M. L., Morris, S. L., Yee, H. K. C., Carlberg, R. G., & Ellingson, E. 1997, *ApJ*, 488, L75

- Balogh, M. L., Navarro, J. F., & Morris, S. L. 2000, *ApJ*, 540, 113
- Balogh, M. L., McGee, S. L., Mok, A., et al. 2016, *MNRAS*, 456, 4364
- Bell, E. F., McIntosh, D. H., Katz, N., & Weinberg, M. D. 2003, *ApJS*, 149, 289
- Bell, E. F., Wolf, C., Meisenheimer, K., et al. 2004, *ApJ*, 608, 752
- Bennett, C. L., Bay, M., Halpern, M., et al. 2003, *ApJ*, 583, 1
- Berlind, A. A., Frieman, J., Weinberg, D. H., et al. 2006, *ApJS*, 167, 1
- Bertin, E., & Arnouts, S. 1996, *A&AS*, 117, 393
- Bielby, R., Hudelot, P., McCracken, H. J., et al. 2012, *A&A*, 545, A23
- Blanc, G. A., Kewley, L., Vogt, F. P. A., & Dopita, M. A. 2015, *ApJ*, 798, 99
- Blanton, M. R., Eisenstein, D., Hogg, D. W., Schlegel, D. J., & Brinkmann, J. 2005, *ApJ*, 629, 143
- Blanton, M. R., & Moustakas, J. 2009, *ARA&A*, 47, 159
- Blanton, M. R., & Roweis, S. 2007, *AJ*, 133, 734
- Bleem, L. E., Stalder, B., de Haan, T., et al. 2015, *ApJS*, 216, 27
- Boissier, S., Boselli, A., Duc, P.-A., et al. 2012, *A&A*, 545, A142
- Boselli, A. 1994, *A&A*, 292, 1
- Boselli, A., Boissier, S., Cortese, L., & Gavazzi, G. 2008, *ApJ*, 674, 742
- Boselli, A., Boissier, S., Cortese, L., et al. 2006, *ApJ*, 651, 811
- Boselli, A., Cortese, L., Boquien, M., et al. 2014a, *A&A*, 564, A67
- . 2014b, *A&A*, 564, A66
- Boselli, A., Fossati, M., Gavazzi, G., et al. 2015, *A&A*, 579, A102
- Boselli, A., & Gavazzi, G. 2006, *PASP*, 118, 517
- . 2014, *A&A Rev.*, 22, 74
- Boselli, A., Voyer, E., Boissier, S., et al. 2014c, *A&A*, 570, A69
- Boselli, A., Cuillandre, J. C., Fossati, M., et al. 2016, *A&A*, 587, A68
- Bower, R. G., Benson, A. J., Malbon, R., et al. 2006, *MNRAS*, 370, 645

- Boylan-Kolchin, M., Springel, V., White, S. D. M., Jenkins, A., & Lemson, G. 2009, MNRAS, 398, 1150
- Brammer, G. B., van Dokkum, P. G., & Coppi, P. 2008, ApJ, 686, 1503
- Brammer, G. B., Whitaker, K. E., van Dokkum, P. G., et al. 2009, ApJ, 706, L173
- Brammer, G. B., van Dokkum, P. G., Franx, M., et al. 2012, ApJS, 200, 13
- Brinchmann, J., Charlot, S., White, S. D. M., et al. 2004, MNRAS, 351, 1151
- Broeils, A. H., & Rhee, M.-H. 1997, A&A, 324, 877
- Bruzual, G., & Charlot, S. 2003, MNRAS, 344, 1000
- Burkert, A., Förster Schreiber, N. M., Genzel, R., et al. 2016, ApJ, 826, 214
- Byrd, G., & Valtonen, M. 1990, ApJ, 350, 89
- Calzetti, D., Armus, L., Bohlin, R. C., et al. 2000, ApJ, 533, 682
- Cappellari, M., & Emsellem, E. 2004, PASP, 116, 138
- Cardamone, C. N., van Dokkum, P. G., Urry, C. M., et al. 2010, ApJS, 189, 270
- Cardelli, J. A., Clayton, G. C., & Mathis, J. S. 1989, ApJ, 345, 245
- Catinella, B., Schiminovich, D., Cortese, L., et al. 2013, MNRAS, 436, 34
- Cayatte, V., Kotanyi, C., Balkowski, C., & van Gorkom, J. H. 1994, AJ, 107, 1003
- Cayatte, V., van Gorkom, J. H., Balkowski, C., & Kotanyi, C. 1990, AJ, 100, 604
- Cedr s, B., Beckman, J. E., Bongiovanni,  ., et al. 2013, ApJ, 765, L24
- Chabrier, G. 2003, PASP, 115, 763
- Cheung, E., Faber, S. M., Koo, D. C., et al. 2012, ApJ, 760, 131
- Cole, S. 1991, ApJ, 367, 45
- Cole, S., & Lacey, C. 1996, MNRAS, 281, 716
- Colless, M., Dalton, G., Maddox, S., et al. 2001, MNRAS, 328, 1039
- Conroy, C., Gunn, J. E., & White, M. 2009, ApJ, 699, 486
- Cooper, M. C., Newman, J. A., Madgwick, D. S., et al. 2005, ApJ, 634, 833
- Cooper, M. C., Newman, J. A., Croton, D. J., et al. 2006, MNRAS, 370, 198

- Cortese, L., Catinella, B., Boissier, S., Boselli, A., & Heinis, S. 2011, *MNRAS*, 415, 1797
- Cortese, L., Gavazzi, G., Boselli, A., et al. 2006, *A&A*, 453, 847
- Cortese, L., Bendo, G. J., Boselli, A., et al. 2010a, *A&A*, 518, L63
- Cortese, L., Davies, J. I., Pohlen, M., et al. 2010b, *A&A*, 518, L49
- Cortese, L., Ciesla, L., Boselli, A., et al. 2012a, *A&A*, 540, A52
- Cortese, L., Boissier, S., Boselli, A., et al. 2012b, *A&A*, 544, A101
- Cowan, N. B., & Ivezić, Ž. 2008, *ApJ*, 674, L13
- Cowie, L. L., & Songaila, A. 1977, *Nature*, 266, 501
- Croton, D. J., Farrar, G. R., Norberg, P., et al. 2005, *MNRAS*, 356, 1155
- Croton, D. J., Springel, V., White, S. D. M., et al. 2006, *MNRAS*, 365, 11
- Cucciati, O., Granett, B. R., Branchini, E., et al. 2014, *A&A*, 565, A67
- da Silva, R. L., Fumagalli, M., & Krumholz, M. R. 2014, *MNRAS*, 444, 3275
- Daddi, E., Dickinson, M., Morrison, G., et al. 2007, *ApJ*, 670, 156
- Darvish, B., Mobasher, B., Sobral, D., et al. 2016, *ArXiv e-prints*, arXiv:1605.03182
- Davis, M., Huchra, J., Latham, D. W., & Tonry, J. 1982, *ApJ*, 253, 423
- de Lapparent, V., Geller, M. J., & Huchra, J. P. 1986, *ApJ*, 302, L1
- De Lucia, G., & Blaizot, J. 2007, *MNRAS*, 375, 2
- De Lucia, G., Boylan-Kolchin, M., Benson, A. J., Fontanot, F., & Monaco, P. 2010, *MNRAS*, 406, 1533
- De Lucia, G., Kauffmann, G., Springel, V., et al. 2004, *MNRAS*, 348, 333
- De Lucia, G., Weinmann, S., Poggianti, B. M., Aragón-Salamanca, A., & Zaritsky, D. 2012, *MNRAS*, 423, 1277
- De Lucia, G., Poggianti, B. M., Aragón-Salamanca, A., et al. 2007, *MNRAS*, 374, 809
- de Vaucouleurs, G. 1959, *Handbuch der Physik*, 53, 275
- Dekel, A., & Birnboim, Y. 2006, *MNRAS*, 368, 2
- Dekel, A., Sari, R., & Ceverino, D. 2009, *ApJ*, 703, 785
- Dicke, R. H., Peebles, P. J. E., Roll, P. G., & Wilkinson, D. T. 1965, *ApJ*, 142, 414

- Dressler, A. 1980, *ApJ*, 236, 351
- Dressler, A., Oemler, Jr., A., Couch, W. J., et al. 1997, *ApJ*, 490, 577
- Ebeling, H., Voges, W., Bohringer, H., et al. 1996, *MNRAS*, 281, 799
- Einasto, J., Einasto, M., Tago, E., et al. 2007, *A&A*, 462, 811
- Eke, V. R., Baugh, C. M., Cole, S., et al. 2004, *MNRAS*, 348, 866
- Erben, T., Hildebrandt, H., Lerchster, M., et al. 2009, *A&A*, 493, 1197
- Erfanianfar, G., Finoguenov, A., Tanaka, M., et al. 2013, *ApJ*, 765, 117
- Erfanianfar, G., Popesso, P., Finoguenov, A., et al. 2016, *MNRAS*, 455, 2839
- Etherington, J., & Thomas, D. 2015, *MNRAS*, 451, 660
- Fabello, S., Kauffmann, G., Catinella, B., et al. 2012, *MNRAS*, 427, 2841
- Fang, J. J., Faber, S. M., Koo, D. C., & Dekel, A. 2013, *ApJ*, 776, 63
- Feast, M. W., & Catchpole, R. M. 1997, *MNRAS*, 286, L1
- Ferland, G. J., Fabian, A. C., Hatch, N. A., et al. 2008, *MNRAS*, 386, L72
- . 2009, *MNRAS*, 392, 1475
- Finoguenov, A., Guzzo, L., Hasinger, G., et al. 2007, *ApJS*, 172, 182
- Finoguenov, A., Watson, M. G., Tanaka, M., et al. 2010, *MNRAS*, 403, 2063
- Finoguenov, A., Tanaka, M., Cooper, M., et al. 2015, *A&A*, 576, A130
- Fitzpatrick, E. L. 1999, *PASP*, 111, 63
- Fontanot, F., De Lucia, G., Monaco, P., Somerville, R. S., & Santini, P. 2009, *MNRAS*, 397, 1776
- Fontanot, F., Springel, V., Angulo, R. E., & Henriques, B. 2012, *MNRAS*, 426, 2335
- Förster Schreiber, N. M., Genzel, R., Bouché, N., et al. 2009, *ApJ*, 706, 1364
- Fossati, M., Fumagalli, M., Boselli, A., et al. 2016a, *MNRAS*, 455, 2028
- Fossati, M., Gavazzi, G., Boselli, A., & Fumagalli, M. 2012, *A&A*, 544, A128
- Fossati, M., Wilman, D. J., Mendel, J. T., & et al. 2016b, *ApJ* *subm.*
- Fossati, M., Gavazzi, G., Savorgnan, G., et al. 2013, *A&A*, 553, A91

- Fossati, M., Wilman, D. J., Fontanot, F., et al. 2015, MNRAS, 446, 2582
- Franx, M., van Dokkum, P. G., Förster Schreiber, N. M., et al. 2008, ApJ, 688, 770
- Fumagalli, M., Fossati, M., Hau, G. K. T., et al. 2014, MNRAS, 445, 4335
- Fumagalli, M., Gavazzi, G., Scaramella, R., & Franzetti, P. 2011, A&A, 528, A46
- Fumagalli, M., Krumholz, M. R., Prochaska, J. X., Gavazzi, G., & Boselli, A. 2009, ApJ, 697, 1811
- Furusawa, H., Kosugi, G., Akiyama, M., et al. 2008, ApJS, 176, 1
- Gallazzi, A., & Bell, E. F. 2009, ApJS, 185, 253
- Gao, L., White, S. D. M., Jenkins, A., Stoehr, F., & Springel, V. 2004, MNRAS, 355, 819
- Gavazzi, G., Boselli, A., Mayer, L., et al. 2001, ApJ, 563, L23
- Gavazzi, G., Fumagalli, M., Cucciati, O., & Boselli, A. 2010, A&A, 517, A73
- Gavazzi, G., Fumagalli, M., Fossati, M., et al. 2013a, A&A, 553, A89
- Gavazzi, G., Savorgnan, G., Fossati, M., et al. 2013b, A&A, 553, A90
- Gavazzi, G., Consolandi, G., Dotti, M., et al. 2015, A&A, 580, A116
- Gavazzi, R., & Soucail, G. 2007, A&A, 462, 459
- Gawiser, E., van Dokkum, P. G., Herrera, D., et al. 2006, ApJS, 162, 1
- Geach, J. E., Simpson, C., Rawlings, S., Read, A. M., & Watson, M. 2007, MNRAS, 381, 1369
- Genzel, R., Förster Schreiber, N. M., Rosario, D., et al. 2014, ApJ, 796, 7
- Genzel, R., Tacconi, L. J., Lutz, D., et al. 2015, ApJ, 800, 20
- Gerke, B. F., Newman, J. A., Davis, M., et al. 2005, ApJ, 625, 6
- Gilli, R., Cimatti, A., Daddi, E., et al. 2003, ApJ, 592, 721
- Giocoli, C., Tormen, G., Sheth, R. K., & van den Bosch, F. C. 2010, MNRAS, 404, 502
- Giovanelli, R., & Haynes, M. P. 1985, ApJ, 292, 404
- Gómez, P. L., Nichol, R. C., Miller, C. J., et al. 2003, ApJ, 584, 210
- Goto, T. 2005, MNRAS, 359, 1415
- Graves, G. J., Faber, S. M., & Schiavon, R. P. 2009, ApJ, 693, 486

- Grogin, N. A., Kocevski, D. D., Faber, S. M., et al. 2011, *ApJS*, 197, 35
- Gunn, J. E., & Gott, III, J. R. 1972, *ApJ*, 176, 1
- Guo, Q., White, S., Angulo, R. E., et al. 2013a, *MNRAS*, 428, 1351
- Guo, Q., White, S., Boylan-Kolchin, M., et al. 2011, *MNRAS*, 413, 101
- Guo, Y., Ferguson, H. C., Giavalisco, M., et al. 2013b, *ApJS*, 207, 24
- Gutiérrez, L., & Beckman, J. E. 2010, *ApJ*, 710, L44
- Haas, M. R., Schaye, J., & Jeason-Daniel, A. 2012, *MNRAS*, 419, 2133
- Haines, C. P., Pereira, M. J., Smith, G. P., et al. 2015, *ApJ*, 806, 101
- Haynes, M. P., & Giovanelli, R. 1984, *AJ*, 89, 758
- Henriksen, M., & Byrd, G. 1996, *ApJ*, 459, 82
- Henriques, B. M. B., White, S. D. M., Thomas, P. A., et al. 2015, *MNRAS*, 451, 2663
- Hinshaw, G., Larson, D., Komatsu, E., et al. 2013, *ApJS*, 208, 19
- Hirschmann, M., De Lucia, G., & Fontanot, F. 2016, *MNRAS*, 461, 1760
- Hirschmann, M., De Lucia, G., Wilman, D., et al. 2014, *MNRAS*, 444, 2938
- Hirschmann, M., Somerville, R. S., Naab, T., & Burkert, A. 2012, *MNRAS*, 426, 237
- Hogg, D. W., Blanton, M. R., Eisenstein, D. J., et al. 2003, *ApJ*, 585, L5
- Hogg, D. W., Blanton, M. R., Brinchmann, J., et al. 2004, *ApJ*, 601, L29
- Hopkins, P. F., Hernquist, L., Cox, T. J., et al. 2006, *ApJS*, 163, 1
- Hsieh, B.-C., Wang, W.-H., Hsieh, C.-C., et al. 2012, *ApJS*, 203, 23
- Hsu, L.-T., Salvato, M., Nandra, K., et al. 2014, *ApJ*, 796, 60
- Hubble, E. 1929, *Proceedings of the National Academy of Science*, 15, 168
- Hubble, E., & Humason, M. L. 1931, *ApJ*, 74, 43
- Hubble, E. P. 1936, *Realm of the Nebulae*
- Ilbert, O., Arnouts, S., McCracken, H. J., et al. 2006, *A&A*, 457, 841
- Ilbert, O., Capak, P., Salvato, M., et al. 2009, *ApJ*, 690, 1236
- Isobe, T., Feigelson, E. D., Akritas, M. G., & Babu, G. J. 1990, *ApJ*, 364, 104

- Jáchym, P., Combes, F., Cortese, L., Sun, M., & Kenney, J. D. P. 2014, *ApJ*, 792, 11
- Jaffé, Y. L., Smith, R., Candlish, G. N., et al. 2015, *MNRAS*, 448, 1715
- Kapferer, W., Sluka, C., Schindler, S., Ferrari, C., & Ziegler, B. 2009, *A&A*, 499, 87
- Kauffmann, G., White, S. D. M., Heckman, T. M., et al. 2004, *MNRAS*, 353, 713
- Kauffmann, G., Heckman, T. M., Tremonti, C., et al. 2003, *MNRAS*, 346, 1055
- Kenney, J. D. P., Abramson, A., & Bravo-Alfaro, H. 2015, *AJ*, 150, 59
- Kenney, J. D. P., Tal, T., Crowl, H. H., Feldmeier, J., & Jacoby, G. H. 2008, *ApJ*, 687, L69
- Kennicutt, Jr., R. C. 1998a, *ARA&A*, 36, 189
- . 1998b, *ApJ*, 498, 541
- Kewley, L. J., Dopita, M. A., Sutherland, R. S., Heisler, C. A., & Trevena, J. 2001, *ApJ*, 556, 121
- Kimm, T., Somerville, R. S., Yi, S. K., et al. 2009, *MNRAS*, 394, 1131
- Knobel, C., Lilly, S. J., Iovino, A., et al. 2012, *ApJ*, 753, 121
- Knobel, C., Lilly, S. J., Kovač, K., et al. 2013, *ApJ*, 769, 24
- Kodama, T., Yamada, T., Akiyama, M., et al. 2004, *MNRAS*, 350, 1005
- Koekemoer, A. M., Faber, S. M., Ferguson, H. C., et al. 2011, *ApJS*, 197, 36
- Komatsu, E., Smith, K. M., Dunkley, J., et al. 2011, *ApJS*, 192, 18
- Koopmann, R. A., Haynes, M. P., & Catinella, B. 2006, *AJ*, 131, 716
- Kovač, K., Lilly, S. J., Cucciati, O., et al. 2010, *ApJ*, 708, 505
- Kovač, K., Lilly, S. J., Knobel, C., et al. 2014, *MNRAS*, 438, 717
- Kriek, M., van Dokkum, P. G., Labbé, I., et al. 2009, *ApJ*, 700, 221
- Kriek, M., Shapley, A. E., Reddy, N. A., et al. 2015, *ApJS*, 218, 15
- Kurk, J., Cimatti, A., Zamorani, G., et al. 2009, *A&A*, 504, 331
- Labbé, I., Huang, J., Franx, M., et al. 2005, *ApJ*, 624, L81
- Lacey, C., & Silk, J. 1991, *ApJ*, 381, 14
- Lang, P., Wuyts, S., Somerville, R. S., et al. 2014, *ApJ*, 788, 11

- Larson, R. B., Tinsley, B. M., & Caldwell, C. N. 1980, *ApJ*, 237, 692
- Le Fèvre, O., Tasca, L. A. M., Cassata, P., et al. 2015, *A&A*, 576, A79
- Lehmer, B. D., Brandt, W. N., Alexander, D. M., et al. 2005, *ApJS*, 161, 21
- Leitherer, C., Schaerer, D., Goldader, J. D., et al. 1999, *ApJS*, 123, 3
- Lewis, I., Balogh, M., De Propriis, R., et al. 2002, *MNRAS*, 334, 673
- Lilly, S. J., Carollo, C. M., Pipino, A., Renzini, A., & Peng, Y. 2013, *ApJ*, 772, 119
- Lilly, S. J., Le Fèvre, O., Renzini, A., et al. 2007, *ApJS*, 172, 70
- Limousin, M., Cabanac, R., Gavazzi, R., et al. 2009, *A&A*, 502, 445
- Ludlow, A. D., Navarro, J. F., Springel, V., et al. 2009, *ApJ*, 692, 931
- Madau, P., & Dickinson, M. 2014, *ARA&A*, 52, 415
- Madau, P., Ferguson, H. C., Dickinson, M. E., et al. 1996, *MNRAS*, 283, 1388
- Mamon, G. A., Sanchis, T., Salvador-Solé, E., & Solanes, J. M. 2004, *A&A*, 414, 445
- Maraston, C., Pforr, J., Renzini, A., et al. 2010, *MNRAS*, 407, 830
- Marchesini, D., van Dokkum, P. G., Förster Schreiber, N. M., et al. 2009, *ApJ*, 701, 1765
- Mastropietro, C., Moore, B., Mayer, L., et al. 2005, *MNRAS*, 364, 607
- McCracken, H. J., Milvang-Jensen, B., Dunlop, J., et al. 2012, *A&A*, 544, A156
- McGee, S. L., Balogh, M. L., Bower, R. G., Font, A. S., & McCarthy, I. G. 2009, *MNRAS*, 400, 937
- McGee, S. L., Bower, R. G., & Balogh, M. L. 2014, *MNRAS*, 442, L105
- McLean, I. S., Steidel, C. C., Epps, H. W., et al. 2012, in *Proc. SPIE*, Vol. 8446, Ground-based and Airborne Instrumentation for Astronomy IV, 84460J
- Mendel, J. T., Simard, L., Palmer, M., Ellison, S. L., & Patton, D. R. 2014, *ApJS*, 210, 3
- Mendel, J. T., Saglia, R. P., Bender, R., et al. 2015, *ApJ*, 804, L4
- Merluzzi, P., Busarello, G., Dopita, M. A., et al. 2016, *MNRAS*, 460, 3345
- . 2013, *MNRAS*, 429, 1747
- Merritt, D. 1984, *ApJ*, 276, 26

- Mihos, J. C. 2004, *Clusters of Galaxies: Probes of Cosmological Structure and Galaxy Evolution*, 277
- Miller, R. H. 1986, *A&A*, 167, 41
- Mo, H. J., Mao, S., & White, S. D. M. 1998, *MNRAS*, 295, 319
- Mok, A., Balogh, M. L., McGee, S. L., et al. 2013, *MNRAS*, 431, 1090
- . 2014, *MNRAS*, 438, 3070
- Momcheva, I. G., Brammer, G. B., van Dokkum, P. G., et al. 2016, *ApJS*, 225, 27
- Monaco, P., Fontanot, F., & Taffoni, G. 2007, *MNRAS*, 375, 1189
- Moore, B., Katz, N., Lake, G., Dressler, A., & Oemler, A. 1996, *Nature*, 379, 613
- Moore, B., Lake, G., & Katz, N. 1998, *ApJ*, 495, 139
- Morgan, W. W. 1961, *Proceedings of the National Academy of Science*, 47, 905
- Moy, E., Barmby, P., Rigopoulou, D., et al. 2003, *A&A*, 403, 493
- Muldrew, S. I., Croton, D. J., Skibba, R. A., et al. 2012, *MNRAS*, 419, 2670
- Muzzin, A., Marchesini, D., Stefanon, M., et al. 2013, *ApJ*, 777, 18
- Muzzin, A., van der Burg, R. F. J., McGee, S. L., et al. 2014, *ApJ*, 796, 65
- Navarro, J. F., Frenk, C. S., & White, S. D. M. 1997, *ApJ*, 490, 493
- Nelson, E. J., van Dokkum, P. G., Förster Schreiber, N. M., et al. 2016, *ApJ*, 828, 27
- Nishino, S., Fukazawa, Y., & Hayashi, K. 2012, *PASJ*, 64, doi:10.1093/pasj/64.1.16
- Noeske, K. G., Weiner, B. J., Faber, S. M., et al. 2007, *ApJ*, 660, L43
- Noll, S., Kausch, W., Kimeswenger, S., et al. 2014, *A&A*, 567, A25
- Nulsen, P. E. J. 1982, *MNRAS*, 198, 1007
- Oemler, Jr., A. 1974, *ApJ*, 194, 1
- Oke, J. B. 1974, *ApJS*, 27, 21
- Oman, K. A., & Hudson, M. J. 2016, *ArXiv e-prints*, arXiv:1607.07934
- Omand, C. M. B., Balogh, M. L., & Poggianti, B. M. 2014, *MNRAS*, 440, 843
- Osterbrock, D. E. 1989, *Astrophysics of gaseous nebulae and active galactic nuclei*

- Osterbrock, D. E., & Ferland, G. J. 2006, *Astrophysics of gaseous nebulae and active galactic nuclei*
- Paccagnella, A., Vulcani, B., Poggianti, B. M., et al. 2016, *ApJ*, 816, L25
- Papovich, C., Dickinson, M., & Ferguson, H. C. 2001, *ApJ*, 559, 620
- Papovich, C., Momcheva, I., Willmer, C. N. A., et al. 2010, *ApJ*, 716, 1503
- Peng, Y.-j., Lilly, S. J., Renzini, A., & Carollo, M. 2012, *ApJ*, 757, 4
- Peng, Y.-j., Lilly, S. J., Kovač, K., et al. 2010, *ApJ*, 721, 193
- Penzias, A. A., & Wilson, R. W. 1965, *ApJ*, 142, 419
- Phleps, S., Wilman, D. J., Zibetti, S., & Budavári, T. 2014, *MNRAS*, 438, 2233
- Planck Collaboration, Ade, P. A. R., Aghanim, N., et al. 2014, *A&A*, 571, A16
- Poggianti, B. M., Bridges, T. J., Komiyama, Y., et al. 2004, *ApJ*, 601, 197
- Poggianti, B. M., Desai, V., Finn, R., et al. 2008, *ApJ*, 684, 888
- Poggianti, B. M., Fasano, G., Omizzolo, A., et al. 2016, *AJ*, 151, 78
- Postman, M., & Geller, M. J. 1984, *ApJ*, 281, 95
- Quadri, R. F., Williams, R. J., Franx, M., & Hildebrandt, H. 2012, *ApJ*, 744, 88
- Reid, B. A., & Spergel, D. N. 2009, *ApJ*, 698, 143
- Rich, J. A., Kewley, L. J., & Dopita, M. A. 2011, *ApJ*, 734, 87
- Rodighiero, G., Daddi, E., Baronchelli, I., et al. 2011, *ApJ*, 739, L40
- Roediger, E., & Brüggen, M. 2007, *MNRAS*, 380, 1399
- Roediger, E., & Hensler, G. 2005, *A&A*, 433, 875
- Rudnick, G., von der Linden, A., Pelló, R., et al. 2009, *ApJ*, 700, 1559
- Saintonge, A., Kauffmann, G., Wang, J., et al. 2011, *MNRAS*, 415, 61
- Salimbeni, S., Castellano, M., Pentericci, L., et al. 2009, *A&A*, 501, 865
- Salpeter, E. E. 1955, *ApJ*, 121, 161
- Sandage, A. 1986, *A&A*, 161, 89
- Sanders, D. B., Soifer, B. T., Elias, J. H., et al. 1988, *ApJ*, 325, 74

- Sanders, D. B., Salvato, M., Aussel, H., et al. 2007, *ApJS*, 172, 86
- Sargent, M. T., Béthermin, M., Daddi, E., & Elbaz, D. 2012, *ApJ*, 747, L31
- Sarzi, M., Falcón-Barroso, J., Davies, R. L., et al. 2006, *MNRAS*, 366, 1151
- Schawinski, K., Urry, C. M., Simmons, B. D., et al. 2014, *MNRAS*, 440, 889
- Schechter, P. 1976, *ApJ*, 203, 297
- Schlafly, E. F., & Finkbeiner, D. P. 2011, *ApJ*, 737, 103
- Schlegel, D. J., Finkbeiner, D. P., & Davis, M. 1998, *ApJ*, 500, 525
- Schmidt, M. 1959, *ApJ*, 129, 243
- Schreiber, C., Pannella, M., Elbaz, D., et al. 2015, *A&A*, 575, A74
- Scoville, N., Aussel, H., Benson, A., et al. 2007, *ApJS*, 172, 150
- Shapley, A. E., Steidel, C. C., Erb, D. K., et al. 2005, *ApJ*, 626, 698
- Sharples, R., Bender, R., Agudo Berbel, A., et al. 2013, *The Messenger*, 151, 21
- Shattow, G. M., Croton, D. J., Skibba, R. A., et al. 2013, *MNRAS*, 433, 3314
- Shectman, S. A., Landy, S. D., Oemler, A., et al. 1996, *ApJ*, 470, 172
- Sivanandam, S., Rieke, M. J., & Rieke, G. H. 2010, *ApJ*, 717, 147
- Skelton, R. E., Whitaker, K. E., Momcheva, I. G., et al. 2014, *ApJS*, 214, 24
- Skibba, R. A., van den Bosch, F. C., Yang, X., et al. 2011, *MNRAS*, 410, 417
- Smith, R. J., Lucey, J. R., & Hudson, M. J. 2009, *MNRAS*, 400, 1690
- Smith, R. J., Lucey, J. R., Hammer, D., et al. 2010, *MNRAS*, 408, 1417
- Smoot, G. F., Bennett, C. L., Kogut, A., et al. 1992, *ApJ*, 396, L1
- Solanes, J. M., Manrique, A., García-Gómez, C., et al. 2001, *ApJ*, 548, 97
- Somerville, R. S., & Primack, J. R. 1999, *MNRAS*, 310, 1087
- Springel, V., White, S. D. M., Tormen, G., & Kauffmann, G. 2001, *MNRAS*, 328, 726
- Springel, V., White, S. D. M., Jenkins, A., et al. 2005, *Nature*, 435, 629
- Storey, P. J., & Zeppen, C. J. 2000, *MNRAS*, 312, 813
- Strateva, I., Ivezić, Ž., Knapp, G. R., et al. 2001, *AJ*, 122, 1861

- Sun, M., Donahue, M., Roediger, E., et al. 2010, *ApJ*, 708, 946
- Sun, M., Donahue, M., & Voit, G. M. 2007, *ApJ*, 671, 190
- Sun, M., Jones, C., Forman, W., et al. 2006, *ApJ*, 637, L81
- Sunyaev, R. A., & Zeldovich, Y. B. 1972, *Comments on Astrophysics and Space Physics*, 4, 173
- Tacconi, L. J., Neri, R., Genzel, R., et al. 2013, *ApJ*, 768, 74
- Tanaka, M., Finoguenov, A., & Ueda, Y. 2010, *ApJ*, 716, L152
- Taniguchi, Y., Scoville, N., Murayama, T., et al. 2007, *ApJS*, 172, 9
- Tasca, L. A. M., Le Fevre, O., Ribeiro, B., et al. 2016, *ArXiv e-prints*, arXiv:1602.01842
- Taylor, E. N., Franx, M., van Dokkum, P. G., et al. 2009, *ApJS*, 183, 295
- Tonnesen, S., & Bryan, G. L. 2009, *ApJ*, 694, 789
- . 2010, *ApJ*, 709, 1203
- . 2012, *MNRAS*, 422, 1609
- Tonnesen, S., Bryan, G. L., & Chen, R. 2011, *ApJ*, 731, 98
- Trevese, D., Castellano, M., Fontana, A., & Giallongo, E. 2007, *A&A*, 463, 853
- Trinh, C. Q., Barton, E. J., Bullock, J. S., et al. 2013, *MNRAS*, 436, 635
- van den Bosch, F. C., Aquino, D., Yang, X., et al. 2008, *MNRAS*, 387, 79
- van der Burg, R. F. J., Muzzin, A., Hoekstra, H., et al. 2013, *A&A*, 557, A15
- Vazdekis, A., Sánchez-Blázquez, P., Falcón-Barroso, J., et al. 2010, *MNRAS*, 404, 1639
- Villalobos, Á., De Lucia, G., Borgani, S., & Murante, G. 2012, *MNRAS*, 424, 2401
- Vollmer, B., Cayatte, V., Balkowski, C., & Duschl, W. J. 2001, *ApJ*, 561, 708
- Wang, J., De Lucia, G., Kitzbichler, M. G., & White, S. D. M. 2008, *MNRAS*, 384, 1301
- Wang, L., Li, C., Kauffmann, G., & De Lucia, G. 2006, *MNRAS*, 371, 537
- Wang, L., Weinmann, S. M., & Neistein, E. 2012, *MNRAS*, 421, 3450
- Weiner, B. J., Phillips, A. C., Faber, S. M., et al. 2005, *ApJ*, 620, 595
- Weinmann, S. M., Kauffmann, G., von der Linden, A., & De Lucia, G. 2010, *MNRAS*, 406, 2249

- Weinmann, S. M., van den Bosch, F. C., Yang, X., & Mo, H. J. 2006, *MNRAS*, 366, 2
- Wetzel, A. R., Tinker, J. L., & Conroy, C. 2012, *MNRAS*, 424, 232
- Wetzel, A. R., Tinker, J. L., Conroy, C., & van den Bosch, F. C. 2013, *MNRAS*, 432, 336
— . 2014, *MNRAS*, 439, 2687
- Whitaker, K. E., van Dokkum, P. G., Brammer, G., & Franx, M. 2012, *ApJ*, 754, L29
- Whitaker, K. E., Labbé, I., van Dokkum, P. G., et al. 2011, *ApJ*, 735, 86
- Whitaker, K. E., Franx, M., Leja, J., et al. 2014, *ApJ*, 795, 104
- White, S. D. M., & Frenk, C. S. 1991, *ApJ*, 379, 52
- White, S. D. M., & Rees, M. J. 1978, *MNRAS*, 183, 341
- Williams, R. J., Quadri, R. F., Franx, M., van Dokkum, P., & Labbé, I. 2009, *ApJ*, 691, 1879
- Wilman, D. J., Fontanot, F., De Lucia, G., Erwin, P., & Monaco, P. 2013, *MNRAS*, 433, 2986
- Wilman, D. J., Zibetti, S., & Budavári, T. 2010, *MNRAS*, 406, 1701
- Wisnioski, E., Förster Schreiber, N. M., Wuyts, S., et al. 2015, *ApJ*, 799, 209
- Woo, J., Dekel, A., Faber, S. M., et al. 2013, *MNRAS*, 428, 3306
- Woudt, P. A., Kraan-Korteweg, R. C., Lucey, J., Fairall, A. P., & Moore, S. A. W. 2008, *MNRAS*, 383, 445
- Wright, E. L. 2006, *PASP*, 118, 1711
- Wuyts, E., Kurk, J., Förster Schreiber, N. M., et al. 2014, *ApJ*, 789, L40
- Wuyts, E., Wisnioski, E., Fossati, M., et al. 2016a, *ApJ*, 827, 74
- Wuyts, S., Franx, M., Cox, T. J., et al. 2009, *ApJ*, 696, 348
- Wuyts, S., Labbé, I., Franx, M., et al. 2007, *ApJ*, 655, 51
- Wuyts, S., Förster Schreiber, N. M., Wisnioski, E., et al. 2016b, *ArXiv e-prints*, arXiv:1603.03432
- Yagi, M., Komiyama, Y., Yoshida, M., et al. 2007, *ApJ*, 660, 1209
- Yagi, M., Yoshida, M., Komiyama, Y., et al. 2010, *AJ*, 140, 1814

-
- Yang, X., Mo, H. J., & van den Bosch, F. C. 2008, *ApJ*, 676, 248
- Yang, X., Mo, H. J., van den Bosch, F. C., & Jing, Y. P. 2005, *MNRAS*, 356, 1293
- Yang, X., Mo, H. J., van den Bosch, F. C., et al. 2007, *ApJ*, 671, 153
- York, D. G., Adelman, J., Anderson, Jr., J. E., et al. 2000, *AJ*, 120, 1579
- Yoshida, M., Yagi, M., Komiyama, Y., et al. 2012, *ApJ*, 749, 43
- Yoshida, M., Yagi, M., Okamura, S., et al. 2002, *ApJ*, 567, 118
- Zibetti, S., Charlot, S., & Rix, H.-W. 2009, *MNRAS*, 400, 1181

Acknowledgements

At the end of this long path, I would like to thank all the people who have been close to me at work and outside, during the alternating fortunes of these years. Foremost, I would like to thank Dr. David (“Dave”) Wilman for his guidance, patience and efforts to help and teach me through my research project. This thesis would not have been possible without the long scientific (and not) discussions we had weekly and sometimes daily. Thanks for giving me advices through these intense years of PhD and stimulating me to always trying to do better. My deepest gratitude goes also to my PhD supervisor P.D. Dr. Roberto Saglia, who gave me the opportunity to work in this exceptional group and environment, and carefully advised me throughout the most important steps that lead to this manuscript. This work would have not been the same without the help of the other members of the KMOS team; I would like to thank Trevor Mendel, Alessandra Beifiori, Audrey Galametz, and Jeffrey Chan for the formal and informal discussions, and for all the time spent answering my questions. Thanks to Martha for your careful job of translating the abstract in German. A special thank goes to Audrey for the long nights spent at the VLT in Paranal and discussing science while hiking up to the telescopes.

I would like to thank my external collaborators Giuseppe (“Peppo”) Gavazzi and Alessandro (“Ale”) Boselli, for infecting me at every Skype call with your endless enthusiasm in astronomy (which is one of the reasons I entered this research field a few years ago). I always look forward to meet you at conferences or when I come back to Italy. An even deeper thank goes to Michele Fumagalli for the prompt feedback on my questions in almost every field of astronomy; I feel honored to be one of your collaborators. Chapter 5 of this thesis would not have existed at all without a series of fortunate coincidences. First the conference organized by Ale for Peppo’s 65th birthday, where we gathered to celebrate the “colors of galaxies”. It is in this wonderful environment on the lake of Como that Michele and I first discussed the possibility of writing a MUSE proposal. This was the first seed that developed into a very exciting research.

I am deeply grateful to my parents for their love, support and presence even if we live in two different countries.

Then I wish to thank my friends for always supporting me during these years. My deepest thank to Giulia for always being present for an afternoon downtown, or hiking, or having dinner at San Marco. Thanks also for your Nespresso machine that provided me the fuel for a lot of difficult starts in the morning. Also I really enjoyed bringing you to Hallbergmoos to have your car fixed, but I hope this is not necessary anymore. Thanks to

Alessandro for always being unbiased and above any problem, I wish I could have been like you in some situations. Thanks to Simone, I enjoyed your company when you have been here. Thanks to Andrea and Lucrezia for remembering me of Cogoleto with your pesto, for asking if the lamb is really lamb at the indian restaurant and for several other occasions which I do not recall now. Lastly I thank Francesco, Marie, Li-Ting, and the new friends from the CAS group: Elena, Michela, Domenico for the jokes, the laughs and all the fun we had together. I will really miss you all.

Thanks to my “italian” friends, starting from Avv. Federico, I hope to see you soon in Cogoleto. Then I thank Paolo and Ale (“il piccolo”) for the two summer adventures on the Alps; the weather has not always been nice but nothing could have stopped us (ok maybe the snow on Bepi Zac was about to change our plans). I missed the 2016 expedition but I am looking forward to start the planning for the next summer. Thanks to Guido, Ale Lupi, Davide, Mery and Laura for always being available for a drink when I come back home.

I acknowledge the financial support of the Deutsche Forschungsgemeinschaft via Projects WI 3871/1-1 and WI 3871/1-2.